RIVER RESPONSE TO SEDIMENT SUPPLY: THE SAND BED CASE

by

Christina M. Leonard

A dissertation submitted in partial fulfillment
of the requirements for the degree

of

DOCTOR OF PHILOSOPHY

in

Watershed Science

Approved:

_____   _____
John C. Schmidt, Ph.D.   Peter R. Wilcock, Ph.D.
Major Professor   Committee Member

_____   _____
Colin B. Phillips, Ph.D.   Joseph M. Wheaton, Ph.D.
Committee Member   Committee Member

_____   _____
Tammy M. Rittenour, Ph.D.   D. Richard Cutler, Ph.D.
Committee Member   Vice Provost of Graduate Studies

UTAH STATE UNIVERSITY
Logan, Utah

2022

ABSTRACT

River Response to Sediment Supply: The Sand Bed Case

by

Christina M. Leonard, Doctor of Philosophy

Utah State University, 2022

Major Professor: John C. Schmidt
Department: Watershed Sciences

The form of rivers is largely determined by the stream-flow regime and the
amount and size of the sediment supplied to the channel. When the water and/or sediment
supply change, the short-term channel response will be a combination of sediment
accumulation and evacuation and changes in the bed grain size. These changes can affect
the capacity of the channel to contain flood flows and can positively or negatively affect
the attributes and availability of aquatic or riparian habitat. Conditions of sediment deficit
or surplus can lead to subsequent morphologic change, but the rate, timing, and
magnitude of this adjustment can be moderated by adjustments in the river bed grain size.
The river bed texture can fine or coarsen, making the river more or less efficient at
transporting sediment, which influences the magnitude of the morphologic response.
From a management perspective, it is important to identify circumstances under which a
watershed disturbance is expected to cause meaningful channel change in contrast to
when the response is predominately textural.

This dissertation examines the interaction among sediment supply rate and grain
size with bed texture and sediment mass balance in sand bed rivers. We infer the bed
textural response in a field setting where the sediment mass balance is measured and use

a set of numerical experiments to help interpret the results from our field setting. We show that sediment is sorted throughout the alluvial channel and floodplain such that a size fractional sediment budget is needed to evaluate the channel response. Even though the overall sand budget is balanced, our size fractional budget shows channel bed coarsening while certain parts of the floodplain accumulate very fine sand. Our numerical modeling indicates bed textural changes can enhance, reverse, or even eliminate potential aggradation in response to an increase in sediment supply depending on how the supply grain size changes. If the supply increase is only temporary, such as in our field study, aggradation may never occur, because bed fining may be sufficient to transport the initial pulse of sediment through the system. There are two major findings that emerged from this dissertation. First, a size fractional sediment budget is needed to evaluate the interaction among supply rate and grain size with bed texture and channel change, and second, the magnitude and style of channel change is strongly influenced by the textural response.

(245 pages)

PUBLIC ABSTRACT

River Response to Sediment Supply: The Sand Bed Case

Christina M. Leonard

Effective management of in-channel and floodplain habitat requires an ability to forecast river response to changes in water and sediment supply. These changes may result from dam construction/decommissioning, changes in reservoir operations, or changes in grazing or forestry practices. If a change in water and sediment supply causes sediment to be delivered faster than the channel's capacity to transport it, sediment will accumulate in the reach, leading to changes in channel form and increasing the potential for flooding. A decrease in sediment supply relative to transport capacity can lead to channel incision. The extent and timing of sediment accumulation or evacuation can be moderated, even reversed, by poorly understood changes in the river bed grain size. This dissertation explores the joint response of river bed texture and sediment storage in order to better predict the magnitude of channel change in response to upstream changes in infrastructure or land use in sand bed rivers. We use a combination of field measurements of sediment transport, analysis of channel change from repeat aerial images, and numerical modeling to explore the interaction among sediment supply rate and grain size with bed grain size and morphologic adjustment. We find that sand sizes are sorted throughout the alluvial channel and floodplain such that the in-channel response may be different than floodplain adjustments. At our field site, certain sand sizes evacuate as the bed coarsened while other sand sizes accumulated in the floodplains. These findings indicate that conditions of sediment accumulation or evacuation cannot reveal important

changes in the river and size fractional sediment budgets are needed to evaluate channel change. Our numerical modeling indicates that the supply grain size has a strong effect on the grain size of sand on the bed, making the river more or less effective at transporting sediment. Under conditions when the sediment supply increases, such as after wildfires, dam removals, or changes in land use or forestry practices, small changes in the grain size of sand on the channel bed can cause sediment to accumulate, evacuate, or there may be no morphologic adjustment depending on the length of the disturbance and how the supply grain size changes. This has important implications for forecasting downstream impacts. Management concerns may be delayed or even eliminated depending on the bed grain size response. These findings demonstrate the importance of considering the supply grain size and behavior and destination of the fractional sizes in transport when predicting a sand-bed river response to a watershed disturbance.

ACKNOWLEDGMENTS

It has not always been apparent to me that I wanted a doctoral degree. My desire to take on this challenge evolved slowly as my career and life experience shaped my professional goals. For this, I owe much gratitude to my early career experience with the U.S. Army Corps of Engineers, where I developed a passion for rivers and intrigue about how we manage them. It was through this work that I became acutely aware of the many challenges involved in managing a finite resource for multiple interests. This motivated me to pursue a Ph.D. and kept my passion for rivers strong throughout my doctoral program. I wouldn't be writing this acknowledgment if I hadn't started my career as a geologist at the U.S. Army Corps of Engineers, so huge thanks to this federal agency!

Many people have shaped my development as a scientist during my doctoral studies. My advisor, Jack Schmidt, is among the most influential. Jack challenges me to see the 'big picture'. He helps pull me out of the weeds so I can see why my research matters in the real world. He taught me to seek questions that are relevant to river management and society and to communicate my findings in a way that can be understood by the broader public, not just those in my narrow academic field. Jack inspires me to be a river scientist who influences policy in the "brave new world". I have learned much from Jack and will continue to learn much from him in the years to come. I'm also grateful for the mentorship of Peter Wilcock. Peter has shown me that sometimes we need to understand the nitty-gritty details of a problem so we can clearly and concisely explain the final solution. Peter has a remarkable ability to effectively communicate very complex concepts. He inspires me to continue honing my communication skills so that I can one day be as eloquent of a communicator. Finally, I'd

like to thank my remaining committee members: Colin Phillips, Tammy Rittenour, and Joe Wheaton, who have supported me in my dissertation research and professional development. I'm grateful for your invitations to participate in reading groups, for passing along job opportunities, and for taking the time to give me constructive feedback on my research.

One of the highlights of my Ph.D. experience has been mentoring several undergraduate students. Thank you, Zach Burgert, Thom Jukes, and Naomi Orchard, for your budding enthusiasm for rivers. I've enjoyed working with each of you, and I'm grateful to have had the opportunity to pass down my knowledge of rivers to the next generation. I also thank the many people who joined me in the field, including Soda Davidson, Cody Perry, John Kemper, Sara Rathburn, Jonathan Freedman, and Erich Mueller. I'm grateful for the support of the sediment group at the USGS Grand Canyon Monitoring and Research Center, including David Topping, Ron Griffiths, and Joel Unema. I also thank Scott Wright for providing a version of the modeling code used in Wright and Parker (2005a), which expedited our development of the morphodynamic model in Chapter 4.

My research was made possible by financial assistance from several funding sources. The Center for Colorado River Studies Doctoral Scholar Program and the P.E.O. foundation funded my Ph.D. program. I'm also grateful for funding provided by the Babbitt Center for Land and Water Policy and the Geologic Society of America which was used to support my dissertation research.

Finally, I could not have taken on this Ph.D. endeavor without the support of my husband, Toby Stegman, and daughter, Malacha Leonard. Toby is the oil that kept my

engine running through this process. Malacha followed me around the country, from

Vermont, to Wyoming, and finally to Utah, as I pursued my various academic degrees.

For this, she deserves some sort of degree herself! I'll end with a quote from 10-year-old

Malacha when asked if we should move, yet again, for her mom to start a Ph.D. program.

"Someone is going to pay you to be a doctor? Of course, you have to do it, Mom!". What

simple, logical advice from a child! Thanks for accompanying me on this adventure,

kiddo.

Christina Leonard

CONTENTS

LIST OF TABLES

LIST OF FIGURES

CHAPTER 1

INTRODUCTION

The form and characteristics of river channels and their floodplains are largely determined by the stream-flow regime and the amount and size of sediment supplied from the watershed. Equilibrium is maintained if the amount of sediment entering a reach is approximately equal to the amount of sediment leaving a reach. Changes in flow or sediment supply from upstream can change one or both of the supply of sediment or the capacity of the reach to transport sediment, thereby perturbing the sediment mass balance. The short-term channel response will be a combination of adjustments in the bed material grain size and sediment accumulation or evacuation. Changes in bed texture and sediment storage then drive bank erosion, channel shifting, or changes in the characteristics of the channel and/or floodplain that affect the ability of the channel to contain floods, damage downstream infrastructure, and change the attributes and characteristics of aquatic and riparian habitats. Effective river management depends on the ability to forecast the river response to change in water or sediment supply.

Predicting how a river channel responds to a change in drivers is an enduring problem in the field of geomorphology. There is a long and rich geomorphic literature that relates the style of channel adjustment to change in flow or sediment supply. The rate, timing, and magnitude of channel change differs wildly among case studies (Schumm, 1969; Leopold, 1973; Trimble, 1981; Williams and Wolman, 1984; Knighton, 1989; Everitt, 1993; Pizzuto, 1994; Brandt, 2000a, 2000b; Clark and Wilcock, 2000; Simon Andrew et al., 2002; Grant et al., 2003; Schmidt and Wilcock, 2008; East et al., 2015). One factor that causes this variability is the interaction between the supply grain

size and the bed grain size. Change in the sediment supply grain size may cause the bed

material to fine or coarsen, making the reach more or less efficient at transporting

sediment (Buffington and Montgomery, 1999; Montgomery et al., 1999; Lisle et al.,

2000; Topping et al., 2000; Cui et al., 2005; Sklar et al., 2009; Ferguson et al., 2015;

Dean et al., 2016; Topping et al., 2018; Dean et al., 2020; Topping et al., 2021). A reach

might quickly respond to an increase in upstream sediment supply that is of a finer grain

size by bed fining, allowing the reach to efficiently transport the increased influx before

any significant channel change occurs. In this instance, the upstream perturbation may

cause little to no morphological response. Alternatively, the bed may coarsen in response

to an increase in sediment supply that is of a coarser grain size, which makes the reach

less efficient at transporting sediment leading to channel change.

The interaction between supply and supply grain size and how it affects the

sediment mass balance is well-documented in gravel-bed rivers (Dietrich et al., 1989;

Buffington and Montgomery, 1999; Lisle et al., 2000; Cui et al., 2003a, 2003c; Sklar et

al., 2009; Venditti et al., 2010). Much less attention has been directed to the influence of

bed textural adjustment on channel change in sand-bed rivers where bed sorting is harder

to observe. In such systems, there is evidence that changes in the grain size of

suspendable sand have a strong effect on bed texture which creates large spatial gradients

in sand transport that allow excess sand to move through the system quickly (Rubin et al.,

2020; Topping et al., 2021). How the textural response influences channel change has not

been fully considered in sand bed rivers and motivates this dissertation research.

Chapters 2 and 3 explore the bed texture and morphological response to a known

perturbation in sediment supply on an alluvial sand-bed section of the Yampa River,

Colorado. Reach-scale sediment accumulation and evacuation are measured over 6 years using high temporal resolution measurements of sediment transport from a network of acoustical sediment gages (Topping and Wright, 2016; Topping et al., 2018). The acoustic sediment gages measure suspended sediment transport at temporal resolutions that directly link sediment accumulation or evacuation to characteristics (or changes) in the flow and sediment regimes. However, such measurements cannot resolve where between the gages the sediment erodes or deposits and, hence, the morphological response. Therefore, change in channel morphology is measured from repeat aerial images and topographic data using a novel technique to estimate uncertainty. Bed textural change is inferred from a sediment budget partitioned by grain size.

Chapter 2 presents a new generalizable method for quantifying the uncertainty associated with measurements of channel change from repeat aerial images. Measurements of channel change from repeat aerial images are only significant if the magnitude of change exceeds uncertainty in the aerial photo analysis (Downward et al., 1994). There is a wide range of methods developed to quantify this uncertainty and each varies in rigor and complexity (Lyons et al., 1992; Winterbottom and Gilvear, 2000; Gaeuman et al., 2005; Lea and Legleiter, 2016). The lack of a standardized uncertainty method is problematic, because channel change may be significant using one method and insignificant with another. The method developed in Chapter 2 is an improvement to previous approaches because uncertainty is allowed to vary along the river corridor. The output is a probability distribution, rather than a single value with an uncertainty bound. The method is generalizable and can be applied to all metrics of channel change from repeat aerial images, and we develop a standalone software program for this purpose.

Chapter 3 compares the change in channel morphology to the change in sediment storage calculated from measurements of sediment transport on the Yampa River. We take a novel approach to sediment budgeting by establishing a sediment mass balance for multiple size fractions. Partitioning the sediment mass balance into grain-size fractions allows for the measurement of small-to-moderate geomorphic adjustments and bed texture change that might be undetectable if all sand sizes are considered together. It also allows consideration of the location of the morphologic change based on size partitioning between channel and floodplain. Planform channel change is calculated using the method in Chapter 2 and converted to a volumetric change in morphology using an innovative extrapolation of sparse topographic data. The grain size distribution of the channel bed and floodplain stratigraphy is used to partition the volumetric change in channel morphology by sand size. Uncertainty is estimated using a Bayesian approach. The volumetric change in channel morphology for each sand grain size is compared to the reach-scale amount of erosion and deposition from transport measurements to determine when and where channel change occurs.

Chapter 4 presents a multi-fraction morphodynamic model that is used to explore the interaction between bed texture and bed topography to changes in sediment supply in sand-bed rivers. The goal is to demonstrate the nature and conditions of strong textural response over topographic response. A morphodynamic model evolves the bed grain size and bed topography from an initial steady-state to a new steady-state in response to a change in the supply rate and grain size. A similar experimental approach has been used to understand how supply causes textural and bed elevation changes in gravel-bed rivers (Cui et al., 2003b, 2003c; Cui and Parker, 2005). This chapter extends that research to

sand-bed rivers. The model uses 1D hydraulics and allows two forms of adjustment: bed texture and channel slope from sediment accumulation or evacuation. In real rivers, textural and topographic bed changes will lead to changes in channel geometry, planform, sinuosity, or organization of in-channel geomorphic features. The purpose of our model is to evaluate the purely transport response between bed texture and sediment storage. Thus, slope adjustment represents change in sediment storage. Upstream sediment supply rates and supply grain sizes are chosen to mimic the range of conditions observed in sand-bed rivers. An initial phase of simulations is used to determine steady-state slope and bed texture as a function of discharge, sediment supply rate, and grain size. A second set of simulations evaluates the path of mutual adjustment between bed texture and topography between initial and final steady state transport conditions.

Chapter 5 summarizes the main contributions of the research. The results are synthesized using a field comparison of two disturbances on the Yampa River that produced different textural and morphologic responses. The numerical modeling is used to help interpret the contrasting textural and morphologic results between the two case studies.

References

Brandt SA. 2000a. Classification of geomorphological effects downstream of dams. CATENA **40** : 375–401. DOI: 10.1016/S0341-8162(00)00093-X

Brandt SA. 2000b. Prediction of downstream geomorphological changes after dam construction: A steam power approach. International Journal of Water Resources Development; Abingdon **16** : 343.

Buffington JM, Montgomery DR. 1999. Effects of sediment supply on surface textures of gravel-bed rivers. Water Resources Research **35** : 3523–3530. DOI: 10.1029/1999WR900232

Clark JJ, Wilcock PR. 2000. Effects of land-use change on channel morphology in northeastern Puerto Rico. GSA Bulletin **112** : 1763–1777. DOI: 10.1130/0016-7606(2000)112<1763:EOLUCO>2.0.CO;2

Cui Y, Parker, G. G, Lisle TE, Gott J, Hansler-Ball ME, Pizzuto JE, Allmendinger NE, Reed JM. 2003a. Sediment pulses in mountain rivers: 1. Experiments. Water Resources Research **39** : 1239. DOI: 10.1029/2002WR001803

Cui Y, Parker G, Lisle TE, Gott J, Hansler-Ball ME, Pizzuto JE, Allmendinger NE, Reed JM. 2003b. Sediment pulses in mountain rivers: 1. Experiments. Water Resources Research **39** DOI: 10.1029/2002WR001803

Cui Y, Parker G, Lisle TE, Pizzuto JE, Dodd AM. 2005. More on the evolution of bed material waves in alluvial rivers. Earth Surface Processes and Landforms **30** : 107–114. DOI: 10.1002/esp.1156

Cui Y, Parker G, Pizzuto J, Lisle TE. 2003c. Sediment pulses in mountain rivers: 2. Comparison between experiments and numerical predictions. Water Resources Research **39** : 1240. DOI: 10.1029/2002WR001805

Cui Y, Parker P. 2005. Numerical Model of Sediment Pulses and Sediment-Supply Disturbances in Mountain Rivers. Journal of Hydraulic Engineering **131** : 646–656. DOI: 10.1061/(ASCE)0733-9429(2005)131:8(646)

Dean DJ, Topping DJ, Grams PE, Walker AE, Schmidt JC. 2020. Does Channel Narrowing by Floodplain Growth Necessarily Indicate Sediment Surplus? Lessons From Sediment Transport Analyses in the Green and Colorado Rivers, Canyonlands, Utah. Journal of Geophysical Research: Earth Surface **125** : e2019JF005414. DOI: 10.1029/2019JF005414

Dean DJ, Topping DJ, Schmidt JC, Griffiths RE, Sabol TA. 2016. Sediment supply versus local hydraulic controls on sediment transport and storage in a river with large sediment loads. Journal of Geophysical Research: Earth Surface **121** : 2015JF003436. DOI: 10.1002/2015JF003436

Dietrich WE, Kirchner JW, Ikeda H, Iseya F. 1989. Sediment supply and the development of the coarse surface layer in gravel-bedded rivers. Nature **340** : 215–217. DOI: 10.1038/340215a0

Downward SR, Gurnell AM, Brookes A. 1994. A methodology for quantifying river channel planform change using GIS. IAHS Publications-Series of Proceedings and Reports-Intern Assoc Hydrological Sciences **224** : 449–456.

East AE et al. 2015. Large-scale dam removal on the Elwha River, Washington, USA: River channel and floodplain geomorphic change. Geomorphology **228** : 765–786. DOI: 10.1016/j.geomorph.2014.08.028

Everitt B. 1993. Channel responses to declining flow on the Rio Grande between Ft. Quitman and Presidio, Texas. Geomorphology **6** : 225–242. DOI: 10.1016/0169-555X(93)90048-7

Ferguson RI, Church M, Rennie CD, Venditti JG. 2015. Reconstructing a sediment pulse: Modeling the effect of placer mining on Fraser River, Canada. Journal of Geophysical Research: Earth Surface **120** : 2015JF003491. DOI: 10.1002/2015JF003491

Gaeuman D, Symanzik J, Schmidt JC. 2005. A map overlay error model based on boundary geometry. Geographical Analysis **37** : 350–369. DOI: 10.1111/j.1538-4632.2005.00585.x

Grant GE, Schmidt JC, Lewis SL. 2003. A Geological Framework for Interpreting Downstream Effects of Dams on Rivers. In A Peculiar River , O'Connor JE and Grant GE (eds). American Geophysical Union; 203–219.

Knighton AD. 1989. River adjustment to changes in sediment load: The effects of tin mining on the Ringarooma River, Tasmania, 1875–1984. Earth Surface Processes and Landforms **14** : 333–359. DOI: 10.1002/esp.3290140408

Lea DM, Legleiter CJ. 2016. Refining measurements of lateral channel movement from image time series by quantifying spatial variations in registration error. Geomorphology **258** : 11–20. DOI: 10.1016/j.geomorph.2016.01.009

Leopold LB. 1973. River Channel Change with Time: An Example: Address as Retiring President of The Geological Society of America, Minneapolis, Minnesota, November 1972. GSA Bulletin **84** : 1845–1860. DOI: 10.1130/0016-7606(1973)84<1845:RCCWTA>2.0.CO;2

Lisle TE, Nelson JM, Pitlick J, Madej MA, Barkett BL. 2000. Variability of bed mobility in natural, gravel-bed channels and adjustments to sediment load at local and reach scales. Water Resources Research **36** : 3743–3755. DOI: 10.1029/2000WR900238

Lyons JK, Pucherelli MJ, Clark RC. 1992. Sediment transport and channel characteristics of a sand-bed portion of the Green River below Flaming Gorge Dam, Utah, USA. Regulated Rivers: Research & Management **7** : 219–232. DOI: 10.1002/rrr.3450070302

Montgomery DR, Panfil MS, Hayes SK. 1999. Channel-bed mobility response to extreme sediment loading at Mount Pinatubo. Geology **27** : 271–274. DOI: 10.1130/0091-7613(1999)027<0271:CBMRTE>2.3.CO;2

Pizzuto JE. 1994. Channel adjustments to changing discharges, Powder River, Montana. GSA Bulletin **106** : 1494–1501. DOI: 10.1130/0016-7606(1994)106<1494:CATCDP>2.3.CO;2

Rubin DM, Buscombe D, Wright SA, Topping DJ, Grams PE, Schmidt JC, Hazel JE, Kaplinski MA, Tusso R. 2020. Causes of Variability in Suspended-Sand Concentration Evaluated Using Measurements in the Colorado River in Grand Canyon. Journal of Geophysical Research: Earth Surface **125** : e2019JF005226. DOI: 10.1029/2019JF005226

Schmidt JC, Wilcock PR. 2008. Metrics for assessing the downstream effects of dams. Water Resources Research **44** : W04404. DOI: 10.1029/2006WR005092

Schumm SA. 1969. River metamorphosis. Journal of the Hydraulics division **95** : 255–274.

Simon Andrew, Thomas Robert E., Curini Andrea, Shields F. Douglas. 2002. Case Study: Channel Stability of the Missouri River, Eastern Montana. Journal of Hydraulic Engineering **128** : 880–890. DOI: 10.1061/(ASCE)0733-9429(2002)128:10(880)

Sklar LS, Fadde J, Venditti JG, Nelson P, Wydzga MA, Cui Y, Dietrich WE. 2009. Translation and dispersion of sediment pulses in flume experiments simulating gravel augmentation below dams. Water resources research **45** DOI: https://doi.org/10.1029/2008WR007346

Topping DJ, Grams PE, Griffiths RE, Dean DJ, Wright SA, Unema JA. 2021. Self-limitation of sand storage in a bedrock-canyon river arising from the interaction of flow and grain size. Journal of Geophysical Research: Earth Surface **n/a** : e2020JF005565. DOI: https://doi.org/10.1029/2020JF005565

Topping DJ, Mueller ER, Schmidt JC, Griffiths RE, Dean DJ, Grams PE. 2018. Long-Term Evolution of Sand Transport Through a River Network: Relative Influences of a Dam Versus Natural Changes in Grain Size From Sand Waves. Journal of Geophysical Research: Earth Surface **123** : 1879–1909. DOI: 10.1029/2017JF004534

Topping DJ, Rubin DM, Vierra LE. 2000. Colorado River sediment transport: 1. Natural sediment supply limitation and the influence of Glen Canyon Dam. Water Resources Research **36** : 515–542. DOI: 10.1029/1999WR900285

Topping DJ, Wright SA. 2016. Long-term continuous acoustical suspended-sediment measurements in rivers - Theory, application, bias, and error . USGS Numbered Series. U.S. Geological Survey: Reston, VA

Trimble SW. 1981. Changes in Sediment Storage in the Coon Creek Basin, Driftless Area, Wisconsin, 1853 to 1975. Science **214** : 181–183. DOI: 10.1126/science.214.4517.181

Venditti JG, Dietrich WE, Nelson PA, Wydzga MA, Fadde J, Sklar L. 2010. Effect of sediment pulse grain size on sediment transport rates and bed mobility in gravel bed rivers. Journal of Geophysical Research: Earth Surface **115**

Williams G, Wolman G. 1984. Downstream effects of dams on alluvial rivers . USGS Professional Paper

Winterbottom SJ, Gilvear DJ. 2000. A GIS-based approach to mapping probabilities of river bank erosion: regulated River Tummel, Scotland. Regulated Rivers: Research & Management: An International Journal Devoted to River Research and Management **16** : 127–140. DOI: 10.1002/(SICI)1099-1646(200003/04)16:2<127::AID-RRR573>3.0.CO;2-Q

CHAPTER 2

MEASURING CHANNEL PLANFORM CHANGE FROM IMAGE TIME SERIES:

A GENERALIZABLE, SPATIALLY DISTRIUBTED, PROBABILISTIC

METHOD FOR QUANTIFYING UNCERTAINTY[1]

Abstract

Channels change in response to natural or anthropogenic fluctuations in streamflow and/or sediment supply and measurements of channel change are critical to many river management applications. Whereas repeated field surveys are costly and time consuming, remote sensing can be used to detect channel change at multiple temporal and spatial scales. Repeat images have been widely used to measure long-term channel change, but these measurements are only significant if the magnitude of change exceeds the uncertainty. Existing methods for characterizing uncertainty have two important limitations. First, while the use of a spatially variable image co-registration error avoids the assumption that errors are spatially uniform, this type of error, as originally formulated, can only be applied to linear channel adjustments, which provide less information on channel change than polygons of erosion and deposition. Second, previous methods use a level-of-detection (LoD) threshold to remove non-significant measurements, which is problematic because real changes that occurred but were smaller than the LoD threshold would be removed. In this study, we present a new method of quantifying uncertainty associated with channel change based on probabilistic, spatially varying estimates of co-registration error and digitization uncertainty that obviates a LoD threshold. The spatially distributed probabilistic (SDP) method can be applied to both linear channel adjustments and polygons of erosion and deposition, making this the first

[1]Coauthored by Christina M. Leonard, Carl J. Legleiter , Devin M. Lea, and John C. Schmidt

uncertainty method generalizable to all metrics of channel change. Using a case study from the Yampa River, Colorado, we show that the SDP method reduced the magnitude of uncertainty and enabled us to detect smaller channel changes as significant. Additionally, the distributional information provided by the SDP method allowed us to report the magnitude of channel change with an appropriate level of confidence in cases where a simple LoD approach yielded an indeterminate result.

1. Introduction

Despite recent advancements in remote sensing platforms, historic aerial images remain invaluable in the analysis of long-term channel change. These data are windows into the past, providing a rich, spatially robust history of channel change during the ~100 years since the first air photos were taken (Rhoades et al., 2009; Comiti et al., 2011; Bollati et al., 2014). Programs like Google Earth are a powerful means to visualize channel evolution, because a sequence of aerial images can be easily compared. Although such programs facilitate the casual inspection of channel evolution, they cannot be used to make the precise measurements of channel change that are required for most management applications. Additionally, the aerial and/or satellite images available in these programs only date to the mid-1990s and thus provide only a limited window to the past. Thus, programs like Google Earth cannot entirely replace detailed analyses of channel change that involve geo-referencing and overlaying historic aerial images to quantify changes in channel location over time.

Predicting channel change is a longstanding problem in the field of geomorphology. Since the mid-20th century, water resource development and climate change have significantly altered the flow and sediment supplied to most of the world's

rivers (Nilsson et al., 2005; Schmidt and Wilcock, 2008b; Best, 2019), creating a societal

need to understand how such disturbances affect flood risk, ecosystem management and

rehabilitation, and land use planning. Case studies of channel change – how much, at

what rate, and why – are the primary means of understanding the trajectory of channel

adjustment after a disturbance. In many cases repeat aerial images are the only record of

the pre-disturbed channel and thus provide the most complete record of the channel's

response. Therefore, studies of channel change using historic aerial images remain of

fundamental interest to geomorphologists and those tasked with effectively managing

river systems.

Channel change measured from aerial images is only significant if the magnitude

of bank erosion or floodplain formation exceeds the magnitude of uncertainty in the

channel change analysis (Downward et al., 1994). The existing body of channel change

literature includes numerous case studies that use a wide range of methods, which vary in

rigor and complexity, to quantify this uncertainty. As a result and for a given case study,

one might conclude that the channel changes identified are, or are not, significant

depending on how the uncertainty of that analysis is quantified. The simplest methods

assume that the magnitude of uncertainty is negligible compared to the magnitude of

channel change and can be disregarded (e.g., Lyons et al., 1992; Merritt and Cooper,

2000; Buckingham and Whitney, 2007; Magilligan et al., 2008; Cadol et al., 2011;

Comiti et al., 2011; Schook et al., 2017; Wellmeyer et al., 2005), or assume that the

uncertainties compensate for one another in the calculation of net channel change and can

be disregarded (Gaeuman et al., 2003; Ham and Church, 2000). A more complex

approach to quantifying uncertainty is to establish a level-of-detection (LoD);

measurements of channel change that are smaller in magnitude than this threshold cannot be distinguished from uncertainty and are removed from the analysis (Urban and Rhoads, 2003). In most studies, the LoD is specified as a spatially uniform threshold for designating measurements as non-significant and excludes these measurements from the analysis (Winterbottom and Gilvear, 2000; White et al., 2010; Martin and Pavlowsky, 2011; Kessler et al., 2013). This approach causes a large number of small planform changes to be removed from the analysis and introduces a bias by ignoring polygons of very small channel change, implying that the reach-scale average will be dominated by polygons of larger channel change. Lea and Legleiter (2016) partially overcame this limitation by allowing the LoD to vary spatially based on local estimates of image co-registration error, which resulted in a larger proportion of measurements being retained as statistically significant and thus improved the ability to detect actual channel change.

Despite an abundance of methods used to quantify the uncertainty in measurements of channel change from aerial images, a generalizable, robust methodology is lacking. Several metrics are used to measure channel change from repeat aerial images, and previous methods to quantify uncertainty have varied depending on the metric of channel change used in individual case studies. This situation has hindered the development of a generalizable uncertainty method and makes comparing case studies of channel change from image time series more difficult and imprecise than studies of repeat topography, for which generalizable methods for characterizing uncertainty have been developed (Brasington et al., 2003; Wheaton et al., 2010). For example, although the method developed by Lea and Legleiter (2016) (hereafter referred to as the spatially variable registration error (SVRE) method) was a significant improvement upon spatially

uniform methods of quantifying image co-registration error, this method can only be

applied to linear channel adjustments, such as comparison of channel centerlines for

measuring rates of meander migration (Nanson and Hickin, 1983; Micheli and Kirchner,

2002; Schook et al., 2017; Donovan and Belmont, 2019) or bank lines for measuring

rates of bank retreat (Urban and Rhoads, 2003; De Rose and Basher, 2011; Day et al.,

2013; Kessler et al., 2013). An alternative to this simplified linear representation of

channel form involves analyzing the area of bank erosion and/or floodplain formation by

delineating polygons of erosion and deposition (Gaeuman et al., 2003; Grams and

Schmidt, 2005; White et al., 2010; Swanson et al., 2011; Nelson et al., 2013; Nardi and

Rinaldi, 2015). Polygons of erosion and deposition are often a more informative measure

of channel change, because these polygons can be used to characterize fundamental

attributes of channels (e.g., lateral channel stability) and evaluate the processes by which

channels change size. An uncertainty method that allows for spatially varying image co-

registration error and can be applied to both linear and areal metrics of channel change

thus would be useful.

Another significant limitation of the SVRE and other uncertainty methods is the

removal of any channel change measurements smaller than a specific threshold. This

LoD approach is problematic, because measured changes less than the specified threshold

are assumed to not represent real change and are removed from the analysis. However,

including as many measurements of channel change as possible, whether small or large,

is important, because those data contribute to our understanding of the processes and

mechanisms by which channels adjust. Additionally, the cumulative effect of many small

measurements of change might be larger than the effect of a few measurements of large

change; thus, excluding small measurements might give the false impression that the channel's response is to adjust in a few areas dominated by large change. Also, preferentially removing small changes could lead to biased removal of erosional areas, because erosion tends to be more spatially focused than deposition (Brasington et al., 2003). Similar concerns with the LoD threshold also exist when estimating volumes of erosion and deposition from two topographic surfaces (Brasington et al., 2003; Anderson and Pitlick, 2014; Leonard et al., 2017a; Anderson, 2019a). In this case, the LoD threshold tends to preferentially remove polygons of deposition, because deposition occurs as relatively thin deposits over large areas (e.g., bars) whereas polygons of erosion are typically localized and thick (Brasington et al., 2003). In some instances, the biased removal of deposition can cause the true value of volumetric change to fall outside the 95% confidence interval of the volumetric change obtained by removing measurements below the LoD threshold (Anderson, 2019a).

In this study, we introduce a generalizable method for quantifying the uncertainty associated with measurements of channel change from repeat aerial images based on spatially varying estimates of uncertainty; we call this the Spatially Distributed Probabilistic (SDP) method. The SDP method can be applied to all metrics of channel change calculated from the comparison of repeat aerial images, making this technique the first robust, generalizable method for quantifying uncertainty in measurements of channel change from an image time series. Moreover, the SDP approach provides a probability distribution of planform change as output, rather than a single value with an associated uncertainty, and thus allows the user to estimate the probability that net change was

erosional, depositional, or within a specified tolerance of a net sediment balance (i.e.,

zero net flux).

2. Spatially distributed probabilistic (SDP) method of quantifying the uncertainty associated with change detection from an image time series

The purpose of this section is to provide a general overview of the SDP method.

Step-by-step instructions for implementing the method can be found in the supplemental

information, and both a standalone application and the corresponding MATLAB® source

code for performing an SDP uncertainty analysis are available at

https://qcnr.usu.edu/coloradoriver/files/leonard_data.

The SDP method considers one source of error - image co-registration - and two

sources of uncertainty - digitization and interpretation - in measurements of channel

change from repeat aerial images. We define a source of error as having a deviation from

a known value and a source of uncertainty as having a range of values that encompass the

true measurement. Unlike previous methods that consider multiple sources of error and

uncertainty in channel change analysis, the SDP method does not use error propagation to

derive a single value to summarize the uncertainty. Instead, each source of error and

uncertainty is used to create a probabilistic delineation of the active channel boundary for

each of the two images from which a distribution of channel change measurements can be

derived.

2.1 Image co-registration error

Image co-registration error is related to misalignment in image overlays that can

mask real channel change or give a false impression of change when none has occurred

(Gaeuman et al., 2005). Image misalignment originates from the need to transform the

original row, column pixel coordinates of each digital image to a real-world coordinate system (e.g., a Universal Transverse Mercator (UTM) projection). This process is referred to as image warping and involves finding pairs of identifiable features on an image whose pixel coordinates are in a row, column, or arbitrary local system, referred to as the warp image, and an image that already has been geo-referenced to the desired real-world coordinate system, referred to as the base image. These pairs of points are termed tie-points and are used to establish a spatial transformation that relates pixel coordinates in the warp image to map coordinates in the base image.

The SDP method uses a spatially distributed image co-registration error that is similar to that of the SVRE method, but we use independent test-points as recommended by Hughes et al. (2006) instead of using tie-points to generate the error surface. Test-points are identified by extracting the map coordinate of the same feature on the image that is being digitized and the most recent image in the time series (Figure 2-1; step 1a). Test-points differ from tie-points in that test-points are extracted from two images that are geo-referenced to a common coordinate system, and thus directly measure image overlay error rather than the residual error in the transformation used for image warping. Test-points also can be used to quantify co-registration error in images that are already geo-referenced and thus do not require warping, such as data acquired through the National Agriculture Imagery Program (NAIP) or from various satellite platforms. The magnitude of each test-point error is calculated in the X and Y directions by subtracting the test-point coordinate in the image being used to delineate the channel boundary (x_i', y_i') from the same test-point coordinate in the most recent image (x_i, y_i) (Figure 2-1 step 1b; Figure 2-2 a,b;):

$$\varepsilon_{xi} = x_i - x_i' ; \qquad\qquad (2-1)$$

$$\varepsilon_{yi} = y_i - y_i' ; \qquad\qquad (2-2)$$

where ε_{xi} is the magnitude of co-registration error in the X direction for the ith test-point

and ε_{yi} is the magnitude of co-registration error in the Y direction for the ith test-point. A

continuous surface of ε_x and ε_y is then created by triangulating between each ε_{xi} and ε_{yi}

point and using bi-linear interpolation within each triangle (Amidror, 2002; Figure 2-2

a,b). The triangulation is dependent on the spatial distribution of the test-points, however,

and we account for this dependency by repeatedly withholding 10% of the test–points

using a 10-fold cross-validation to generate 10 ε_x and ε_y surfaces (Figure 2-1 step 1c-e).

2.2 Interpretation uncertainty

Uncertainty in deciphering whether an alluvial surface is part of the active

channel or part of the floodplain was originally discussed by Winterbottom and Gilvear

(1997), but this aspect of uncertainty is rarely included in studies of channel change.

Common indicators used to classify a surface as channel or floodplain include breaks in

slope or the elevation of the surface relative to the surrounding floodplain. Such

topographic features can only be identified in aerial images when viewed in stereo, but

most studies of channel change delineate channel boundaries based on single images (i.e.,

not stereo pairs) examined within a geographic information system (GIS) software

environment. Therefore, the location of the channel boundary is often inferred on the

basis of vegetation density (Dean and Schmidt, 2011; Nelson et al., 2013) rather than

topographic changes at the edge of the active channel. These delineations thus are subject

to greater uncertainty than if image pairs were analyzed in stereo. Using vegetation

SDP Algorithm

1) Generate co-registration error surfaces

2) Interpretation error

1a) Generate independent test-points

2a) Digitize maximum (A_{max}) and minimum (A_{min}) extents of active channel and vegetated islands

1b) Calculate error for each test-point

1c) Withhold 10% of test-points

1d) Create spatially continuous εx and εy surfaces (Figure 2)

1e) Repeat 1c-d to create 10 co-registration error surfaces

3) Move each vertex of A_{max} & A_{min} boundaries by the magnitude and direction of the co-registration error for each of the 10 error surfaces (Figure 4a)

4) Randomly sample 100 digitizing uncertainties from a normal distribution and move the adjusted boundaries in step 3 along a normal vector with a magnitude given by the sampled digitizing uncertainty (Figure 4b)

5) Repeat steps 1-4 for the second image date

6) Generate probability distributions of channel change by randomly sampling a delineation from step 4 for both time periods and overlaying these delineations to create polygons of erosion and deposition; repeat using different A_{max} & A_{min} overlays

7a) $A_{min(t1)}$ & $A_{min(t2)}$

7b) $A_{max(t1)}$ & $A_{max(t2)}$

7c) $A_{min(t1)}$ & $A_{max(t2)}$

7d) $A_{max(t1)}$ & $A_{min(t2)}$

Figure 2-1. SDP algorithm flow chart.
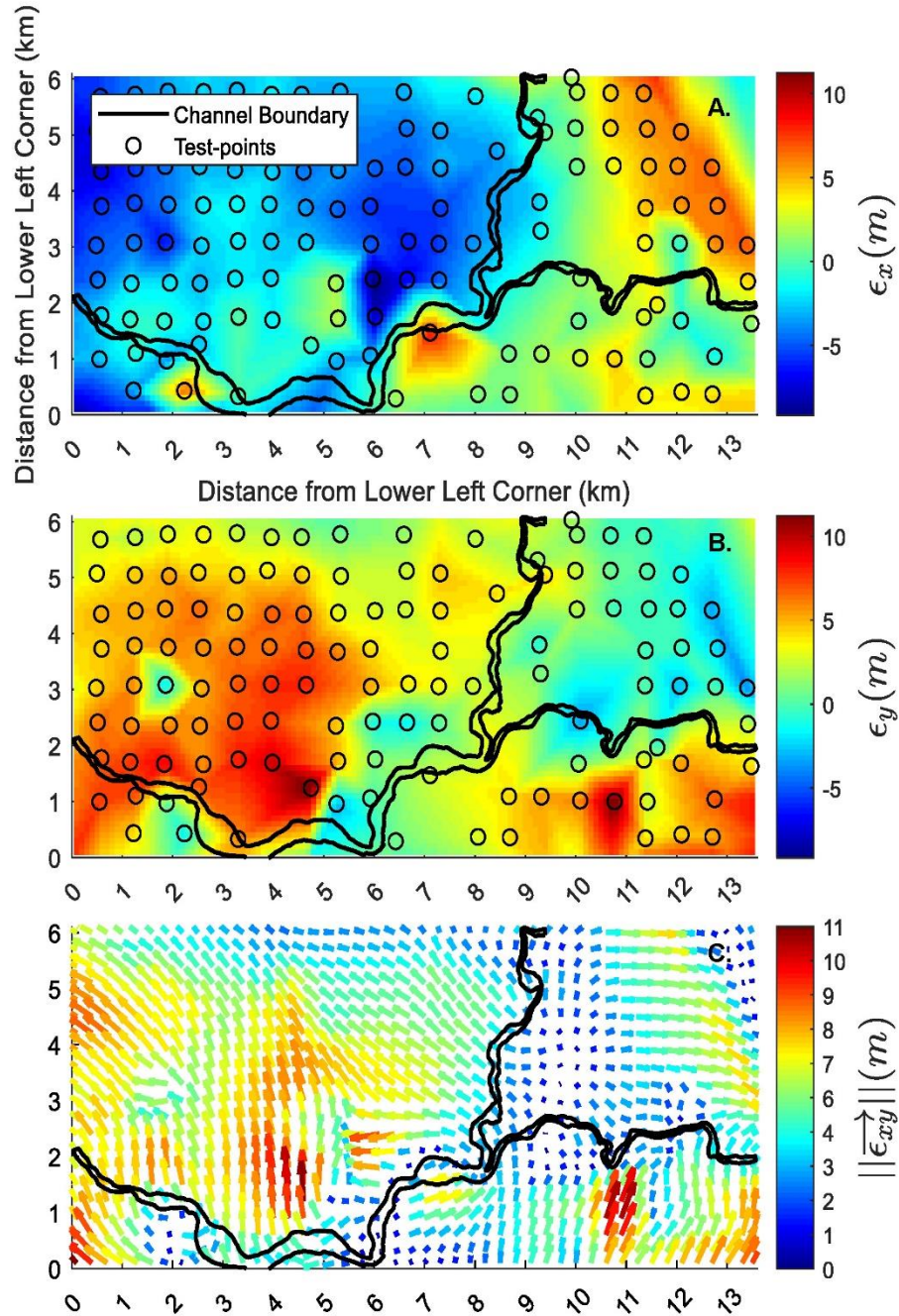
Figure 2-2. Spatially distributed image co-registration error surface. (A) Image co-registration error in the X direction (ε_x). (B) Image co-registration error in the Y direction (ε_y). Positive ε_x and ε_y values point east and north, respectively. ε_x and ε_y were calculated by equations 3 and 4. (C) Resultant vectors of ε_x and ε_y calculated by equations 5 and 6.

density as a threshold for defining the edge of the channel is also problematic, because
fast-growing perennial vegetation can encroach upon low elevation bars that are regularly
inundated during the annual flood but exposed for long periods during base flow.

The SDP method explicitly incorporates the uncertainty inherent to interpreting
the edge of the channel by delineating minimum and maximum active channel boundaries
(Figure 2-1 step 2); Dean and Schmidt (2011, 2013) used a similar approach. We define
the maximum active channel boundary (A_{max}) as the smallest extent of the vegetated
islands and the largest extent of the active channel and the minimum active channel
boundary (A_{min}) as the largest extent of the vegetated islands and the smallest extent of
the active channel (Figure 2-3). Thus, A_{max} represents the maximum area of the active
channel whereas A_{min} represents the minimum area of the active channel.
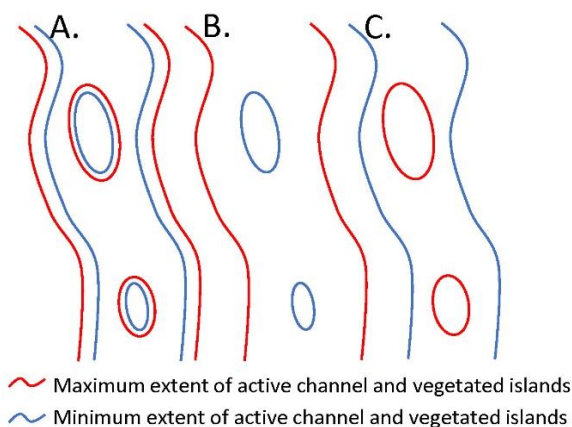
Figure 2-3. Schematic showing minimum and maximum active channel delineations for
interpretation uncertainty. (A) Minimum and maximum extent of the active channel and
vegetated islands. These extents represent uncertainty in interpreting the channel and
vegetated island boundaries. (B) Maximum area of the active channel (A_{max}) is the
minimum extent of the vegetated islands subtracted from the maximum extent of the
active channel. (C) Minimum area of the active channel (A_{min}) is the maximum extent of
the vegetated islands subtracted from the minimum extent of the active channel.

2.3 Digitization uncertainty

Uncertainty in digitizing the edge of the channel is the accuracy with which the

same operator can repeatedly delineate the same boundary (Gurnell et al., 1994; Micheli

and Kirchner, 2002; Donovan et al., 2019) and previously has been quantified using a

single value, such as half the product of the width of a pencil line and the scale of the

aerial image (Ham and Church, 2000; Gaeuman et al., 2003; Nelson et al., 2013). When

digitizing the channel extent on an aerial image, the digitizing uncertainty is not uniform

throughout the image and we account for this variability in the SDP method by

characterizing the uncertainty probabilistically using a normal distribution with a mean of

zero and a standard deviation assumed to be one-third of the maximum digitizing

uncertainty. The maximum digitizing uncertainty can be estimated on a case-by-case

basis by repeatedly delineating the same boundary or using the image scale and pencil

width. Alternatively, the maximum digitizing uncertainty can be assumed to be similar to

that of previous studies and taken to be a constant value, such as 2 m (e.g., Legleiter,

2014; Lea and Legleiter, 2016; Donovan et al, 2019).

2.4 Implementation of the SDP method

The SDP method creates a probabilistic delineation of the active channel

boundary using information on all three sources of error and uncertainty described above:

image co-registration, interpretation, and digitization. First, the method adjusts the A_{max}

and A_{min} boundaries based on the local co-registration error by moving each vertex (x_j, y_j)

along a vector whose magnitude $\left(\left\|\overrightarrow{\varepsilon_{xy}}\right\|\right)$ and direction (θ) (Figure 2-2c) are given by:

$$\left\|\overrightarrow{\varepsilon_{xy}}\right\| = \left(\varepsilon_{xj}{}^2 + \varepsilon_{yj}{}^2\right)^{0.5}; \qquad\qquad (2-3)$$

$$\theta = tan^{-1}\left(\frac{\varepsilon_{yj}}{\varepsilon_{xj}}\right); \qquad\qquad (2-4)$$

where ε_{xj} and ε_{yj} are the co-registration errors at point (x_j, y_j) extracted from the ε_x and

ε_y surfaces (Figure 2-4a). This procedure is repeated for each of the 10 co-registration

error surfaces to create 10 A_{max} and A_{min} boundaries (Figure 2-1 step 3). Along each of

the 10 A_{max} and A_{min} boundaries, a band of delineations that represents digitizing

uncertainty is generated by randomly sampling 100 digitization uncertainty values from

the normal distribution and moving each vertex along a normal vector by the magnitude

of the sampled uncertainty value (Figure 2-1 step 4; Figure 2-4b). The final probabilistic

delineation for each A_{max} and A_{min} boundary consists of 1,000 delineations whose

distribution represents co-registration and digitization uncertainty (Figure 2-4c).

After the probabilistic delineations for A_{max} and A_{min} boundaries are created for

two aerial images (Figure 2-1 step 5), probability distributions of channel change are

calculated by randomly sampling, with replacement, 5,000 A_{max} or A_{min} delineations from

both aerial images and overlaying each sampled boundary to create polygons of erosion

and deposition (Figure 2-1 step 6). This step is performed separately for each

combination of A_{max} and A_{min} overlays, creating a total of 20,000 calculations of channel

change (Figure 2-1 steps 7a-d): (a) minimum active channel boundary in both images

($A_{Min(t1)}$&$A_{Min(t2)}$); where the subscripts *t1* and *t2* denote the earlier and later images,

respectively; (b) maximum active channel boundary in both images ($A_{Max(t1)}$&$A_{Max(t2)}$);

(c) minimum active channel boundary in the earlier image and maximum active channel

boundary in the later image ($A_{Min(t1)}$&$A_{Max(t2)}$); and (d) maximum active channel
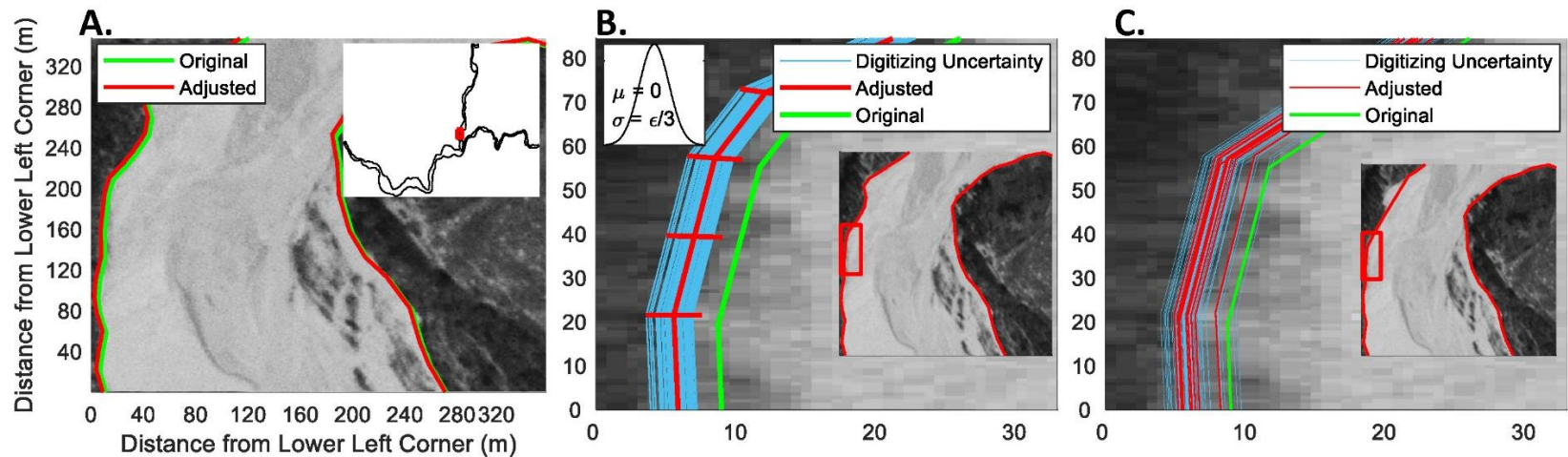
Figure 2-4. Steps used to create a probabilistic boundary delineation. (A) Original boundary delineation in green and boundary delineation adjusted for co-registration error in red. The red line was created by moving each vertex of the green line by a distance of $\left\| \overline{\varepsilon_{xy}} \right\|$ in the direction θ (Figure 2-1c). (B) Subset of A. Blue lines represent the distribution of probable channel delineations around the adjusted red boundary. The distribution of blue lines was populated by randomly sampling a digitizing uncertainty from a normal distribution with a mean (μ) of zero and standard deviation (σ) of one-third the maximum digitizing uncertainty (inset). Each vertex on the red line was moved along a normal vector with a magnitude equal to the sampled value. This was repeated 100 times. (C) Same location as B showing the full probabilistic boundary delineation. Each red line was adjusted from the original green boundary using one of the 10 co-registration error surfaces. The blue lines represent the digitization uncertainty around each of the 10 red lines.

boundary in the earlier image and minimum active channel boundary in the later image ($A_{Max(t1)}$&$A_{Min(t2)}$). The distribution of areal changes for all combinations of overlays represents the combined uncertainty in co-registration, digitization, and interpretation.

The same method can be used to create a probabilistic delineation of channel centerlines or bank lines to obtain a distribution of centerline migration or bank retreat rates. Here, we focus on applying the SDP method to polygons of erosion and deposition because, as discussed in Section 1, these measurements yield more geomorphic information.

3. Channel change case study

To illustrate how the SDP method can be applied in a specific channel change analysis, we describe application of the SDP method to a 23-km alluvial segment of the Yampa and Little Snake Rivers in northwestern Colorado, USA. Here, we describe our analysis of channel change based on analysis of aerial images collected in 1954 and 1961 (Figure 2-5). We demonstrate the advantages of the SDP method by comparing our results to those obtained using two methods that do not use a spatially variable image co-registration error and do not characterize uncertainty in a probabilistic manner. The data used in this case study are available from the U.S. Geological Survey (USGS) ScienceBase (Legleiter and Leonard, 2020). Both historical images were collected from late August to early September at base flow (i.e., 7.16 and 9.03 m^3s^{-1} in 1954 and 1961, respectively, estimated at the Deerlodge gage by summing the discharge at the Maybell (USGS station number: 09251000) and Lily (USGS station number: 09260000) gages); Figure 2-5). The flow regimes of the Yampa and Little Snake Rivers are largely unregulated and dominated by spring snowmelt floods. The mean annual flood at the

Deerlodge gage is 408 m^3s^{-1}, and late summer is a time of low discharge (Manners et al., 2014a; Topping et al., 2018). Both rivers in the study area have wide active channels with many active bars, as well as bars adjacent to the channel that were formed by floods of different magnitudes. The Little Snake River is the primary source of fine sediment to the Yampa River in Yampa Canyon in Dinosaur National Monument (Topping et al., 2018) and provides a disproportionately large supply of fine sediment relative to the river's contribution of streamflow (Andrews, 1980). We selected this location for our channel change case study, because the National Park Service is concerned about the maintenance of valued park resources that might be affected by upstream water development and recognizes the need to distinguish natural patterns of channel change from changes associated with anthropogenic perturbations.

3.1 Channel change case study methods

The 1954 and 1961 images were not geo-referenced to a projected coordinate system, so we warped both images to a common projected coordinate system using the 2017 NAIP image as a base. The 1954 and 1961 images were downloaded from the USGS Earth Explorer website (USGS, 2019) as 24 single frame images. In Section 2, we described the general process of image warping whereby tie-points are identified on an individual single frame image to develop a transformation equation for warping that particular image. In this case study, however, we used a Structure-from-Motion (SfM) software package (Agisoft LLC, 2016) to first align and merge the single frame images into a mosaic and then warp and rectify the mosaic by using 12 tie-points with elevations extracted from the National Elevation Dataset (USGS, 2012) to define a 7-parameter similarity transformation with three parameters for translation, three for rotation, and one
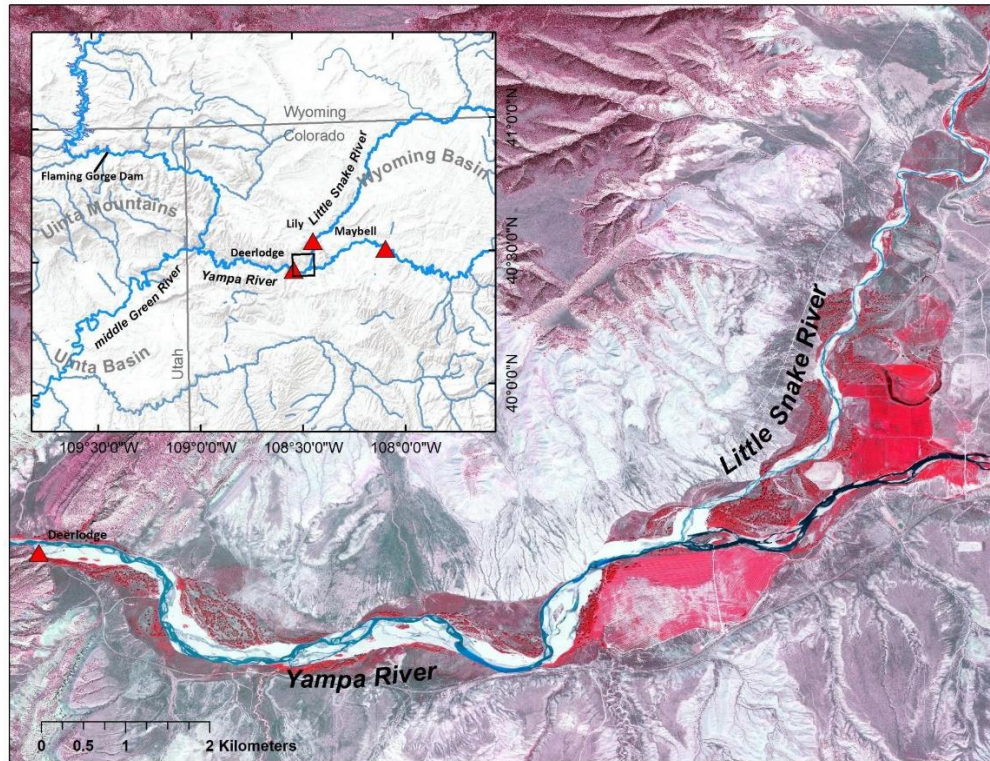
Figure 2-5. Study area used to illustrate the SDP method. The study area is located in northwestern Colorado along a 17 km alluvial section of the Yampa River spanning the Little Snake confluence and a 7 km reach of the Little Snake River directly upstream from the confluence. The Deerlodge gage (USGS station #: 09260050) is located at the downstream end of the study area. The direction of flow is from right to left. Base aerial image is from the 2017 NAIP.

for scaling. Other studies have demonstrated the utility of using SfM to reconstruct elevation models of landforms from historic aerial images (Riquelme et al., 2019), and we found that the same method was useful for geo-referencing a large number of historic aerial images; however, difficulties may arise when the overlap between adjoining images is small. Also, we avoided the misalignments that can occur at the seams of the images when they are individually geo-referenced and overlaid by using SfM to geo-reference the mosaic rather than the individual images (e.g., Donovan et al., 2019).

As described in Section 2, we used independent test-points to characterize co-registration error in our case study. These test-points indicated how well the 1954 and 1961 images overlaid on the 2017 NAIP image. In our case study, test-points were difficult to visually identify, because roads and buildings in the 2017 image were not present in the 1954 and 1961 images and "soft" tie-points were limited. Therefore, we used an area-based matching algorithm in the remote sensing software package ENVI® (L3Harris Geospatial) to automatically generate test-points (Figure 2-2a). The area-based matching algorithm compared grayscale values of each image within a moving search window and identified similarities and patterns using normalized cross-correlation. We removed test-points with correlation coefficients of less than 0.8, and we manually inspected the remaining test-points with the lowest correlation coefficients to ensure test-point accuracy. The algorithm produced approximately 450 test-points in both images, but the points were predominantly located on adjacent hillslopes with high textural variability, because the landscape in our case study was rural with high topographic variability. Therefore, we supplemented the ENVI-generated test-points with manually selected points along the valley bottom.

We used the methodology described in Section 2 to create spatially distributed ε_x and ε_y surfaces from the test-points generated above and calculate $\left\lVert \overrightarrow{\varepsilon_{xy}} \right\rVert$ and θ at any x_j, y_j point (Figure 2-1 steps 1 and 3). The spatially uniform root mean square error (RMSE) was calculated using a subset of test-points from our case study that were close to the active channel as:

$$RMSE = \left[\frac{\sum_{j=1}^{n} \varepsilon_j^2}{n} \right]^{0.5}, \qquad\qquad (2-5)$$

where *n* is the number of test-points and $\mathcal{E}_j$ is the linear distance between the jth test-point

in the transformed warp image (x_j', y_j') and the base image (x_j, y_j), calculated as:

$$\varepsilon_j = \left[(x_j - x_j')^2 + (y_j - y_j')^2 \right]^{0.5}. \qquad (2-6)$$

We used a subset of test-points close to the active channel to eliminate the influence of

unusually large test-point errors located on adjacent hillslopes that were automatically

selected by the area-based matching algorithm and would not have affected channel

change measurements. The RMSEs for 1954 and 1961 were 4.95 and 4.52 m,

respectively. We assumed that the maximum digitizing uncertainty in our case study was

2 m based on previous studies (Donovan et al, 2019) and defined the digitizing

uncertainty using a normal distribution with a mean of zero and a standard deviation of

2/3, as described in Section 2 (Figure 2-1 step 4).

Interpretation uncertainty was estimated by separately digitizing the minimum

and maximum extent of the active channel and vegetated islands (Figure 2-1 step 2). For

our case study, we used an initial threshold of 10% vegetation density to classify surfaces

as channel (<10% vegetation density) or floodplain (>10% vegetation density). However,

we were uncertain in several locations whether a surface with >10% vegetation had

aggraded to a height similar to that of the surrounding floodplain with denser, more

mature vegetation because the images were not viewed in stereo. This sort of uncertainty

is inevitable in any channel change study but the A_{min} and A_{max} boundaries described in

Section 2 provided a means of classifying these uncertain surfaces as both active channel

and floodplain.

We also used a sequence of aerial images that were collected before and after the

image being digitized to help us understand the evolution of alluvial surfaces with

interpretation uncertainty through time. For example, if an ambiguous surface showed a clear evolution from an unambiguous active channel in the earlier image to unambiguous floodplain in the later image, we knew that during the image sequence the surface changed from channel to floodplain and assumed that the ambiguous surface in the intermediate image being digitized was within this gradual transition. In this instance, we would use the A_{min} and A_{max} bounds to classify the surface as both channel and floodplain. Conversely, if the surface was unambiguously active channel in both the earlier and later images, we would assume that the surface in the intermediate image being digitized was also active channel and the increase in vegetation on that surface might have been caused by the proliferation of vegetation on bars during a period when the annual snowmelt floods were small.

Figure 2-6 presents two examples from our case study where we used a sequence of aerial images to guide our interpretation of ambiguous alluvial surfaces. The partly vegetated surface in Figure 2-6 a,b is an example of a vegetated island where the secondary back channel was unambiguously part of the active channel in an image from 1938 and unambiguously part of the floodplain in an image from 1975, but in the 1954 and 1961 images, there was ambiguity in whether the surface was the channel or floodplain. This interpretation uncertainty implied that the surface could be classified as a vegetated island in A_{max} (Figure 2-6a) or as part of the floodplain in A_{min} (Figure 2-6b). Similarly, Figure 2-6c,d is an example of a vegetated bank-attached bar that was unambiguously active channel in the 1938 image and unambiguously floodplain in the 1975 image, but there was ambiguity in whether the surface was floodplain or channel in the 1954 and 1961 images. Therefore, the surface was included as part of the active

channel in the A_{max} delineation (Figure 2-6c) and part of the floodplain in the A_{min}

delineation (Figure 2-6d).
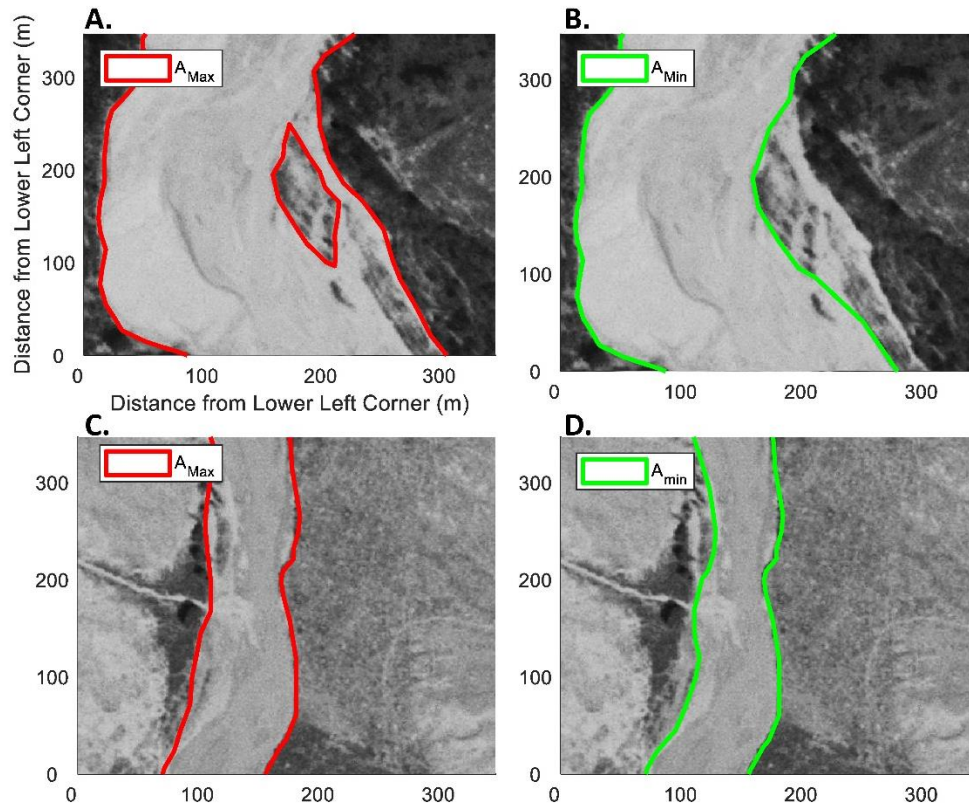
Figure 2-6. Interpretation uncertainty characterized by minimum and maximum channel boundary delineations. (A) Partly vegetated surface on the left bank was classified as a vegetated island and a secondary channel using the A_{max} delineation. (B) Same vegetated surface as A was classified as floodplain in the A_{min} delineation. (C) Vegetated bank-attached bar on the right bank was classified as active channel in the A_{max} delineation. (D) Same bank-attached bar as C was classified as floodplain in the A_{min} delineation. Direction of flow is from top to bottom in all images and minimum and maximum boundaries were delineated from the 1954 aerial image.

The net planform change was calculated as the amount of erosion subtracted from

the amount of deposition, with positive values indicating net deposition and negative

values indicating net erosion. The total net planform change using the SDP method, as

evaluated in our case study, was calculated by overlaying the probabilistic delineations in

1954 and 1961 to create a distribution of erosion and deposition polygons for each A_{Max}

and A_{Min} overlay and then merging the net planform change from all A_{Max} and A_{Min} overlays (Figure 2-1 step 7) into a single probability distribution. This distribution represented the combined uncertainty associated with co-registration, digitization, and interpretation. We also normalized the distribution of net planform change by dividing the net areal change by the channel centerline length to facilitate interpretation and comparison among reaches. For example, if the magnitude of net change was 100 m^2 of erosion and the channel length was 10 m, the normalized net change would be 10 m of erosion for every downstream meter, which we would consider a large amount of erosion. Conversely, if this amount of areal change occurred over a channel length of 10,000 m, the normalized net change would only be 0.1 m of erosion per a downstream meter, which we would consider a small amount of erosion. Additionally, normalizing the net planform change by the channel centerline length allowed us to interpret the results in terms of net changes in channel width. In case studies where multiple sets of aerial images are used, the net planform change should also be normalized by the number of years between each set of aerial images so that the magnitude of change between image pairs is comparable; this form of standardization would also aid in comparing channel change case studies from the literature.

3.2 Comparison of the SDP method with existing methods of characterizing channel change uncertainty

The uncertainty inherent to measurements of channel change from aerial images implies that any channel change analysis must consider the impact of these uncertainties on the results. We evaluated whether the SDP method improved upon previous methods by comparing the results from our case study when the uncertainty was quantified using the SDP method and two existing methods that used a spatially uniform image co-

registration error and did not characterize the uncertainty probabilistically. The first

method (ε_1) was similar to that of Urban and Rhoads (2003) and Micheli and Kirchner

(2002) in that we created an uncertainty bound with a width of the propagated co-

registration error and digitization uncertainty using:

$$\varepsilon_1 = \left[rmse_{t1}{}^2 + rmse_{t2}{}^2 + \varepsilon_{digitizing}{}^2\right]^{0.5}; \qquad\qquad (2-7)$$

where $rmse_{t1}$ and $rmse_{t2}$ were the spatially uniform co-registration errors for each image

(i.e., 4.95 and 4.52 m for the 1954 and 1961 images, respectively) and $\mathcal{E}_{digitizing}$ was the

maximum digitization uncertainty, which we assumed to be 2 m. The maximum area for

each erosional or depositional polygon was the area of the $\mathcal{E}_1$ uncertainty band added to

the original polygon (Figure 2-7a-c), and the minimum area was the $\mathcal{E}_1$ uncertainty band

subtracted from the original polygon (Figure 2-7d-f). The minimum net planform change

was the sum of the maximum area of erosion for all polygons (Figure 2-7c) subtracted

from the sum of the minimum area of deposition (Figure 2-7f). The maximum net

planform change was the sum of the minimum area of erosion (Figure 2-7f) subtracted

from the sum of the maximum area of deposition (Figure 2-7c).

The second method (ε_2) was developed by Swanson et al. (2011) and involved

estimating uncertainty in the width of each polygon of erosion and deposition using

equation 7 and converting the width uncertainty to an area by multiplying by the polygon

length. The total magnitude of uncertainty in erosion or deposition was the sum of

uncertainty across all erosional or depositional polygons, and the minimum and

maximum bounds for net planform change were calculated in the same way as for ε_1.
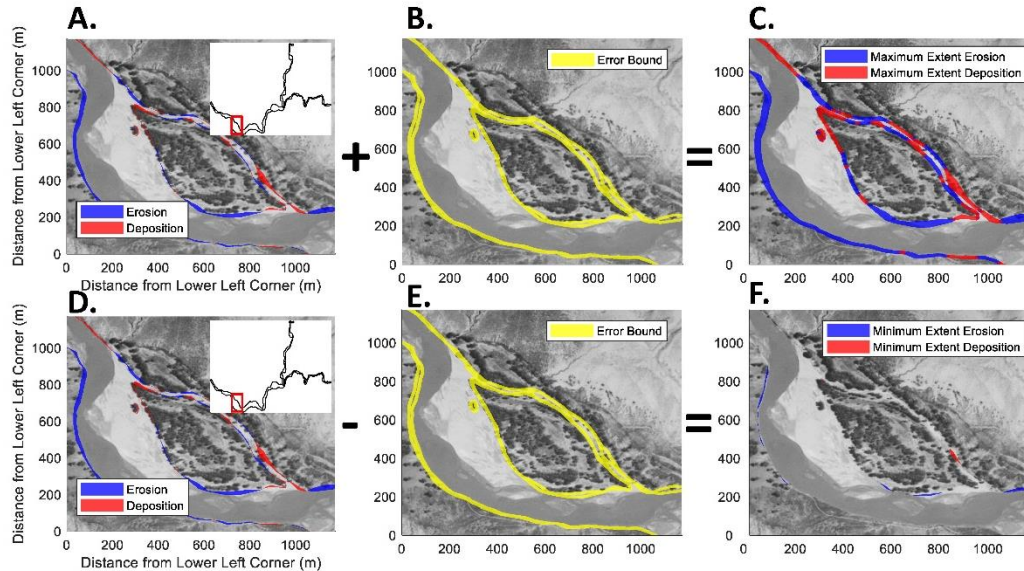
Figure 2-7. Minimum and maximum extent of erosion and deposition was calculated by adding or subtracting a spatially uniform uncertainty bound around each polygon of erosion and deposition. Flow is from right to left and the 1954 image was used as the base image. The maximum area of erosion or deposition is the uncertainty bound added to each polygon (A, B, C) and the minimum area of erosion or deposition is the uncertainty bound subtracted from each polygon (D, E, F). The minimum bound of net planform change was the sum of erosional polygons in C subtracted from the sum of depositional polygons in F, and the maximum bound of net planform change was the sum of erosional polygons in F subtracted from the sum of depositional polygons in C.

3.3 Results: Comparison of methods to quantify the uncertainty with channel change

The output from the SDP method was a distribution of planform change that we used to calculate the probability that net change in our case study was erosional or depositional along with a 95% credible interval as a summary metric of uncertainty. The 95% credible interval contained 95% of the most probable values and thus provided a measure of uncertainty comparable to the spatially uniform $\mathcal{E}_1$ and $\mathcal{E}_2$ methods. We suggest that the 95% credible interval could be a useful metric of uncertainty in other

studies that are not necessarily focused on directly comparing uncertainty methods, as was the main objective of our case study.

The SDP method, as implemented in our case study, significantly reduced the magnitude of uncertainty in measurements of areal channel change compared to the $\mathcal{E}_1$ and $\mathcal{E}_2$ methods. The maximum extents of erosion and deposition using the $\mathcal{E}_1$ method (Figure 2-8a) were greater than the maximum extents using the SDP method (Figure 2-8c) because the $\mathcal{E}_1$ uncertainty bound (Equation 7) was generally larger than the local probabilistic delineation of the channel extent generated by the SDP method. Conversely, the minimum extent of erosion and deposition using the $\mathcal{E}_1$ method (Figure 2-8b) was much smaller than the SDP method (Figure 2-8d) because $\mathcal{E}_1$ uncertainty band was greater than the size of several polygons, which caused those polygons to be completely removed from the $\mathcal{E}_1$ minimum extent (Figure 2-8b). The combined effect of these differences was a reduction in the uncertainty of deposition by 72% and 78% relative to $\mathcal{E}_1$ and $\mathcal{E}_2$, respectively, and in erosion by 84% and 87% relative to $\mathcal{E}_1$ and $\mathcal{E}_2$, respectively (Figure 2-8c,d inset; Table 2-1). The negative minimum bound of erosion and deposition in the $\mathcal{E}_2$ method (Table 2-1; inset Figure 2-8c,d) had no physical meaning because the amount of erosion and deposition could not be less than zero. This spurious result was caused by the uncertainty being greater than the planform change (e.g., $A_{Max(t1)}$&$A_{Min(t2)}$ deposition was 6.5 ± 14.0; Table 2-1).

In our case study, we could not conclude with confidence whether the channel margins or vegetated islands accumulated or evacuated sediment, nor the direction of the total net planform change, using the $\mathcal{E}_1$ and $\mathcal{E}_2$ methods, because the uncertainty band spanned zero (Figure 2-9). Although the SDP 95% credible interval also spanned zero,
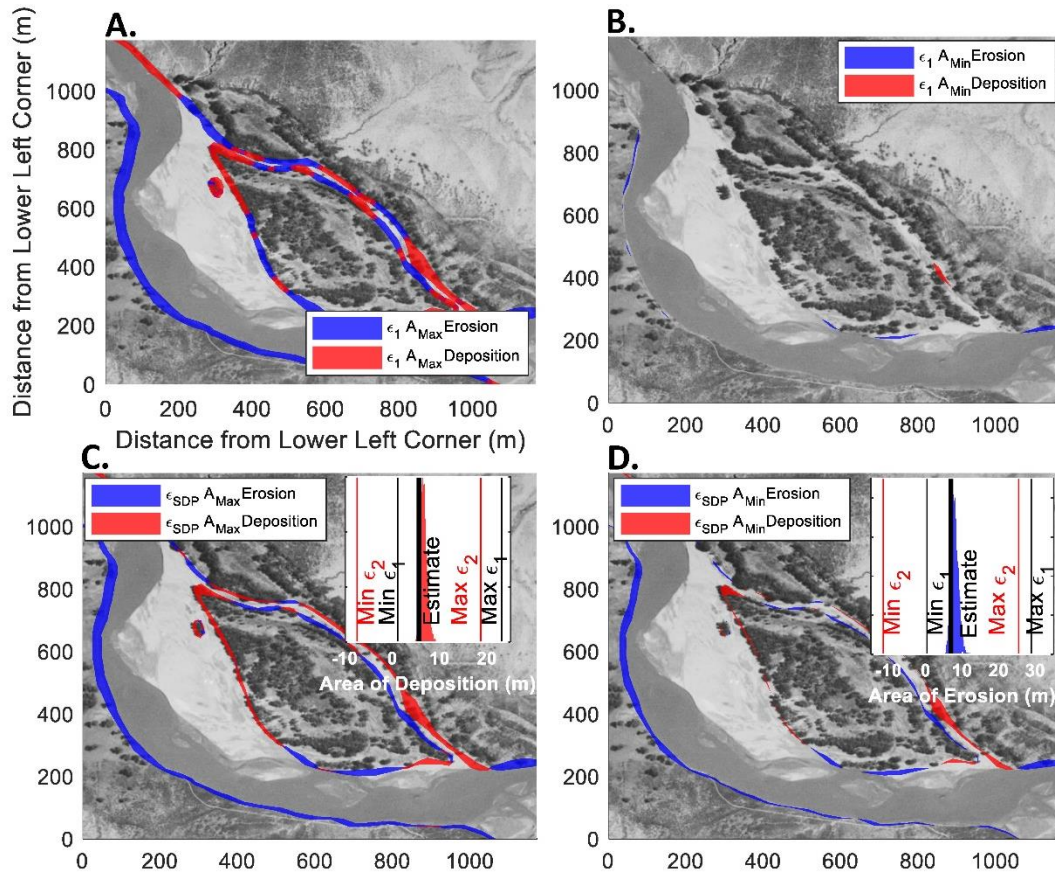
Figure 2-8. Minimum and maximum extent of erosion and deposition using the $A_{max(t1)}$&$A_{max(t2)}$ overlay. Flow is from right to left and the 1954 image was used as the base image. (A) Maximum extent of deposition and erosion using the ε_1 method. (B) Minimum extent of deposition and erosion using the ε_1 method. (C) Maximum extent of erosion and deposition using the SDP method. Inset shows the estimate for the normalized area of deposition and minimum and maximum bound of uncertainty using the ε_1 and ε_2 methods overlaid on the SDP distribution. (D) Minimum extent of erosion and deposition using the SDP method. Inset shows the estimate for the normalized area of erosion and minimum and maximum bound of uncertainty using the ε_1 and ε_2 methods overlaid on the SDP distribution. The maximum and minimum extent of erosion and deposition using the ε_2 method was not overlaid on the images because the ε_2 method calculated the magnitude of uncertainty, not the spatial extent. The SDP method reduced the magnitude of uncertainty by 72-78% for deposition and 84-87% for erosion (Table 2-1).

Table 2-1. Uncertainty bounds for the ϵ_1 and ϵ_2 methods and the 95% credible intervals for the SDP method. All values are normalized by the channel centerline length. Also included are the percent change between the ϵ_1 and SDP method ($\%\Delta SDP_{\epsilon_1}$) and between the ϵ_2 and SDP method ($\%\Delta SDP_{\epsilon_2}$).

	ϵ_1 (m)	ϵ_2 (m)	SDP (m)	$\%\Delta SDP_{\epsilon_1}$	$\%\Delta SDP_{\epsilon_2}$
Deposition					
$A_{Max(t1)}$&$A_{Min(t2)}$	2.6 – 26.9	-7.6 – 20.5	8.4 – 11.2	89%	90%
$A_{Min(t1)}$&$A_{Max(t2)}$	0.6 – 20.5	-3.7 – 20.7	4.12 – 6.7	87%	89%
$A_{Max(t1)}$&$A_{Max(t2)}$	1.1 – 23.1	-6.2 – 20.0	5.5 – 8.1	88%	90%
$A_{Min(t1)}$&$A_{Min(t2)}$	1.3 – 23.4	-6.3 – 19.9	5.9 - 8.7	87%	89%
TOTAL	0.6 – 23.4	-7.6 – 20.7	4.4 – 10.6	72%	78%
Erosion					
$A_{Max(t1)}$&$A_{Min(t2)}$	0.4 – 26.4	-10.5 – 23.4	5.6 – 9.6	85%	88%
$A_{Min(t1)}$&$A_{Max(t2)}$	0.9 - 31.2	-10.3 – 27.3	7.5 – 11.6	86%	89%
$A_{Max(t1)}$&$A_{Max(t2)}$	0.4 – 28.8	-11.6 – 25.4	6.1 – 10.1	86%	89%
$A_{Min(t1)}$&$A_{Min(t2)}$	0.4 – 27.5	-10.6 – 24.2	5.8 – 10.0	85%	88%
TOTAL	0.4 – 31.2	-11.6 – 27.3	5.92 – 10.8	84%	87%
Δ Planform Change					
$A_{Max(t1)}$&$A_{Min(t2)}$	-23.8 – 26.6	-28.7 – 13.8	-1.1 - 5.5	87%	84%
$A_{Min(t1)}$&$A_{Max(t2)}$	-30.5 – 19.6	-35.2 – 7.6	-7.4 – 0.8	87%	84%
$A_{Max(t1)}$&$A_{Max(t2)}$	-27.8 – 22.7	-32.9 – 9.4	-4.6 – 1.9	87%	85%
$A_{Min(t1)}$&$A_{Min(t2)}$	-26.2 – 23.0	-31.1 – 10.0	-4.1 – 2.8	83%	83%
TOTAL	-27.4 – 26.6	-35.2 – 13.8	-6.3 – 4.5	80%	78%

the results were more informative, because we could estimate the probability of change. More specifically, we found a 37% probability that the total net planform change was depositional (Figure 2-9a; Table 2-1), a 19% probability that the channel boundary accumulated sediment (Figure 2-9b; Table 2-1), and a 100% probability that vegetated islands accumulated sediment (Figure 2-9c; Table 2-1). Also, the magnitude of the 95% credible interval associated with the distribution generated by the SDP method was 80% and 78% smaller than the $\mathcal{E}_1$ and $\mathcal{E}_2$ uncertainty bounds, respectively (Table 2-1). Thus, the SDP method significantly reduced the bound of uncertainty compared to the $\mathcal{E}_1$ and $\mathcal{E}_2$ methods.
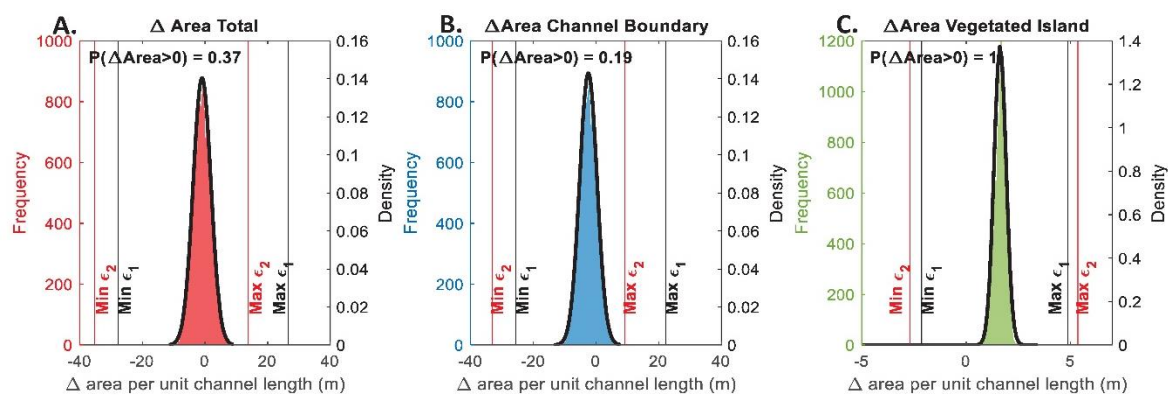
Figure 2-9. (A) All A_{max} and A_{min} overlay solutions merged into a single histogram fit with a probability density function which represents uncertainty in the normalized net change in area caused by co-registration, digitization, and interpretation uncertainty. The minimum and maximum bounds of uncertainty for the $\mathcal{E}_1$ and $\mathcal{E}_2$ methods are also shown. (B) Net areal change in A for changes that occurred along the channel margin. (C) Net areal change in A for changes that occurred along vegetated islands.

The distribution of change generated from the SDP method provided a quantitative basis for deciding whether the probability of change in our case study was large enough to support meaningful geomorphic conclusions. For the purposes of this case study, there was an inconsequential risk associated with accepting the channel

change results as true change when the change might have been caused by co-registration error or digitization and interpretation uncertainty, so we decided that a 19% probability of deposition along the channel boundary was sufficient to justify the conclusion that the channel boundary evacuated sediment. Similarly, we concluded that the vegetated islands accumulated sediment based on a 100% probability of vegetated island deposition. Overall, the net channel change was erosional rather than depositional based on a 37% probability that the net change was depositional. Conversely, the only conclusion that could be made for our case study based on the $\mathcal{E}_1$ and $\mathcal{E}_2$ method was that the results implied an indeterminate net sediment balance.

3.3.1. The relative magnitude of each type of error and uncertainty

The SDP method processes each source of error and uncertainty individually, which avoids the requirement that errors and uncertainties be normally distributed with a mean of zero for error propagation. This is an important improvement to the $\mathcal{E}_1$ and $\mathcal{E}_2$ methods that incorrectly assume that the RMSE has a mean error of zero. Additionally, processing uncertainties individually allowed us to assess the net effect of each type of uncertainty on channel change to identify the primary driver of uncertainty in our case study. Such an analysis could not have been performed using traditional methods that rely on error propagation.

The magnitude of the co-registration error in our case study was defined by extracting $\left\| \overrightarrow{\varepsilon_{xy}} \right\|$ from each A_{max} and A_{min} vertex for the 10 error surfaces. The magnitude of the digitization uncertainty was simply the normal distribution defined in Section 3.1 as having a mean of zero and a standard deviation of 2/3. Interpretation uncertainty was

calculated as the difference between the minimum and maximum active channel areas in our study reach calculated within 150 channel-spanning cells spaced at 150-m streamwise intervals along the channel centerline. The difference in area within each cell was normalized by the channel centerline length, which allowed us to express the interpretation uncertainty in units of length comparable to the co-registration error and digitization uncertainty.

In our case study, co-registration was the largest source of error, followed by interpretation and digitization uncertainty (Figure 2-10). The median of the image co-registration error was larger than the interpretation uncertainty (3.0 vs. 0.0 m), but the mean was comparable (3.7 vs. 3.3 m). By definition, the mean of the digitization uncertainty was 0 m and smaller than interpretation uncertainty and co-registration error. The median of the interpretation uncertainty was extremely small because in 56% of the study area the extent of the channel boundary was unambiguous. Conversely, the co-registration error was greater than zero throughout the entire study area. If we only considered cells where the interpretation uncertainty was greater than 0 m, the median interpretation uncertainty increased to 2.4 m and the mean increased to 7.4 m. The results of our case study suggest that interpretation uncertainty can be much larger than any other source of uncertainty, implying that interpretation uncertainty should be considered in all studies of channel change. However, we emphasize that the results presented here are unique to our case study and that the magnitude of each source of uncertainty could be different in other studies.
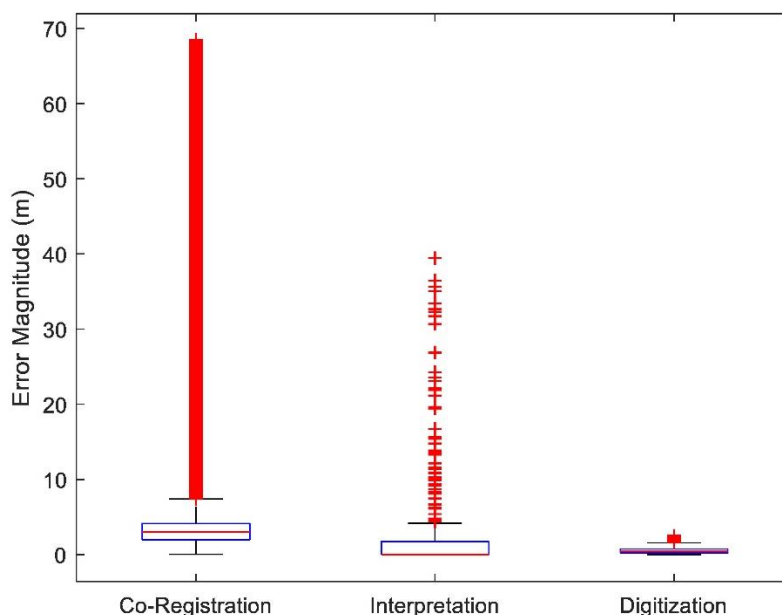
Figure 2-10. Box and whisker plot for each error and uncertainty type showing the median and interquartile range within the box, values ±2.7σ within the whiskers, and values < ±2.7σ as outliers.

3.3.2. Net effect of interpretation uncertainty

The overall effect of interpretation uncertainty in our case study was characterized by individually examining the net change in different A_{max} and A_{min} overlays and we found that different A_{max} and A_{min} overlays tended toward net erosion or deposition (Figure 2-11). The difference was greatest when A_{Min} and A_{Max} were overlaid: $A_{Max(t1)}$&$A_{Min(t2)}$ had a 90% probability of net deposition whereas $A_{Min(t1)}$&$A_{Max(t2)}$ only had a 1% probability of net deposition (Figure 2-11a,b; Table 2-1). We attributed this result to the $A_{Max(t1)}$&$A_{Min(t2)}$ overlay favoring net deposition along the channel margins and vegetated islands (Figure 2-12), which created a high probability that the net planform change was depositional (Figure 2-11a). The magnitude of vegetated island deposition was smaller for the $A_{Min(t1)}$&$A_{Max(t2)}$ overlay (Figure 2-12a) and sediment was

evacuated from the channel margin (Figure 2-12b), decreasing the probability that net

planform change was depositional for the $A_{Min(t1)}\&A_{Max(t2)}$ overlay (Figure 2-11b). The

net planform change along the channel margins and vegetated islands differed little

between the $A_{Max(t1)}\&A_{Max(t2)}$ and $A_{Min(t1)}\&A_{Min(t2)}$ overlays (Figure 2-12), and the

probability that each overlay was depositional was similar (Figure 2-11c,d). Thus, the

$A_{Max(t1)}\&A_{Max(t2)}$ and $A_{Min(t1)}\&A_{Min(t2)}$ overlays represented the most conservative amount

of channel change and the probability of this scenario occurring in the overall

distribution of net change was 50%. Conversely, the $A_{Min(t1)}\&A_{Max(t2)}$ and

$A_{Max(t1)}\&A_{Min(t2)}$ overlays represented the most extreme amount of deposition or erosion

and each of these scenarios had a 25% chance of occurring in the overall distribution of

net change.

4. Discussion

Numerous studies have analyzed repeat aerial images to detect channel change,

but the lack of a consistent methodology to quantify and incorporate uncertainty has led

to the use of many methods for estimating uncertainty in measurements of channel

change with varying degrees of rigor and complexity (Gurnell et al., 1994; Winterbottom

and Gilvear, 1997; Mount et al., 2003; Mount and Louis, 2005). Previous methods to

quantify uncertainty could only be applied to one type of channel change measurement

(i.e., linear channel adjustments or polygons of change), which prevents these methods

from being applicable to all channel change studies. The SDP method presented here is

the first generalizable method for characterizing uncertainty associated with

measurements of channel change that can be used with all forms (i.e., both linear and

areal metrics) of channel change measurements from an image time series.
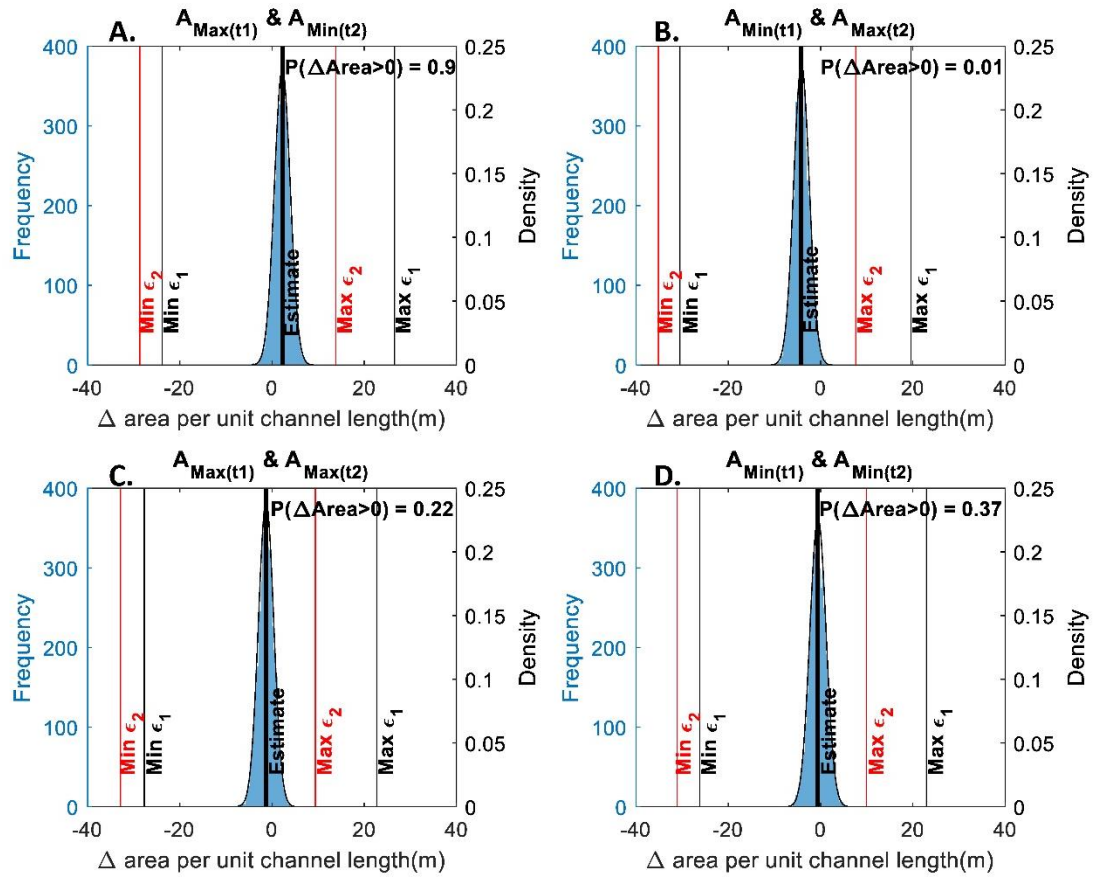
Figure 2-11. Net planform change using each A_{min} and A_{max} overlay. Each panel shows the estimate for the normalized net change in area, the minimum and maximum bound of uncertainty using the ε_1 and ε_2 methods, and a histogram of the SDP solutions fit with a probability density function. (A) $A_{max(t1)}$&$A_{min(t2)}$ overlay. (B) $A_{min(t1)}$&$A_{max(t2)}$ overlay. (C) $A_{max(t1)}$&$A_{max(t2)}$ overlay. (D) $A_{min(t1)}$&$A_{min(t2)}$ overlay.
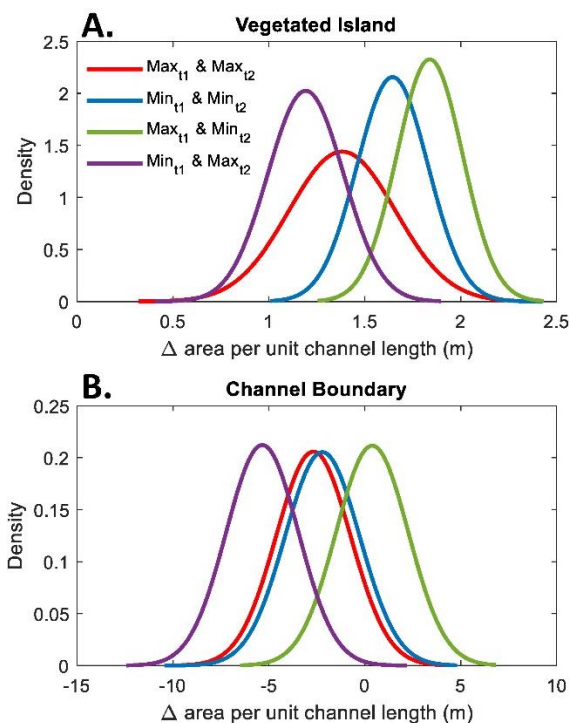
Figure 2-12. Probability density functions fit to the A_{min} and A_{max} overlay distributions partitioned by change along the channel margins and vegetated islands. (A) Normalized area of deposition along the channel margins. (B) Normalized net change along the channel margins.

The SDP method improves upon other methods of quantifying uncertainties by estimating planform change probabilistically, rather than specifying a LoD threshold and discarding measured changes less than this threshold (Winterbottom and Gilvear, 1997; Martin, 2003; Urban and Rhoads, 2003; Surian et al., 2009; White et al., 2010; De Rose and Basher, 2011; Kessler et al., 2013). By avoiding the use of a LoD threshold, the SDP method retains all polygons of channel change and calculates a distribution of each polygon's area given the uncertainty. The retention of all channel change measurements is a significant improvement to previous methods that discard changes smaller than a threshold because all polygons of change, whether small or large, contribute to our

understanding of the processes and mechanisms by which channels adjust. Additionally,

eliminating the LoD threshold has the potential to significantly improve the accuracy of

channel change studies that use bank line retreat to estimate volumes of bank erosion

(Rhoades et al., 2009; De Rose and Basher, 2011; Day et al., 2013; Kessler et al., 2013),

because point bars are commonly constructed to a lower elevation than eroding cutbanks

(Lauer and Parker, 2008) and slivers of bank retreat removed by the LoD threshold can

sum to large volumes of erosion when they extend over a large area and are multiplied by

the bank height.

The case study presented in this paper demonstrated that the SDP method can

significantly reduce the uncertainty in measurements of channel change from repeat

aerial images. While the SDP method is rigorous and robust, the technique is

computationally intensive. For example, in our case study we sampled our probabilistic

distributions 5,000 times to create a distribution of 20,000 channel change measurements

and the runtime for this analysis was ~20 minutes on a computer with 32 gigabytes of

RAM and a 3.70 GHz processor. In comparison, the runtime for the $\mathcal{E}_1$ and $\mathcal{E}_2$ methods

was less than 1 minute.

One way to decrease the SDP processing time is to reduce the number of

randomly sampled channel boundary delineations used to calculate the distribution of

channel change measurements (Figure 2-1 step 6). To test the sensitivity of the

distribution of channel change to sample size, we ran the SDP method using a range of

sample sizes from 1,000 to 10,000. This sensitivity analysis showed that the distributions

of channel change measurements were similar for all sample sizes (Figure 2-13),

implying that we could have reduced the number of samples to 1,000 without

significantly changing our results. If computation time is a concern in other studies, we

suggest performing a similar sensitivity analysis on a subset of the study area to

determine the optimal number of sampled boundary delineations used to create the

distribution of channel change.
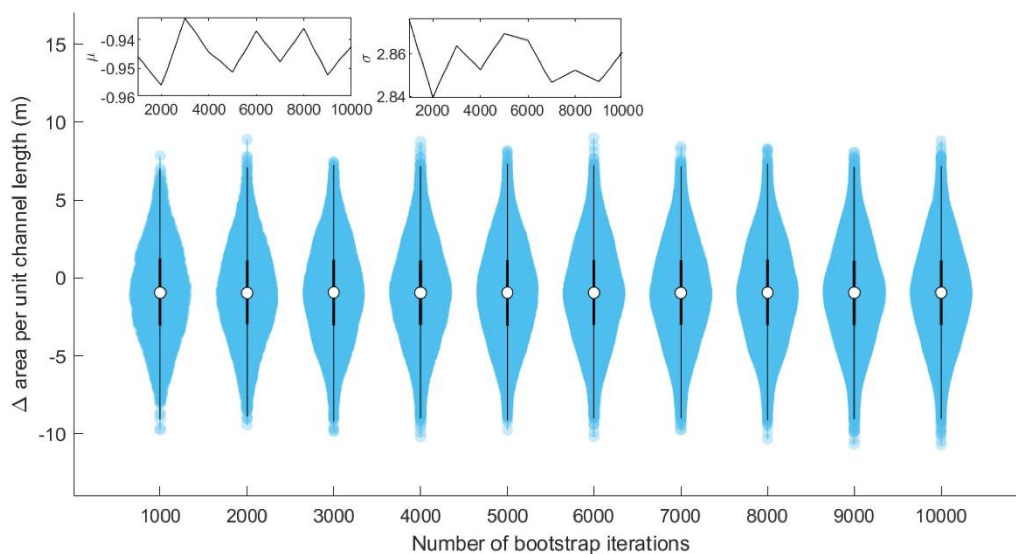
Figure 2-13. Violin plots showing the distribution of net planform change calculated by the SDP method using 1,000 to 10,000 randomly sampled channel boundary delineations indicated by the number of bootstrap iterations. Insets show the mean and standard deviation for each violin plot.

4.1. When to use the SDP method

Not all channel change studies require a method as rigorous and robust as the SDP

method to quantify uncertainty. We suggest that the level of complexity and rigor

appropriate for any effort to detect channel change depends on three factors: the

magnitude of uncertainty compared to the magnitude of channel change, the objective of

the study, and the amount of time between the aerial images used to detect change.

In small rivers, the uncertainty can be a large proportion of the total channel area (Swanson et al., 2011) and channel change may need to be quite large (e.g., greater than 25% of the width of the channel) compared to the size of the river to overcome the geospatial uncertainty. In such instances, the smaller bound of uncertainty produced by the SDP method will increase the likelihood of detecting channel change. When the signal of channel change is extremely large, as in laterally unstable rivers, a less complex uncertainty characterization method might be suitable regardless of the channel size (e.g., Surian, 1999; Cadol et al., 2011; Ziliani and Surian, 2012; Moretto et al., 2014; Righini et al., 2017).

We identified two sites of bank erosion from our channel change case study where channel change was large enough that a less robust uncertainty method could be used and where channel change was small and only detectable by the SDP method. Bank erosion at both sites was visible by comparing the 1954 to 1961 aerial images but the $\mathcal{E}_1$ and $\mathcal{E}_2$ methods produced an indeterminate result when the magnitude of erosion was small, whereas the SDP method could detect this small erosional signal (Figure 2-14a,b). Conversely, the $\mathcal{E}_1$, $\mathcal{E}_2$, and SPD methods could all detect bank erosion when the signal was large (Figure 2-14c,d). This example from our case study highlights the benefit of using the SDP method when the signal of channel change is small compared to the uncertainty.

When the study objective is to calculate the absolute magnitude of planform change, rather than the direction of change as erosional or depositional, the SDP method significantly reduces the uncertainty bound (Table 2-1) and enables a more precise estimate of the magnitude of channel change. We demonstrate this capability using the

two sites of bank erosion from our channel change case study discussed above (Figure 2-14. The $\mathcal{E}_1$ and $\mathcal{E}_2$ methods predicted anywhere from 0.65 m of deposition to 15 m of erosion at the site with a smaller amount of bank erosion, whereas the SDP method predicted 3.5 to 8 m of bank erosion (Figure 2-14a,b). At the site with a larger amount of bank erosion, there was anywhere from 2 to 28 m of erosion using the $\mathcal{E}_1$ and $\mathcal{E}_2$ methods but that uncertainty bound was reduced to 13 to 18 m of erosion using the SDP method (Figure 2-14c,d). These examples demonstrate how well the SDP method can constrain
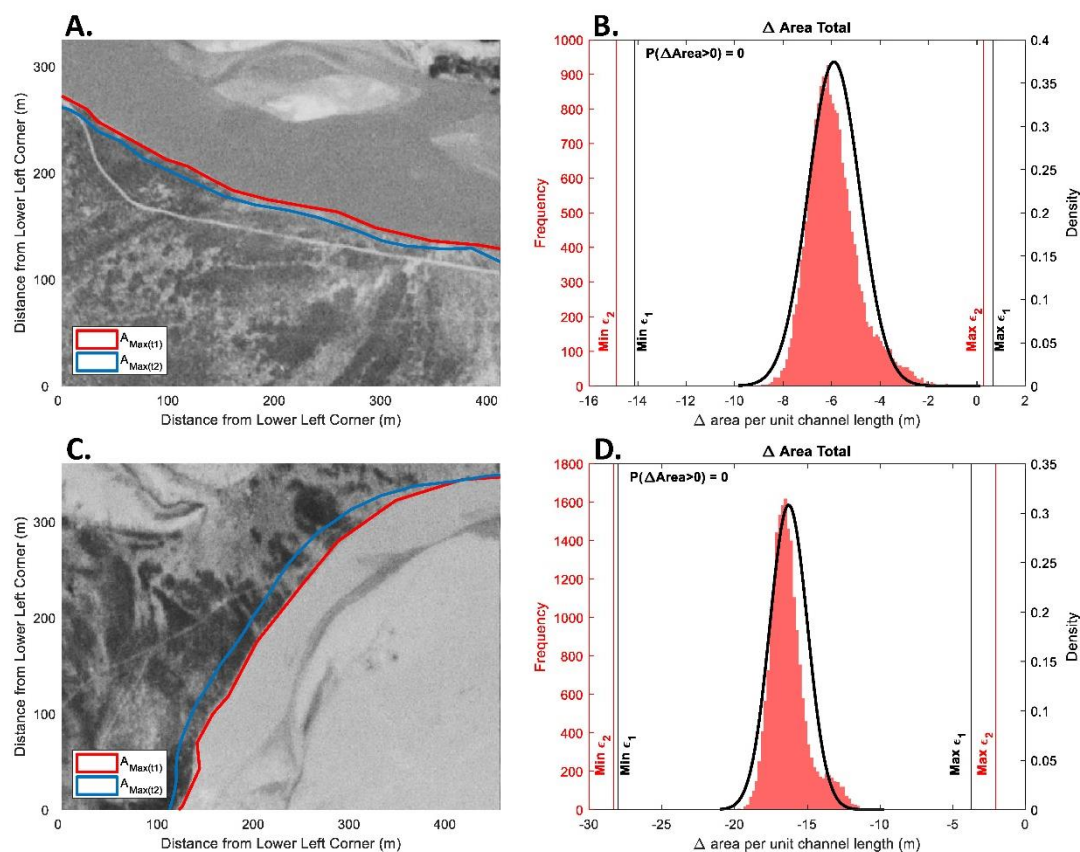
Figure 2-14. Example of the $\mathcal{E}_1$ and $\mathcal{E}_2$ methods and SDP method applied to two locations of bank retreat in our study area. (A) Location of small bank retreat. (B) Magnitude of channel change at the site in A calculated by the $\mathcal{E}_1$ and $\mathcal{E}_2$ methods and SDP method. (C) Location of large bank retreat. (D) Magnitude of channel change at the site in C calculated by the $\mathcal{E}_1$ and $\mathcal{E}_2$ methods and SDP method.

the magnitude of channel change, and we suggest that this method be used when the study objective is to calculate the absolute magnitude of change.

Lastly, the temporal interval between aerial images compared to the activity of the channel during that interval will govern the amount of channel change recorded and, therefore, the type of uncertainty analysis needed to detect significant channel change. When aerial images are acquired in closely spaced time intervals and channel change is small (e.g., Manners et al., 2014), the SDP method might facilitate channel change detection. Conversely, when channel changes are large, significant channel change might be detectable with a less robust form of uncertainty analysis, regardless of the time interval between aerial images.

4.2. When does each type of error and uncertainty matter?

In the SDP method, we distinguish between error and uncertainty by defining error as a deviation from a known value and uncertainty as a range of values that encompasses the true measurement. One advantage of the SDP method is that errors and uncertainties are added individually rather than being propagated to a single value, and by doing so, the user can evaluate the relative magnitude of each source of error and uncertainty and assess the effects on the channel change analysis. In our case study, co-registration error was the greatest source of error, followed by interpretation and digitization uncertainty (Figure 2-10), but the significance of each type of uncertainty might be different in other study areas, or within the same study area when using different aerial images. In the following sections, we describe scenarios when each source of uncertainty is significant and other scenarios when that type of uncertainty might be

disregarded. Understanding which sources of uncertainty are important in a given study

can help guide the selection of an appropriate uncertainty method.

4.2.1. Spatially distributed image co-registration error

Image co-registration error is relevant when two images are overlaid to calculate

planform change. When planform metrics are derived from a single image (e.g., width

and active channel area), the co-registration error is irrelevant, because the images are not

overlaid, although image distortion can still cause uncertainty in these planform metrics if

the images are not orthorectified. The co-registration error can be quantified as uniform

across the study area using the RMSE (Equation 5) of tie-points used to warp the image,

the RMSE (Equation 5) of independent test-points, or the co-registration error can be

allowed to vary spatially, as done in the SDP method (Figure 2-1 step1). When planform

change is small (e.g., less than 25% of the width of the channel), a spatially variable co-

registration error is necessary, because this error is often lower than the uniform RMSE

near the channel, which allows smaller planform changes to be detected. In our case

study, using a spatially variable co-registration error reduced the error at ~83% of the

A_{min} and A_{max} vertices in the 1954 and 1961 images (Figure 2-15) and shrunk the overall

uncertainty bounds by 78-90% (Table 2-1). If the planform change is extremely large, the

uniform RMSE might be small compared to the channel change signal and a spatially

variable co-registration error would not be necessary. To decide whether the co-

registration error should be allowed to vary spatially, the magnitude of uncertainty in the

ε_1 method can be compared to estimated planform change when uncertainty is not

considered. If the ε_1 uncertainty bound is greater than the magnitude of change, co-

registration error should be allowed to vary spatially.
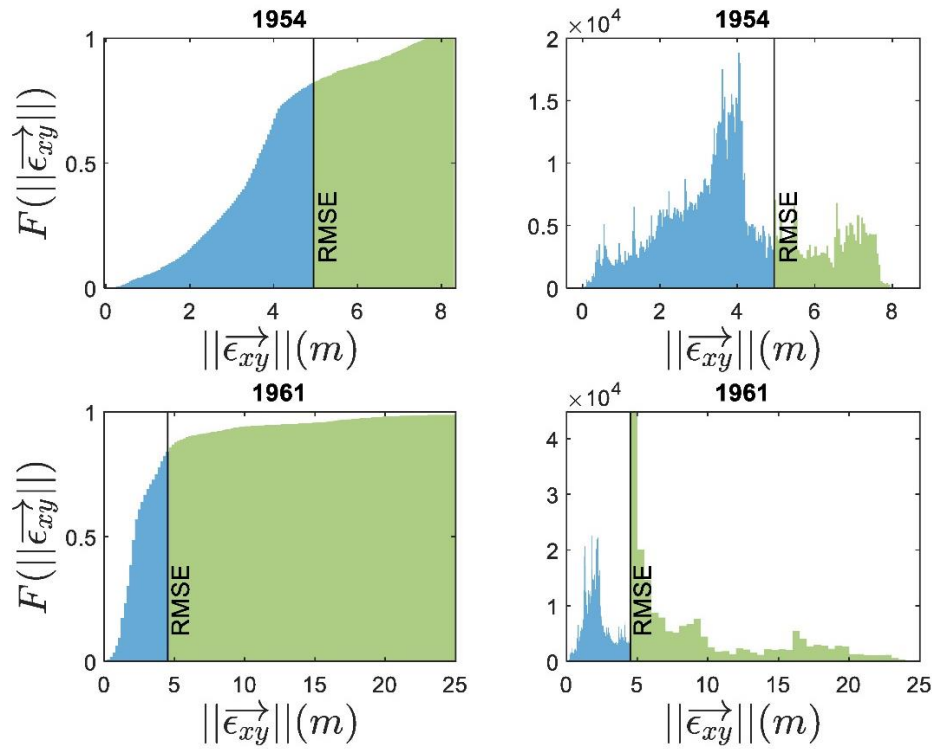
Figure 2-15. Distribution of co-registration errors extracted from each vertex along the A_{max} and A_{min} boundaries in 1954 and 1961. These data are displayed as a cumulative density function estimate and a histogram. The blue portion of these distributions have a co-registration error that is lower than the uniform RMSE and the green portion have a co-registration error that is above the uniform RMSE. 82% of the co-registration errors were above the uniform RMSE in 1954 and 84% in 1961.

The effectiveness of the spatially variable co-registration error in reducing uncertainty will depend on the number, distribution, and quality of test-points. We suggest using an automated procedure to generate test-points throughout the study area (e.g., Carbonneau et al., 2010) and supplementing those test-points with manually selected test-points near the channel. Additionally, the user could test the sensitivity of the SDP method to the number, density, and distribution of test-points in their study area.

4.2.2. Digitization uncertainty

Digitization uncertainty is affected by the spatial and spectral resolution of the image. The spatial resolution determines the smallest object that can be observed in an image. The appropriate spatial resolution for a channel change analysis will depend on the channel dimensions and might vary within the study area. If the spatial resolution is low and the channel is narrow, a single pixel may contain a portion of the active channel and the channel boundary, introducing uncertainty as to where to place the boundary within the pixel. The greater the proportion of pixels that contain both the active channel and the channel boundary, the larger the digitization uncertainty. Spectral resolution refers to the range of wavelengths within each one of the sensor's spectral bands. Aerial images collected by sensors with a high spectral resolution are more likely to have a near-infrared wavelength band. This type of band is helpful, because the near-infrared wavelength can be used to distinguish the boundary between vegetation, water, and bare channel bars, which reduces the digitization uncertainty.

The crispness of the boundary can also affect digitizing uncertainty. Easily identifiable features with sharp boundaries, like roads or buildings, will have a smaller digitizing uncertainty than fuzzy boundaries that are less crisp, such as trees. Along rivers in arid regions with little vegetation, actively eroding banks create crisp boundaries and have low digitizing uncertainty. In humid or mountainous regions, vegetation along the channel boundary is denser and eroding banks cause trees to fall into the channel, making the boundary fuzzier and subject to larger digitizing uncertainty. Shadows can cause crisp boundaries to become fuzzy during certain times of the day; digitization uncertainty is thus sensitive to flight timing.

Most study areas contain both crisp and fuzzy boundaries, which will cause the digitizing uncertainty to vary spatially. Currently, a spatially variable digitizing uncertainty has not been used in a channel change study; this is an area for future work. Although the SDP method does not directly incorporate a spatially variable digitizing uncertainty, the distribution used to describe the digitizing uncertainty can be adjusted to account for fuzzy and crisp boundaries by increasing the standard deviation or creating a mixed normal distribution. In this way, the SDP method is a significant improvement to previous methods that use a single value to define digitizing uncertainty.

4.2.3. Interpretation uncertainty

Interpretation uncertainty occurs when there are different plausible interpretations of the extent of the active channel. If the channel boundary can be identified based on breaks in topography from stereo images or digital elevation models, the interpretation uncertainty will tend to be smaller. However, freely available aerial images that are regularly acquired typically are not collected in stereo, and current practice involves delineating channel boundaries in GIS software without the aid of stereo images.

In our case study, interpretation uncertainty was a large source of uncertainty in some localized areas, but there was no uncertainty elsewhere. This caused the median of this uncertainty to be small (Figure 2-10; 0.00 m), because the uncertainty was not present in 56% of the study area. In other case studies, interpretation uncertainty might be small in localized areas or more pervasive throughout the study area. We suspect that interpretation uncertainty will be high in rivers that experience a large change in wetted channel area given a proportionately small change in discharge (e.g., braided rivers), because low-elevation bars are frequently wetted but not scoured, which allows fast-

growing vegetation to encroach on these surfaces (Werbylo et al., 2017). In such rivers, vegetation density is a poor proxy for the active channel, and the digitizer must use professional judgment in placing the active channel boundary. Similarly, vegetation might be a poor indication of the channel extent in rivers that experience flashy hydrology or that are subjected to large reset floods and very low base flows, because there might be a mosaic of bare alluvial surfaces at multiple elevations after a large flood that are hard to interpret (Dean and Schmidt, 2011, 2013; Thompson and Croke, 2013). Additionally, in humid environments where plants grow quickly, vegetation growing in the active channel during base flow can introduce ambiguity.

Interpretation uncertainty is likely to be larger for channels that are narrowing as compared to those that are widening. Channels widen through bank erosion that removes an entire section of sediment and creates an abrupt, crisp contact between the channel and floodplain with minimal interpretation uncertainty. Conversely, channel narrowing occurs over a continuum as alluvial surfaces transition from active channel bars to floodplains by vertically aggrading sediment (Allred and Schmidt, 1999; Grams and Schmidt, 2002; Moody et al., 1999; Pizzuto, 1994). Determining when enough sediment has accumulated on an alluvial surface to form a stable floodplain that is inundated by floods of an annual or greater recurrence is highly uncertain and subject to large interpretation uncertainty.

5. Conclusions

In this paper, we introduced a new method for quantifying uncertainty associated with channel change detection based on probabilistic, spatially varying estimates of co-registration error and digitization uncertainty. We also presented a framework that can be used to incorporate interpretation uncertainty into the channel change analysis. The SDP

method can be used to calculate uncertainty at specific locations of linear channel adjustment or polygons of erosion and deposition, while also estimating the central tendency of net planform change, making this the first generalizable method for quantifying uncertainty that can be applied to all metrics of channel change derived from aerial image overlays. Although the focus of this paper was the detection of channel change, the SDP method can be applied to other geomorphic and landscape change detection analyses, such as glacial change (DeVisser and Fountain, 2015), shoreline or tidal wetland change (Del Río et al., 2013), and changes in water body surfaces (Necsoiu et al., 2013).

The SDP method as applied to our case study reduced the magnitude of uncertainty by 83-87% compared to two existing methods that used a spatially uniform image co-registration error and did not characterize uncertainty probabilistically. By reducing the bounds of uncertainty, we were able to detect channel changes of a smaller magnitude. More importantly, the distribution information from the SDP method allowed us to report a magnitude of channel change in our case study with an appropriate level of confidence even though the uncertainty bound included zero. We could not make a similar inference using the existing methods, because their uncertainty bounds had no distribution information and included zero, making the results indeterminate.

The SDP method was an improvement to existing methods that quantify uncertainty without distributional information, but the method was computationally intensive and might not be necessary for all change detection studies. We suggest that the SDP method should be used in channel change studies where 1) the uncertainty is a large proportion of the total channel area, as in small rivers; 2) when the temporal spacing

between aerial images is short and the channel change is expected to be small; and 3)

when the purpose of the study is to calculate the absolute magnitude of change, such as

studies that use bank retreat to calculate the volume of bank erosion.

Data Availability

  A MATLAB® script for performing an SDP uncertainty analysis is available at

https://qcnr.usu.edu/coloradoriver/files/leonard_data. The data used in this case study are

available from the U.S. Geological Survey (USGS) ScienceBase at

https://doi.org/10.5066/P9SEBJ3X (Legleiter and Leonard, 2020).

References

Agisoft LLC. 2016. Agisoft Photoscan Professional edition

Ahammad M, Czuba JA, Pfeiffer AM, Murphy BP, Belmont P. 2021. Simulated
  Dynamics of Mixed Versus Uniform Grain Size Sediment Pulses in a Gravel-Bedded
  River. Journal of Geophysical Research: Earth Surface **126** : e2021JF006194. DOI:
  10.1029/2021JF006194

Alexander J. 2007. The timing and magnitude of channel adjustments in the Upper Green
  River below Flaming Gorge Dam in Browns Park and Lodore Canyon, Colorado: An
  analysis of the pre- and post-dam river using high-resolution dendrogemorphology
  and repeat topographic surveys, Thesis, Utah State University: Logan, UT

Allred TM, Schmidt JC. 1999. Channel narrowing by vertical accretion along the Green
  River near Green River, Utah. GSA Bulletin **111** : 1757–1772. DOI: 10.1130/0016-
  7606(1999)111<1757:CNBVAA>2.3.CO;2

Amidror I. 2002. Scattered Data Interpolation Methods for Electronic Imaging Systems:
  A Survey. Journal of Electronic Imaging **11** : 157–176. DOI: 10.1117/1.1455013

An C, Gong Z, Naito K, Parker G, Hassan MA, Ma H, Fu X. 2021. Grain Size-Specific
  Engelund-Hansen Type Relation for Bed Material Load in Sand-Bed Rivers, With
  Application to the Mississippi River. Water Resources Research **57** :
  e2020WR027517. DOI: 10.1029/2020WR027517

Anderson S, Pitlick J. 2014. Using repeat LiDAR to estimate sediment transport in a steep stream. Journal of Geophysical Research: Earth Surface **119** : 621–643. DOI: 10.1002/2013JF002933

Anderson SW. 2019a. Uncertainty in quantitative analyses of topographic change: error propagation and the role of thresholding. Earth Surface Processes and Landforms **44** : 1015–1033. DOI: 10.1002/esp.4551

Anderson SW. 2019b. Uncertainty in quantitative analyses of topographic change: error propagation and the role of thresholding. Earth Surface Processes and Landforms **44** : 1015–1033. DOI: 10.1002/esp.4551

Andrews E. 1978. Present and potential sediment yields in the Yampa River Basin, Colorado and Wyoming . USGS Numbered Series. U.S. Geological Survey, Water Resources Division,

Andrews E. 1980. Effective and bankfull discharges of streams in the Yampa River basin, Colorado and Wyoming. Journal of Hydrology **46** : 311–330. DOI: 10.1016/0022-1694(80)90084-0

Antoniazza G, Bakker M, Lane SN. 2019. Revisiting the morphological method in two-dimensions to quantify bed-material transport in braided rivers. Earth Surface Processes and Landforms **44** : 2251–2267.

Arbós CY, Blom A, Viparelli E, Reneerkens M, Frings RM, Schielen RMJ. 2021. River Response to Anthropogenic Modification: Channel Steepening and Gravel Front Fading in an Incising River. Geophysical Research Letters **48** : e2020GL091338. DOI: 10.1029/2020GL091338

Ashida K, Michiue M. 1972. Study on Hydraulic Resistance and Bedload Transport Rate in Alluvial Streams. Trans. Jpn. Soc. Civil Engng. **206** : 59–69.

Best J. 2019. Anthropogenic stresses on the world's big rivers. Nature Geoscience **12** : 7–21. DOI: 10.1038/s41561-018-0262-x

Bollati IM, Pellegrini L, Rinaldi M, Duci G, Pelfini M. 2014. Reach-scale morphological adjustments and stages of channel evolution: The case of the Trebbia River (northern Italy). Geomorphology **221** : 176–186. DOI: 10.1016/j.geomorph.2014.06.007

Borland WM. 1960. Stream channel stability. United States Bureau of Reclamation. Denver

Brakenridge GR. 1984. Alluvial stratigraphy and radiocarbon dating along the Duck River, Tennessee: Implications regarding flood-plain origin. GSA Bulletin **95** : 9–25. DOI: 10.1130/0016-7606(1984)95<9:ASARDA>2.0.CO;2

Brandt SA. 2000a. Classification of geomorphological effects downstream of dams. CATENA **40** : 375–401. DOI: 10.1016/S0341-8162(00)00093-X

Brandt SA. 2000b. Prediction of downstream geomorphological changes after dam construction: A steam power approach. International Journal of Water Resources Development; Abingdon **16** : 343.

Brasington J, Langham J, Rumsby B. 2003. Methodological sensitivity of morphometric estimates of coarse fluvial sediment transport. Geomorphology **53** : 299–316. DOI: 10.1016/S0169-555X(02)00320-3

Brasington J, Rumsby BT, McVey RA. 2000. Monitoring and modelling morphological change in a braided gravel-bed river using high resolution GPS-based survey. Earth Surface Processes and Landforms **25** : 973–990. DOI: 10.1002/1096-9837(200008)25:9<973::AID-ESP111>3.0.CO;2-Y

Buckingham SE, Whitney JW. 2007. GIS Methodology for Quantifying Channel Change in Las Vegas, Nevada. JAWRA Journal of the American Water Resources Association **43** : 888–898. DOI: 10.1111/j.1752-1688.2007.00073.x

Buffington JM, Montgomery DR. 1999. Effects of sediment supply on surface textures of gravel-bed rivers. Water Resources Research **35** : 3523–3530. DOI: 10.1029/1999WR900232

Cadol D, Rathburn SL, Cooper DJ. 2011. Aerial photographic analysis of channel narrowing and vegetation expansion in Canyon De Chelly National Monument, Arizona, USA, 1935–2004. River Research and Applications **27** : 841–856. DOI: 10.1002/rra.1399

Carbonneau PE, Dietrich JT. 2017. Cost-effective non-metric photogrammetry from consumer-grade sUAS: implications for direct georeferencing of structure from motion photogrammetry. Earth Surface Processes and Landforms **42** : 473–486. DOI: 10.1002/esp.4012

Carbonneau PE, Dugdale SJ, Clough S. 2010. An automated georeferencing tool for watershed scale fluvial remote sensing. River Research and Applications **26** : 650–658. DOI: 10.1002/rra.1263

Church M. 1995. Geomorphic response to river flow regulation: Case studies and time-scales. Regulated Rivers: Research & Management **11** : 3–22. DOI: 10.1002/rrr.3450110103

Church M. 2006. Bed Material Transport and the Morphology of Alluvial River Channels. Annual Review of Earth and Planetary Sciences **34** : 325–354. DOI: 10.1146/annurev.earth.33.092203.122721

Clark JJ, Wilcock PR. 2000. Effects of land-use change on channel morphology in northeastern Puerto Rico. GSA Bulletin **112** : 1763–1777. DOI: 10.1130/0016-7606(2000)112<1763:EOLUCO>2.0.CO;2

Colby BR, Hembree CC. 1955. Computations of total sediment discharge of the Niobrara River near Cody, Nebraska. USGS Water Supply Paper 1357 . USGS Washington

Comiti F, Da Canal M, Surian N, Mao L, Picco L, Lenzi MA. 2011. Channel adjustments and vegetation cover dynamics in a large gravel bed river over the last 200 years. Geomorphology **125** : 147–159. DOI: 10.1016/j.geomorph.2010.09.011

Croke J, Todd P, Thompson C, Watson F, Denham R, Khanal G. 2013. The use of multi temporal LiDAR to assess basin-scale erosion and deposition following the catastrophic January 2011 Lockyer flood, SE Queensland, Australia. Geomorphology **184** : 111–126. DOI: 10.1016/j.geomorph.2012.11.023

Cui Y, Paola C, Parker G. 1996. Numerical simulation of aggradation and downstream fining. Journal of Hydraulic Research **34** : 185–204. DOI: 10.1080/00221689609498496

Cui Y, Parker, G. G, Lisle TE, Gott J, Hansler-Ball ME, Pizzuto JE, Allmendinger NE, Reed JM. 2003a. Sediment pulses in mountain rivers: 1. Experiments. Water Resources Research **39** : 1239. DOI: 10.1029/2002WR001803

Cui Y, Parker G, Lisle TE, Gott J, Hansler-Ball ME, Pizzuto JE, Allmendinger NE, Reed JM. 2003b. Sediment pulses in mountain rivers: 1. Experiments. Water Resources Research **39** DOI: 10.1029/2002WR001803

Cui Y, Parker G, Lisle TE, Pizzuto JE, Dodd AM. 2005. More on the evolution of bed material waves in alluvial rivers. Earth Surface Processes and Landforms **30** : 107–114. DOI: 10.1002/esp.1156

Cui Y, Parker G, Pizzuto J, Lisle TE. 2003c. Sediment pulses in mountain rivers: 2. Comparison between experiments and numerical predictions. Water Resources Research **39** : 1240. DOI: 10.1029/2002WR001805

Cui Y, Parker P. 2005. Numerical Model of Sediment Pulses and Sediment-Supply Disturbances in Mountain Rivers. Journal of Hydraulic Engineering **131** : 646–656. DOI: 10.1061/(ASCE)0733-9429(2005)131:8(646)

Curry CW, Bennett RH, Hulbert MH, Curry KJ, Faas RW. 2004. Comparative Study of Sand Porosity and a Technique for Determining Porosity of Undisturbed Marine Sediment. Marine Georesources & Geotechnology **22** : 231–252. DOI: 10.1080/10641190490900844

Day SS, Gran KB, Belmont P, Wawrzyniec T. 2013. Measuring bluff erosion part 2: pairing aerial photographs and terrestrial laser scanning to create a watershed scale sediment budget. Earth Surface Processes and Landforms **38** : 1068–1082. DOI: 10.1002/esp.3359

De Rose RC, Basher LR. 2011. Measurement of river bank and cliff erosion from sequential LIDAR and historical aerial photography. Geomorphology **126** : 132–147. DOI: 10.1016/j.geomorph.2010.10.037

Dean DJ, Schmidt JC. 2011. The role of feedback mechanisms in historic channel changes of the lower Rio Grande in the Big Bend region. Geomorphology **126** : 333–349. DOI: 10.1016/j.geomorph.2010.03.009

Dean DJ, Schmidt JC. 2013. The geomorphic effectiveness of a large flood on the Rio Grande in the Big Bend region: Insights on geomorphic controls and post-flood geomorphic response. Geomorphology **201** : 183–198. DOI: 10.1016/j.geomorph.2013.06.020

Dean DJ, Topping DJ, Grams PE, Walker AE, Schmidt JC. 2020. Does Channel Narrowing by Floodplain Growth Necessarily Indicate Sediment Surplus? Lessons From Sediment Transport Analyses in the Green and Colorado Rivers, Canyonlands, Utah. Journal of Geophysical Research: Earth Surface **125** : e2019JF005414. DOI: 10.1029/2019JF005414

Dean DJ, Topping DJ, Schmidt JC, Griffiths RE, Sabol TA. 2016. Sediment supply versus local hydraulic controls on sediment transport and storage in a river with large sediment loads. Journal of Geophysical Research: Earth Surface **121** : 2015JF003436. DOI: 10.1002/2015JF003436

Del Río L, Gracia FJ, Benavente J. 2013. Shoreline change patterns in sandy coasts. A case study in SW Spain. Geomorphology **196** : 252–266. DOI: 10.1016/j.geomorph.2012.07.027

DeVisser MH, Fountain AG. 2015. A century of glacier change in the Wind River Range, WY. Geomorphology **232** : 103–116. DOI: 10.1016/j.geomorph.2014.10.017

Dietrich WE, Kirchner JW, Ikeda H, Iseya F. 1989. Sediment supply and the development of the coarse surface layer in gravel-bedded rivers. Nature **340** : 215–217. DOI: 10.1038/340215a0

Donovan M, Belmont P. 2019. Timescale dependence in river channel migration measurements. Earth Surface Processes and Landforms **44** : 1530–1541. DOI: 10.1002/esp.4590

Donovan M, Belmont P, Notebaert B, Coombs T, Larson P, Souffront M. 2019. Accounting for uncertainty in remotely-sensed measurements of river planform change. Earth-Science Reviews **193** : 220–236. DOI: 10.1016/j.earscirev.2019.04.009

Downs PW. 1995. Estimating the probability of river channel adjustment. Earth Surface Processes and Landforms **20** : 687–705. DOI: 10.1002/esp.3290200710

Downward SR, Gurnell AM, Brookes A. 1994. A methodology for quantifying river channel planform change using GIS. IAHS Publications-Series of Proceedings and Reports-Intern Assoc Hydrological Sciences **224** : 449–456.

Doyle MW, Shields FD. 2000. Incorporation of bed texture into a channel evolution model. Geomorphology **34** : 291–309. DOI: 10.1016/S0169-555X(00)00014-3

Doyle MW, Stanley EH, Harbor JM. 2003. Channel adjustments following two dam removals in Wisconsin. Water Resources Research **39** DOI: 10.1029/2002WR001714

Dyni JR. 1968. Geologic map of the Elk Springs quadrangle, Moffatt County, Colorado . Report [online] Available from: http://pubs.er.usgs.gov/publication/gq702

East AE et al. 2015. Large-scale dam removal on the Elwha River, Washington, USA: River channel and floodplain geomorphic change. Geomorphology **228** : 765–786. DOI: 10.1016/j.geomorph.2014.08.028

East AE, Logan JB, Dartnell P, Lieber-Kotz O, Cavagnaro DB, McCoy SW, Lindsay DN. 2021. Watershed Sediment Yield Following the 2018 Carr Fire, Whiskeytown National Recreation Area, Northern California. Earth and Space Science **8** : e2021EA001828. DOI: 10.1029/2021EA001828

East AE, Sankey JB. 2020. Geomorphic and Sedimentary Effects of Modern Climate Change: Current and Anticipated Future Conditions in the Western United States. Reviews of Geophysics **58** : e2019RG000692. DOI: 10.1029/2019RG000692

Eaton B, Millar R. 2017. Predicting gravel bed river response to environmental change: the strengths and limitations of a regime-based approach. Earth Surface Processes and Landforms **42** : 994–1008. DOI: 10.1002/esp.4058

Eaton BC, Lapointe MF. 2001. Effects of large floods on sediment transport and reach morphology in the cobble-bed Sainte Marguerite River. Geomorphology **40** : 291–309. DOI: 10.1016/S0169-555X(01)00056-3

Egiazaroff IV. 1965. Calculation of Nonuniform Sediment Concentrations. Journal of the Hydraulics Division **91** : 225–247. DOI: 10.1061/JYCEAJ.0001277

Elliott JG, Anders SP. 2004. Summary of sediment data from the Yampa River and Upper Green River basins, Colorado and Utah, 1993-2002 . US Department of the Interior, US Geological Survey

Elliott JG, Kircher JE, Von Guerard P. 1984. Sediment transport in the lower Yampa River, northwestern Colorado . US Geological Survey

Erwin SO, Schmidt JC, Wheaton JM, Wilcock PR. 2012. Closing a sediment budget for a reconfigured reach of the Provo River, Utah, United States. Water Resources Research **48** : W10512. DOI: 10.1029/2011WR011035

Everitt B. 1993. Channel responses to declining flow on the Rio Grande between Ft. Quitman and Presidio, Texas. Geomorphology **6** : 225–242. DOI: 10.1016/0169-555X(93)90048-7

Ferguson RI, Church M, Rennie CD, Venditti JG. 2015a. Reconstructing a sediment pulse: Modeling the effect of placer mining on Fraser River, Canada. Journal of Geophysical Research: Earth Surface **120** : 2015JF003491. DOI: 10.1002/2015JF003491

Ferguson RI, Church M, Rennie CD, Venditti JG. 2015b. Reconstructing a sediment pulse: Modeling the effect of placer mining on Fraser River, Canada. Journal of Geophysical Research: Earth Surface **120** : 1436–1454.

Fonstad MA, Dietrich JT, Courville BC, Jensen JL, Carbonneau PE. 2013. Topographic structure from motion: a new development in photogrammetric measurement. Earth Surface Processes and Landforms **38** : 421–430. DOI: 10.1002/esp.3366

Fryirs K, Brierley G. 2022. Assemblages of geomorphic units: A building block approach to analysis and interpretation of river character, behaviour, condition and recovery. Earth Surface Processes and Landforms **47** : 92–108. DOI: 10.1002/esp.5264

Fryirs KA. 2017. River sensitivity: a lost foundation concept in fluvial geomorphology. Earth Surface Processes and Landforms **42** : 55–70. DOI: 10.1002/esp.3940

Fryirs KA, Brierley GJ. 2012. Geomorphic analysis of river systems: an approach to reading the landscape . John Wiley & Sons: Chichester, U.K.

Fuller IC, Large ARG, Charlton ME, Heritage GL, Milan DJ. 2003. Reach-scale sediment transfers: an evaluation of two morphological budgeting approaches. Earth Surface Processes and Landforms **28** : 889–903. DOI: 10.1002/esp.1011

Gaeuman D, Stewart R, Schmandt B, Pryor C. 2017. Geomorphic response to gravel augmentation and high-flow dam release in the Trinity River, California. Earth Surface Processes and Landforms **42** : 2523–2540. DOI: 10.1002/esp.4191

Gaeuman D, Symanzik J, Schmidt JC. 2005. A map overlay error model based on boundary geometry. Geographical Analysis **37** : 350–369. DOI: 10.1111/j.1538-4632.2005.00585.x

Gaeuman DA, Schmidt JC, Wilcock PR. 2003. Evaluation of in-channel gravel storage with morphology-based gravel budgets developed from planimetric data. Journal of Geophysical Research: Earth Surface **108** : 6001. DOI: 10.1029/2002JF000002

Garcia M, Parker G. 1991. Entrainment of Bed Sediment into Suspension. Journal of Hydraulic Engineering **117** : 414–435. DOI: 10.1061/(ASCE)0733-9429(1991)117:4(414)

Gomez B, Coleman SE, Sy VWK, Peacock DH, Kent M. 2007. Channel change, bankfull and effective discharges on a vertically accreting, meandering, gravel-bed river. Earth Surface Processes and Landforms **32** : 770–785. DOI: 10.1002/esp.1424

Grams PE, Buscombe D, Topping DJ, Kaplinski M, Hazel JE. 2019. How many measurements are required to construct an accurate sand budget in a large river? Insights from analyses of signal and noise. Earth Surface Processes and Landforms **44** : 160–178. DOI: https://doi.org/10.1002/esp.4489

Grams PE, Dean DJ, Walker AE, Kasprak A, Schmidt JC. 2020. The roles of flood magnitude and duration in controlling channel width and complexity on the Green River in Canyonlands, Utah, USA. Geomorphology **371** : 107438. DOI: 10.1016/j.geomorph.2020.107438

Grams PE, Schmidt JC. 2002. Streamflow regulation and multi-level flood plain formation: channel narrowing on the aggrading Green River in the eastern Uinta Mountains, Colorado and Utah. Geomorphology **44** : 337–360. DOI: 10.1016/S0169-555X(01)00182-9

Grams PE, Schmidt JC. 2005. Equilibrium or indeterminate? Where sediment budgets fail: Sediment mass balance and adjustment of channel form, Green River downstream from Flaming Gorge Dam, Utah and Colorado. Geomorphology **71** : 156–181. DOI: 10.1016/j.geomorph.2004.10.012

Grams PE, Topping DJ, Schmidt JC, Hazel JE, Kaplinski M. 2013. Linking morphodynamic response with sediment mass balance on the Colorado River in Marble Canyon: Issues of scale, geomorphic setting, and sampling design: Flow, sediment supply, and morphodynamics. Journal of Geophysical Research: Earth Surface **118** : 361–381. DOI: 10.1002/jgrf.20050

Gran KB. 2012. Strong seasonality in sand loading and resulting feedbacks on sediment transport, bed texture, and channel planform at Mount Pinatubo, Philippines. Earth Surface Processes and Landforms **37** : 1012–1022. DOI: 10.1002/esp.3241

Gran KB, Montgomery DR. 2005. Spatial and temporal patterns in fluvial recovery following volcanic eruptions: Channel response to basin-wide sediment loading at Mount Pinatubo, Philippines. Geological Society of America Bulletin **117** : 195–211.

Grant GE, Schmidt JC, Lewis SL. 2003. A Geological Framework for Interpreting Downstream Effects of Dams on Rivers. In A Peculiar River , O'Connor JE and Grant GE (eds). American Geophysical Union; 203–219.

Griffiths GA. 1979. Recent sedimentation history of the Waimakariri River, New Zealand. Journal of Hydrology(New Zealand) **18**

Griffiths RonaldG, Topping DJ, Leonard CM, Unema JA. In Review. Resurvey of cross sections on the Little Snake and Yampa rivers in, and upstream from, Deerlodge Park, Colorado . Open-File Report. U.S. Geological Survey

Gudmundsson L, Boulange J, Do HX, Gosling SN, Grillakis MG, Koutroulis AG, Leonard M, Liu J, Müller Schmied H, Papadimitriou L. 2021. Globally observed trends in mean and extreme river flow attributed to climate change. Science **371** : 1159–1162.

Gurnell AM, Downward SR, Jones R. 1994. Channel planform change on the River Dee meanders, 1876–1992. Regulated Rivers: Research & Management **9** : 187–204. DOI: 10.1002/rrr.3450090402

Ham DG, Church M. 2000. Bed-material transport estimated from channel morphodynamics: Chilliwack River, British Columbia. Earth Surface Processes and Landforms **25** : 1123–1142. DOI: 10.1002/1096-9837(200009)25:10<1123::AID-ESP122>3.0.CO;2-9

Hansen WR. 1984. Post-laramide tectonic history of the Eastern Uinta Mountains, Utah, Coloardo, and Wyoming. The Mountain Geologist **21** : 5–29.

Hazel JE, Grams PE, Schmidt JC, Kaplinski M. 2010. Sandbar response in Marble and Grand Canyons, Arizona, following the 2008 high-flow experiment on the Colorado River . U.S. Geological Survey Scientific Investigation Report. US Department of the Interior, US Geological Survey

Henderson FM. 1966. Open channel flow . Macmillan: New York

Hirano M. 1971. On riverbed variation with armoring. Trans. Jpn. Soc. Civil Engng. **195** : 55–65.

Hoey TB, Ferguson R. 1994. Numerical simulation of downstream fining by selective transport in gravel bed rivers: Model development and illustration. Water Resources Research **30** : 2251–2260. DOI: 10.1029/94WR00556

Hoffman DF, Gabet EJ. 2007. Effects of sediment pulses on channel morphology in a gravel-bed river. GSA Bulletin **119** : 116–125. DOI: 10.1130/B25982.1

Hughes ML, McDowell PF, Marcus WA. 2006. Accuracy assessment of georectified aerial photographs: implications for measuring lateral channel movement in a GIS. Geomorphology **74** : 1–16. DOI: 10.1016/j.geomorph.2005.07.001

Julien PY, Klaassen GJ. 1995. Sand-Dune Geometry of Large Rivers during Floods. Journal of Hydraulic Engineering **121** : 657–663. DOI: 10.1061/(ASCE)0733-9429(1995)121:9(657)

Kemper JT, Rathburn SL, Friedman JM, Nelson JM, Mueller ER, Vincent KR. 2022a. Fingerprinting historical tributary contributions to floodplain sediment using bulk geochemistry. CATENA **214** : 106231. DOI: 10.1016/j.catena.2022.106231

Kemper JT, Thaxton RD, Rathburn SL, Friedman JM, Mueller ER, Scott ML. 2022b. Sediment-Ecological Connectivity in a Large River Network. Earth Surface Processes and Landforms **47** DOI: 10.1002/esp.5277

Kessler AC, Gupta SC, Brown MK. 2013. Assessment of river bank erosion in Southern Minnesota rivers post European settlement. Geomorphology **201** : 312–322. DOI: 10.1016/j.geomorph.2013.07.006

Knighton AD. 1989. River adjustment to changes in sediment load: The effects of tin mining on the Ringarooma River, Tasmania, 1875–1984. Earth Surface Processes and Landforms **14** : 333–359. DOI: 10.1002/esp.3290140408

Kondolf GM. 1997. Hungry water: Effect of dams and gravel mining on river channels. Environmental Management **21**

Kondolf GM, Matthews WVG. 1991. Unmeasured Residuals in Sediment Budgets: A Cautionary Note. Water Resources Research **27** : 2483–2486. DOI: 10.1029/91WR01625

Kondrashov D, Ghil M. 2006. Spatio-temporal filling of missing points in geophysical data sets. Nonlinear Processes in Geophysics **13** : 151–159.

Lane EW. 1955. Importance of fluvial morphology in hydraulic engineering. Proceedings (American Society of Civil Engineers); v. 81, paper no. 745

Lane SN, Westaway RM, Murray Hicks D. 2003. Estimation of erosion and deposition volumes in a large, gravel-bed, braided river using synoptic remote sensing. Earth Surface Processes and Landforms **28** : 249–271. DOI: 10.1002/esp.483

Lauer JW, Parker G. 2008. Net local removal of floodplain sediment by river meander migration. Geomorphology **96** : 123–149. DOI: 10.1016/j.geomorph.2007.08.003

Lea DM, Legleiter CJ. 2016a. Refining measurements of lateral channel movement from image time series by quantifying spatial variations in registration error. Geomorphology **258** : 11–20. DOI: 10.1016/j.geomorph.2016.01.009

Lea DM, Legleiter CJ. 2016b. Refining measurements of lateral channel movement from image time series by quantifying spatial variations in registration error. Geomorphology **258** : 11–20.

Legleiter CJ. 2012. Remote measurement of river morphology via fusion of LiDAR topography and spectrally based bathymetry. Earth Surface Processes and Landforms **37** : 499–518. DOI: 10.1002/esp.2262

Legleiter CJ. 2014. Downstream Effects of Recent Reservoir Development on the Morphodynamics of a Meandering Channel: Savery Creek, Wyoming, Usa. River Research and Applications : 1328–1343. DOI: 10.1002/rra.2824

Legleiter CJ. 2015. Calibrating remotely sensed river bathymetry in the absence of field measurements: Flow REsistance Equation-Based Imaging of River Depths (FREEBIRD). Water Resources Research **51** : 2865–2884. DOI: 10.1002/2014WR016624

Legleiter CJ, Kyriakidis PC. 2007. Forward and Inverse Transformations between Cartesian and Channel-fitted Coordinate Systems for Meandering Rivers. Mathematical Geology **38** : 927–958. DOI: 10.1007/s11004-006-9056-6

Legleiter CJ, Leonard CM. 2020. Aerial photographs from the Yampa and Little Snake Rivers in northwest Colorado used to characterize channel changes occuring between 1954 and 1961. U.S. Geological Survey data release [online] Available from: https://doi.org/10.5066/P9SEBJ3X

Leonard C, Legleiter C, Overstreet B. 2017a. Effects of lateral confinement in natural and leveed reaches of a gravel-bed river: Snake River, Wyoming, USA. Earth Surface Processes and Landforms **42** : 2119–2138. DOI: 10.1002/esp.4157

Leonard C, Legleiter C, Overstreet B. 2017b. Effects of lateral confinement in natural and leveed reaches of a gravel-bed river: Snake River, Wyoming, USA. Earth Surface Processes and Landforms **42** : 2119–2138.

Leonard CM, Legleiter CJ, Lea DM, Schmidt JC. 2020. Measuring channel planform change from image time series: A generalizable, spatially distributed, probabilistic method for quantifying uncertainty. Earth Surface Processes and Landforms **45** : 2727–2744. DOI: https://doi.org/10.1002/esp.4926

Leopold LB. 1973. River Channel Change with Time: An Example: Address as Retiring President of The Geological Society of America, Minneapolis, Minnesota, November

1972. GSA Bulletin **84** : 1845–1860. DOI: 10.1130/0016-7606(1973)84<1845:RCCWTA>2.0.CO;2

Liébault F, Piégay H. 2001. Assessment of channel changes due to long-term bedload supply decrease, Roubion River, France. Geomorphology **36** : 167–186. DOI: 10.1016/S0169-555X(00)00044-1

Lisenby PE, Fryirs KA, Thompson CJ. 2020. River sensitivity and sediment connectivity as tools for assessing future geomorphic channel behavior. International Journal of River Basin Management **18** : 279–293. DOI: 10.1080/15715124.2019.1672705

Lisle TE, Nelson JM, Pitlick J, Madej MA, Barkett BL. 2000. Variability of bed mobility in natural, gravel-bed channels and adjustments to sediment load at local and reach scales. Water Resources Research **36** : 3743–3755. DOI: 10.1029/2000WR900238

Lyons JK, Pucherelli MJ, Clark RC. 1992. Sediment transport and channel characteristics of a sand-bed portion of the Green River below Flaming Gorge Dam, Utah, USA. Regulated Rivers: Research & Management **7** : 219–232. DOI: 10.1002/rrr.3450070302

Mackin JH. 1948. Concept of the graded river. Geological Society of America Bulletin **59** : 463–512.

Magilligan FJ, Haynie HJ, Nislow KH. 2008. Channel Adjustments to Dams in the Connecticut River Basin: Implications for Forested Mesic Watersheds. Annals of the Association of American Geographers **98** : 267–284. DOI: 10.1080/00045600801944160

Major JJ, Zheng S, Mosbrucker AR, Spicer KR, Christianson T, Thorne CR. 2019. Multidecadal Geomorphic Evolution of a Profoundly Disturbed Gravel Bed River System—A Complex, Nonlinear Response and Its Impact on Sediment Delivery. Journal of Geophysical Research: Earth Surface **124** : 1281–1309. DOI: 10.1029/2018JF004843

Manners R, Schmidt J, Wheaton JM. 2013. Multiscalar model for the determination of spatially explicit riparian vegetation roughness. Journal of Geophysical Research: Earth Surface **118** : 65–83. DOI: 10.1029/2011JF002188

Manners RB, Schmidt JC, Scott ML. 2014a. Mechanisms of vegetation-induced channel narrowing of an unregulated canyon river: Results from a natural field-scale experiment. Geomorphology **211** : 100–115. DOI: 10.1016/j.geomorph.2013.12.033

Manners RB, Schmidt JC, Scott ML. 2014b. Mechanisms of vegetation-induced channel narrowing of an unregulated canyon river: Results from a natural field-scale experiment. Geomorphology **211** : 100–115. DOI: 10.1016/j.geomorph.2013.12.033

Manners RB, Wilcox AC, Kui L, Lightbody AF, Stella JC, Sklar LS. 2015. When do plants modify fluvial processes? Plant-hydraulic interactions under variable flow and sediment supply rates. Journal of Geophysical Research: Earth Surface **120** : 325–345. DOI: 10.1002/2014JF003265

Martin DJ, Pavlowsky RT. 2011. Spatial Patterns of Channel Instability Along an Ozark River, Southwest Missouri. Physical Geography **32** : 445–468. DOI: 10.2747/0272-3646.32.5.445

Martin Y. 2003. Evaluation of bed load transport formulae using field evidence from the Vedder River, British Columbia. Geomorphology **53** : 75–95. DOI: 10.1016/S0169-555X(02)00348-3

Merritt DM, Cooper DJ. 2000. Riparian vegetation and channel change in response to river regulation: a comparative study of regulated and unregulated streams in the Green River Basin, USA. Regulated Rivers: Research & Management **16** : 543–564. DOI: 10.1002/1099-1646(200011/12)16:6<543::AID-RRR590>3.0.CO;2-N

Micheli ER, Kirchner JW. 2002. Effects of wet meadow riparian vegetation on streambank erosion. 1. Remote sensing measurements of streambank migration and erodibility. Earth Surface Processes and Landforms **27** : 627–639. DOI: 10.1002/esp.338

Miller SO, Ritter DF, Kochel RC, Miller JR. 1993. Fluvial responses to land-use changes and climatic variations within the Drury Creek watershed, southern Illinois. Geomorphology **6** : 309–329. DOI: 10.1016/0169-555X(93)90053-5

Montgomery DR, Panfil MS, Hayes SK. 1999. Channel-bed mobility response to extreme sediment loading at Mount Pinatubo. Geology **27** : 271–274. DOI: 10.1130/0091-7613(1999)027<0271:CBMRTE>2.3.CO;2

Moody JA, Pizzuto JE, Meade RH. 1999. Ontogeny of a flood plain. GSA Bulletin **111** : 291–303. DOI: 10.1130/0016-7606(1999)111<0291:OOAFP>2.3.CO;2

Moretto J, Rigon E, Mao L, Picco L, Delai F, Lenzi MA. 2014a. Channel Adjustments and Island Dynamics in the Brenta River (Italy) Over the Last 30 Years. River Research and Applications **30** : 719–732. DOI: 10.1002/rra.2676

Moretto J, Rigon E, Mao L, Picco L, Delai F, Lenzi MA. 2014b. Channel Adjustments and Island Dynamics in the Brenta River (Italy) Over the Last 30 Years. River Research and Applications **30** : 719–732. DOI: 10.1002/rra.2676

Mount N, Louis J. 2005. Estimation and propagation of error in measurements of river channel movement from aerial imagery. Earth Surface Processes and Landforms **30** : 635–643. DOI: 10.1002/esp.1172

Mount NJ, Louis J, Teeuw RM, Zukowskyj PM, Stott T. 2003. Estimation of error in bankfull width comparisons from temporally sequenced raw and corrected aerial photographs. Geomorphology **56** : 65–77. DOI: 10.1016/S0169-555X(03)00046-1

Nadler CT, Schumm SA. 1981. Metamorphosis of South Platte and Arkansas Rivers, Eastern Colorado. Physical Geography **2** : 95–115. DOI: 10.1080/02723646.1981.10642207

Nanson GC. 1980. Point bar and floodplain formation of the meandering Beatton River, northeastern British Columbia, Canada. Sedimentology **27** : 3–29. DOI: 10.1111/j.1365-3091.1980.tb01155.x

Nanson GC. 1986. Episodes of vertical accretion and catastrophic stripping: A model of disequilibrium flood-plain development. GSA Bulletin **97** : 1467–1475. DOI: 10.1130/0016-7606(1986)97<1467:EOVAAC>2.0.CO;2

Nanson GC, Hickin EJ. 1983. Channel migration and incision on the Beatton River. Journal of Hydraulic Engineering **109** : 327–337.

Nardi L, Rinaldi M. 2015. Spatio-temporal patterns of channel changes in response to a major flood event: the case of the Magra River (central–northern Italy). Earth Surface Processes and Landforms **40** : 326–339. DOI: 10.1002/esp.3636

Necsoiu M, Dinwiddie CL, Walter GR, Larsen A, Stothoff SA. 2013. Multi-temporal image analysis of historical aerial photographs and recent satellite imagery reveals evolution of water body surface area and polygonal terrain morphology in Kobuk Valley National Park, Alaska. Environmental Research Letters **8** : 025007. DOI: 10.1088/1748-9326/8/2/025007

Neill CR. 1987. Sediment balance considerations linking long-term transport and channel processes. Sediment Transport in Gravel-Bed Rivers. John Wiley and Sons New York. 1987. p 225-249, 9 fig, 25 ref.

Nelson NC, Erwin SO, Schmidt JC. 2013. Spatial and temporal patterns in channel change on the Snake River downstream from Jackson Lake dam, Wyoming. Geomorphology **200** : 132–142. DOI: 10.1016/j.geomorph.2013.03.019

van Niekerk A, Vogel KR, Slingerland RL, Bridge JS. 1992. Routing of Heterogeneous Sediments over Movable Bed: Model Development. Journal of Hydraulic Engineering **118** : 246–262. DOI: 10.1061/(ASCE)0733-9429(1992)118:2(246)

Nilsson C, Reidy CA, Dynesius M, Revenga C. 2005. Fragmentation and Flow Regulation of the World's Large River Systems. Science **308** : 405–408. DOI: 10.1126/science.1107887

Nordin CF, Dempster GR. 1963. Vertical distribution of velocity and suspended sediment, Middle Rio Grande, New Mexico . Report [online] Available from: http://pubs.er.usgs.gov/publication/pp462B

Page KJ, Nanson GC, Frazier PS. 2003. Floodplain Formation and Sediment Stratigraphy Resulting from Oblique Accretion on the Murrumbidgee River, Australia. Journal of Sedimentary Research **73** : 5–14. DOI: 10.1306/070102730005

Parker G, Hassan M, Wilcock P. 2007. 10 Adjustment of the bed surface size distribution of gravel-bed rivers in response to cycled hydrographs. In Developments in Earth Surface Processes , Habersack H, Piégay H, and Rinaldi M (eds). Elsevier; 241–285.

Parker G, Wilcock PR. 1993. Sediment feed and recirculating flumes: Fundamental difference. Journal of Hydraulic Engineering **119** : 1192–1204.

Phillips CB. 2021. Alluvial River Bankfull Hydraulic Geometry. HydroShare DOI: doi.org/10.4211/hs.fa5503b04af343ffbaf33d5a15cb2579

Pizzuto JE. 1994. Channel adjustments to changing discharges, Powder River, Montana. GSA Bulletin **106** : 1494–1501. DOI: 10.1130/0016-7606(1994)106<1494:CATCDP>2.3.CO;2

Pizzuto JE, Moody JA, Meade RH. 2008. Anatomy and Dynamics of a Floodplain, Powder River, Montana, U.S.A. Journal of Sedimentary Research **78** : 16–28. DOI: 10.2110/jsr.2008.005

Popov IV. 1962. A sediment balance of river reaches and its use for the characteristics of the channel process. Trudy GGI **94** : 3–21.

Rantz SE. 1982. Measurement and computation of streamflow . Geological Survey

Raudkivi AJ. 1976. Loose boundary hydraulics . Pergamom Press: Oxford

Rhoades EL, O'Neal MA, Pizzuto JE. 2009. Quantifying bank erosion on the South River from 1937 to 2005, and its importance in assessing Hg contamination. Applied Geography **29** : 125–134. DOI: 10.1016/j.apgeog.2008.08.005

Righini M, Surian N, Wohl E, Marchi L, Comiti F, Amponsah W, Borga M. 2017. Geomorphic response to an extreme flood in two Mediterranean rivers (northeastern Sardinia, Italy): Analysis of controlling factors. Geomorphology **290** : 184–199. DOI: 10.1016/j.geomorph.2017.04.014

van Rijn LC. 1984. Sediment Transport, Part II: Suspended Load Transport. Journal of Hydraulic Engineering **110** : 1613–1641. DOI: 10.1061/(ASCE)0733-9429(1984)110:11(1613)

Riquelme A, Del Soldato M, Tomás R, Cano M, Jordá Bordehore L, Moretti S. 2019. Digital landform reconstruction using old and recent open access digital aerial photos. Geomorphology **329** : 206–223. DOI: 10.1016/j.geomorph.2019.01.003

Rubin DM, Buscombe D, Wright SA, Topping DJ, Grams PE, Schmidt JC, Hazel JE, Kaplinski MA, Tusso R. 2020. Causes of Variability in Suspended-Sand Concentration Evaluated Using Measurements in the Colorado River in Grand Canyon. Journal of Geophysical Research: Earth Surface **125** : e2019JF005226. DOI: 10.1029/2019JF005226

Rubin DM, Topping DJ. 2001. Quantifying the relative importance of flow regulation and grain size regulation of suspended sediment transport α and tracking changes in grain size of bed sediment β. Water Resources Research **37** : 133–146.

Rubin DM, Topping DJ. 2008. Correction to "Quantifying the relative importance of flow regulation and grain size regulation of suspended sediment transport α and tracking changes in grain size of bed sediment β." Water Resources Research **44** : W09701. DOI: 10.1029/2008WR006819

Schmidt JC. 1999. Summary and synthesis of geomorphic studies conducted during the 1996 controlled flood in Grand Canyon. Geophysical Monograph - American Geophysical Union **110** : 329–342.

Schmidt JC, Wilcock PR. 2008a. Metrics for assessing the downstream effects of dams. Water Resources Research **44** : W04404. DOI: 10.1029/2006WR005092

Schmidt JC, Wilcock PR. 2008b. Metrics for assessing the downstream effects of dams. Water Resources Research **44** : W04404. DOI: 10.1029/2006WR005092

Schoellhamer DH. 2001. Singular spectrum analysis for time series with missing data. Geophysical Research Letters **28** : 3187–3190.

Schook DM, Rathburn SL, Friedman JM, Wolf JM. 2017. A 184-year record of river meander migration from tree rings, aerial imagery, and cross sections. Geomorphology **293** : 227–239. DOI: 10.1016/j.geomorph.2017.06.001

Schumm SA. 1969. River metamorphosis. Journal of the Hydraulics division **95** : 255–274.

Schumm SA, Harvey MD, Watson CC. 1984. Incised channels: morphology, dynamics, and control . Water Resources Publications

Schumm SA, Khan HR. 1972. Experimental Study of Channel Patterns. GSA Bulletin **83** : 1755–1770. DOI: 10.1130/0016-7606(1972)83[1755:ESOCP]2.0.CO;2

Schumm SA, Lichty RW. 1965. Time, space, and causality in geomorphology. American Journal of Science **263** : 110–119. DOI: 10.2475/ajs.263.2.110

Shelley J, Hotchkiss RH, Boyd P, Gibson S. 2022. Discharging Sediment Downstream: Case Studies in Cost Effective, Environmentally Acceptable Reservoir Sediment Management in the United States. Journal of Water Resources Planning and Management **148** : 05021028. DOI: 10.1061/(ASCE)WR.1943-5452.0001494

Simon A. 1989. A model of channel response in disturbed alluvial channels. Earth Surface Processes and Landforms **14** : 11–26. DOI: 10.1002/esp.3290140103

Simon Andrew, Thomas Robert E., Curini Andrea, Shields F. Douglas. 2002. Case Study: Channel Stability of the Missouri River, Eastern Montana. Journal of Hydraulic Engineering **128** : 880–890. DOI: 10.1061/(ASCE)0733-9429(2002)128:10(880)

Sklar LS, Fadde J, Venditti JG, Nelson P, Wydzga MA, Cui Y, Dietrich WE. 2009. Translation and dispersion of sediment pulses in flume experiments simulating gravel augmentation below dams. Water resources research **45** DOI: https://doi.org/10.1029/2008WR007346

Surian N. 1999. Channel changes due to river regulation: the case of the Piave River, Italy. Earth Surface Processes and Landforms **24** : 1135–1151. DOI: 10.1002/(SICI)1096-9837(199911)24:12<1135::AID-ESP40>3.0.CO;2-F

Surian N, Cisotto A. 2007. Channel adjustments, bedload transport and sediment sources in a gravel-bed river, Brenta River, Italy. Earth Surface Processes and Landforms **32** : 1641–1656. DOI: 10.1002/esp.1591

Surian N, Mao L, Giacomin M, Ziliani L. 2009. Morphological effects of different channel-forming discharges in a gravel-bed river. Earth Surface Processes and Landforms **34** : 1093–1107. DOI: 10.1002/esp.1798

Sutherland DG, Ball MH, Hilton SJ, Lisle TE. 2002. Evolution of a landslide-induced sediment wave in the Navarro River, California. GSA Bulletin **114** : 1036–1048. DOI: 10.1130/0016-7606(2002)114<1036:EOALIS>2.0.CO;2

Swanson BJ, Meyer GA, Coonrod JE. 2011. Historical channel narrowing along the Rio Grande near Albuquerque, New Mexico in response to peak discharge reductions and engineering: magnitude and uncertainty of change from air photo measurements. Earth Surface Processes and Landforms **36** : 885–900. DOI: 10.1002/esp.2119

Takasu T, Yasuda A. 2009. Development of the low-cost RTK-GPS receiver with an open source program package RTKLIB

Thayer JB, Ashmore P. 2016. Floodplain morphology, sedimentology, and development processes of a partially alluvial channel. Geomorphology **269** : 160–174. DOI: 10.1016/j.geomorph.2016.06.040

Thompson C, Croke J. 2013. Geomorphic effects, flood power, and channel competence of a catastrophic flood in confined and unconfined reaches of the upper Lockyer valley, southeast Queensland, Australia. Geomorphology **197** : 156–169. DOI: 10.1016/j.geomorph.2013.05.006

Toffaleti FB. 1968. A procedure for computation of the total river sand discharge and detailed distribution, bed to surface . Technical Report. U.S. Army Corps of Engineers

Topping DJ, Grams PE, Griffiths RE, Dean DJ, Wright SA, Unema JA. 2021a. Self-limitation of sand storage in a bedrock-canyon river arising from the interaction of flow and grain size. Journal of Geophysical Research: Earth Surface **n/a** : e2020JF005565. DOI: https://doi.org/10.1029/2020JF005565

Topping DJ, Grams PE, Griffiths RE, Dean DJ, Wright SA, Unema JA. 2021b. Self-Limitation of Sand Storage in a Bedrock-Canyon River Arising From the Interaction of Flow and Grain Size. Journal of Geophysical Research: Earth Surface **126** DOI: 10.1029/2020JF005565

Topping DJ, Mueller ER, Schmidt JC, Griffiths RE, Dean DJ, Grams PE. 2018. Long-Term Evolution of Sand Transport Through a River Network: Relative Influences of a Dam Versus Natural Changes in Grain Size From Sand Waves. Journal of Geophysical Research: Earth Surface **123** : 1879–1909. DOI: 10.1029/2017JF004534

Topping DJ, Rubin DM, Grams PE, Griffiths RE, Sabol TA, Voichick N, Tusso RB, Vanaman KM, McDonald RR. 2010. Sediment transport during three controlled-flood experiments on the Colorado River downstream from Glen Canyon Dam, with implications for eddy-sandbar deposition in Grand Canyon National Park . US Geological Survey

Topping DJ, Rubin DM, Vierra LE. 2000. Colorado River sediment transport: 1. Natural sediment supply limitation and the influence of Glen Canyon Dam. Water Resources Research **36** : 515–542. DOI: 10.1029/1999WR900285

Topping DJ, Wright SA. 2016. Long-term continuous acoustical suspended-sediment measurements in rivers - Theory, application, bias, and error . USGS Numbered Series. U.S. Geological Survey: Reston, VA

Toro-Escobar CM, Paola C, Parker G. 1996. Transfer function for the deposition of poorly sorted gravel in response to streambed aggradation. Journal of Hydraulic Research **34** : 35–53. DOI: 10.1080/00221689609498763

Trimble SW. 1981. Changes in Sediment Storage in the Coon Creek Basin, Driftless Area, Wisconsin, 1853 to 1975. Science **214** : 181–183. DOI: 10.1126/science.214.4517.181

Trimble SW. 1983. A sediment budget for Coon Creek basin in the Driftless Area, Wisconsin, 1853-1977. American Journal of Science **283** : 454–474. DOI: 10.2475/ajs.283.5.454

Urban MA, Rhoads BL. 2003. Catastrophic human-induced change in stream-channel planform and geometry in an agricultural watershed, Illinois, USA. Annals of the Association of American Geographers **93** : 783–796. DOI: 10.1111/j.1467-8306.2003.09304001.x

USGS. 2012. United States Geological Survey National Elevation Dataset [online] Available from: https://www.usgs.gov/core-science-systems/national-geospatial-program/national-map

USGS. 2019. United States Geological Survey Earth Explorer [online] Available from: https://earthexplorer.usgs.gov/

Venditti JG, Dietrich WE, Nelson PA, Wydzga MA, Fadde J, Sklar L. 2010. Effect of sediment pulse grain size on sediment transport rates and bed mobility in gravel bed rivers. Journal of Geophysical Research: Earth Surface **115**

Viparelli E, Haydel R, Salvaro M, Wilcock PR, Parker G. 2010a. River morphodynamics with creation/consumption of grain size stratigraphy 1: laboratory experiments. Journal of Hydraulic Research **48** : 715–726. DOI: 10.1080/00221686.2010.515383

Viparelli E, Nittrouer JA, Parker G. 2015. Modeling flow and sediment transport dynamics in the lowermost Mississippi River, Louisiana, USA, with an upstream alluvial-bedrock transition and a downstream bedrock-alluvial transition: Implications for land building using engineered diversions. Journal of Geophysical Research: Earth Surface **120** : 534–563. DOI: 10.1002/2014JF003257

Viparelli E, Sequeiros OE, Cantelli A, Wilcock PR, Parker G. 2010b. River morphodynamics with creation/consumption of grain size stratigraphy 2: numerical model. Journal of Hydraulic Research **48** : 727–741. DOI: 10.1080/00221686.2010.526759

Walker AE, Moore JN, Grams PE, Dean DJ, Schmidt JC. 2020. Channel narrowing by inset floodplain formation of the lower Green River in the Canyonlands region, Utah. GSA Bulletin **132** : 2333–2352. DOI: 10.1130/B35233.1

Webb RH, Schmidt JC, Marzolf GR, Valdez RA. 1999. The controlled flood in Grand Canyon. Washington DC American Geophysical Union Geophysical Monograph Series **110**

Wellmeyer JL, Slattery MC, Phillips JD. 2005. Quantifying downstream impacts of impoundment on flow regime and channel planform, lower Trinity River, Texas. Geomorphology **69** : 1–13. DOI: 10.1016/j.geomorph.2004.09.034

Werbylo KL, Farnsworth JM, Baasch DM, Farrell PD. 2017. Investigating the accuracy of photointerpreted unvegetated channel widths in a braided river system: a Platte River case study. Geomorphology **278** : 163–170. DOI: 10.1016/j.geomorph.2016.11.003

Wheaton JM, Brasington J, Darby SE, Sear DA. 2010. Accounting for uncertainty in DEMs from repeat topographic surveys: improved sediment budgets. Earth Surface Processes and Landforms **35** : 136–156. DOI: 10.1002/esp.1886

White JQ, Pasternack GB, Moir HJ. 2010. Valley width variation influences riffle–pool location and persistence on a rapidly incising gravel-bed river. Geomorphology **121** : 206–221. DOI: 10.1016/j.geomorph.2010.04.012

Wilcock PR, DeTemple BT. 2005. Persistence of armor layers in gravel-bed streams. Geophysical Research Letters **32** DOI: 10.1029/2004GL021772 [online] Available from: https://onlinelibrary.wiley.com/doi/abs/10.1029/2004GL021772 (Accessed 20 June 2022)

Wilcox AC, O'Connor JE, Major JJ. 2014. Rapid reservoir erosion, hyperconcentrated flow, and downstream deposition triggered by breaching of 38 m tall Condit Dam, White Salmon River, Washington. Journal of Geophysical Research: Earth Surface **119** : 1376–1394. DOI: 10.1002/2013JF003073

Williams G, Wolman G. 1984. Downstream effects of dams on alluvial rivers . USGS Professional Paper

Winterbottom SJ, Gilvear DJ. 1997. Quantification of channel bed morphology in gravel-bed rivers using airborne multispectral imagery and aerial photography. Regulated Rivers: Research & Management **13** : 489–499. DOI: 10.1002/(SICI)1099-1646(199711/12)13:6<489::AID-RRR471>3.0.CO;2-X

Winterbottom SJ, Gilvear DJ. 2000. A GIS-based approach to mapping probabilities of river bank erosion: regulated River Tummel, Scotland. Regulated Rivers: Research & Management: An International Journal Devoted to River Research and Management **16** : 127–140. DOI: 10.1002/(SICI)1099-1646(200003/04)16:2<127::AID-RRR573>3.0.CO;2-Q

Wright S, Parker G. 2004. Flow Resistance and Suspended Load in Sand-Bed Rivers: Simplified Stratification Model. Journal of Hydraulic Engineering **130** : 796–805. DOI: 10.1061/(ASCE)0733-9429(2004)130:8(796)

Wright S, Parker G. 2005a. Modeling downstream fining in sand-bed rivers. I: formulation. Journal of Hydraulic Research **43** : 613–620. DOI: 10.1080/00221680509500381

Wright S, Parker G. 2005b. Modeling downstream fining in sand-bed rivers. II: application. Journal of Hydraulic Research **43** : 621–631. DOI: 10.1080/00221680509500382

Wu F-C, Shen HW, Chou Y-J. 1999. Variation of Roughness Coefficients for Unsubmerged and Submerged Vegetation. Journal of Hydraulic Engineering **125** : 934–942. DOI: 10.1061/(ASCE)0733-9429(1999)125:9(934)

Ziliani L, Surian N. 2012. Evolutionary trajectory of channel morphology and controlling factors in a large gravel-bed river. Geomorphology **173–174** : 104–117. DOI: 10.1016/j.geomorph.2012.06.001

CHAPTER 3

PARTITIONING A SEDIMENT BUDGET BY SAND SIZES[1]

Abstract

When the supply of water and/or sediment to a river change, sediment will accumulate or evacuate. A sediment budget can be used to determine conditions of sediment deficit or surplus and forecast the subsequent channel response to such perturbations in flow and/or sediment supply. Sediment budgets are typically calculated over broad grain size categories, such as total sand or gravel. It is known that different size fractions can transport and deposit in different parts of a channel and floodplain. Coarser sediment may be expected to be found primarily in channel bed material and finer sediment in the floodplain. If a sediment budget does not account for the different behavior and destination of these grain sizes, a sediment budget cannot reveal important changes in the river. In this study, we partition a sand sediment budget into multiple-size fractions to evaluate the channel response. The grain-size fractional sediment budget is calculated using measurements of sediment transport from acoustic sensors and geomorphic adjustments are measured from an aerial image time series and topographic data. We find that the total sand budget is in deficit, but the grain-size fractional budget shows very fine sand accumulates and fine and medium sand evacuates. The in-channel adjustment is mostly textural, driven by the winnowing of fine and medium sand from the channel bed. Very fine sand accumulates in the floodplains. The results of this study demonstrate that morphologic change can occur but be undetected if one only considers a sediment budget for total mass.

---

[1]Coauthored by Christina M. Leonard and John C. Schmidt

1. Introduction

The form, characteristics, and lateral stability of river channels and their

floodplains are largely determined by the stream-flow regime, the amount and size of

sediment supplied from the watershed and the transport capacity of the river channel.

Management of upstream water resource infrastructure, changes in land use, and natural

disturbance have the potential to alter the flow regime and/or the amount and grain size

of sediment supplied to the river. If the disturbance is large and of long duration, there is

the potential for wholescale channel change and equilibrium is achieved at a new graded

state (Mackin, 1948). This adjustment process may occur over years, decades, or

centuries. Smaller changes in water and sediment supply of shorter duration may be

within the natural capacity of the river to transport sediment. The channel can maintain

dynamic equilibrium through small adjustments without changing the geomorphic

attributes of the river (Fryirs and Brierley, 2012; Fryirs, 2017; Lisenby et al., 2020; Fryirs

and Brierley, 2022). Effective river management requires an ability to forecast the

channel response and determine whether the system can maintain dynamic equilibrium or

whether wholesale channel change will occur.

A sediment budget can be used to evaluate the channel response when the

streamflow and/or sediment supply change (Trimble, 1981, 1983). Using conservation of

mass, a sediment budget explicitly links the influx and efflux of sediment in a reach to

changes in sediment storage by:

$$\Delta S = I - O \qquad\qquad (3-1)$$

where ΔS is the change in sediment storage in the channel and floodplain and I and O are

sediment influx and efflux, respectively, during a period of time. Calculation of ΔS based

on the influx and efflux of sediment (i.e., right side of Equation 3-1) implies loss or

accumulation of sediment in the intervening channel and floodplain. We use the term *flux-based sediment budget* when calculating the sediment budget from the right side of (3-1). An alternative approach is to directly calculate ΔS from repeat measurements of channel morphology (i.e., the left side of Equation 3-1) and make inferences about changes in the sediment influx and efflux. We use the term *morphological sediment budget* when the sediment budget is calculated from the left side of (3-1).

When the flux-based and morphological sediment budgets are calculated independently, the insights of each approach are complementary. The flux-based budget gives insights as to *when* sediment accumulates or evacuates and the morphological budget gives insights as to *where* the change in sediment storage occurs. In this circumstance, we have the potential to assign specific attributes of the flow and sediment regimes to specific attributes of channel change or channel behavior (Popov, 1962; Griffiths, 1979; Neill, 1987; Ham and Church, 2000; Church, 2006). Considering both sides of the sediment budget can be useful, even essential, to forecasting or evaluating the channel response to a disturbance.

Sediment budgets are typically calculated for single-grain sizes, such as sand or gravel. It is known that different-size fractions can transport and deposit in different parts of the channel and floodplain (Nanson, 1980; Brakenridge, 1984; Nanson, 1986; Allred and Schmidt, 1999; Moody et al., 1999; Page et al., 2003; Grams and Schmidt, 2005; Dean and Schmidt, 2011; Thayer and Ashmore, 2016; Dean et al., 2020). If the sediment budget does not account for the different behavior of these grain sizes, the budget cannot reveal important changes in the river. Consider the case where the flux-based sediment budget for total sand is balanced but finer sizes of sand accumulate along the channel

margin and evacuate from the channel bed. The net result is channel narrowing and bed coarsening. In this example, the flux-based budget for total sand is a poor predictor of the channel response and a grain-size fractional sediment budget is needed to observe (or predict) the morphologic and bed textural adjustment.

In this study, we partition a flux-based and morphological sediment budget on a sand-bed river into multiple sand-size fractions. The flux-based budget is calculated from high-temporal resolution measurements of sediment transport from acoustic sediment gages. These gages allow for the precise calculation of the timing of when different sand sizes accumulate or evacuate. Repeat aerial images and sparse measurements of channel and floodplain topography and grain size are used to calculate the grain-size fractional morphologic sediment budget. We show that even though the flux-based budget for all sand sizes combined is in deficit, the fractional flux-based- and morphological- sediment budgets reveal channel bed coarsening and floodplain deposition of very fine sand. By partitioning the sediment budgets into multiple sand-size fractions, we can evaluate how a sand-bed river adjusts to maintain dynamic equilibrium in the presence of small changes in water and sediment fluxes.

2. Study Area

2.1. Location and existing data

The study area is located on a 23-km alluvial segment of the Yampa and Little Snake rivers in northwestern Colorado, USA (Figure 3-1). The Yampa River has two equally sized sub-basins: (1) the Little Snake River and (2) the upper Yampa River. Approximately 75% of the total flow in the reach originates in the headwaters of the upper Yampa River near Steamboat Springs, Colorado. After leaving the Park Range, the

upper Yampa River flows through a broad lowland until reaching the eastern Uinta Mountains at Cross Mountain. Immediately downstream from Cross Mountain, the Yampa River enters the study area at Deerlodge Park where the Little Snake River enters from the north. Deerlodge Park is a 7.5-km long alluvial valley formed in the Lily Park syncline (Dyni, 1968). The downstream end of Deerlodge Park is truncated by the eastern plunge of the Uinta anticline (Hansen, 1984) where the Yampa River enters the 74-km long, deeply incised Yampa Canyon that extends to the confluence with the upper Green River (Figure 3-1). The Little Snake River drains the Sierra Madre mountains to the north and flows through highly erodible badlands composed of fluvial and lacustrine deposits before entering the Yampa River in Deerlodge Park (Kemper et al., 2022a).

The suspended flux of silt/clay and sand entering and leaving the study area has been continuously monitored by a network of acoustic sediment gages operated by the USGS Grand Canyon Monitoring and Research Center (GCMRC) since 2013 (Figure 3-1; Topping et al., 2018). The sediment gages measure suspended sediment transport using single- or multi-frequency side-looking acoustic Doppler profilers and an automatic pump sampler. These gages were installed at existing streamflow gaging stations on the Yampa River (USGS gage 09251000 Yampa River near Maybell and USGS gage 09260050 Yampa River at Deerlodge Park) and on the Little Snake River (USGS gage 09260000 Little Snake River near Lily). The side-looking acoustic Doppler profilers were calibrated to suspended sediment concentrations from pump samples and cross-sectionally averaged equal-width-increment (EWI) samples. The grain size of physical samples is calculated using a wet sieve method followed by a dry sieve calibrated by laser diffraction (Topping et al., 2018). The concentration of silt/clay and sand is

measured at 15-minute intervals using the methods of Topping and Wright (2016) and multiplied by discharge to calculate the load.

The bed load flux was estimated by GCMRC using a rating relation for the ratio of bed load-to-suspended load flux as a function of discharge. The rating relation was calculated from paired measurements of bed load transport from bedform migration and Helley-Smith bedload samplers and suspended load transport from the cross-sectionally averaged EWI samples (Topping et al., 2018). Bed material samples were collected at equal intervals along the gaging cross-section at the time of paired bed load-suspended load measurements. Each bed material sample is sieved and the cross-sectionally averaged bed material grain size is calculated as the average grain size for all bed material samples along the cross-section.

Uncertainty in measurements of the sand and silt/clay loads from acoustical sensors results from small systematic biases in measurements of discharge, suspended sediment concentration from physical samples, and acoustic measurements (Topping and Wright, 2016). The systematic bias is small compared to random error in individual measurements, but these small biases are additive and accumulate with each transport measurement when calculating the cumulative load. In contrast, random errors cancel one another when the sample size is large and can be ignored (Topping and Wright, 2016).

2.2 Hydrology, sediment supply, and sediment waves

The Yampa and upper Green Rivers are co-equal headwater branches of the Green River. Between 2001 and 2020, the mean annual flow of the Yampa River, measured at Deerlodge Park was 54.2 m^3/sec and the mean annual flow of the upper

B.

Sand bed reach
Gravel bed reach
Acoustic sediment gage
Cross-section locations
LiDAR extent
RTK survey extent

0   2.5   5   10 Kilometers

Little Snake River

Lily

Cross Mountain

Maybell

upper Yampa River

Yampa Canyon

Deerlodge

XS 6

XS 3

XS 4

XS 5

Yampa River

A.

Flaming Gorge Dam

Wyoming

upper Green River

Sand Creek

Muddy Creek

Sand Wash

Little Snake River

Lodore

Lily

Maybell

middle Green River

Yampa River

Deerlodge

Jensen

Ouray

Utah   Colorado

Dinosaur National Monument

C.

Pre-1938 floodplain

Post-1938 floodplain

Active channel

Elevation (m)

1710

1709

1708

1707

Distance from left floodplain (m)

0   50   100   150   200   250   300

Figure 3-1. Maps showing the location of the study area. (A) Overview map with the study area shown in the red outlined box. (B) Study area showing the extent of gravel- and sand-bed segments on the Yampa and Little Snake Rivers. Deerlodge Park reach extends from the confluence of the Yampa and Little Snake Rivers to the Deerlodge gage. The location of cross-sections surveyed in Deerlodge Park are shown as black lines and the extent of the 2015 and 2011 LiDAR surveys and the 2020 RTK survey are shaded as green and red, respectively. (C) Cross-section 6 survey (XS6) showing the pre- and post-1938 floodplain.

Green River, measured near Greendale, was 48.8 m^3/sec. The flow regimes of the Yampa and Little Snake rivers are minimally regulated. There has been no significant long-term change in the mean annual discharge of either river but, in recent decades, there has been an increase in multi-year sequences of wet and dry runoff on the Yampa River (Manners et al., 2014; Topping et al., 2018).

The hydrology during the study period from 2013 to 2019 was typical of the long-term Deerlodge Park gaging record. The annual hydrograph was dominated by the spring snowmelt flood and very low late-summer base flow. Average-to-moderate annual floods with recurrence intervals of 3 to 3.5 years were nested between average-to-below-average floods with recurrence intervals of less than 2 years (Figure 3-2). The largest peak flood occurred in 2014 and had a discharge of 463 m^3/sec with a recurrence interval of ~4 years.
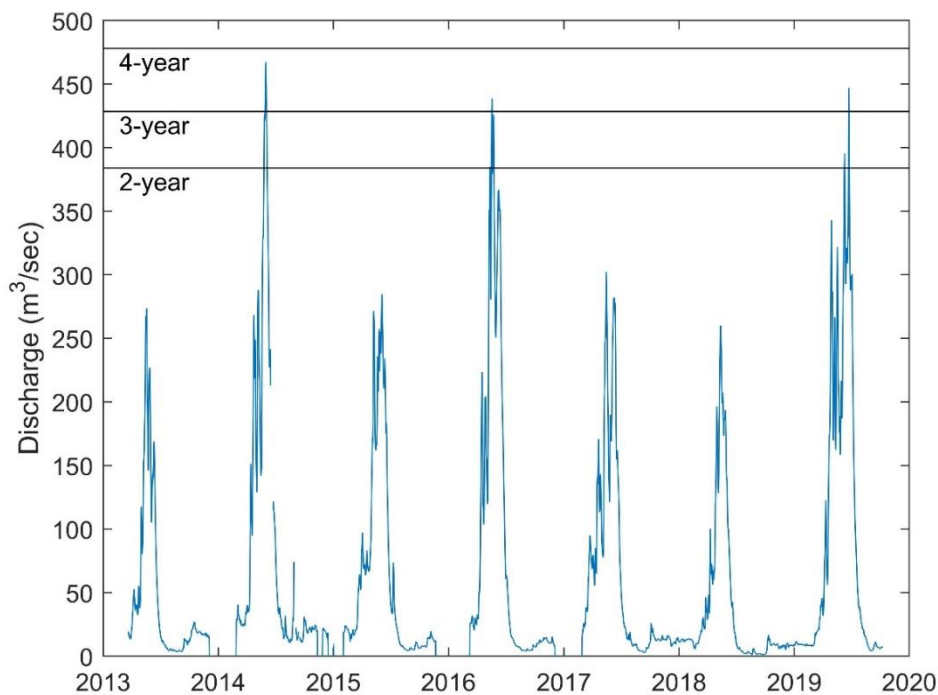
Figure 3-2. Deerlodge Park gage hydrograph during the study period. Solid black horizontal lines show the discharge for selected recurrence intervals.

The contribution of sediment and discharge supplied by the upper Yampa and Little Snake Rivers is very different. Although the upper Yampa River contributes most of the flow, only ~30% of the sediment that passes the Deerlodge gage originates in the upper Yampa River watershed (Andrews, 1978; Topping et al., 2018). The majority of this sediment originates from Sand and Muddy creeks and Sand Wash in the Little Snake River watershed (Figure 3-1). Wide-spread arroyo cutting in Sand Wash and Muddy Creek at the turn of the 20th century temporarily increased sediment delivery to the Yampa River by 30-60% (Kemper et al., 2022b). Between the mid-1950s to mid-1960s, there was another increase in sand supplied to the Little Snake River by tributary floods on Sand Creek. The sand from this disturbance moved downstream as an elongated sediment wave through the Yampa River to the Green River, evidenced by changes in the suspended load, bed load, and channel bed material grain size (Topping et al., 2018; Dean et al., 2020). The leading edge of this wave was finer than the antecedent bed material, and the bed quickly fined in response. As the leading edge of the sand-wave progressed downstream, the bed was slowly winnowed of the finest grain sizes, and the winnowing of the bed continues today (Topping et al., 2018).

2.3. Geomorphology and floodplain characteristics

Downstream from the Little Snake River, the Yampa River in Deerlodge Park has a sand bed. The average channel width, 213.5 m, is more than twice that of the Yampa River upstream from the Little Snake River. The planform is weakly sinuous at channel filling flows, and emergent sand bars are exposed at low flows, giving the channel a braided planform. Upstream from the Little Snake River to Maybell, Colorado, the upper Yampa River is a single-thread, meandering channel with gravel bed and bars, except for

the canyon-bound segment through Cross Mountain where boulder cascades and rapids dominate (Figure 3-1; Elliott and Anders, 2004).

The Little Snake River between the Lily gage and confluence with the Yampa River alternates between gravel- and sand-bed reaches. Sand-bed reaches are located in wide alluvial valleys and the channel planform is meandering with large lateral bars that are emergent during low flow. Gravel-bed reaches occur where bedrock outcrops and terraces partly constrict the river. Repeat aerial images indicate that a 1.5 km segment of the Little Snake River near the confluence with the Yampa River was realigned and straightened between 1961 and 1965, and the confluence was realigned between 1961 and 1975.

Floodplains on the Yampa and Little Snake rivers are similar to other composite bank floodplains found throughout the Green River Basin (Allred and Schmidt, 1999; Grams and Schmidt, 2002; Alexander, 2007; Manners et al., 2014; Walker et al., 2020). These floodplains are composites of a muddy cap facies overlain on a base facies. The base facies has a grain size similar to the active channel bars and the cap facies has a grain size similar to the suspended load. The base facies are composed of gravel on the Yampa River upstream from the Little Snake River confluence where the bed is gravel. Downstream from the Little Snake River confluence, the Yampa River alternates to sand bed and the base facies is composed of sand. The base facies on the Little Snake River alternates between gravel and sand depending on the reach bed material grain size (Figure 3-1).

There are two categories of floodplain on the Yampa River downstream from the Little Snake River confluence in Deerlodge Park. The floodplain that formed after 1938

appears undulating in a digital elevation model (DEM) derived from a 2015 LiDAR

survey and the topography is similar to the emergent bars of the adjacent active channel

(Figure 3-1c). These floodplains form on the inside of low curvature bends where

emergent bank-attached bars have been colonized by willow, cottonwood, and tamarisk

(Kemper et al., 2022b). The post-1938 floodplain is regularly inundated by floods that

exceed a 2.5-year recurrence interval (i.e., 448 m^3/sec). The stratigraphy of the post-1938

floodplain is similar throughout the study area. We only include a stratigraphic

description from the site shown in Figure 3-3a. An angular unconformity typically

truncates downstream migrating ripples of the base deposit and forms a very abrupt

contact between the cap and base facies. The lower portion of the base deposit has 30-cm

thick co-sets of ripple drift cross-lamination that indicate downstream migration of

ripples and dunes. The upper portion of the base deposit is composed of an alternating

sequence of well-sorted fine to medium sand with intervening layers of mud that are ~6

cm thick. The stratigraphy of the cap facies is generally comprised of 1-2 cm of thin

laminations and occasional 1-2 mm thick ripple-drift cross-laminated beds. Bulk samples

from the base deposit indicate that the grain size is similar to the active channel bed and

bars and bulk samples from the cap deposit show the grain size is similar to the

suspended load (Figure 3-3b). We found no evidence of erosional contacts suggesting

that the complete stratigraphic sequence is preserved and the floodplain height had not

been lowered by floodplain stripping.

The floodplain that formed before 1938 is located on the outside of weakly

meandering bends and is colonized by mature cottonwood (*Populus spp.*) stands that

were established between 1890 and 1929 (Kemper et al., 2022b). These floodplains
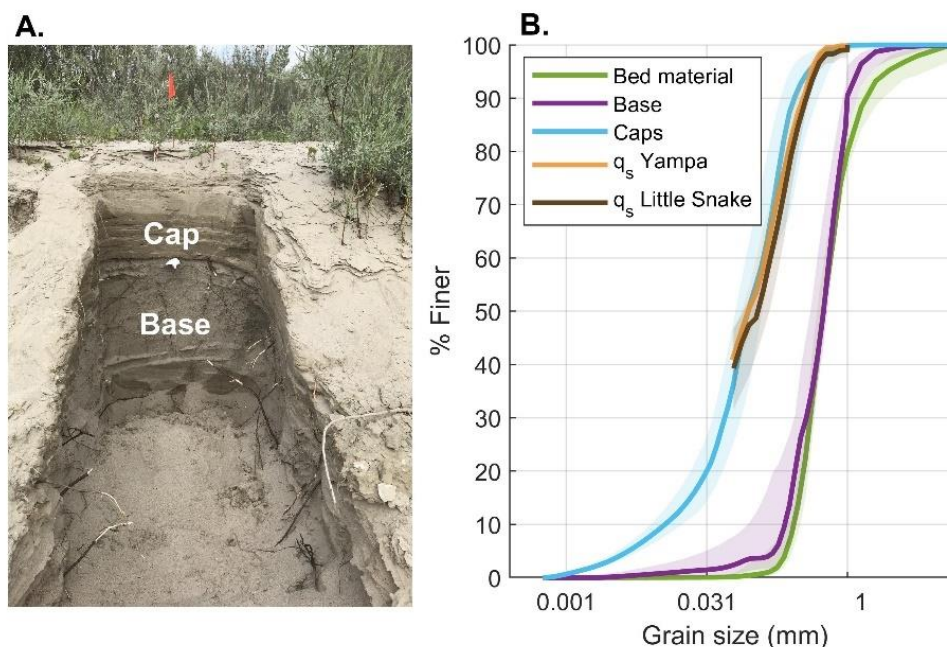
Figure 3-3. (A) Photograph of the characteristic stratigraphy of the post-1938 floodplain, showing a finer-grained cap overlain on a coarser-grain base facies separated by a sharp angular unconformity. (B) Average grain size distribution of physical samples collected from the cap facies, the base facies, and the channel bed. Shading represents the interquartile range for all samples. The average grain size distribution for the suspended load at the Deerlodge Park gage (qs Yampa) and the Lily gage (qs Little Snake) is also shown. The grain size distribution of the cap facies is similar to that of the grain size distribution of the suspended load and the grain size distribution of the base facies is similar to that of the bed material.

appear topographically smooth in the 2015 DEM and are partly overlain by active

alluvial fans deposited by ephemeral streams draining the adjacent badlands (Figure 3-

1c). Today, the pre-1938 floodplain is only inundated by floods that exceed 506 m^3/sec;

which is a flow of 4-year recurrence and has not occurred since 2011. The pre-1938

floodplain has an upper cap facies that is ~1.5 to 2 m thicker than the post-1938

floodplain, which gives this floodplain more relief (Figure 3-1c). With time, the post-

1938 floodplain may vertically aggrade to a similar relief and the undulating topography

may become muted. We found no topographic evidence of levee-trough topography on

the pre-1938 floodplain that is characteristic of other vertically accreting floodplains

(Allred and Schmidt, 1999; Moody et al., 1999; Pizzuto et al., 2008; Walker et al., 2020).

The levee-trough topography may have been eroded by lateral migration and the modern

topographic expression may only be that of the floodplain troughs. The levee topography

may have also been buried by vertical aggradation during a large flood.

3. Methods

3.1. Partitioning the flux-based sediment budget

We partitioned the suspended load and bed load among silt/clay (<0.0625 mm),

and very fine ($\leq$0.0625<0.125 mm), fine ($\leq$0.125<0.25 mm), medium ($\leq$0.25<0.5 mm),

coarse ($\leq$0.5<1.0 mm), and very coarse ($\leq$1.0<2.0 mm) sand classes. The partitioning

method involved calculating the average daily suspended load and bed load flux and

estimating the grain-size distribution of each load for a given day (see Text Appendix A-

1). We used the cross-sectionally averaged grain-size distributions from the EWI samples

to predict the suspended load grain size on each day. This was done by identifying the

cross-sectionally averaged EWI samples with a median grain size (D_{50}) that bracketed the

estimated D_{50} of the suspended load on that day and using a weighted linear interpolation

to produce a new grain-size distribution. The suspended load D_{50} was estimated from the

multi-frequency acoustical sensor at the Deerlodge Park gage. The Maybell and Lily

gages had a single-frequency acoustical sensor that could not be used to estimate the D_{50}.

We linearly interpolated between the closest physical samples to estimate the D_{50} at these

gages. We found the linear interpolation method produced a similar grain size partition as

the multi-frequency acoustical sensor at the Deerlodge gage. A similar method was used

to partition the bed load flux, except the D_{50} was estimated using a metric of relative bed

coarseness from the suspended load (see Text Appendix A-1) and the grain-size

distribution of cross-sectionally averaged bed material samples was used to interpolate

the bed load grain-size distribution.

The general equation used to compute the partitioned flux-based sediment budget

in units of mass is:

$$\Delta S_{k(flux)} = (I_{Maybell(k)} + I_{Lily(k)}) - E_{Deerlodge(k)}; \qquad (3-2)$$

where $\Delta S_{k(flux)}$ is the net change in sediment storage for the kth sediment size, $I_{Maybell(k)}$ and

$I_{Lily(k)}$ is the influx of the kth sediment size measured as the cumulative sediment load at

the Maybell and Lily gages, respectively, and $E_{Deerlodge(k)}$ is the efflux of the kth sediment

size measured as the cumulative sediment load at the Deerlodge Park gage. The net

change in storage was calculated separately for the suspended load and the bed load using

the partitioned fluxes for silt/clay, total sand, very fine sand, fine sand, medium sand,

coarse sand, and very coarse sand described above. The total change in sediment storage

was the sum of the change in sediment storage for the suspended load and the bed load.

Uncertainty in the partitioned bed load and suspended load fluxes were calculated

as a fixed percent of the flux. We used the same fixed percentage of the daily load at each

gage as Topping et al. (2018), using 10% of the suspended load and 50% of the bedload.

The 10% uncertainty assigned to the suspended load was based on the understanding that

uncertainty in discharge measurements is typically between ±3 and ±5% for excellent

records (Rantz, 1982; Grams et al., 2019) and the spatial variability in sediment

concentrations can cause up to a 5% bias in acoustical flux-based sediment budgets on

the Colorado River in Grand Canyon (Topping et al., 2010). The level of uncertainty for

the bed load was an arbitrary value.

The lower bound of uncertainty in the flux-based sediment budget ($\Delta S_{k(flux)}$) was taken to be the maximum uncertainty of the load leaving the reach ($E_{Deerlodge(k)}$) subtracted from the minimum uncertainty of the load entering the reach ($I_{Maybell(k)}$ and $I_{Lily(k)}$) and *vice versa* for the upper bound. The flux-based budget was deemed indeterminant when uncertainty was >1.5 times the absolute value of $\Delta S_{k(flux)}$; likely in deficit (or surplus) when uncertainty was between 1 and 1.5 times larger than the absolute value of $\Delta S_{k(flux)}$; and in deficit (or surplus) when uncertainty was less than the magnitude of $\Delta S_{k(flux)}$ (Topping et al., 2021).

3.1.1. Validating the suspended load partitioned flux-based budget

We compared the percent of each sand size in 45 cross-sectionally averaged EWI measurements made between 2013 to 2019 at the Deerlodge Park gage to the predicted percentage calculated by our partitioning method (Figure 3-4). Our partitioning method performed best for fine and coarse sand (RMSE: 10% and 3% for fine and coarse sand, respectively) and worst for very fine and medium sand (RMSE: 27% and 19% for very fine and medium sand, respectively). There was a tendency to underpredict the amount of very fine sand and overpredict the amount of medium sand in EWI samples collected at a low discharge with a small suspended sediment concentration. The large RMSE for very fine and medium sand was caused by these few EWI samples (Figure 3-4). If these EWI samples were excluded, we find no systematic bias between the estimated and observed fraction of each sand size in the load. Very coarse sand was not included in the validation, because this sand size is not carried in suspension and, therefore, was not measured in the EWI samples.
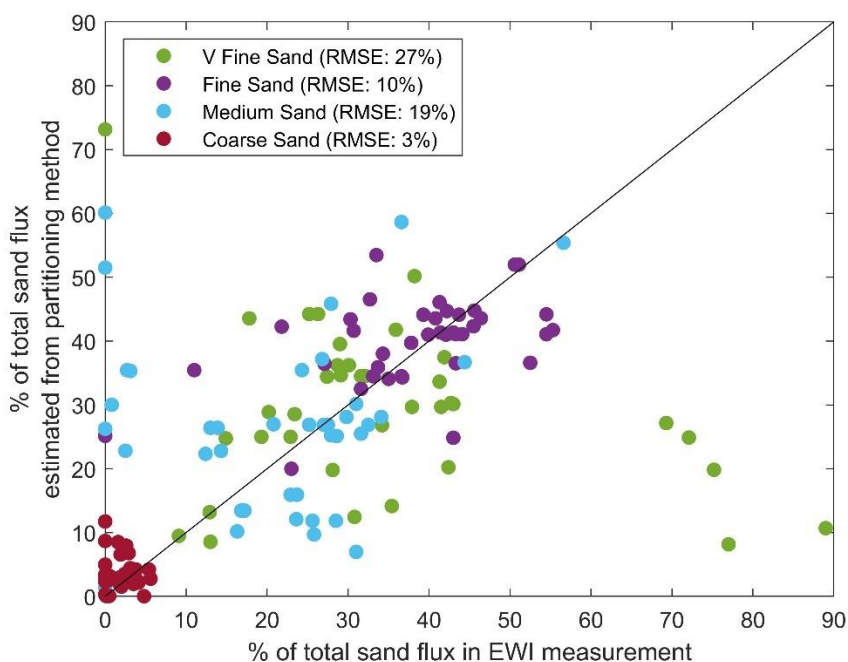
Figure 3-4. Percent of each sand-size in the partitioned acoustical flux compared to the percent of each sand-size in the cross-sectionally averaged EWI sample at the Deerlodge Park gage. Each dot is a single measurement. The 1:1 line is shown in black. Values below the black line indicate that the partitioning method underestimated the percent of the grain size in the total flux and values above the black line indicate that the percent of the grain size in the total flux was overestimated.

3.2. Calculating the morphological sediment budget

We measured channel planform change using aerial images collected in 2013, 2015, 2017, and 2019 by the National Agriculture Imagery Program (NAIP). The planimetric channel change analysis involved overlaying the active channel boundaries delineated from two aerial images to identify polygons of erosion and deposition that resulted from bank erosion or floodplain formation. We characterized uncertainty associated with measurements of planimetric change using the spatially distributed probabilistic (SDP) method (Leonard et al., 2020). The SDP method characterizes one source of error – image co-registration – and two sources of uncertainty – digitization and

interpretation – in measurements of planimetric change determined from repeat aerial images (see Text Appendix A-2). The output of this analysis is a distribution of areal change by the accretion and erosion of floodplains and vegetated islands. The accreted floodplains identified by this analysis are the youngest surfaces of the post-1938 floodplain.

Measurements of channel change based on planimetric data have been used in many studies to infer the sign of the sediment mass balance. Such interpretations are uncertain because they fail to account for bed elevation changes, changes in channel and floodplain topography, or floodplain shaving. A more robust analysis of channel change involves differencing repeat high-resolution topographic surveys (e.g., Lane et al., 2003; Wheaton et al., 2010; Croke et al., 2013) or converting planimetric change to volumes using the height of eroded or aggraded floodplains (Gaeuman et al., 2003). In this study, repeat near-infrared (NIR) LiDAR surveys collected in 2011 and 2015 only covered part of the study area, so we could not directly measure the change in sediment storage from repeat topography. We developed a method to convert planimetric adjustment throughout the sand-bed portion of the study area to volumetric change using a Bayesian model to estimate the height of eroded and deposited floodplains (Figure 3-5).

The input data for our Bayesian model were elevations from the pre- and post-1938 floodplain and the channel bed that were detrended to remove the channel slope (Figure 3-5; see Text Appendix A-3). Detrended elevations were calculated from the 2015 LiDAR survey in Deerlodge Park and the 2020 Real-time kinematic (RTK) survey in the Little Snake River (Figure 3-1). The Bayesian model was used to predict 5000 detrended elevations of the floodplain and channel bed (see Text Appendix A-4; Figure

3-5 a, b). The predicted detrended elevations represent variability in floodplain topography that had eroded or deposited during our study period and channel bed topography throughout the reach. The height of eroded and aggraded floodplains was calculated by subtracting the Bayesian-predicted detrended floodplain elevations from the Bayesian-predicted detrended bed elevations (see Text Appendix A-4; Figure 3-5c). We found that the height of the Yampa River floodplain was greater than the Little Snake River floodplain (Wilcoxon rank sum test; $\alpha = 0.05$; see Table Appendix A-2), and we created a separate Bayesian model for each river to account for this height difference.

We validated our Bayesian height model by comparing the height of eroded and deposited floodplains measured from repeat cross-sections in Deerlodge Park to our modeled distribution (Figure 3-5 d, e). Cross-sections were placed 1.2 to 2.8 km apart and surveyed in 1983, 1997, 2011, and 2017 (Griffiths et al., *In Review*). The measured height of eroded and deposited floodplains from repeat cross-sections was in the center of our Bayesian-predicted heights (Figure 3-5d, e). The Bayesian-predicted heights had a larger range of floodplain heights than was measured among a few cross-sections, because the height distribution included uncertainty and the natural variability in the floodplain throughout the study area.

Finally, the total volume of eroded and deposited sediment was calculated by multiplying the distribution of the planimetric change for the entire study period (2013 to 2019) and temporal subsets from 2013 to 2015, 2015 to 2017, and 2017 to 2019 by the Bayesian-predicted floodplain height. The net volumetric change ($\Delta S_{(morph)}$) was calculated by subtracting the distribution of the volume of erosion from the distribution of the volume of deposition, with positive values indicating net deposition and negative
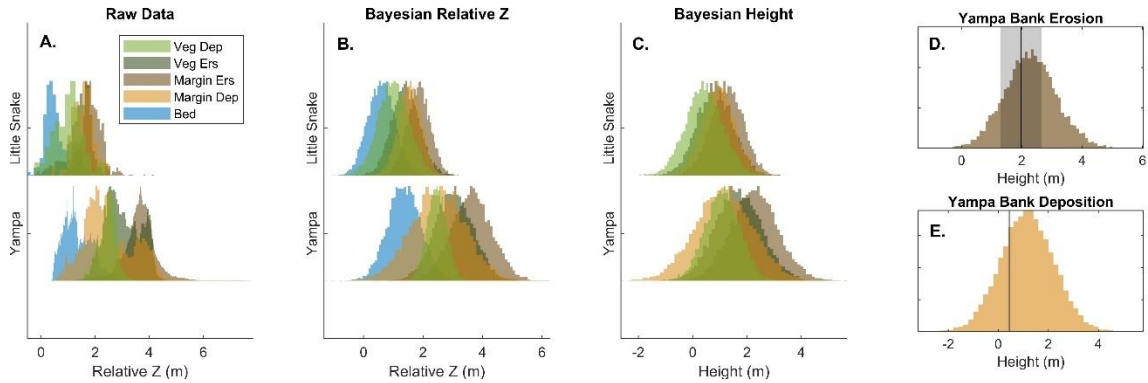
Figure 3-5. Histograms generated from the Bayesian height model for floodplains on the Yampa River in Deerlodge Park and the Little Snake River. (A) Detrended elevations extracted from recently eroded pre- and post-1938 floodplains, recently accreted post-1938 floodplains, and active channel bed. Floodplains were segregated by channel margins and the vegetated islands. Veg Dep = deposited surfaces along vegetated islands; Veg Ers = eroded surfaces along vegetated islands; Margin Ers = eroded surfaces along the channel margins; Margin Dep = deposited surfaces along the channel margins; Bed = active channel bed. (B) Posterior distribution of detrended elevations in (A) generated by the Bayesian model. (C) The height of each floodplain category (i.e., Veg Dep, Veg Ers, Margin Ers, Margin Dep) was calculated by subtracting the active channel bed distribution in (B) from the eroded and deposited distributions in (B). (D) Bayesian model for the height of eroded floodplains along the channel margin in Deerlodge Park overlain with field measurements of erosional heights from repeat cross-sections. The mean and standard deviation of the measured erosional heights from repeat cross-sections are shown as the black line and gray-shaded region, respectively. (E) Bayesian model for the height of deposited floodplains along the channel margin in Deerlodge Park overlain with field measurements of depositional heights from repeat cross-sections. The mean and standard deviation of the measured depositional heights from repeat cross-sections are shown as the black line and gray-shaded region, respectively.

values indicating net erosion. The distribution of $\Delta S_{(morph)}$ defines the aggregated

uncertainty in the planimetric channel change analysis and height of eroded and deposited

floodplains. We calculated a 95% and 68% credible interval (CI) from the distribution of

$\Delta S_{(morph)}$ as summary metrics of uncertainty. The 95% and 68% CI intervals are summary

metrics of uncertainty that contain 95% and 68% of the most probable values of $\Delta S_{(morph)}$,

respectively. We considered $\Delta S_{(morph)}$ to be depositional (or erosional) when the 95% CI is

positive (or negative), likely depositional (or erosional) when the 68% CI is positive (or

negative), and indeterminate when the 68% CI contains positive and negative values. We segregated $\Delta S_{(morph)}$ into changes that occurred along the channel margins and vegetated islands. The volumetric $\Delta S_{(morph)}$ was converted to mass by assuming a porosity of 0.4 and a density of 2.65 g/cm^3 (Curry et al., 2004; Wright and Parker, 2005; Grams et al., 2013; Viparelli et al., 2015). We did not directly measure density or porosity, which is an additional source of uncertainty not included in our budgeting approach. We excluded the gravel-bed portion of the Yampa River upstream from the confluence with the Little Snake River from $\Delta S_{(morph)}$, because only the cap of the floodplain contained fine sediment and we did not find a significant planimetric adjustment or change in channel width in this reach (see Appendix Figure A-1).

3.2.1. Validating the morphological sediment budget

We found that the measured change in floodplain storage from repeat cross-sections was within the 95% CI of the estimated volumetric change from our morphological sediment budget (Table 3-1). We used repeat aerial images acquired during the same years as the cross-section surveys to calculate the morphological sediment budget within a rectangle that spanned each cross-section. An exception was that an aerial image was not available for the 1997 survey, so we used a 1993 image, which was the closest-in-time image with a sufficient resolution for delineating the channel boundary. This was an acceptable substitution because the bank location on the 1993 image aligned well with the bank in the 1997 survey, indicating that significant channel narrowing or widening did not occur from 1993 to 1997. The morphological sediment budget spanning each cross-section was normalized by downstream distance and compared against the sum of the measured floodplain elevation change between

cross-section surveys. Cross-sections 3 and 4 were relocated in the 1997 survey and excluded from the validation (Griffiths et al., *In Review*). The only cross-section included for the 2011 to 2017 period was cross-section 6, because this was the only cross-section surveyed in 2011.

Table 3-1. Comparison of volumetric change in floodplain storage calculated from repeat cross-sections and estimated by the morphological sediment budget. Results from the morphological sediment budget are shown as the mean and the 95% credible interval (CI) which represents the 95% most probable estimates from our morphological sediment budget analysis. Positive values indicate deposition and negative values erosion.

	1983-1997		1997-2017		2011-2017	
	XS ΔS[I]	Morph ΔS (95% CI)	XS ΔS[I]	Morph ΔS[I] (95% CI)	XS ΔS[I]	Morph ΔS[I] (95% CI)
XS 3	------------	------------	-100.5	-100.0 (-172.8 to -25.3)	------------	------------
XS 4	------------	------------	-224.0	-143.7 (-279.3 to -7.5)	------------	------------
XS 5	-53.9	-72.2 (-136.8 to -12.4)	14.7	41.3 (-34.2 to 126.1)	------------	------------
XS 6	-43.5	-107.8 (-229.6 to -15.0)	-12.1	50.9 (-67.1 to 194.5)	8.4	31.4 (-3.6 to 71.5)

[I]All measurements in units of m^2

There was a high probability (i.e., 97%) that our morphological sediment budget was within the uncertainty bounds of volumetric change in floodplain storage measured from repeat LiDAR surveys in Deerlodge Park. We calculated changes in floodplain topography from DEMs that fused subaerial topography from the NIR LiDAR surveys with bathymetry calculated by optically-derived predictions of depth using the flow resistance equation-based imaging of river depths (FREEBIRD) algorithm (Legleiter, 2015; see Text Appendix A-5 and A-6; Figure 3-6). We found that the spatial distribution of floodplain changes measured by topographic differencing was concentrated along the channel margins and vegetated islands and coincided with the location of floodplain erosion and deposition measured by our morphological sediment budget (Figure 3-6).
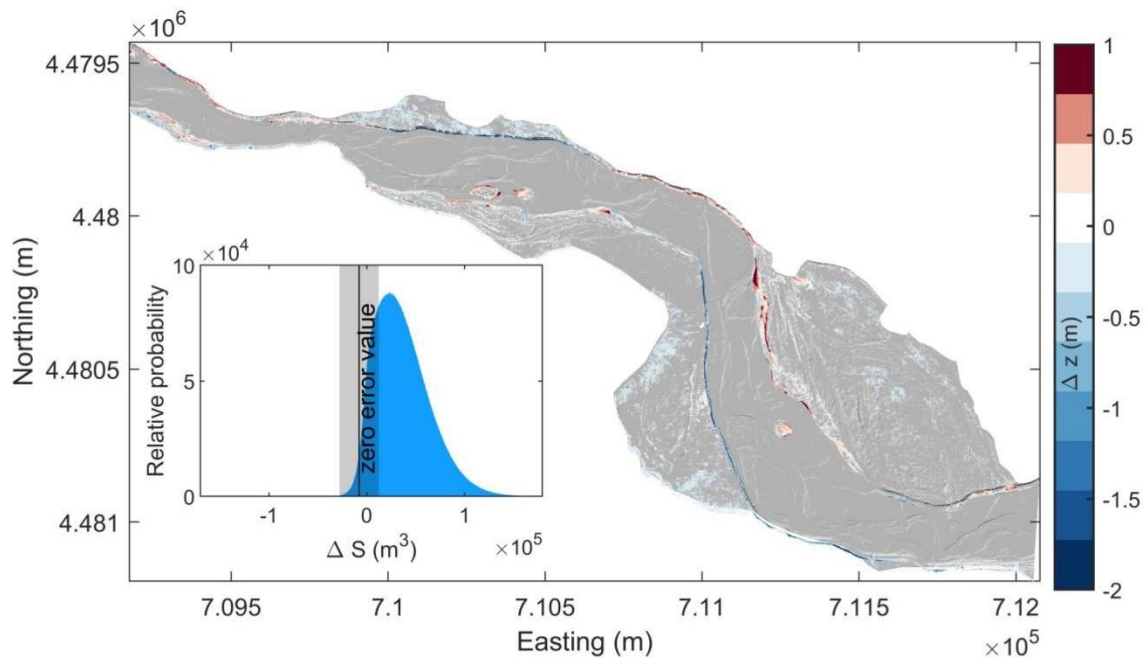
Figure 3-6. Map of changes in floodplain topography from topographic differencing of the 2011 and 2015 fused DEMs. Positive values indicate floodplain aggradation and negative values floodplain erosion. Only cells above a level of detection set at a 95% confidence interval are displayed for visualization purposes. Inset figure shows the distribution of changes in floodplain sediment storage from our morphological sediment budget overlain on the change in floodplain sediment storage calculated from topographic differencing. The black vertical line is the zero-bias ΔS calculated from topographic differencing and the gray band is the uncertainty.

3.2.2. Partitioning the morphological sediment budget by grain-size classes

In this section, we describe our method to segregate the morphological budget for total sand by the same grain sizes used in the partitioned flux-based budget in Section 3.1. The general framework involved (1) estimating the grain-size composition of each floodplain and vegetated island and (2) segregating the volume of erosion or deposition by the proportion of each grain size in the floodplain.

We characterized the grain size of the floodplains and vegetated islands by collecting 32 samples from the banks of the pre- and post-1938 floodplain in June 2019.

Of the 32 samples, 13 were collected from banks that were recently eroded and the remaining were collected from banks that were stable or had recently accreted. Of the recently eroded sites, 3 samples were collected from the pre-1938 floodplain and the other samples were collected from the post-1938 floodplain. We collected a bulk sediment sample from the cap and base facies at each bank site and analyzed the grain size distribution by sieving for grain sizes ≥1 mm and used a laser diffraction particle size analyzer for grain sizes <1mm (Figure 3-7a). These data were used in a Bayesian model to predict the grain size characteristics of each facies throughout the study reach using a similar approach as the floodplain height in Section 3.2 (Figure 3-7 b, c).

We segregated the total floodplain height into the height associated with the cap and base facies so we could partition the volumetric change in each facies by grain size. For each of the 32 bank samples, we measured the thickness and used that data in the same Bayesian reasoning as the height and grain size models predict cap thicknesses throughout the study reach. The base thickness was taken to be the predicted cap thickness subtracted from the predicted floodplain heights developed in Section 3.2.

The morphological sediment budget in Section 3.2 was partitioned into silt/clay and sand by estimating the volumetric change in the cap and base facies and multiplying those volumes by the fraction of silt/clay and sand in each facies. Volumetric change in the cap and base facies was taken to be the distribution of planimetric change from the aerial image time series multiplied by the Bayesian-predicted cap and base thickness. The volumes of each facies were then multiplied by the Bayesian-predicted fraction of silt/clay and sand to calculate the volumetric change of each grain-sizefraction. We
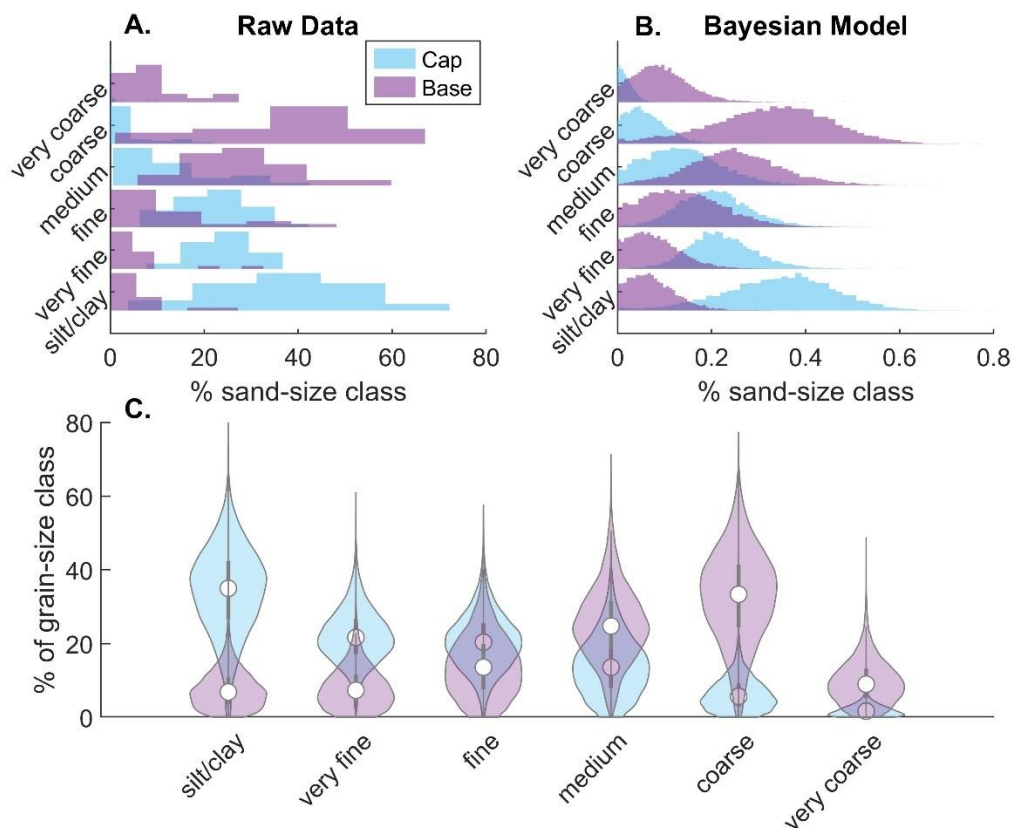
Figure 3-7. (A) Histograms for the percent of each grain size measured in the cap and the base facies. (B) The posterior distribution for the percent of each grain size in the cap and the base facies predicted by the Bayesian model. (C) Violin plots of (B) show the distribution of the percent of each grain size in the cap and the base facies.

further segregated the sand portion of the morphological sediment budget into very fine, fine, medium, coarse, and very coarse sand by multiplying the sand volume by the Bayesian-predicted fraction of each sand size in the cap and base facies. The base facies in the gravel-bed portion of the Little Snake River was not included in this analysis.

The output of the partitioned morphological sediment budget described above is 5000 estimates of volumetric change for the kth grain size ($\Delta S_{k(morph)}$). The distribution of these 5000 estimates characterizes the uncertainty in $\Delta S_{k(morph)}$) from planimetric channel change in the aerial image analysis, the height of eroded and deposited floodplains, the

thickness of cap and base facies, and the grain size of the cap and base facies deposits.

Positive $\Delta S_{k(morph)}$ indicate net deposition and negative $\Delta S_{k(morph)}$ net erosion. We

segregated $\Delta S_{k(morph)}$ by volumetric change along the channel margins and vegetated

islands. We calculated the 95% and 68% CI of the distribution of $\Delta S_{k(morph)}$ as summary

metrics of uncertainty. We considered $\Delta S_{k(morph)}$ depositional (or erosional) when the 95%

CI was positive (or negative), likely depositional (or erosional) when the 68% CI was

positive (or negative), and indeterminate when the 68% CI contained positive and

negative values.

3.3. Comparing the partitioned flux-based and morphological sediment budgets

We assessed the similarity between the flux-based and morphological sediment

budgets by calculating the probability that $\Delta S_{k(morph)}$ was within the uncertainty bounds of

$\Delta S_{k(flux)}$. We considered the sediment budget closed when there was a greater than 50%

probability that $\Delta S_{k(morph)}$ was within the uncertainty bounds of $\Delta S_{k(flux)}$. This probability

was calculated as the percent of the 5000 estimates of $\Delta S_{k(morph)}$ in Section 3.2.2 that were

within the uncertainty bound of the flux-based net change in sediment storage in Section

3.1.

3.4. Predicting floodplain inundation depth and frequency

The detrended elevations described in Text Appendix A-3 were used to calculate

the depth of inundation on the post-1938 floodplain for a range of flows in the

downstream section of Deerlodge Park where LiDAR data were available. This

information was used to determine what flows inundated floodplain surfaces and the

timing and potential for floodplain sediment storage. We did this by normalizing the

detrended elevations from the post-1938 floodplain to the Deerlodge Park gage stage

datum and using the stage-discharge rating relation to calculate the difference between the normalized floodplain height and the stage height. We estimated the frequency that the post-1938 floodplain was inundated by calculating the percent of time the floodplain was submerged. The height of the post-1938 floodplain was variable, so we calculated the frequency that 5%, 25%, and 50% of the floodplain was inundated.

4. Results

4.1 Partitioned flux-based sediment budget

The silt/clay budget uncertainty exceeded 1.5 times the absolute value of $\Delta S_{k(flux)}$ at the end of the study period, and the budget was indeterminant (Figure 3-8a). Silt/clay eroded during the 2014 flood, as shown by a large downward step in the zero-bias $\Delta S_{k(flux)}$ line (Figure 3-8a). However, a large upward step during the next year's flood brought $\Delta S_{k(flux)}$ closer to zero, and the silt/clay budget was indeterminant for the remainder of the study period.

The influx of sand into the study area was less than what was exported past the Deerlodge Park gage and sand was eroded (Figure 3-8a). The magnitude of the deficit can be expressed as 0.01 m to 0.2 m of bed degradation. The downward steps in the flux-based sand storage indicate sand was predominately evacuated during the flood peak and recession. Larger floods tended to evacuate more sand.

The partitioned flux-based budget for fine and medium sand was erosional, and these fractions account for 78% of the total sand eroded from the study reach (Figure 3-8b). The magnitude of fine and medium sand erosion was large enough that uncertainty did not exceed the absolute value of $\Delta S_{k(flux)}$, but the depth of bed degradation could be as small as 0.03 m or as large as 0.14 m if spread evenly over the sand bed portion of the

study area. Uncertainty in the flux-based budget for coarse and very coarse sand

exceeded 1.5 times the absolute value of $\Delta S_{k(flux)}$ and the budget was indeterminant

(Figure 3-8b). The flux-based budget for very fine sand was strikingly different from

other sand sizes. In the 2014 and 2017 floods, the flux-base storage decreased, whereas,

in the 2016 flood, the storage clearly increased, and in the 2019 flood storage likely

increased (Figure 3-8b). At the end of the study period, uncertainty exceeded 1.5 times

$\Delta S_{k(flux)}$ and the very fine sand budget was indeterminant.
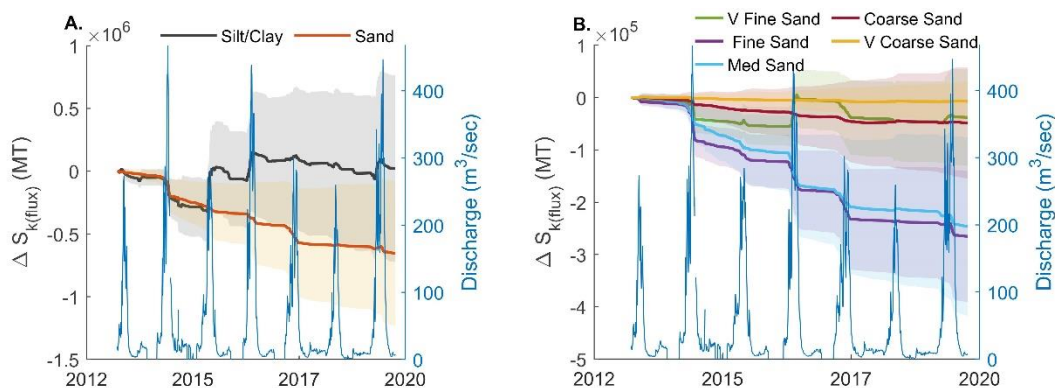
Figure 3-8. Results of the partitioned flux-based sediment budget. (A) Cumulative $\Delta S_{k(flux)}$
for sand and silt/clay storage. The hydrograph measured at the Deerlodge Park gage is
shown in blue. Solid lines are the cumulative zero-bias error value of $\Delta S_{k(flux)}$ for silt/clay
and sand. Shaded regions represent the cumulative uncertainty in $\Delta S_{k(flux)}$ for silt/clay and
sand. (B) Cumulative $\Delta S_{k(flux)}$ for each sand-size. The hydrograph measured at the
Deerlodge Park gage is shown in blue. Solid lines are the cumulative zero-bias error
value of $\Delta S_{k(flux)}$ for each sand size. Shaded regions represent the cumulative uncertainty
in $\Delta S_{k(flux)}$.

We found that very fine sand accumulated during a discrete range of flows

between 275 and 446 m^3/sec (Figure 3-9). Flows of this magnitude were exceeded

between 5% and 0.3% of the study period and inundated between ~5% and ~50% of the

post-1938 floodplains. The annual floods in 2014, 2016, and 2019 were the only time

when this range of flows occurred. However, very fine sand did not accumulate during

the 2014 flood when the peak discharge exceeded 446 m^3/sec and very fine sand was

evacuated instead. The influx and efflux of very fine sand were generally balanced during

flows less than 275 m^3/sec (Figure 3-9).

We compared the flux-based budget to the morphological budget by recalculating

the flux-based budget to the same temporal resolution as the morphological budget: 2013

to 2015; 2015 to 2017; and 2017 to 2019 (Table 3-2). The flux-based budget indicated

that sand was evacuated during each temporal subset, except from 2017 to 2019, when

the budget was indeterminant. Uncertainty in transport measurements during this period

would only need to be reduced by 20% for the total sand budget to be likely erosional.

Fine and medium sand were evacuated during each temporal subset, except between 2017

and 2019 when medium sand evacuation was only probable. Coarse sand was likely

eroded between 2013 and 2015 and erosion would have continued from 2015 to 2017 if

the transport uncertainty were reduced by a mere 10%. The silt/clay and very coarse sand

budgets were indeterminant during each period. Very fine sand was deposited during the

2016 and 2019 floods, but the budgets were indeterminant by the end of each temporal

subset.

4.2 Morphological sediment budget

4.2.1. Characteristics of the floodplain

The recently eroded floodplains were generally taller than the recently accreted

floodplains on both rivers (Figure 3-5; see Appendix Table A-1), because the eroded

floodplains included the pre-1938 floodplain that had aggraded to a higher elevation than

the post-1938 floodplain. Our Bayesian model indicated that the finer grain cap facies
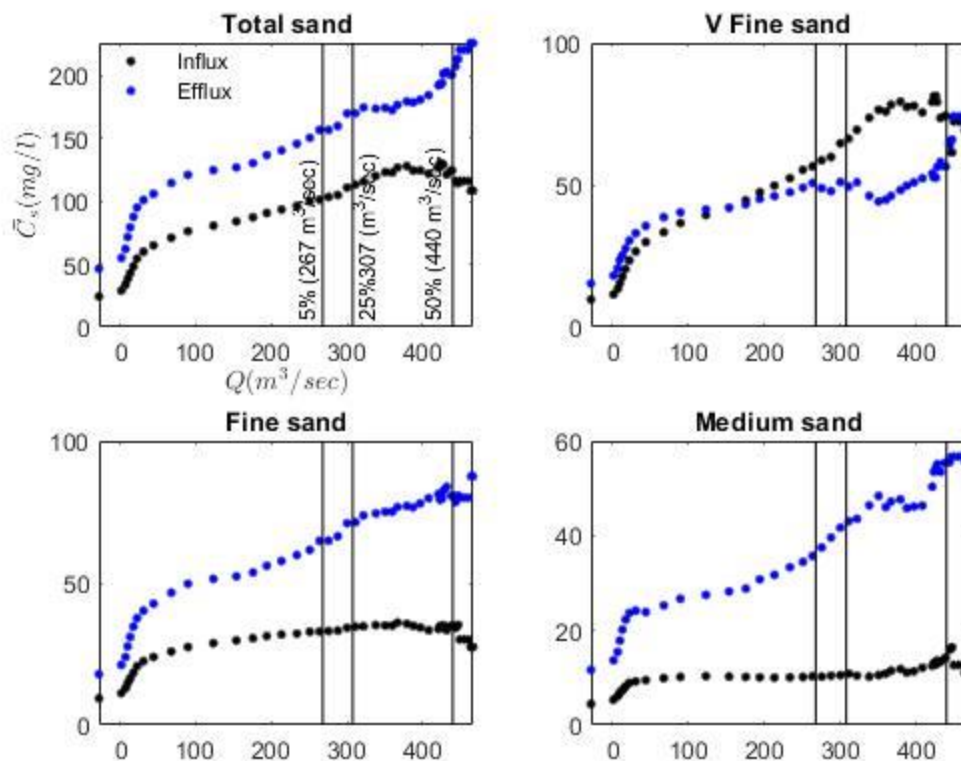
Figure 3-9. (A) Concentration of total sand averaged over daily flows above a certain threshold. The influx concentration (black dots) is the sum of the acoustically measured concentration at the Maybell and Lily gages. The efflux concentration (blue dots) is the acoustically measured concentration at the Deerlodge Park gage. Vertical black lines show the percent of time different fractions of the post-1938 floodplain was inundated. 5% of the post-1938 floodplain was inundated at 267 (m³/sec); 25% of the floodplain was inundated at 307 (m³/sec); and 50% of the floodplain was inundated at 440 (m³/sec). (B-D) Same as (A) except for very fine, fine, and medium sand, respectively.

Table 3-2. Partitioned net change in sediment storage for the flux-based sediment budget and the morphological sediment budget during each temporal subset. The uncertainty range for the flux-based budget is the cumulative uncertainty at a 10% and 50% fixed percent in the suspended and bed loads, respectively. The uncertainty range for the morphological budget is the 95% CI. Bolded text indicates periods of time when there was a greater than 50% probability that the morphological- and flux-based-budgets overlap within the bounds of uncertainty.

	2013 to 2019		2013 to 2015		2015 to 2017		2017 to 2019	
	flux-based[a]	morph-based[a,b]	flux-based[a]	morph-based[a,b]	flux-based[a]	morph-based[a,b]	flux-based[a]	morph-based[a,b]
silt/clay	-12.0 to 13	**-0.4 to 1.2 [1]**	-12 to 20	**-1.18 to 3.6 [1]**	-8.4 to 11	**-3.3 to 1.8 [1]**	-10.9 to 6.8	**-1.8 to 2.7 [1]**
total sand	-1.3 to -20	-3.2 to 4.3 [0.32]	-5.7 to 2.5	-7.2 to 14 [0.04]	-23 to -2.2	**-15 to 7.0 [0.61]**	-1.1 to 3.0	**-9.5 to 10 [0.75]**
very fine sand	-2.2 to 0.91	**-3.2 to 7.8 [0.62]**	-4 to -0.87	-0.86 to 2.4 [0.10]	-1.0 to 2.5	**-2.3 to 1.3 [0.53]**	-1.0 to 1.1	**-1.4 to 1.8 [0.62]**
fine sand	-6.5 to -2.3	-0.6 to 1.0 [0.02]	-7.7 to -3.5	-1.5 to 3.2 [0]	-8.1 to -3.3	-3.2 to 1.6 0.03]	-3.0 to -0.17	-2.1 to 2.2 [0.35]
medium sand	-7.0 to -1.3	-0.98 to 1.3 [0.14]	-7.9 to -2.0	-2.3 to 4.1 [0.02]	-8.7 to -2.4	-4.5 to 1.9 [0.17]	-3.8 to 0.27	**-3.0 to 2.8 [0.63]**
coarse sand	-2.6 to 1.0	**-1.3 to 1.4 [0.64]**	-3.0 to 0.50	-2.5 to 4.9 [0.49]	-3.0 to 0.77	**-5.4 to 2.2 [0.76]**	-1.4 to 1.3	**-3.9 to 3.0 [0.67]**
very coarse sand	-0.73 to 0.50	**-0.4 to 0.48 [0.76]**	-0.86 to 0.36	**-0.83 to 1.51 [0.68]**	-0.82 to 0.42	**-1.8 to 0.63 [0.79]**	-0.42 to 0.52	**-1.3 to 0.9 [0.74]**

[a]net change in sediment storage in 10^4xMT/yr

[b]Probability that the morph-based budget falls within the bounds of the flux-based budget is shown in square brackets [ ].

comprised 29% (±20% SD) of the total floodplain and vegetated island height, which is similar to the proportion of the cap facies found in floodplain deposits from other studies (Page et al., 2003; Thayer and Ashmore, 2016).

There was no significant difference between the grain size of the fine sediment in the floodplains and vegetated islands on the Yampa and Little Snake rivers (Wilcoxon rank sum test α=0.05), so we developed one Bayesian grain size model for both rivers. The grain size distribution of the base facies on the Yampa River and sand-bed portions of the Little Snake River closely matched the grain size distribution of the bed material, and the cap facies closely matched the grain size distribution of the suspended load (Figure 3-3b). Thus, we infer that the base of the deposit was a former active channel bar built by bed load transport and the cap of the deposit was overbank deposition of the suspended and wash load. The cap deposit was predominately composed of silt/clay with large proportions of very fine and fine sand and a lesser amount of medium sand (Figure 3-7; see Appendix Table A-3). There was no coarse or very coarse sand in the cap facies. The base facies on the Yampa River and sand bed reaches of the Little Snake River were predominately composed of medium and coarse sand with a significant amount of fine sand (Figure 3-7). The fraction of very coarse sand in the base facies was small and comparable to the fraction of silt/clay and very fine sand (see Appendix Table A-3).

4.2.2. Partitioned morphological sediment budget

There was no evidence of sand erosion from the floodplains, despite our careful accounting of uncertainty in computing $\Delta S_{k(morph)}$ (Figure 3-10; see Appendix Table A-4). Vegetated islands accumulated sediment during some periods. Floodplain deposition along the channel margins was balanced by bank erosion such that the overall change in

floodplain storage was indeterminant over the entire study period (Figure 3-10b). Vegetated islands expanded and accumulated sand from 2013 to 2015 and likely expanded from 2017 to 2019; there was no change in vegetated island storage from 2015-2017 (Figure 3-10b; see Appendix Table A-4). Vegetated island expansion did not cause a change in channel width or channel activity (i.e., the total amount of erosion and deposition per unit distance; see Appendix Figure A-2).

4.3. Comparing the flux-based and morphological sediment budgets

The uncertainty bounds of the silt/clay $\Delta S_{k(morph)}$ were completely within the bounds of the silty/clay $\Delta S_{k(flux)}$ during each temporal subset and the budgets were closed. Both budgets were indeterminant over the entire study period, but uncertainty in the flux-based budget was substantially greater than the morphological budget (Figure 3-10a; Table 3-2). Sand evacuation measured by the flux-based budget was not observed in the morphological budget, except for the period between 2015 and 2017 when both budgets were erosional and the budget was closed. Both total sand budgets were indeterminant between 2017 and 2019 (Figure 3-10b; Table 3-2).

When the sand budgets were partitioned into multiple sand fractions, the largest difference between $\Delta S_{k(flux)}$ and $\Delta S_{k(morph)}$ occurred in the fine and medium grain size of sand. We found no morphological evidence for the erosion of fine and medium sand that was detected in the flux-based budget (Figure 3-10d, e; Table 3-2). The flux- and morphological-budgets aligned well for very fine, coarse, and very coarse sand, and the budgets were closed (Figure 3-10 c, f, g; Table 3-2).

4.3.1. Missing dimension of the morphological sediment budget

A major factor that limits our morphological sediment budget approach is that changes in channel bed topography were not measured such that erosion and deposition of bed material could not be documented. Our grain-size analysis indicated that the channel bed and the base facies deposits were composed of medium and coarse sand and to a lesser degree, fine sand (Figure 3-7). If the fine and medium sand evacuation from the flux-based budget occurred from the channel bed, this would equate to 0.03 to 0.14 m (0.005 to 0.02 m/yr) of bed degradation that was undetected by the methods used to analyze morphological change. Because we carefully accounted for uncertainty in our morphological sediment budget, we feel confident that the difference between $\Delta S_{k(flux)}$ and $\Delta S_{k(morph)}$ for fine and medium sand was not caused by measurement error and that these grain sizes were eroded from the channel bed (Kondolf and Matthews, 1991).

We used the fused 2011 and 2015 DEMs in the downstream section of Deerlodge Park to estimate whether the average change in bed elevation was similar to fine and medium sand bed degradation measured by the flux-based sediment budget. We found there were zones of bed erosion and deposition, but these areas of change compensated for one another such that the average bed elevation change was -0.09 ± 0.25 m and the total change in bed sediment storage was $-2.9x10^4 \pm 1.9x10^5$ m^3 (Figure 3-11 A-B). The amount of fine and medium sand degradation measured by the flux-based budget was smaller than the propagated error in the DEMs and therefore, could not be detected.

We speculate that the 0.005 to 0.02 m/yr of fine and medium sand evacuation is a short-term adjustment to a relatively recent perturbation, because we found no significant
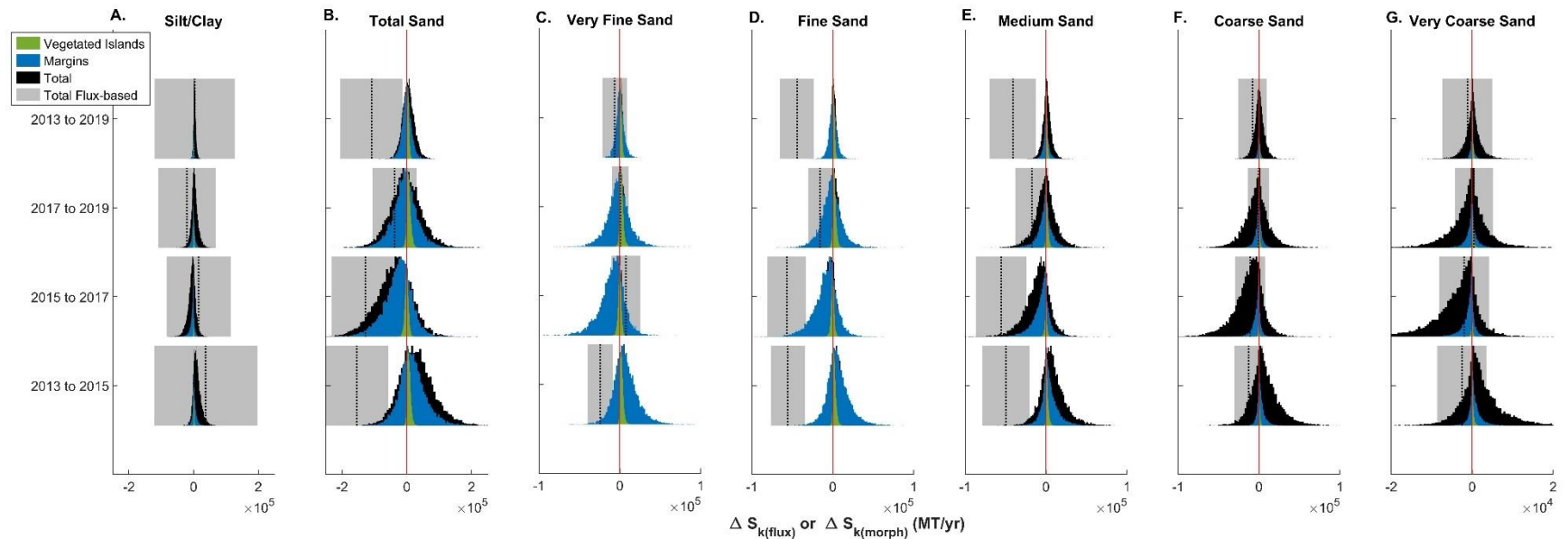
Figure 3-10. Morphological and flux-base sediment budgets for different temporal subsets partitioned by (A) silt/clay, (B) total sand, (C) very fine sand, (D) fine sand, (E) medium sand, (F) coarse sand, and (G) very coarse sand in units of metric tons per year. The morphological sediment budget is shown as a distribution of $\Delta S_{k(morph)}$ segregated by the vegetated islands (green), the channel margins (blue), and total change (black). Positive values indicate net deposition and negative values net erosion. The flux-based sediment budget ($\Delta S_{k(flux)}$) for the same temporal subset is shown as a gray band with the zero-error value shown as a black dashed line. The red vertical line is at zero, indicating no net change in sediment storage.
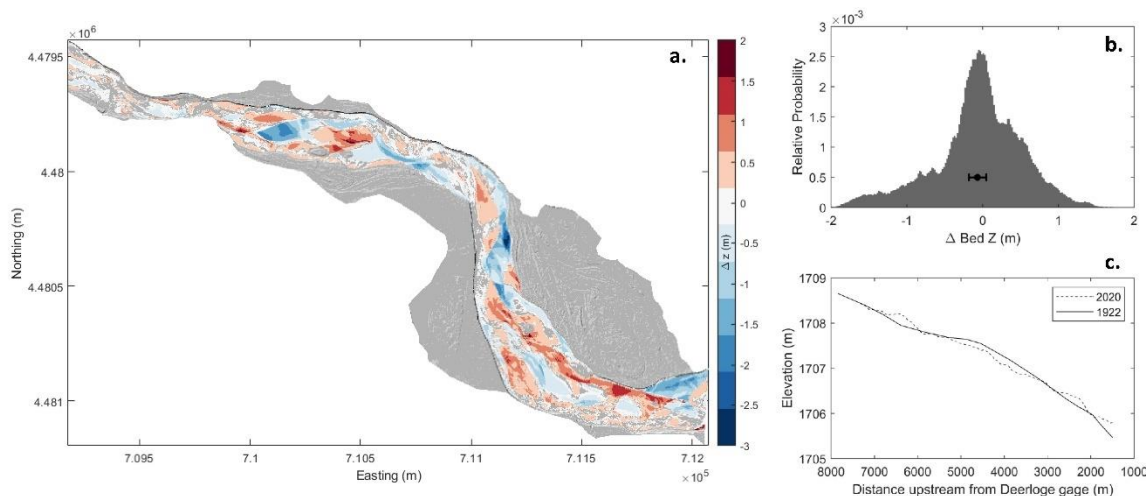
Figure 3-11. (A) Topographic changes in bed elevation from 2011 to 2015 in the extent of LiDAR coverage in Deerlodge Park (Figure 3-1). Positive values (red) indicate deposition and negative values (blue) indicate erosion. Only cells above a level of detection corresponding to a 95% confidence interval are displayed for visualization purposes. (B) Histogram of the bed elevation change for all channel bed cells. The average bed elevation change is shown as the error bars in the center of the histogram. (C) Longitudinal profile in the sand-bedded portion of the Yampa River for 1922 and 2020.

long-term change in the longitudinal profiles of the sand bed portion of the Yampa River from 1922 to 2020 (Figure 3-11c). Our results suggest that fine sand is preferentially evacuated from the channel bed while coarse and very coarse sand are in balance, causing the bed material grain-size distribution to coarsen. Moreover, fine sand is winnowed at a faster rate than medium sand, which likely exacerbates bed coarsening. For example, degradation of fine sand measured by the flux-based budget would cause a 2 to 14% decrease in fine sand from the bed whereas medium sand would only decrease by 1 to 4%. Bed coarsening has also been observed in historic measurements of sediment transport since the 1980s (Topping et al., 2018).

5. Discussion

5.1. Channel adjustment observed from a grain-size fractional sediment budget

Sediment is sorted and stored throughout the alluvial channel and floodplain in our study area. Morphologic adjustment occurred in different places as a result of the storage and evacuation of different sand fractions. We found that a grain-size fractional flux-based and morphological sediment budget were needed to evaluate these changes. The sediment budgets were calculated for a short timeframe — 6 years — to make use of the continuous record of the acoustical sediment gages. The flux-based budget showed that sand was evacuated from the study area, but we found no morphological evidence of this evacuation; such as channel widening, increase in channel activity, or bed degradation. A closer examination of the grain-size fractional sediment budget revealed that only fine and medium sand were evacuated from the channel bed and the geomorphic response was a bed textural adjustment.

The bed coarsening suggested here may be part of a longer-term channel adjustment. Sediment waves originating from Sand Creek during the late-1950s to early-1960s caused an initial, rapid phase of bed fining, followed by long-term, slower bed coarsening (Topping et al., 2018). We propose that the bed will continue to coarsen until the sediment transport capacity is reduced to a magnitude where the fine and medium sand budget is balanced. Thus, it is probable that the geomorphic response to the sediment pulse generated by tributary floods on Sand Creek is primarily textural and the channel can absorb the pulse of sediment without necessitating wholescale channel change. We find the flux-based sediment budget, although in deficit, reflects a system in dynamic equilibrium that is adjusting to fluctuations in sediment supply.

The bed textural response inferred to be the residual term in our sediment budget has rarely been measured or discussed in the sediment budget literature, partly because grain-size fractional sediment budgets are rarely calculated. Yet, changes in the grain size of the sediment supply may cause the bed material to fine or coarsen, allowing the reach to transport the changed supply without significant morphologic changes, as demonstrated by numerous studies (e.g., Buffington and Montgomery, 1999; Montgomery et al., 1999; Topping et al., 2000; Lisle et al., 2000; Cui et al., 2005; Sklar et al., 2009; Ferguson et al., 2015; Dean et al., 2016; Topping et al., 2018; Dean et al., 2020; Topping et al., 2021). The grain-size fractional approach to sediment budgeting can be used to evaluate the interaction between bed texture and morphologic adjustment. Such an approach can be useful for predicting the sensitivity of a river to channel change.

The only measurable morphological change measured in our study resulted from a very small amount of very fine sand aggradation on the upper surface of vegetated islands during moderate-to-large flows. This aggradation was not large enough to change the characteristics of the channel (i.e., width, sinuosity, lateral migration). We found that very fine sand accumulated for a discrete range of flows when between 5% and 50% of the post-1938 floodplain was inundated. Very fine sand was the only grain size to accumulate, because coarser grain sizes were not carried high enough in the water column to be deposited on the floodplains. For example, suspended sediment concentration profiles indicate that the very fine sand concentration was 2 to 4 times greater than the fine sand concentration when very fine sand accumulation was measured in the floodplains (Figure 3-13a).

Very fine sand advected onto the floodplains no longer accumulated during large flows that inundated greater than 50% of the post-1938 floodplain. We speculate very fine sand stops accumulating once floodplain vegetation becomes submerged, because the velocity is large enough to keep very fine sand in suspension. This occurs because roughness abruptly drops when vegetation is submerged, leading to large increases in velocity over the floodplain (Wu et al., 1999; Manners et al., 2013, 2015). We found that between 34% to 44% of LiDAR returns in the 2015 survey classified as vegetation were fully submerged at the discharge when very fine sand stopped accumulating. Thus, it is plausible that vertical aggradation is confined to a discrete range of overbank flows where floodplain vegetation is still emergent. This interpretation requires further investigation, but such a mechanism could be used to target flows that prevent floodplain growth and reverse channel narrowing in regulated rivers downstream from dams (Allred and Schmidt, 1999; Grams and Schmidt, 2002; Dean et al., 2020; Grams et al., 2020; Walker et al., 2020).

The finding that measurable floodplain building can result from small-to-unmeasurable storage of very fine sand over a discrete range of flows is likely a ubiquitous characteristic of sand-bed rivers. Floodplain growth may account for a small portion of the total sediment budget or could be unrelated to the sign of the sediment budget calculated over broad grain size categories (i.e., net aggradation or degradation of total sand). For example, Walker et al. (2020) found that floodplain formation accounted for a small amount of the total sediment load on the lower Green River in Canyonlands National Park, and that very fine sand was the only sand size in aggrading floodplain
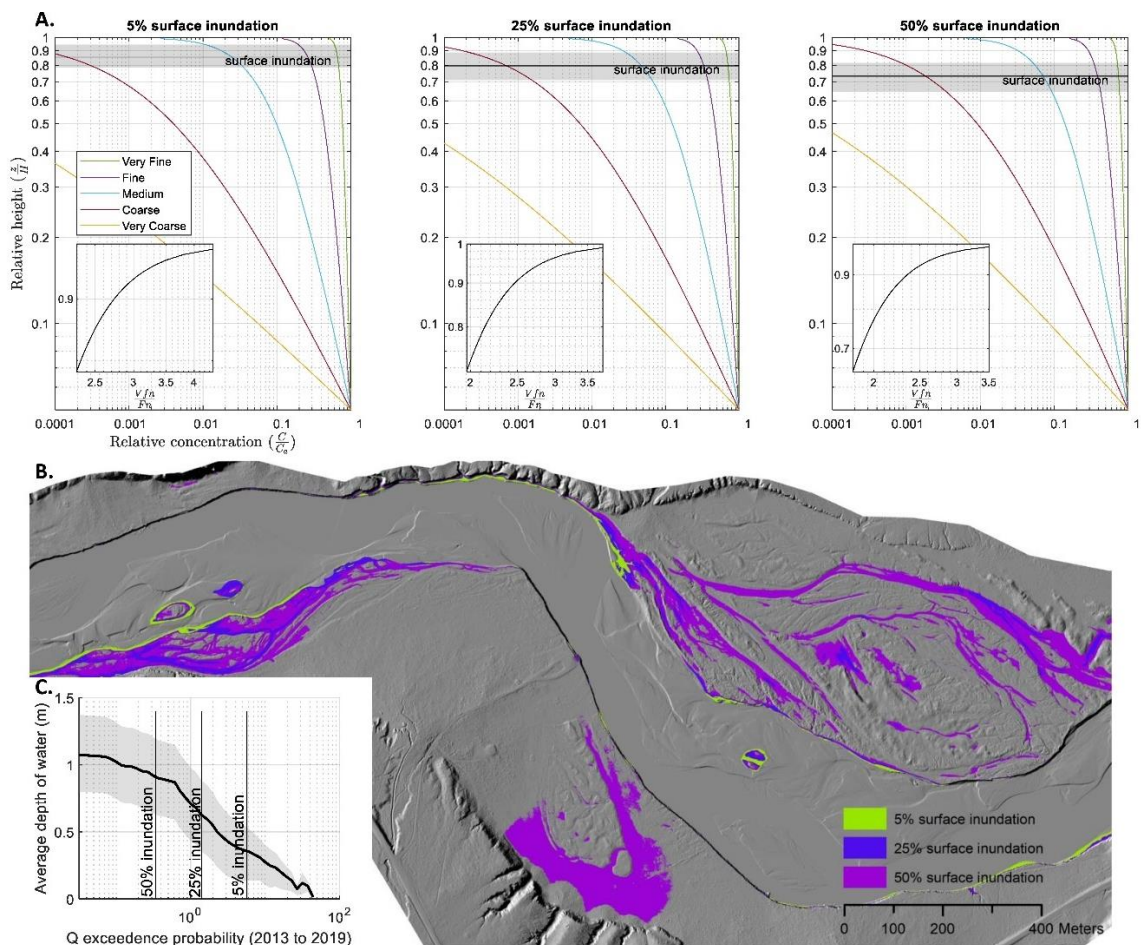
Figure 3-12. (A) Rouse profiles at the discharge to inundate 5%, 25%, and 50% of the post-1938 floodplain. The rouse profiles were calculated separately for very fine, fine, medium, coarse, and very coarse sand. The relative concentration is the ratio of the near-bed concentration, calculated by the Wright and Parker (2004) entrainment function, to the concentration at various depths in the water column. The black line shows the mean height in the water column that submerges the floodplain and gray bands represent the interquartile range given the variability in floodplain elevation. Inset figures show the ratio of the relative concentration of very fine to fine sand in the upper region of the water column that inundates the floodplain. (B) Spatial extent of floodplain inundation at the discharge required to inundate 5%, 25%, and 50% of the post-1938 floodplain in the section of Deerlodge Park where LiDAR data were available (Figure 3-1). (C) Depth of inundation on the floodplains formed during our study period (2013 to 2017) plotted as a function of the percent of time a given discharge was exceeded during our study period. The gray band represents the interquartile range of inundation depth. The black vertical lines show inundation depth for discharges that inundate 5%, 25%, and 50% of the post-1938 floodplain.

surfaces. Similarly, Grams and Schmidt (2005) found that floodplain formation on the

Green River in Dinosaur National Monument accounted for a small fraction of the

annualsediment load. A grain-size fractional sediment budget is necessary to observe or

predict this kind of floodplain development.

5.2. Uncertainty in the flux-based and morphological budgets

Flux-based and morphological sediment budgets have different sources of

uncertainty that accumulate over different timescales. The most significant source of

uncertainty in the flux-based sediment budget is caused by persistent bias in

measurements of sediment transport. These biases accumulate through time and lead to

large uncertainties in $\Delta S_{k(flux)}$ when calculated over long timeframes (Erwin et al., 2012;

Grams et al., 2013). Conversely, the primary source of uncertainty in the morphological

sediment budget is caused by measurement error in channel morphology, which is

independent of the time between morphologic measurements (Erwin et al., 2012).

We used a Bayesian method to characterize uncertainty in the morphological

budget to predict a distribution of probable $\Delta S_{k(morph)}$ values from repeat aerial images and

topographic and grain size data. We characterized the morphologic sediment budget as

indeterminant when the 68% CI spanned zero, however, the results are more informative

because we can also estimate the probability of morphologic change. For example, the

68% CI spanned zero for the total sand $\Delta S_{(morph)}$ between 2013 and 2015 and the budget

was indeterminant, but there was a relatively high probability (i.e., 71%) that $\Delta S_{(morph)}$

was positive and sand accumulated. If the risk of accepting $\Delta S_{(morph)}$ as true change when

the change might be caused by uncertainty is inconsequential, a 71% probability of

deposition might be large enough to support geomorphic interpretations. The distribution

of uncertainty in a flux-based budget is unknown and every value within the uncertainty band has an equal probability of being true. Thus, we have no way to calculate the probability that $\Delta S_{(flux)}$ is erosional or depositional when the flux-based budget is indeterminant.

We find that small changes in the uncertainty assigned to acoustical measurements of sediment transport have a large effect on the determinacy of the flux-based budget. The flux-based budget for sand was indeterminant between 2017 and 2019, but uncertainty in the suspended load would only need to be reduced to ±5%, a value regularly applied to other rivers in the region (Grams et al., 2019; Dean et al., 2020; Topping et al., 2021), for the budget to be in deficit. Similarly, the grain-size fractional $\Delta S_{k(flux)}$ for very fine sand between 2017 and 2019 was indeterminant; however, if uncertainty in the suspended load measurements were again reduced to 5%, we could detect very fine sand accumulation. These findings suggest there should be careful consideration of the uncertainty assigned to the acoustical measurements of sediment transport. A robust framework to characterize this uncertainty at individual gages is an important area of future work.

5.3. New morphological sediment budget framework

The method we developed to calculate a grain-size fractional morphological sediment budget was supported by the consistent thickness and grain size of two dominant floodplain facies. We expect that the thickness and grain size of the floodplain facies will remain consistent if the planform and sediment supply do not change longitudinally and a single Bayesian model can be developed. Multiple Bayesian models may be needed if the behavior of the river changes longitudinally.

The total floodplain height and the thickness and grain size of the facies will vary among rivers, meaning that the Bayesian models are not transferrable. This is due to differences in the sediment load, the channel sinuosity, and the channel lateral stability. The floodplain is composed of a larger portion of the base facies in bed load-dominated rivers whereas oblique and vertical accretion increase the cap facies thickness in suspended load-dominated rivers (Page et al., 2003; Thayer and Ashmore, 2016). Thicker base facies and thinner caps are expected on rivers with high sinuosity because lateral instability leads to faster bar accretion (Thayer and Ashmore, 2016).

A significant limitation of our morphological sediment budget method is that changes in the channel bed topography and bed texture were not measured. This might be problematic in rivers where the total sediment flux is small compared to the volume of erosion and deposition from the channel bed (e.g., braided gravel-bed rivers) or where the channel slope adjusts through degradation and aggradation rather than changes in sinuosity. In such rivers, the morphological budget may need to be measured as the difference between two topographic surveys (Brasington et al., 2000; Fuller et al., 2003; Lane et al., 2003; Eaton and Lapointe, 2001; Croke et al., 2013; Leonard et al., 2017; Antoniazza et al., 2019; Grams et al., 2019; among others). Recent advancements in unmanned aircraft system (UAS) technologies have increased the availability of high-resolution topography for such purposes (Fonstad et al., 2013; Carbonneau and Dietrich, 2017). However, in large rivers, spatially continuous measurements of repeat channel and floodplain topography over long reaches remain difficult and expensive to collect even with the most advanced mapping methods.

6. Conclusion

In this study, we partition a flux-based and morphological sediment budget on a 23-km reach of a sand-bed river into multiple sand-size fractions. We found that different grain sizes were transported and deposited in different parts of the alluvial channel and floodplain. For a sediment budget to reveal these important changes in the river, a budget must account for the different behavior of these grain sizes, and a grain-size fractional sediment budget was needed.

The flux-based budget was calculated from high-temporal resolution measurements of sediment transport and grain size at acoustic sediment gages. The morphological budget was calculated from an aerial image time series and sparse measurements of channel and floodplain topography and grain size. We show that even though the flux-based budget for all sand sizes combined was in deficit, the grain-size fractional flux-based and morphological budgets revealed that the fine and medium sand were evacuated from the bed and the bed coarsened while the floodplains accumulated very fine sand. Very fine sand accumulated during a discrete range of flows when floodplain vegetation was not yet fully submerged.

Effective river management requires an ability to forecast river response to changes in water and sediment supply. Small changes in water and sediment supply may be within the natural capacity of the river to transport sediment such that dynamic equilibrium is maintained. Larger changes, however, have the potential to cause wholesale channel change that impacts the ability of the channel to contain flood flows, damages downstream infrastructure, or adversely affects in-channel and floodplain habitats. The sensitivity of a river to wholescale channel change is dependent on the ease

by which the river can adjust within its current behavioral regime. In our study, the

adjustment was primarily bed textural and the process-form relations did not change

despite sand evacuation. A grain-size fractional flux-based and morphologic sediment

budget were needed to observe this kind of adjustment.

Data Availability

Datasets used to calculate the flux-based budget are available for download from

the USGS Grand Canyon Monitoring and Research website at:

https://www.gcmrc.gov/discharge_qw_sediment/. Aerial images used to calculate the

morphological sediment budget can be downloaded from the USGS EarthExplorer

website at: https://earthexplorer.usgs.gov/. LiDAR datasets are available on request.

References

Alexander J. 2007. The timing and magnitude of channel adjustments in the Upper Green River below Flaming Gorge Dam in Browns Park and Lodore Canyon, Colorado: An analysis of the pre- and post-dam river using high-resolution dendrogemorphology and repeat topographic surveys, Thesis, Utah State University: Logan, UT

Allred TM, Schmidt JC. 1999. Channel narrowing by vertical accretion along the Green River near Green River, Utah. GSA Bulletin **111** : 1757–1772. DOI: 10.1130/0016-7606(1999)111<1757:CNBVAA>2.3.CO;2

Andrews E. 1978. Present and potential sediment yields in the Yampa River Basin, Colorado and Wyoming . USGS Numbered Series. U.S. Geological Survey, Water Resources Division,

Antoniazza G, Bakker M, Lane SN. 2019. Revisiting the morphological method in two-dimensions to quantify bed-material transport in braided rivers. Earth Surface Processes and Landforms **44** : 2251–2267.

Brakenridge GR. 1984. Alluvial stratigraphy and radiocarbon dating along the Duck River, Tennessee: Implications regarding flood-plain origin. GSA Bulletin **95** : 9–25. DOI: 10.1130/0016-7606(1984)95<9:ASARDA>2.0.CO;2

Brasington J, Rumsby BT, McVey RA. 2000. Monitoring and modelling morphological change in a braided gravel-bed river using high resolution GPS-based survey. Earth

Surface Processes and Landforms **25** : 973–990. DOI: 10.1002/1096-9837(200008)25:9<973::AID-ESP111>3.0.CO;2-Y

Buffington JM, Montgomery DR. 1999. Effects of sediment supply on surface textures of gravel-bed rivers. Water Resources Research **35** : 3523–3530. DOI: 10.1029/1999WR900232

Carbonneau PE, Dietrich JT. 2017. Cost-effective non-metric photogrammetry from consumer-grade sUAS: implications for direct georeferencing of structure from motion photogrammetry. Earth Surface Processes and Landforms **42** : 473–486. DOI: 10.1002/esp.4012

Church M. 2006. Bed Material Transport and the Morphology of Alluvial River Channels. Annual Review of Earth and Planetary Sciences **34** : 325–354. DOI: 10.1146/annurev.earth.33.092203.122721

Croke J, Todd P, Thompson C, Watson F, Denham R, Khanal G. 2013. The use of multi temporal LiDAR to assess basin-scale erosion and deposition following the catastrophic January 2011 Lockyer flood, SE Queensland, Australia. Geomorphology **184** : 111–126. DOI: 10.1016/j.geomorph.2012.11.023

Cui Y, Parker G, Lisle TE, Pizzuto JE, Dodd AM. 2005. More on the evolution of bed material waves in alluvial rivers. Earth Surface Processes and Landforms **30** : 107–114. DOI: 10.1002/esp.1156

Curry CW, Bennett RH, Hulbert MH, Curry KJ, Faas RW. 2004. Comparative Study of Sand Porosity and a Technique for Determining Porosity of Undisturbed Marine Sediment. Marine Georesources & Geotechnology **22** : 231–252. DOI: 10.1080/10641190490900844

Dean DJ, Schmidt JC. 2011. The role of feedback mechanisms in historic channel changes of the lower Rio Grande in the Big Bend region. Geomorphology **126** : 333–349. DOI: 10.1016/j.geomorph.2010.03.009

Dean DJ, Topping DJ, Grams PE, Walker AE, Schmidt JC. 2020. Does Channel Narrowing by Floodplain Growth Necessarily Indicate Sediment Surplus? Lessons From Sediment Transport Analyses in the Green and Colorado Rivers, Canyonlands, Utah. Journal of Geophysical Research: Earth Surface **125** : e2019JF005414. DOI: 10.1029/2019JF005414

Dean DJ, Topping DJ, Schmidt JC, Griffiths RE, Sabol TA. 2016. Sediment supply versus local hydraulic controls on sediment transport and storage in a river with large sediment loads. Journal of Geophysical Research: Earth Surface **121** : 2015JF003436. DOI: 10.1002/2015JF003436

Dyni JR. 1968. Geologic map of the Elk Springs quadrangle, Moffatt County, Colorado . Report. U.S. Geologic Survey Geologic Quadrangle **702**: DOI: 10.3133/gq702

Eaton BC, Lapointe MF. 2001. Effects of large floods on sediment transport and reach morphology in the cobble-bed Sainte Marguerite River. Geomorphology **40** : 291–309. DOI: 10.1016/S0169-555X(01)00056-3

Elliott JG, Anders SP. 2004. Summary of sediment data from the Yampa River and Upper Green River basins, Colorado and Utah, 1993-2002 . US Department of the Interior, US Geological Survey

Erwin SO, Schmidt JC, Wheaton JM, Wilcock PR. 2012. Closing a sediment budget for a reconfigured reach of the Provo River, Utah, United States. Water Resources Research **48** : W10512. DOI: 10.1029/2011WR011035

Ferguson RI, Church M, Rennie CD, Venditti JG. 2015. Reconstructing a sediment pulse: Modeling the effect of placer mining on Fraser River, Canada. Journal of Geophysical Research: Earth Surface **120** : 2015JF003491. DOI: 10.1002/2015JF003491

Fonstad MA, Dietrich JT, Courville BC, Jensen JL, Carbonneau PE. 2013. Topographic structure from motion: a new development in photogrammetric measurement. Earth Surface Processes and Landforms **38** : 421–430. DOI: 10.1002/esp.3366

Fryirs K, Brierley G. 2022. Assemblages of geomorphic units: A building block approach to analysis and interpretation of river character, behaviour, condition and recovery. Earth Surface Processes and Landforms **47** : 92–108. DOI: 10.1002/esp.5264

Fryirs KA. 2017. River sensitivity: a lost foundation concept in fluvial geomorphology. Earth Surface Processes and Landforms **42** : 55–70. DOI: 10.1002/esp.3940

Fryirs KA, Brierley GJ. 2012. Geomorphic analysis of river systems: an approach to reading the landscape . John Wiley & Sons: Chichester, U.K.

Fuller IC, Large ARG, Charlton ME, Heritage GL, Milan DJ. 2003. Reach-scale sediment transfers: an evaluation of two morphological budgeting approaches. Earth Surface Processes and Landforms **28** : 889–903. DOI: 10.1002/esp.1011

Gaeuman DA, Schmidt JC, Wilcock PR. 2003. Evaluation of in-channel gravel storage with morphology-based gravel budgets developed from planimetric data. Journal of Geophysical Research: Earth Surface **108** : 6001. DOI: 10.1029/2002JF000002

Grams PE, Buscombe D, Topping DJ, Kaplinski M, Hazel JE. 2019. How many measurements are required to construct an accurate sand budget in a large river? Insights from analyses of signal and noise. Earth Surface Processes and Landforms **44** : 160–178. DOI: https://doi.org/10.1002/esp.4489

Grams PE, Dean DJ, Walker AE, Kasprak A, Schmidt JC. 2020. The roles of flood magnitude and duration in controlling channel width and complexity on the Green River in Canyonlands, Utah, USA. Geomorphology **371** : 107438. DOI: 10.1016/j.geomorph.2020.107438

Grams PE, Schmidt JC. 2002. Streamflow regulation and multi-level flood plain formation: channel narrowing on the aggrading Green River in the eastern Uinta Mountains, Colorado and Utah. Geomorphology **44** : 337–360. DOI: 10.1016/S0169-555X(01)00182-9

Grams PE, Schmidt JC. 2005. Equilibrium or indeterminate? Where sediment budgets fail: Sediment mass balance and adjustment of channel form, Green River downstream from Flaming Gorge Dam, Utah and Colorado. Geomorphology **71** : 156–181. DOI: 10.1016/j.geomorph.2004.10.012

Grams PE, Topping DJ, Schmidt JC, Hazel JE, Kaplinski M. 2013. Linking morphodynamic response with sediment mass balance on the Colorado River in Marble Canyon: Issues of scale, geomorphic setting, and sampling design: Flow, sediment supply, and morphodynamics. Journal of Geophysical Research: Earth Surface **118** : 361–381. DOI: 10.1002/jgrf.20050

Griffiths GA. 1979. Recent sedimentation history of the Waimakariri River, New Zealand. Journal of Hydrology(New Zealand) **18**

Griffiths RonaldG, Topping DJ, Leonard CM, Unema JA. In Review. Resurvey of cross sections on the Little Snake and Yampa rivers in, and upstream from, Deerlodge Park, Colorado . Open-File Report. U.S. Geological Survey

Ham DG, Church M. 2000. Bed-material transport estimated from channel morphodynamics: Chilliwack River, British Columbia. Earth Surface Processes and Landforms **25** : 1123–1142. DOI: 10.1002/1096-9837(200009)25:10<1123::AID-ESP122>3.0.CO;2-9

Hansen WR. 1984. Post-laramide tectonic history of the Eastern Uinta Mountains, Utah, Coloardo, and Wyoming. The Mountain Geologist **21** : 5–29.

Kemper JT, Rathburn SL, Friedman JM, Nelson JM, Mueller ER, Vincent KR. 2022a. Fingerprinting historical tributary contributions to floodplain sediment using bulk geochemistry. CATENA **214** : 106231. DOI: 10.1016/j.catena.2022.106231

Kemper JT, Thaxton RD, Rathburn SL, Friedman JM, Mueller ER, Scott ML. 2022b. Sediment-Ecological Connectivity in a Large River Network. Earth Surface Processes and Landforms **47** DOI: 10.1002/esp.5277

Kondolf GM, Matthews WVG. 1991. Unmeasured Residuals in Sediment Budgets: A Cautionary Note. Water Resources Research **27** : 2483–2486. DOI: 10.1029/91WR01625

Lane SN, Westaway RM, Murray Hicks D. 2003. Estimation of erosion and deposition volumes in a large, gravel-bed, braided river using synoptic remote sensing. Earth Surface Processes and Landforms **28** : 249–271. DOI: 10.1002/esp.483

Legleiter CJ. 2015. Calibrating remotely sensed river bathymetry in the absence of field measurements: Flow REsistance Equation-Based Imaging of River Depths (FREEBIRD). Water Resources Research **51** : 2865–2884. DOI: 10.1002/2014WR016624

Leonard C, Legleiter C, Overstreet B. 2017. Effects of lateral confinement in natural and leveed reaches of a gravel-bed river: Snake River, Wyoming, USA. Earth Surface Processes and Landforms **42** : 2119–2138.

Lisenby PE, Fryirs KA, Thompson CJ. 2020. River sensitivity and sediment connectivity as tools for assessing future geomorphic channel behavior. International Journal of River Basin Management **18** : 279–293. DOI: 10.1080/15715124.2019.1672705

Lisle TE, Nelson JM, Pitlick J, Madej MA, Barkett BL. 2000. Variability of bed mobility in natural, gravel-bed channels and adjustments to sediment load at local and reach scales. Water Resources Research **36** : 3743–3755. DOI: 10.1029/2000WR900238

Mackin JH. 1948. Concept of the graded river. Geological Society of America Bulletin **59** : 463–512.

Manners R, Schmidt J, Wheaton JM. 2013. Multiscalar model for the determination of spatially explicit riparian vegetation roughness. Journal of Geophysical Research: Earth Surface **118** : 65–83. DOI: 10.1029/2011JF002188

Manners RB, Schmidt JC, Scott ML. 2014. Mechanisms of vegetation-induced channel narrowing of an unregulated canyon river: Results from a natural field-scale experiment. Geomorphology **211** : 100–115. DOI: 10.1016/j.geomorph.2013.12.033

Manners RB, Wilcox AC, Kui L, Lightbody AF, Stella JC, Sklar LS. 2015. When do plants modify fluvial processes? Plant-hydraulic interactions under variable flow and sediment supply rates. Journal of Geophysical Research: Earth Surface **120** : 325–345. DOI: 10.1002/2014JF003265

Montgomery DR, Panfil MS, Hayes SK. 1999. Channel-bed mobility response to extreme sediment loading at Mount Pinatubo. Geology **27** : 271–274. DOI: 10.1130/0091-7613(1999)027<0271:CBMRTE>2.3.CO;2

Moody JA, Pizzuto JE, Meade RH. 1999. Ontogeny of a flood plain. GSA Bulletin **111** : 291–303. DOI: 10.1130/0016-7606(1999)111<0291:OOAFP>2.3.CO;2

Nanson GC. 1980. Point bar and floodplain formation of the meandering Beatton River, northeastern British Columbia, Canada. Sedimentology **27** : 3–29. DOI: 10.1111/j.1365-3091.1980.tb01155.x

Nanson GC. 1986. Episodes of vertical accretion and catastrophic stripping: A model of disequilibrium flood-plain development. GSA Bulletin **97** : 1467–1475. DOI: 10.1130/0016-7606(1986)97<1467:EOVAAC>2.0.CO;2

Neill CR. 1987. Sediment balance considerations linking long-term transport and channel processes. Sediment Transport in Gravel-Bed Rivers. John Wiley and Sons New York. 1987. p 225-249, 9 fig, 25 ref.

Page KJ, Nanson GC, Frazier PS. 2003. Floodplain Formation and Sediment Stratigraphy Resulting from Oblique Accretion on the Murrumbidgee River, Australia. Journal of Sedimentary Research **73** : 5–14. DOI: 10.1306/070102730005

Pizzuto JE, Moody JA, Meade RH. 2008. Anatomy and Dynamics of a Floodplain, Powder River, Montana, U.S.A. Journal of Sedimentary Research **78** : 16–28. DOI: 10.2110/jsr.2008.005

Popov IV. 1962. A sediment balance of river reaches and its use for the characteristics of the channel process. Trudy GGI **94** : 3–21.

Rantz SE. 1982. Measurement and computation of streamflow . Geological Survey

Sklar LS, Fadde J, Venditti JG, Nelson P, Wydzga MA, Cui Y, Dietrich WE. 2009. Translation and dispersion of sediment pulses in flume experiments simulating gravel augmentation below dams. Water resources research **45** DOI: 10.1029/2008WR007346

Thayer JB, Ashmore P. 2016. Floodplain morphology, sedimentology, and development processes of a partially alluvial channel. Geomorphology **269** : 160–174. DOI: 10.1016/j.geomorph.2016.06.040

Topping DJ, Grams PE, Griffiths RE, Dean DJ, Wright SA, Unema JA. 2021. Self-limitation of sand storage in a bedrock-canyon river arising from the interaction of flow and grain size. Journal of Geophysical Research: Earth Surface **126** : e2020JF005565. DOI: https://doi.org/10.1029/2020JF005565

Topping DJ, Mueller ER, Schmidt JC, Griffiths RE, Dean DJ, Grams PE. 2018. Long-Term Evolution of Sand Transport Through a River Network: Relative Influences of a Dam Versus Natural Changes in Grain Size From Sand Waves. Journal of Geophysical Research: Earth Surface **123** : 1879–1909. DOI: 10.1029/2017JF004534

Topping DJ, Rubin DM, Grams PE, Griffiths RE, Sabol TA, Voichick N, Tusso RB, Vanaman KM, McDonald RR. 2010. Sediment transport during three controlled-flood experiments on the Colorado River downstream from Glen Canyon Dam, with implications for eddy-sandbar deposition in Grand Canyon National Park . US Geological Survey

Topping DJ, Rubin DM, Vierra LE. 2000. Colorado River sediment transport: 1. Natural sediment supply limitation and the influence of Glen Canyon Dam. Water Resources Research **36** : 515–542. DOI: 10.1029/1999WR900285

Topping DJ, Wright SA. 2016. Long-term continuous acoustical suspended-sediment measurements in rivers - Theory, application, bias, and error . U.S. Geological Survey Professional Paper **1823**

Trimble SW. 1981. Changes in Sediment Storage in the Coon Creek Basin, Driftless Area, Wisconsin, 1853 to 1975. Science **214** : 181–183. DOI: 10.1126/science.214.4517.181

Trimble SW. 1983. A sediment budget for Coon Creek basin in the Driftless Area, Wisconsin, 1853-1977. American Journal of Science **283** : 454–474. DOI: 10.2475/ajs.283.5.454

Viparelli E, Nittrouer JA, Parker G. 2015. Modeling flow and sediment transport dynamics in the lowermost Mississippi River, Louisiana, USA, with an upstream alluvial-bedrock transition and a downstream bedrock-alluvial transition: Implications for land building using engineered diversions. Journal of Geophysical Research: Earth Surface **120** : 534–563. DOI: 10.1002/2014JF003257

Walker AE, Moore JN, Grams PE, Dean DJ, Schmidt JC. 2020. Channel narrowing by inset floodplain formation of the lower Green River in the Canyonlands region, Utah. GSA Bulletin **132** : 2333–2352. DOI: 10.1130/B35233.1

Wheaton JM, Brasington J, Darby SE, Sear DA. 2010. Accounting for uncertainty in DEMs from repeat topographic surveys: improved sediment budgets. Earth Surface Processes and Landforms **35** : 136–156. DOI: 10.1002/esp.1886

Wright S, Parker G. 2005. Modeling downstream fining in sand-bed rivers. I: formulation. Journal of Hydraulic Research **43** : 613–620. DOI: 10.1080/00221680509500381

Wu F-C, Shen HW, Chou Y-J. 1999. Variation of Roughness Coefficients for Unsubmerged and Submerged Vegetation. Journal of Hydraulic Engineering **125** : 934–942. DOI: 10.1061/(ASCE)0733-9429(1999)125:9(934)

CHAPTER 4

BED TEXTURE AND TOPOGRAPHIC ADJUSTMENT IN SAND BED RIVERS[1]

Abstract

When sediment supply and discharge change, the short-term river channel response will be a combination of adjustments in bed grain size (texture) and the accumulation or evacuation of sediment in the channel (topography). This response has been documented for gravel-bed rivers, but little attention has been given to sand-bed rivers, which is the focus of this paper. If the channel response is predominantly textural, changes in channel geometry may be relatively minor. If the channel response is predominately aggradation or degradation, longer-term changes in channel geomorphology, including adjustments of channel dimension, planform, and slope may occur. In this paper, we use a mixed-size morphodynamic model to explore the interaction between textural and topographic responses to changes in sediment supply in sand-bed rivers. First, we consider how the steady-state transport condition varies as a function of sediment supply rate and grain size. We then evaluate the path to steady-state using numerical experiments. We find that as the supply rate increases, the amount of aggradation can be reduced, eliminated, or even reversed depending on the sediment supply grain size. During the transient adjustment for an increased sediment supply, an initial pulse of very fine sand quickly fines the bed, increasing transport capacity. The initial pulse of very fine sand brings transport close to the new sediment supply when the supply fines, limiting the short-term morphological response. When the supply coarsens,

the pulse of very fine sand is less effective at increasing transport and the morphologic response is immediate.

1. Introduction

When the supply of water and sediment to a river change, such that the balance between sediment supply and transport capacity is altered, the short-term river response will be a combination of adjustments in the bed grain size (texture) and aggradation or degradation (topography). If the channel response is predominately textural, changes in the channel geometry may be relatively minor. If the channel response is predominately in sediment accumulation or evacuation, broader, long-term changes in channel geomorphology, including adjustments of channel dimension, planform, slope, and associated changes in aquatic habitat are more likely. There is increasing awareness the textural response may have a strong influence on the extent of aggradation or degradation in gravel-bed rivers (Buffington and Montgomery, 1999; Cui et al., 2003; Sklar et al., 2009; Venditti et al., 2010; East et al., 2015; Ferguson et al., 2015; Ahammad et al., 2021), but less is known about the influence of textural adjustment on aggradation and degradation in sand-bed rivers. In this paper, we examine the bed texture and topographic interaction in sand-bed rivers.

There is a vast geomorphic literature exploring channel response to a change in sediment supply or discharge. Long-term, large perturbations in sediment supply undoubtedly produce changes in channel width, planform, and in-channel geomorphic features (Schumm, 1969; Leopold, 1973; Trimble, 1981; Williams and Wolman, 1984; Everitt, 1993; Brandt, 2000a, 2000b; Clark and Wilcock, 2000; Simon Andrew et al., 2002; Grant et al., 2003; Schmidt and Wilcock, 2008; East et al., 2015), but the rate,

timing, and magnitude of those changes differ widely among case studies. We hypothesize that variability in channel response to changes in supply and discharge may be related to textural adjustments of the river bed. Several studies have shown that changes in the supply grain size may cause the bed grain size to fine or coarsen, making a reach more or less efficient at transporting the perturbed sediment supply (Iseya and Ikeda, 1987; Buffington and Montgomery, 1999; Montgomery et al., 1999; Lisle et al., 2000; Topping et al., 2000; Cui et al., 2005; Curran and Wilcock, 2005; Sklar et al., 2009; Ferguson et al., 2015; Dean et al., 2016; Topping et al., 2018; Dean et al., 2020; Topping et al., 2021). The bed texture also adjusts when the supply rate increases or decreases, even if the supply grain size is constant (Wilcock and DeTemple, 2005). Although the interaction between supply and bed grain size is well-documented, how bed textural changes influence morphologic change is less well understood. For example, potential aggradation of the bed in response to an increase in sediment supply can be enhanced, reduced, eliminated, or even reversed depending on the nature of bed textural adjustments and their effect on transport capacity. A better understanding of the mutual adjustment between bed texture and topography is useful for predicting the channel response to an anticipated or ongoing perturbation in water or sediment supply.

This study uses mixed-size transport models to explore the interaction between textural and topographic response to changes in sediment supply in sand-bed rivers, to demonstrate the nature and conditions of strong textural influence on river bed response. Our focus is on the initial, within-channel response, with particular emphasis on the tradeoff between textural response and sediment storage. First, we consider the variation in steady-state conditions as a function of sediment supply rate and grain size for a

constant water discharge. The channel slope and bed surface texture for a graded

condition indicates the direction of adjustment. We then evaluate the path to equilibrium

using the transport relations in a morphodynamic model. Finally, we consider the time

scale of adjustment in comparison to examples of channel bed response in natural

systems.

2. Background

Sediment supply to a river may increase or decrease, and the bed grain size and

channel form may change in response. Dam construction, channelization, levees, gravel

mining, grade control, and reforestation all reduce the supply of sediment to a river

(Williams and Wolman, 1984; Kondolf, 1997; Liébault and Piégay, 2001; Schmidt and

Wilcock, 2008; Ziliani and Surian, 2012; Moretto et al., 2014; Leonard et al., 2017;

Arbós et al., 2021). The bed often coarsens in response to a reduction in sediment supply

which can limit bed degradation and promote channel widening (Brandt, 2000a; Schmidt

and Wilcock, 2008).

The amount of sediment delivered to a river may increase for several reasons.

Spatially-extensive increases in sediment supply can be due to anthropogenic

modifications in land use, such as poor grazing, forestry, or farming practice (Nadler and

Schumm, 1981; Trimble, 1981; Miller et al., 1993; Clark and Wilcock, 2000; Gomez et

al., 2007), or naturally caused by volcanic eruptions, extreme hydrologic events,

wildfires, or shifts in vegetation induced by climate change (Montgomery et al., 1999;

Gran and Montgomery, 2005; Hoffman and Gabet, 2007; Major et al., 2019; East and

Sankey, 2020; East et al., 2021). Sediment input can also increase at a discrete point.

Landslides, debris flows, gravel augmentation, mining operations, or dam removals are

all spatially isolated inputs of excess sediment (Knighton, 1989; Sutherland et al., 2002; Doyle et al., 2003; Wilcox et al., 2014; East et al., 2015; Gaeuman et al., 2017). In some instances, the increase in supply may be episodic and short-term, such as with dam removal or additions of fine sediment from flash floods, whereas other times increased supply is sustained, such as long-term inputs from mining operations. Increased sediment is sometimes explicitly used for management purposes, such as on the Colorado River downstream from Glen Canyon Dam where additions of fine sediment from flash floods on the Paria River are used to rebuild sand bars in Grand Canyon (Schmidt, 1999; Webb et al., 1999; Hazel et al., 2010).

Increased sediment supply causes textural and topographic changes in both gravel-bed and sand-bed rivers, although considerably more attention has been given to the sorting more readily observed in gravel-bed rivers. Flume and numerical experiments have demonstrated that if the supply becomes finer, the main response could be textural without much change in channel form as the fine-grain pulse translates through the reach (Cui et al., 2003; Sklar et al., 2009; Venditti et al., 2010; Ferguson et al., 2015; Ahammad et al., 2021). Several field studies have also demonstrated that bed fining can effectively move a pulse of sediment through a gravel-bed river with minimal change in channel form (Gran and Montgomery, 2005; Gran, 2012; East et al., 2015).

In sand-bed rivers, bed sorting is harder to observe and the interaction between bed texture and topography has not been well studied. Most of the existing research has focused on canyon-bound rivers that involve an increase in supply and change in supply grain size. In such systems, there is evidence that the textural response dominates because the bed grain size can produce large spatial gradients in sand transport that move

increased sand through the system quickly with minimal bed aggradation (Rubin et al., 2020; Topping et al., 2021). In sand bed alluvial rivers, textural changes inferred from the grain size of suspended sand have been linked to periods of increased or decreased sand supply (Dean et al., 2016; Topping et al., 2018; Dean et al., 2020; Grams et al., 2020), but the interaction between textural and topographic response has not been fully considered (An et al., 2021).

When water discharge and the rate and grain-size distribution of sediment supply are specified, the number of governing relations matches the number of unknowns such that the bed surface grain size and channel slope for steady-state transport are fully determined by the boundary conditions and are independent of initial conditions (Parker and Wilcock, 1993). Steady-state bed conditions can be found as a function of water and sediment supply through the inverse application of mixed-size transport models. The forward application gives transport rate and grain size as a function of bed shear stress and bed surface grain size and the inverse application gives bed shear stress and bed surface grain size as a function of transport rate and grain size. Hydraulic relations (continuity, momentum, and flow resistance) link bed shear stress and bed surface grain size to water discharge. The new steady-state condition is represented in terms of the channel slope and bed texture necessary to transport the supplied sediment with the specified discharge.

Channel response can be usefully divided into two parts – the direction of the adjustment (set by the new steady-state) and the path to adjustment, which includes a mutual adjustment between bed texture and topography over time and along a stream reach. Although a full response to changed supply may include longer-term adjustments

in channel dimension and pattern and may not be complete before the water and sediment supply change yet again, the final steady-state condition provides a useful context by providing the general direction of channel adjustment.

3. Methods

We used a morphodynamic model to develop a platform for a general description of the interaction between textural and topographic adjustment. Morphodynamic models evolve the bed surface grain size and topography from initial conditions to a steady-state using conservation of mass and momentum for open channel flow and sediment mass conservation. We used a simplified version of channel geometry with no floodplain in which the channel can only adjust through bed texture and bed aggradation or degradation, which we refer to as bed topography. In real rivers, bed aggradation and degradation can lead to cross-section change, planform change, and slope change, but the purpose of our model was to capture the initial channel bed response.

The model starts with a specified slope and bed grain size at each model node and calculates bed shear stress from a specified discharge to predict the transport rate and grain size. Mass is conserved between model nodes at each timestep for sediment size fractions through aggradation and degradation and changes in the bed surface grain size, such that there is a balance between the mass of sediment delivered to and transported from each node. The morphodynamic model evaluates the direction of the channel response and the path of adjustment to the new steady-state. The steady-state condition can also be found through inverse application in which the bed grain size and slope are determined from a specified discharge and supply rate and grain size (Wilcock and DeTemple, 2005). The inverse solution is identical to the final steady-state condition

found with a morphodynamic model using the forward application. We developed an approximate inverse model using the steady-state solution of many morphodynamic modeling runs. An overview of our 1D morphodynamic modeling approach, boundary conditions for water, sediment supply rate and grain size, and the inverse application of the transport relations are described in the following sections.

3.1 Model formulation

The model formulation builds on previous models of 1D river morphodynamics (van Niekerk et al., 1992; Hoey and Ferguson, 1994; Cui et al., 1996; Wright and Parker, 2005a; Viparelli et al., 2010b, 2015). The model governing equations are based on conservation of mass and momentum for open channel flow and sediment mass conservation. A general description of the model is provided below and a full description of the governing equations is provided in Appendix B. The following simplifying assumptions were made.

1. The channel has a rectangular geometry and constant width with no exchange with the floodplain. Erosion and deposition only occur from the channel bed.

2. The channel is sufficiently wide that side wall effects can be neglected.

3. Flow and sediment are introduced at the upstream end of the model and are held constant until the model reaches equilibrium.

4. The downstream boundary condition is specified as a water surface elevation and is held constant through time.

5. Sediment is noncohesive and restricted to bed material load carried as bed and suspended load. The cutoff size for the bed material load is set at 0.0625 mm (Raudkivi, 1976), meaning that the model only considers sand.

Flow within the rectangular channel is described by the 1D shallow water equation of mass and momentum conservation. Flow resistance and the skin friction portion of the

total boundary stress are specified using the Wright and Parker (2004b) formulation

which accounts for the effects of density stratification and flow resistance over dunes. A

grain-size-specific formulation of the Exner equation, which conserves sediment mass for

individual size fractions (Parker et al., 2007), is used to determine bed grain size and

topography. The channel bed is divided into an upper active layer that exchanges with the

bed material load, a lower substrate layer that maintains a constant grain size, and an

interface layer that exchanges sediment between the active layer and the substrate as the

bed aggrades and degrades (Hirano, 1971). The active layer thickness is specified as the

height of the bedforms, predicted as a function of flow depth using the relation of Julien

and Klaassen (1995). The grain size of the interface layer evolves as the bed aggrades and

erodes using the relation formulated by Hoey and Ferguson (1994) and Toro-Escobar et

al. (1996). During erosion, the interface grain size becomes that of the substrate and

during aggradation, the interface grain size becomes that of the active layer (Wright and

Parker, 2005a).

Grain-size specific volumetric bed material transport rates are calculated using a

separate transport relation for the bed and suspended load. Total volumetric bed material

transport is the sum of each grain size fraction in the bed load and suspended load. We

use the Wright and Parker (2004b) entrainment model (W-P) coupled with a Rouse

profile and van Rijn (1984) initiation of suspension criterion to estimate suspended load

transport. W-P is a modified version of the Garcia and Parker (1991) entrainment model

that accounts for reduced mixing due to density stratification in the presence of large

suspended loads. G-P and W-P are the only entrainment models that include a mixed-size

hiding function tested against field data, making this relation ideal for predicting size-

selective transport in the suspended load that drives the bed grain size sorting. Bed load is

calculated from the Ashida and Michiue (1972) relation (A-M) which includes the

Egiazaroff (1965) hiding function. A-M was developed from flume measurements of

sand bed load, making this relation ideal for our modeling purpose.

3.2. Model validation

The morphodynamic model was validated with field data from the Niobrara River

(Colby and Hembree, 1955), the Rio Grande River (Nordin and Dempster, 1963), and the

Red River (Toffaleti, 1968). For each validation run, the channel width, discharge,

sediment supply rate, and sediment supply grain size were set to the measured field

values. The initial slope was set to a value less than the graded condition, and the bed

topography and grain size were aggraded to steady-state. We had a total of 8 validation

runs. Model performance was measured by comparing the simulated bed material grain

size, slope, and fractional transport rate at steady-state to the measured values.

Equilibrium was defined as a condition where the transport rate was constant throughout

the reach, resulting in stable bed conditions and indicating that the transport capacity was

balanced to the sediment supply rate. The ratio of the transport standard deviation (σ_{qs}) to

the mean transport (μ_{qs}) among all cross-sections were used to evaluate the similarity of

transport throughout the reach (Viparelli et al., 2010). Steady-state was achieved when

this ratio was less than or equal to 0.0005 ($\sigma_{qs}/\mu_{qs} \leq 0.0005$). We found that our model

produced a steady-state bed grain size and slope that was similar to field observations and

is capable of predicting accurate mobile bed equilibrium conditions (Figure 4-1).
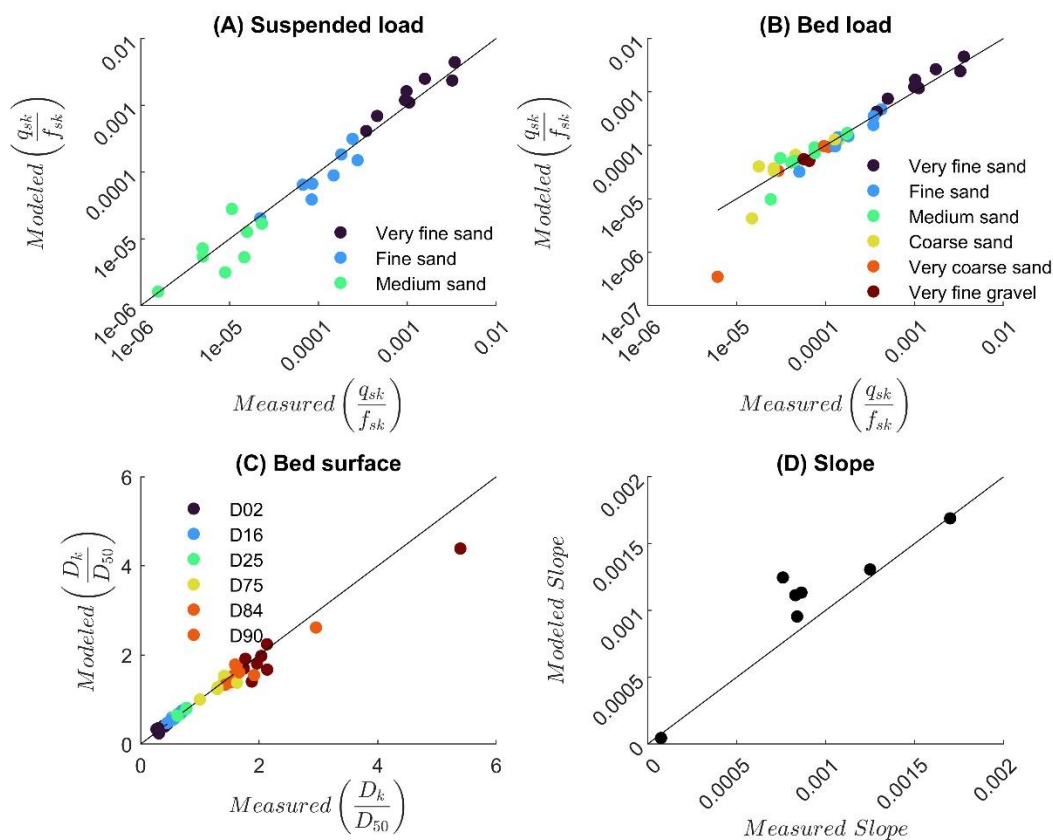
Figure 4-1. (A) Comparison between the measured and predicted suspended sediment transport rate for the kth grain size scaled by the proportion of the kth grain size on the bed surface. (B) Comparison between the measured and predicted bed load sediment transport rate for the kth grain size scaled by the proportion of the kth grain size on the bed surface. Colored dots in A and B distinguish the different k^{th} grain sizes. (C) Comparison between measured and modeled D_k of the bed material grain size, where D_k is the grain size for the kth percentile of the bed material, scaled by the median grain size of the bed material (D_{50}). Colored dot distinguishes the percentile for D_k. (D) Comparison between he measured and modeled slope.

3.4. Model simulations

We ran two phases of model simulations. The initial phase was used to determine steady-state conditions for a specified discharge, sediment supply, and sediment supply grain size. The second set of simulations was used to evaluate the path to equilibrium

when the feed rate and grain size change from steady-state conditions in the first phase of modeling.

Discharge and sediment supply rate and grain size of our initial simulations were chosen to represent the range of bankfull conditions observed in sand-bed rivers. We selected a unit discharge of 3 m^2/sec based on the 50th percentile of a compilation of bankfull discharge measurements in rivers with a median grain size less than 1 mm (Phillips, 2021). We developed four sediment supply size distributions to represent a range of transport observed in sand bed rivers (Figure 4-2). The finest of the supply grain size is similar to transport on the Red River at Alexandria, Louisiana (Toffaleti, 1968), we refer to this as the finest feed composition. The second finest composition (hereafter called the fine feed composition) was based on transport data from the Rio Grande River near Socorro, New Mexico (Nordin and Dempster, 1963). The medium and coarse feed compositions were based on transport data from the Rio Grande River near Bernalillo, New Mexico (Nordin and Dempster, 1963) and Yampa River at Deerlodge Park, Colorado (USGS 09260050; Elliott et al., 1984; Topping et al., 2018), respectively. Sediment supply rates were based on a series of forward transport calculations using our specified unit discharge, slopes ranging from low (0.00005) to high (0.001) gradient, and bed material grain size distributions ranging from fine (D_{50} = 0.17 mm) to coarse (D_{50} = 0.5 mm). We considered the 25th percentile of these forward calculations to be a small supply rate (0.00005 m^2/sec), the 50th percentile to be a moderate supply rate (0.0005 m^2/sec), and the 75th percentile to be a large supply rate (0.005 m^2/sec).
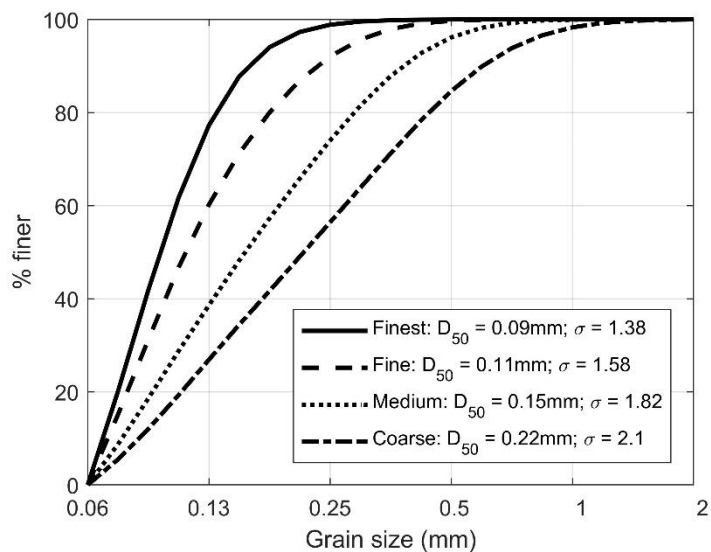
Figure 4-2. Grain size distribution for finest, fine, medium, and coarse supply compositions used for boundary conditions in modeling runs. D_{50} is the median grain size for each distribution and σ is the geometric standard deviation.

We used each combination of sediment supply rate (small, moderate, and large) and grain size (finest, fine, medium, and coarse composition) as boundary conditions for the initial phase of runs; totaling 12 simulations. For each run, the channel length was set to 10 km, cross-sections were spaced at 100 m, the unit discharge, sediment supply rate and grain size were held constant, and the bed topography and grain size were allowed to aggrade to the steady-state condition. We used the same definition of equilibrium as the validation runs ($\sigma_{qs}/\mu_{qs} \leq 0.0005$). The second phase of simulations was used to estimate the transient response under a change in sediment supply rate and grain size by changing the boundary conditions from the initial steady-state.

4. Results

4.1 Steady-state response

A graded river is a condition where the river has a sufficient slope to transport the supplied sediment with the available flow (Mackin, 1948). The graded condition can be expressed as a balance between sediment supply and transport capacity:

$$Q_s \cdot D \sim Q \cdot S \qquad\qquad (4-1)$$

where Q_s and D are the rate and grain size of sediment supply, Q is water discharge, S is slope, which together represents transport capacity (Lane, 1955; Borland, 1960). By defining the controlling variables of the steady-state condition, we can assess the departure from steady-state and how the steady-state adjusts to a change in the water and sediment supply (Henderson, 1966; Schmidt and Wilcock, 2008). Water and sediment supply are defined by Q, Qs, and D, leaving S as the only channel response variable, providing a convenient way to visualize the adjustment in S to a change in drivers (Schumm and Khan, 1972). If the combined change in Q, Qs, and D necessitates a steeper S to transport the supplied sediment, the reach is in a state of sediment surplus and deposition will occur. Conversely, if the combination of Q, Qs, and D changes requires less S, the reach is in a state of sediment deficit and erosion will occur. A change in S is an indication of sediment deficit or surplus which, in real rivers, can lead to subsequent changes in channel morphology.

In unisize sediment, size-selective transport and bed sorting is not considered, and the only channel response variable is slope (Equation 4-1). As sediment supply increases at a constant water discharge, the left side of (4-1) increases and a larger slope is needed to produce the stress necessary to transport the supplied sediment (Figure 4-3 A; A→B).

An increase in sediment supply that also coarsens needs an even larger slope to produce the shear stress to transport the supplied sediment, because coarser grains are harder to transport (Figure 4-3 B; A→B compared to A→C). As the sediment supply increases and fines at a constant discharge, the slope may need to be larger or smaller depending on how much the supply increases. A small increase in supply that fines requires less slope to transport the available load, because finer grains are easier to move and smaller shear stress is needed to transport the supplied load (Figure 4-3 B; A→D). The slope will eventually have to steepen once the supply increase gets large enough that a greater amount of shear stress is necessary to transport the load even though the load is finer (Figure 4-3 B; A→E).

The available flow to transport sediment can also change in combination with the sediment supply. As the discharge increases at a constant supply rate and grain size, the shear stress needed to transport the supplied load is unchanged, and the slope must lower (Figure 4-3 C; B→A). The opposite is true if the discharge decreases, and the slope must increase to maintain constant shear stress (Figure 4-3 C; A→B). When the change in drivers is a combination of discharge and sediment supply, both sides of (4-1) adjust, and the slope may aggrade or degrade depending on the relative change in flow rate to supply rate. In the case where flow and supply increase, if the shear stress produced by the new flow rate transports more sediment than is supplied, the slope will lower (Figure 4-3 C; B→C), and if the shear stress produces less transport than is supplied, the slope will increase (Figure 4-3 C; B→D). In the case where the flow rate decreases and the supply rate increases at a consistent supply grain size, the shear stress needed to transport the supplied sediment will always increase and the slope will aggrade. However, the new

steady-state slope for this condition will always be steeper than if the flow rate had

remained constant, because less water is available to transport the supplied sediment

(Figure 4-3 C; A→E compared with A→F).
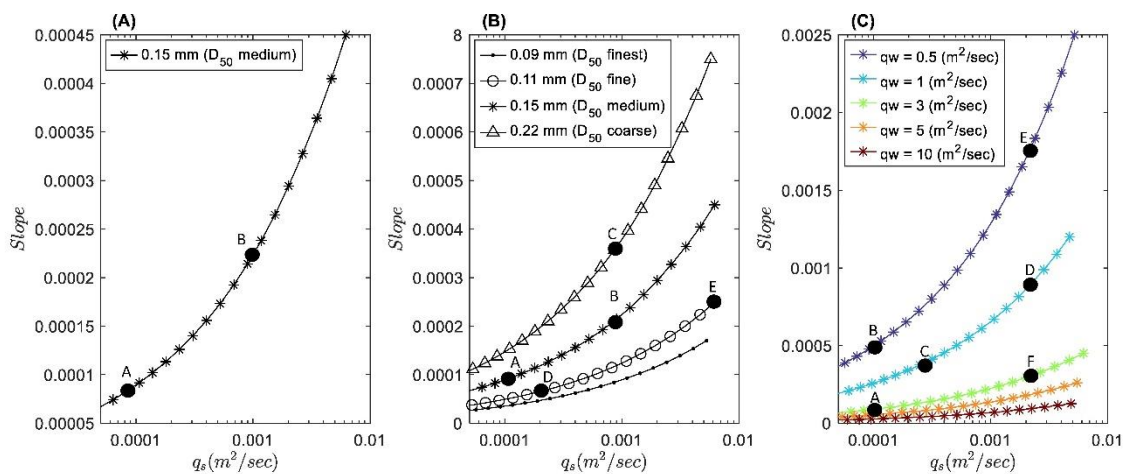
Figure 4-3. Unisize slope transport relation. (A) Slope transport relation for unisize
sediment with a diameter equal to the median grain size of the medium supply
compositions and unit discharge (qw) set to 3 m^2/sec. (B) Slope transport relation for
unisize sediment with a diameter equal to the median grain size of the finest, fine,
medium, and coarse supply compositions and qw set to 3 m^2/sec. (C) Slope transport
relation for unisize sediment with a diameter equal to the median grain size of the
medium composition and qw varies between 0.5 and 10 m^2/sec.

In mixed-size sediment, the bed response to a change in supplied sediment

involves a mutual adjustment between the bed surface grain size and bed

aggradation/degradation. Coarser grains in mixed-size sediment are inherently less

mobile than finer grains. As a result, the bed surface in steady-state transport is coarser

than the bed load (Figure 4-4 A). Differences in mobility with relative grain size become

smaller with increasing transport rate for bed load, such that the size difference between

the transport and bed surface also becomes smaller (Figure 4-4 A). As a result, the bed-

load becomes coarser with increasing transport from a bed of constant grain size

(Wilcock and DeTemple, 2005; Figure 4-4 A). The amount of load coarsening is relatively minor, however, because the critical shear stress for sand size fractions is small, leading to near-equal mobility conditions at all transport rates. The suspended load is much finer than the bed, because the load is dominated by the finest sand sizes that are most evenly distributed throughout the water column (Figure 4-4 A). A change in mobility for sand-sizes in the suspended load occurs as coarser grains become entrained at higher transport rates through the van Rijn suspension criteria. As a result, the suspended load also coarsens with increasing transport even though the relative mobility between grain sizes is constant. Coarsening of the bed and suspended load with increasing transport over a fixed bed necessitates that if the transport were to remain a fixed grain size, the bed grain size must fine as transport increases. Bed fining reduces the shear stress needed to transport larger rates of the same grain size, which *dampens* how much the slope must steepen.

The sediment supplied to sand-bed rivers is typically a mixture of what can be transported as bed load and suspended load, and when the two loads are mixed, the total load grain size becomes finer as transport increases over a fixed grain size bed (Figure 4-4 C). This contrast in behavior between bed load and suspended load individually and their sum as total load occurs, because the suspended fraction of the total load increases with transport rate. The difference is driven by the suspended load being much finer-grained than the bed load (Figure 4-4 A), such that increasing its proportion of the total load causes the total load to fine with increasing transport from a bed of constant grain size (Figure 4-4 B). For a condition where the supply rate increases at a constant grain size, the bed will coarsen for mixed load transport (Figure 4-4 C inset). Bed coarsening

enhances the shear stress needed to transport a larger sediment supply, because coarser

grains are harder to move, which necessitates a steeper slope. The contrasting behavior of

the adjustment in bed grain size and bed slope in mixed load and suspended or bed load

rivers illustrates the nature and importance of the mutual adjustment. The bed textural

response can either *dampen* or *enhance* the extent of sediment accumulation or

evacuation and thereby slope response.
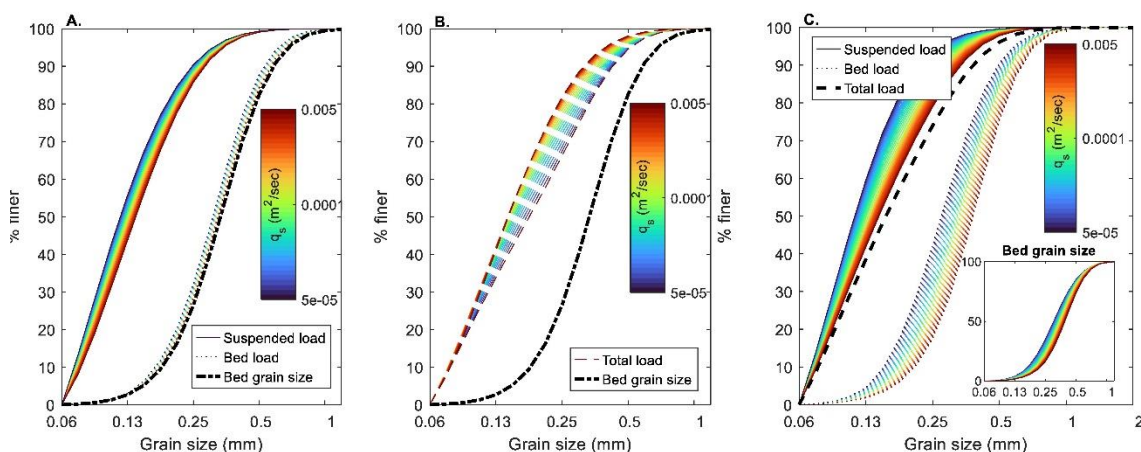
Figure 4-4. Change in suspended and bed load grain size when bed material grain size is fixed (A). Change in total load grain size when the bed grain size is fixed (B). Change in suspended and bed load grain size and bed material grain size (inset) when the total load grain size is fixed (C). Cooler colors correspond to smaller transport rates and warmer colors to larger transport rates. The suspended and bed load coarsen with transport when the bed material grain size is fixed (A) but the total load coarsens (B). The suspended and bed load coarsen when the total load composition is fixed and the bed material coarsens with increasing transport (C).

Next, we consider the mutual adjustment between texture and slope when supply

grain size changes. In the case where the supply grain size fines at a constant rate and

discharge, the bed grain size will fine, and the same supply rate can be transported at

smaller shear stress, causing the slope to decrease (Figure 4-5 A; B→A). The opposite

slope response occurs when the supply coarsens at a constant rate and discharge, and the

bed must aggrade, because larger shear stress is needed to transport the coarser supply (Figure 4-5 A; A→B).

As the supply rate increases and fines, the amount of aggradation can be reduced, eliminated, or even reversed depending on the relative change in the supply rate to the supply grain size. For example, the bed grain size fines and degrades when the supply rate increase is small (Figure 4-5 A; B→C), because the transport capacity of the finer bed at the existing slope exceeds the supply rate. As the supply continues to increase, the amount of bed fining decreases, which reduces the imbalance between transport capacity and supplied sediment, leading to less bed degradation (Figure 4-5 A and B; moving from B→C to B→D).

A special condition occurs when the supply increase is balanced by the increase in transport capacity caused by bed fining, and the bed neither aggrades nor degrades (Figure 4-5 A; B→D). This condition is of particular interest, because the river can accommodate excess supply while maintaining the same steady-state slope, suggesting that the morphological response will be minimal. The amount the supply must increase at a constant rate of fining to achieve this special condition depends on the initial supply rate. A river carrying a large initial load will require a greater proportional increase in supplied sediment compared to a river carrying a small initial load, because the amount of bed fining is greater when the initial supply is large (Figure 4-5 B; B→D compared to E→F). This also suggests that rivers carrying large loads are more prone to bed degradation under conditions of supply increase and fining (bed degradation occurs over a larger range of transport rates from B→D than E→F). The increase in supply needed to maintain a constant steady-state slope also depends on how much the supply grain size

fines. The more the supply fines, the more the bed fines, and therefore a larger increase in supplied sediment is needed to balance the change in transport capacity induced by bed fining (Figure 4-5 A; change in transport from B→D is less than from G→H).

As the supply rate increases and coarsens at a constant discharge, the bed slope must steepen to increase the shear stress available to transport the supplied sediment. The amount of aggradation will be *enhanced* by bed grain size coarsening, because coarse grains are transported by larger shear stress. The amount that the slope is *enhanced* by bed coarsening will depend on how much the supply rate increases and coarsens. The bed grain size naturally coarsens with increasing mixed load transport at a constant supply grain size, so bed coarsening will be further *enhanced* at larger sediment supply rates. We find that the degree of bed coarsening, and slope *enhancement*, is also sensitive to the initial supply rate. A small initial load will result in less bed coarsening for the same proportional increase in supply as a large initial load. Thus, aggradation is most *enhanced* when the initial supply rate is large and the supply rate increases by a large amount. Unsurprisingly, the amount of supply coarsening has the largest effect on the textural response, and aggradation becomes more *enhanced* the more the load coarsens (Figure 4-5 A; slope difference between A→I is less than between A→G).

4.2. Transient response

The pattern of adjustment over time and along the channel can be complex and depends on the direction and magnitude of change in bed grain size and slope from the initial to the final steady-state condition. Consider the common example of when the supply rate increases and fines, such as after dam removal, a large-scale arroyo cutting event, wildfire, tributary flash flooding, or widespread grazing. The steady-state
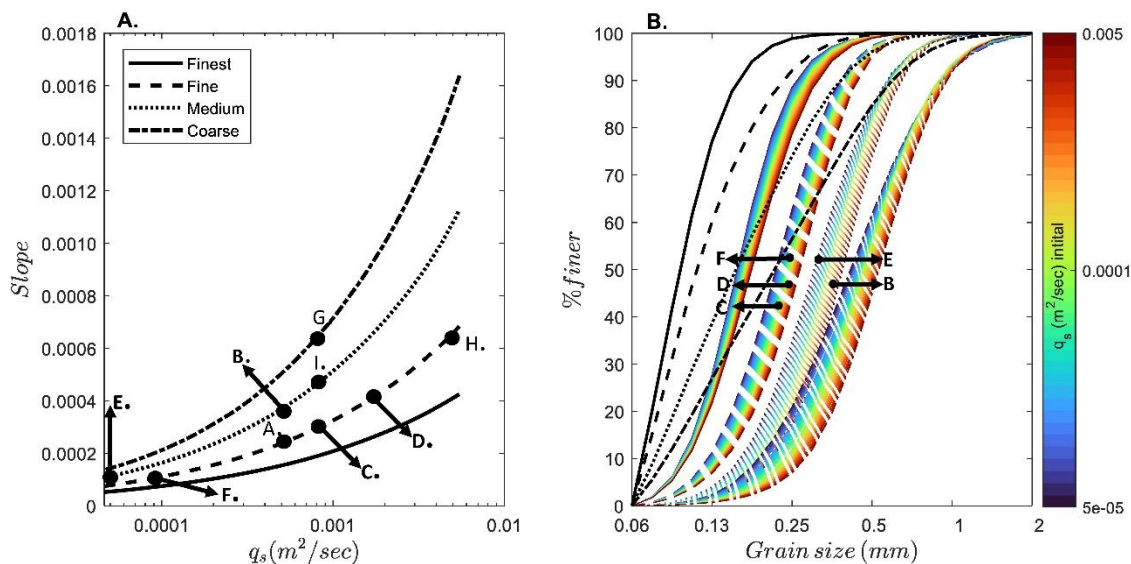
Figure 4-5. Slope transport relation for mixed-size sediment of a fixed grain size distribution. (A) Slope transport relation for a fixed transport grain size with unit discharge (qw) set to 3 (m^2/sec). Line patterns correspond to different transport compositions (i.e., finest, fine, medium, and coarse). (B) Bed material grain size needed to maintain a fixed transport composition with increasing transport rate. Black lines are the fixed transport grain size for each composition. Colored lines show how the bed grain size distribution evolves with increasing transport. Cooler colors correspond to smaller transport rates and warmer colors to larger transport rates. The line patterns for the black and colored grain size distributions distinguish between the different transport compositions shown in (A). Points in (B) are the bed grain size distribution of the transport rates shown as points in (A).

response will be bed fining and depending on the increase in supply rate compared to the amount of fining, the slope may aggrade, degrade, or remain constant. How fast the textural change happens relative to the topographic slope response matters, because the new steady-state may not be fully reached before the drivers change again. A change in bed texture is likely to happen quickly, which can reduce the amount of aggradation or induce degradation. If the immediate response is a bed textural change and aggradation (or degradation) takes much longer, the risk of flooding or damage to infrastructure might not be a management issue for some time. Or, if the supply increase is only temporary, bed textural changes might be the only response, alleviating management concerns.

We use 4 transient runs to evaluate the pace and extent of textural and topographic adjustment when the supply increases and the grain size fines or coarsens at a constant discharge. The initial condition for each run was set to the steady-state condition for the medium supply rate and grain size. The sediment supply rate is increased by an order of magnitude, from 0.0005 m^2/sec (medium) to 0.005 m^2/sec (large). We keep the supply grain size constant for one run, coarsen the supply for another run (from the medium to coarse composition), and fine the supply for two runs (from the medium to finest and the medium to fine composition).

Greater than 60% of the load is transported in suspension for all steady-state conditions, and at the largest supply rate, greater than 80% of the load is transported in suspension. Although suspended load dominates, both suspended and bed load contribute to the steady-state bed grain size and slope through size-selective transport. Thus, we examine how both transport modes influence the result.

We evaluate the effect of bed and suspended load transport on bed grain size and slope using a subset in which only the suspended load relation was used for transport. We find that the steady-state bed grain size is coarser when transport is calculated using the suspended load relation compared to when the loads are mixed, because the suspended load is more size-selective and transport is dominated by the finest sizes (Figure 4-6). Thus, it is necessary to have more coarse grains on the bed surface to match the transport grain size. The steady-state slope is steeper for the suspended load condition, because bed load transport predicted from the Wright and Parker (2004b) entrainment function at 5% of the flow depth is at least 2 orders of magnitude smaller than transport predicted from the Ashida and Michiue (1972) bed load relation, so more slope is needed to produce the

same transport (Figure 4-6). The difference between the steady-state slope for the

suspended load relation compared to the mixed load relation decreases with transport for

two reasons (Figure 4-6B). First, the effect of the bed load function wanes with

increasing transport because more of the load is carried in suspension. Second, the bed

coarsens with transport for the mixed load causing the slope to increase at a faster rate.

The bed grain size hardly changes with transport for the suspended load, because the

entrainment rate is fixed.
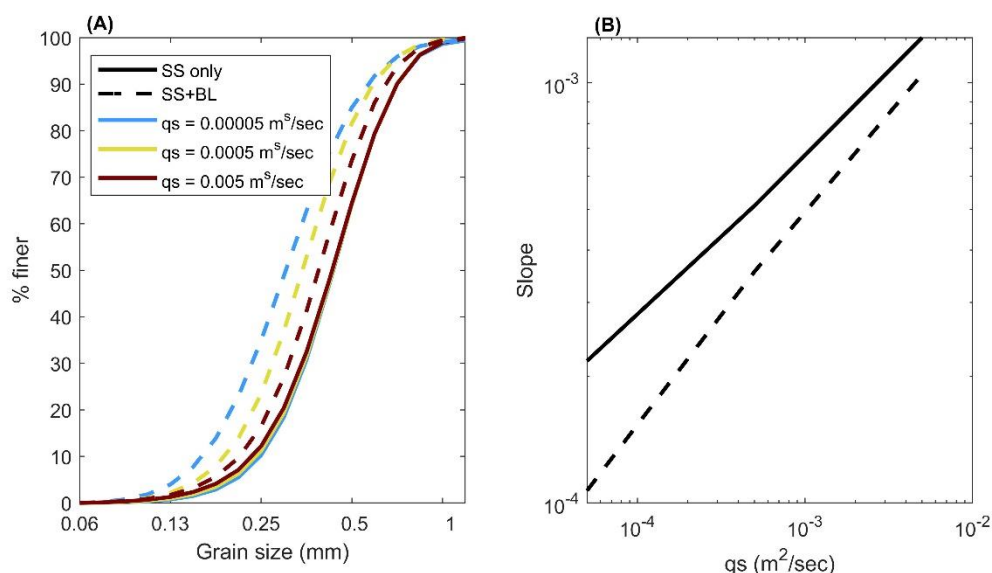
Figure 4-6. Comparison of steady-state bed grain size (A) and slope (B) with increasing
transport when only the suspended load relation (SS) is used to calculate transport and
when the suspended and bed loads are mixed (SS+BL).

When both the bed and suspended load are considered together, an increase in

supply rate induces bed sorting waves that propagate downstream. The behavior of the

bed sorting waves and their interaction with bed topography, both in time and distance

downstream, depend on the direction and magnitude of the change in the steady-state

slope and grain size. If the final bed state is considerably finer and steeper than the

original state, we find that an immediate phase of bed fining is followed by slower,

gradual aggradation, coupled with bed coarsening that eventually brings the system into the new steady-state condition. Such was the case when the supply rate increased by an order of magnitude and changed from medium to fine grain size. Very fine and fine sand pulses initially cause the bed to become finer than the steady-state condition, and the total transport capacity approaches 54% of the incoming supply, even though the slope increase is only 14% of the new steady-state condition (Figure 4-7 D-F). A small depositional wedge forms as the fine sand pulse moves downstream, and very fine sand winnows from the bed. As bed aggradation continues, pulses of coarser sand move downstream as bed load at an increasingly slower rate (Figure 4-7 D). With each consecutive sorting wave, the bed grain size and bed slope adjust towards the new steady-state condition. The coarsest sand sizes are the last to reach equilibrium.

If the final bed state is only somewhat finer and steeper than the original state, phases of bed fining and coarsening are accompanied by aggradational and degradational waves. Such was the case when the supply rate increased by an order of magnitude and fined from the medium to finest grain size. Although the new steady-state slope is only 1.08 times the original slope, the path to the new steady-state condition was complex. The slope initially over steepens and bed grain size initially over fines as the pulse of very fine and fine sand move downstream (Figure 4-7 A-C). The pulse of very fine sand almost instantaneously transports through the reach, causing substantial bed fining and increasing the total transport capacity to ~75% of the new supply rate with little change in bed slope. The bed slope initially over steepens as fine sand moves downstream, initiating a degradational wave that ultimately brings this sand size into equilibrium. Although the total transport capacity reaches 95% of the new supply rate in 20 days, it

takes ~530 days for fractional transport rates to reach the new steady-state condition, because the slope must aggrade for the coarse fraction of the supply to reach equilibrium.

A larger fraction of the total adjustment is accomplished by slow, long-term aggradation when the final bed state is coarser and considerably steeper. In the simulation where the supply rate increases and the grain size remains constant, the final bed slope is 2.8 times steeper and the bed slightly coarser. The initial phase of bed fining only increases the transport capacity to 28% of the incoming supply (Figure 4-7 G-I). It takes 300 days for the slope to aggrade to a transport capacity that is 95% of the incoming supply, which is twice as long as when the final bed state was finer and slightly less steep. The longer, slower adjustment between bed slope and bed texture is caused by a larger fraction of the supply necessitating a steeper slope, which takes time to aggrade. When the final bed state is even coarser, such as when the supply rate increased and coarsened, it takes even longer (an additional 91 days) for the slope to aggrade to a transport capacity that is 95% of the supplied sediment, because there is an even larger supply of coarser sand that necessitates higher shear stress to transport (Figure 4-7 J-L). The initial phase of bed fining does less to increase the transport capacity (transport capacity is only increased to 18% of the supply through bed fining) because fewer fine grains are in the new supply.

We observe that, under the right conditions, the system can achieve a transport capacity that is a large fraction of the new sediment supply rate long before the system has reached full equilibrium. That is, early in the transient response, bed elevation and bed surface grain size adjustment may be only a fraction of their eventual steady-state values, but in combination provide a transport capacity that is a large fraction of the new
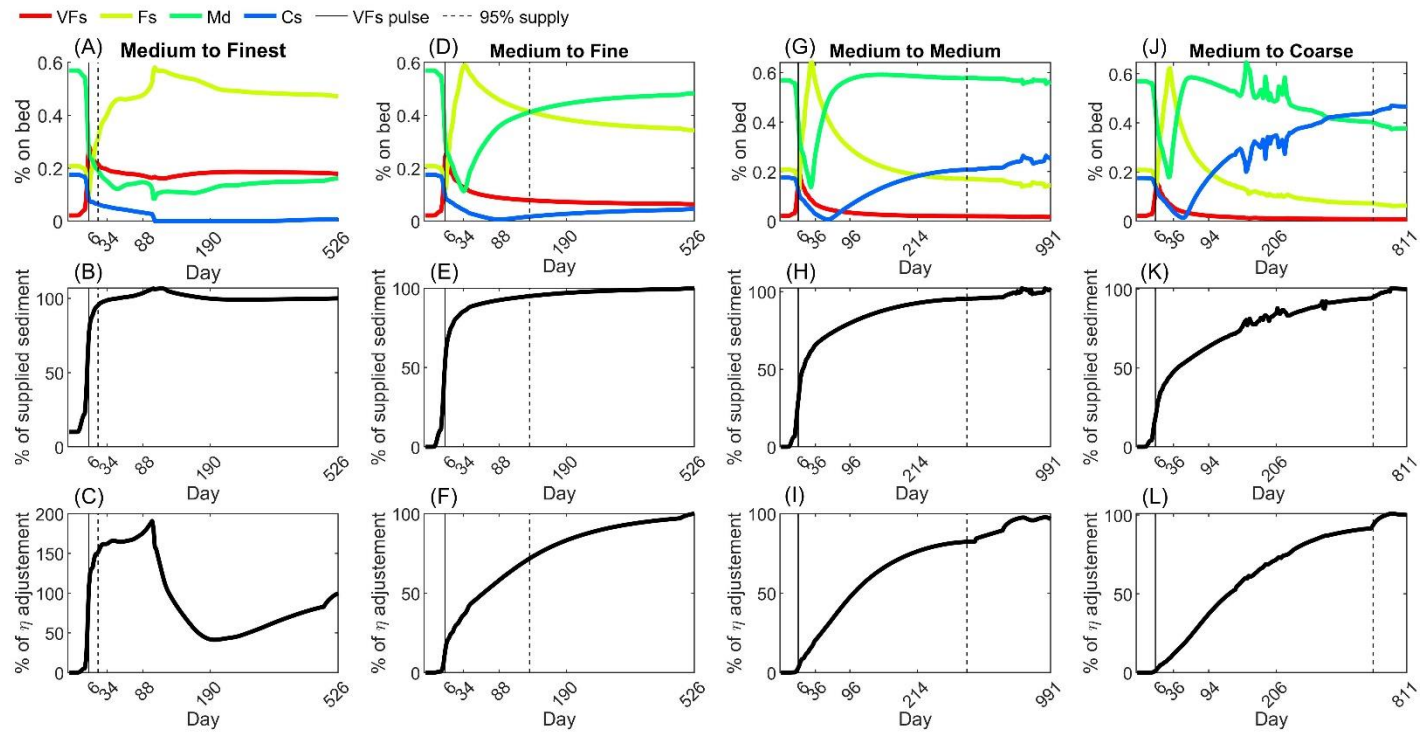
Figure 4-7. Summary of transient textural and topographic response at the downstream end (7.5 km) of the modeling reach. Each run was started at the medium supply rate and grain size steady-state condition. The supply rate increased by an order of magnitude in each run and the supply grain size fined (A-C and D-F), remained constant (G-I), or coarsened (J-K). The top row tracks the change in sand fractions on the bed through time. The middle row shows the total load transport rate as a function of the percent of upstream supply through time. The bottom row shows the percent of the total topographic adjustment. Solid black vertical lines on each plot shows when the very fine sand pulse moved through the cross-section and dashed vertical lines indicate when the total transport rate had adjusted to 95% of the upstream sediment supply.

sediment supply rate. This phenomenon may limit the initial topographic response of the

river bed. Complete adjustment of the coarsest fraction in the bed and an accompanying

full adjustment of bed slope can take much longer. When the supply grain size is

constantor coarsens, the initial phase of bed fining is less effective at increasing the

transport capacity, and slower, longer topographic changes are necessary to move the

supplied sediment downstream.

The transport rate, transport grain size, and bed grain size are closely linked in

sand-bed rivers. When stress is fixed, bed coarsening causes a reduction in concentration

and an increase in transport grain size, such that concentration varies inversely with

transport grain size (Rubin and Topping, 2001). Some combination of change in stress

and bed texture affects concentration when the concentration and transport grain size are

positively correlated. In our model, discharge is fixed, so stress only changes through bed

aggradation and degradation which changes water depth ad bed roughness. We use the

relation between concentration and transport grain size to infer the influence of bed

texture and bed topography on the total adjustment along the path to the new steady-state.

We find that concentration varies inversely with transport grain size for the first 1-2 days

regardless of the supply grain size, and bed fining is solely responsible for the increase in

transport during this time. Bed fining is so small that only the 2nd percentile (D_{02}) of the

bed grain size distribution reduces in size, and there is no change in the median (D_{50}) bed

grain size (Figure 4-8). After the first couple of days, the bed begins to aggrade as very

fine sand accumulates, and this causes a change in stress leading to a positive relation

between concentration and transport grain size. However, the majority of the increase in

transport is still driven by bed textural change during this time. The tail end of the very

fine sand pulse reaches 7.5 km downstream in 6 days, regardless of the supply grain size (Figure 4-8). After the pulse of very fine sand passes, bed texture and slope mutually adjust until the transport rate is approximately 95% of the incoming supply. This phase of adjustment takes longer with more supply coarsening, because the slope must aggrade more to transport the coarser fraction of the supply. The bed is almost fully adjusted after the transport rate reaches 95% of the supply, and transport is driven predominately by slope adjustment.

5. Discussion

5.1. Using transport measurements to make inferences about bed texture in sand bed rivers

The bed texture response to a change in sediment supply is rarely measured on sand-bed rivers, even though bed grain size has a strong influence on transport capacity, and the adjustment between transport and bed grain size is the key determinant as to whether channel topographic response to changes in input is large or small. In place of field measurements, Rubin and Topping (2001) developed an alternative approach to infer bed grain size change from measurements of suspended sediment concentration (Cs) and transport grain size (Ds). These measurements are more commonly collected on sand bed rivers. Bed textural changes are responsible for changes in transport when Cs and Ds are inversely correlated and a mutual adjustment between bed texture and morphodynamic changes cause the transport to change when Cs and Ds are positively correlated (Rubin and Topping, 2001; Rubin et al., 2020).

The relation between Cs and Ds in our morphodynamic modeling is consistent with the findings of Rubin and Topping (2001). The controlled nature of our numerical
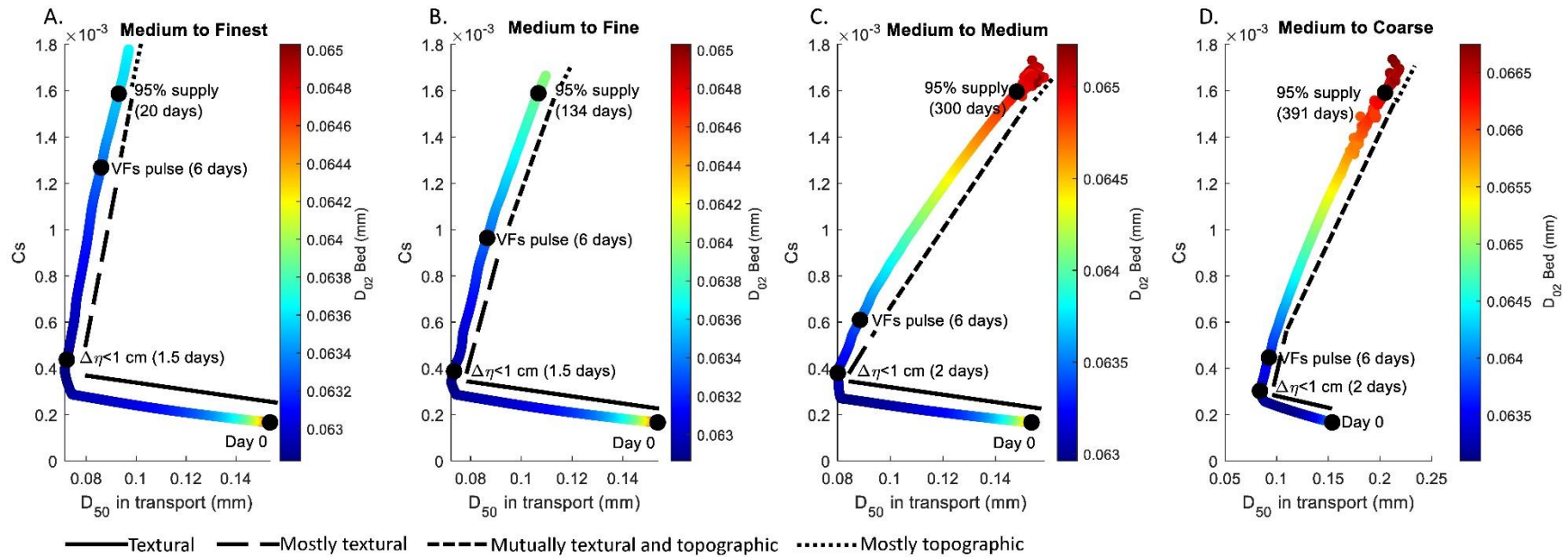
Figure 4-8. Variation in suspended sediment concentration as a function of transport grain size at 7.5 km downstream when the supply increases by an order of magnitude and the supply grain size fines (A and B), coarsens (D), or remains constant (C). Colors show a change in the fine tail of the bed grain size distribution (D02) as a function of Cs and Ds. Black dots show the progression of time through the modeling run. Δη<1cm shows when bed aggradation exceeded 1 cm. VFs show when the very fine sand pulse moved through the cross-section. 95% supply shows when transport had adjusted to 95% of the incoming supply. Black solid and patterned lines indicate periods when the adjustment was completely textural, mostly textural, both textural and topographic, and mostly topographic

experiments gives further insights into the temporal variation of Cs with Ds in response to a change in sediment supply. Cs and Ds are inversely related, such that transport is solely controlled by bed texture for a very short period. In our modeling, as little as 1 cm of bed aggradation causes stress to change and Cs is positively correlated with Ds (Figure 4-8). Furthermore, we show that Cs and Ds are positively correlated even when bed fining dominates the adjustment. In our model, stress changes through bed aggradation or degradation, but in real sand bed rivers, other morphological changes can affect stress, leading to a positive relation between Cs and Ds; such as local or large-scale changes in sediment storage or changes in bedform geometry (Rubin et al., 2020). Our modeling results suggest that even a small morphological adjustment is enough to cause a positive correlation between Cs and Ds, even if bed textural change still dominates transport.

5.2. Limitations of the modeling approach

Our numerical modeling approach allowed us to evaluate transport dynamics isolated from other complicating factors. How well the model mimics what happens in real rivers depends on the extent the governing equations capture relevant hydraulic, transport, grain size sorting processes, and feedbacks in the field. Among the processes not modeled are those producing sediment exchange between the channel and floodplain. Finer sand is carried higher in the water column and preferentially stored in the floodplain. Preferential sequestering of finer sand in the floodplain rather than on the channel bed may limit bed fining (Nanson, 1980; Brakenridge, 1984; Nanson, 1986; Allred and Schmidt, 1999; Moody et al., 1999; Page et al., 2003; Grams and Schmidt, 2005; Thayer and Ashmore, 2016; Walker et al., 2020). This suggests our model may overestimate how much bed fining influences aggradation in rivers where the channel is

highly coupled to the floodplain. Similarly, our model does not account for the development of inset floodplains that partially sequester finer grain sand and potentially limit the amount of bed fining (Nanson, 1980; Brakenridge, 1984; Nanson, 1986; Allred and Schmidt, 1999; Moody et al., 1999; Grams and Schmidt, 2002; Page et al., 2003; Dean and Schmidt, 2011; Thayer and Ashmore, 2016; Dean et al., 2020; Walker et al., 2020).

The active layer model has a strong effect on the evolution of the bed grain size under transient conditions but no effect on the final steady-state. A key component of a mixed-sized morphodynamic model is the thickness and behavior of the bed surface that immediately interacts with the flow and through which size-selective transfer of sediment from the active layer to the subsurface occurs when the bed aggrades. We use a 2-layer model that exchanges sediment between the active and substrate layers through an interface layer (Hirano, 1971). During aggradation, the size distribution of sediment passed to the subsurface is a mixture of sediment in transport and the active layer. Parameter C in Hoey and Ferguson (1994) controls the ratio of transport and active layer sediment that passes to the interface layer. Research on gravel-bed rivers suggests C varies between 0.8 and 0.7 (Toro-Escobar et al., 1996; Viparelli et al., 2010), but there are no experimental results for sand-bed rivers (An et al 2020). Wright and Parker (2005a) suggest C be set to zero because the downward movement of sediment in transport is impeded by a narrow grain size distribution and a thick active layer. We follow Wright and Parker (2005a) and set C to zero, but explore the influence of C on model results in a subset of runs in which C varies between 0.1 to 0.6.

We find that the active layer adjusts more slowly when C is large. It takes longer to reach steady-state, because the active layer grain size is less sensitive to how the transport grain size changes. When C is small, the active layer responds quickly to transport grain size, and bed texture has a stronger influence on transport, reducing the time to steady-state. The selection of C can have an important effect on the path to steady-state, and future investigation on this parameter is warranted (An et al., 2020; Wright and Parker, 2005a).

Sorting in the active layer and the active layer thickness influences the pace of the texture response (Ribberink, 1987; Blom et al., 2003; Blom and Parker, 2004; Blom et al., 2008). Downward sorting in the active layer arises from coarser grains avalanching down the lee face of dunes, which can form a coarse armor layer that is occasionally exposed to the flow by relatively deep bedform troughs (Kleinhans, 2002, 2004; Blom et al., 2003). The active layer in our morphodynamic model neglects this sorting process and fully mixes at each timestep. Again, this does not affect the steady-state solution, but it does increase how quickly bed texture adapts to the new incoming supply. The active layer thickness in our model is set to a uniform bedform height and calculated as a function of the flow depth (Julien and Klaassen, 1995). In reality, the bedform height may vary and the depth may be limited by a coarse armor layer. If the active layer thickness is overpredicted, the model may adjust the bed texture more slowly than what happens in real rivers.

During bed degradation, the interface layer grain size becomes the substrate grain size, and material from the substrate is passed to the active layer. Bed degradation occurs when the change in steady-state slope is small and the path to equilibrium involves an

aggradational/degradational wave (Figure 4-7). During aggradation, active layer material is passed to the substrate, but our model does not save new substrate layers, and the substrate grain size is fixed (Viparelli et al., 2010a). The result is that the substrate layer is coarser during the degradational cycle than if new substrate layers were saved. Eroding into a coarser substrate causes faster, more pronounced bed coarsening in the active layer (An et al., 2020), which likely limits degradation in our model.

5.3. Implications for real rivers

There is a wide range of channel adjustments that can occur in response to an increase in sediment supply depending on how the supply grain size changes. Figure 4-9 summarizes the slope response as a function of supply rate increase and supply grain size change. The sediment mass balance is likely degradational when the supply D_{50} decreases by 0.01 mm and the rate increase is less than a factor of 6, but aggradation will occur if the supply D_{50} remains constant or coarsens by 0.01 mm. At first, the finding that a river may evacuate sediment in response to an increase in supply might seem peculiar or even impossible. However, if the supply grain size sufficiently fines, the bed textural response can increase the transport capacity beyond the new supply rate, pushing the mass balance into deficit. A given increase in supply can have a vastly different morphological response depending on whether the supply grain size fines or coarsens. An increase in the supply rate by an order of magnitude will cause the slope to aggrade by 0.0005, but the slope increase will be double that if the supply coarsens by only 0.15 mm or aggradation can be completely reversed if the supply fines by 0.15 mm (Figure 4-9).
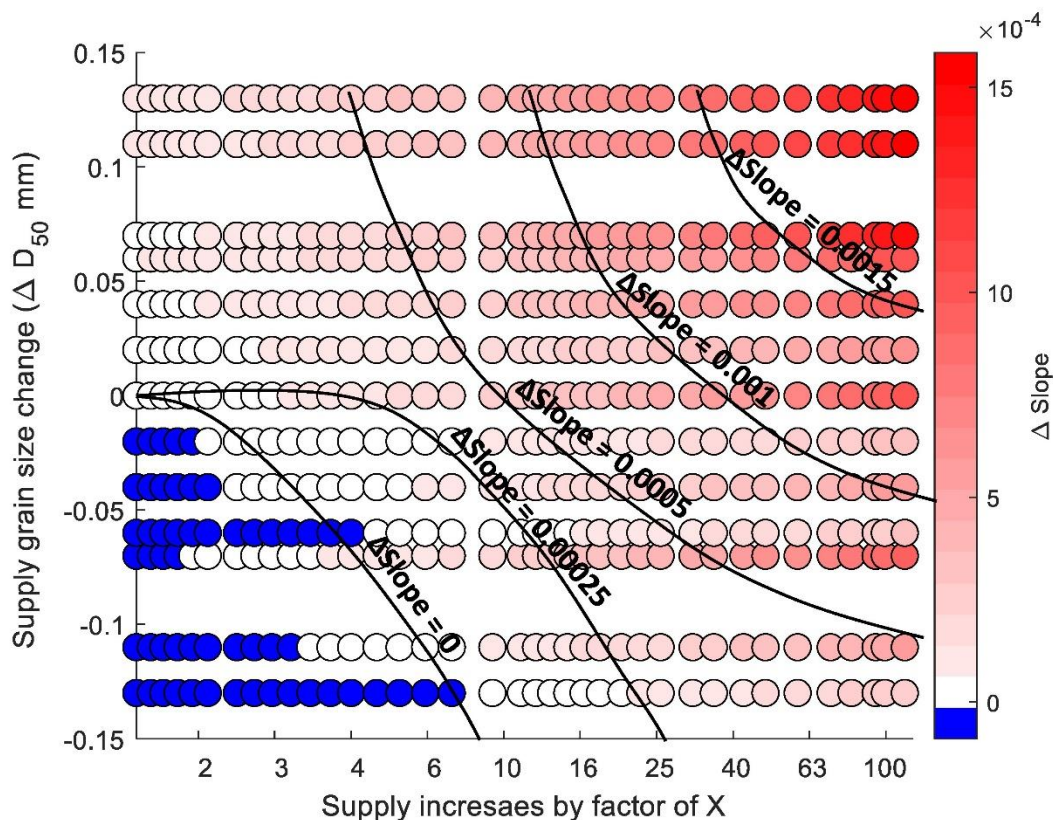
Figure 4-9. Change in steady-state slope (ΔSlope) as a function of change in the supply median grain size (ΔD$_{50}$) and supply increase. The slope lowers in blue zones, aggrades in red zones, and there is no slope change in white zones. Contours of ΔSlope are fit by eye.

The effect of supply grain size on the sediment mass balance in Figure 4-9 provides a context for understanding why channel response to an increased sediment supply may be large in some field settings and small in others. Two small dam removal projects on similar rivers in Wisconsin had a dramatically different downstream channel response depending on whether the grain size of sediment eroded from the upstream reservoir was mud and fine sand or coarser sand (Doyle et al., 2003). When the style of reservoir head-cutting prohibited access to sand, there were few changes in the downstream channel morphology. Our results suggest aggradation was minimized by bed

fining. There was a clear change in channel morphology when sand was eroded from the reservoir, because the supply coarsened and the mass balance shifted towards aggradation.

A common condition is that the supply rate increases and fines (e.g., volcanic eruptions, wildfires, and land use changes). A key question under these conditions is whether bed fining may offset bed aggradation from the increased sediment supply. Figure 4-9 can help guide management decisions by identifying combinations of supply rate increase and fining that produce a minimal morphologic adjustment. For example, reservoir flushing or sluicing operations might target a supply rate increase that is balanced by an increase in transport capacity from bed fining based on how the supply grain size is expected to change (Kondolf et al., 2014; Randle et al., 2021). Such a procedure would reduce the downstream risk of flooding and damage to infrastructure. Similarly, dam decommissioning might be planned in stages of removal based on the expected grain size of the sediment eroded from the upstream reservoir through time to limit the threat of downstream aggradation (e.g., Wilcox et al., 2014; East et al., 2015; Harrison et al., 2018).

The mutual adjustment between bed texture and slope should be considered at the spatial scale the problem is defined. For example, the local slope and bed grain size at tributary junctions is adjusted to transport the flow and sediment supplied by the tributary. As a result, different morphological conditions occur at tributary junctions than the reach upstream and downstream (Benda et al., 2004). If the tributary supply slightly increases and fines, say because of a wood jam release or beaver dam blowout, our steady-state results indicate conditions of sediment deficit are likely (Figure 4-9).

However, the bed slope and grain size may only adjust at the tributary junction and the reach averaged slope may not change. Other times, supply increases may occur over large sections of the watershed, such as when grazing or agricultural practices change, and textural and topographic adjustments may occur throughout the system. Thus, it is important to consider the spatial scale of the response in addition to the interaction between the supply grain size and bed texture in real rivers.

5.4. Texture and topography conceptual model

A change in water and sediment supply can produce changes in bed texture or cause sediment accumulation or evacuation. Their mutual adjustment can be complex, varying over time as the system approaches a new steady-state. Our modeling results indicate that patterns of adjustment can be defined, depending on the magnitude of the supply increase and whether the supply becomes finer or coarser (Figure 4-10). Conditions of sediment surplus are often assumed when the sediment supply to a river increases and the expected channel response may include bed aggradation, channel narrowing, floodplain accretion, increase in avulsion frequency or migration, or change in planform. Our results indicate that bed textural changes complicate this assumption and conditions of sediment deficit, surplus, or little to no change in the sediment mass balance are all possible outcomes depending on how the supply grain size changes relative to the supply rate (Figure 4-10). Our modeling shows there is an initial pulse of very fine sand that quickly fines the bed and increases transport whenever the supply rate increases regardless of the supply grain size. This phase of bed fining has a large effect on transport when the supply fines, increasing the total transport to greater than 75% of the incoming supply. The mass imbalance (i.e., the difference between sediment influx and efflux) is

relatively small for most of the adjustment period which limits sediment accumulation early in the response and minimizes short-term morphologic change. This kind of response has been observed on the Colorado River in Grand Canyon immediately following tributary floods that fine the bed and increase transport by greater than a factor of 20, reducing the amount of time sediment is stored in the canyon (Topping et al., 2021).

If the supply is sufficiently finer than antecedent conditions, the initial bed fining phase can increase transport beyond the incoming supply, such that slow, long-term sediment evacuation reduces transport to the new steady-state. The amount of evacuated sediment is likely to be relatively small and potentially undetectable with modern surveying equipment, because conditions of sediment deficit only occur when the supply increase is very small. For example, maximum bed degradation is two orders of magnitude smaller than the maximum amount of aggradation in our modeling.

The initial phase of bed fining is less effective at increasing transport when the supply coarsens and morphologic adjustment is immediate. This response was observed downstream of Spenser Dam on the Niobrara River during a 4-week reservoir flushing event where sand accumulation led to the formation of large sandbars (Shelley et al., 2022). Our modeling suggests that had the supply increase from the dam been permanent, bed coarsening would enhance downstream sand accumulation.

There are numerous case studies where the supply rate increases and fines, but the influence of bed textural adjustment makes the channel response variable and difficult to predict. On the Colorado River in Grand Canyon, a tributary episodically supplies finer sand that migrates downstream and fines the bed (Topping et al., 2000a, 2007). Because

the increase in sand supply is caused by flash floods of very short duration, stored sand

on the channel bed is quickly exported from the canyon (Figure 4-10; Topping et al.,

2000; Rubin et al., 2020; Topping et al., 2021).
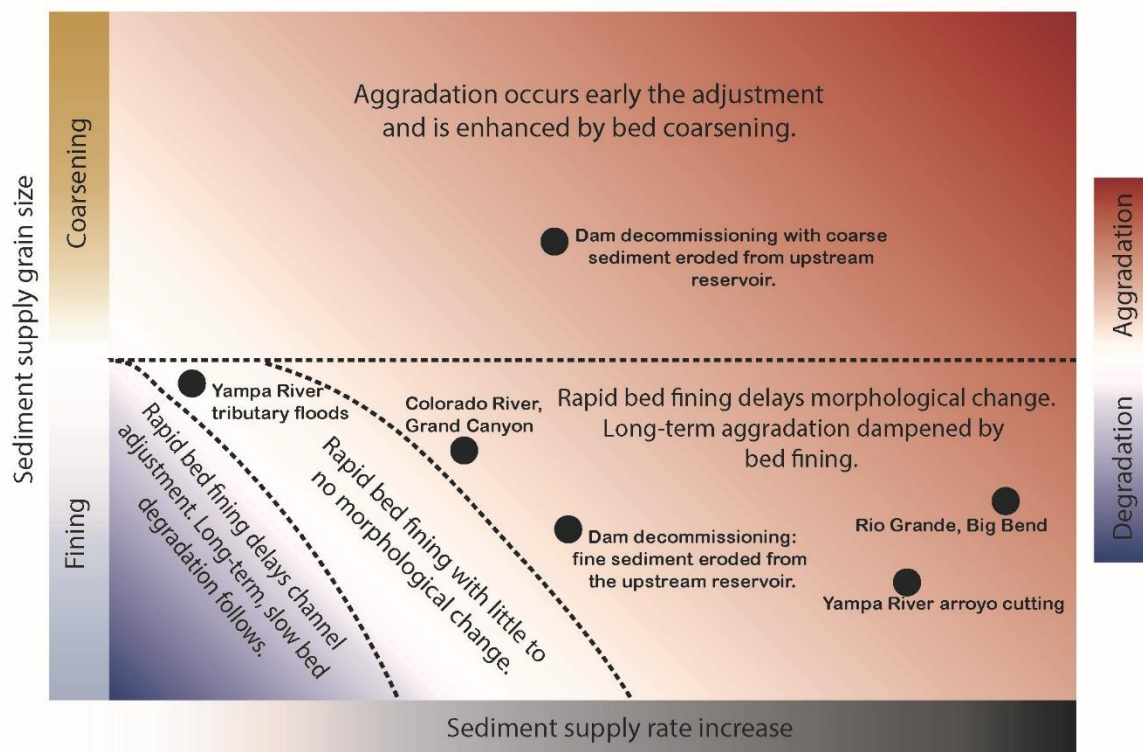
Figure 4-10. Conceptual model for the interaction between texture and sediment accumulation and evacuation when the supply rate increases and the supply grain size fines or coarsens.

The texture-dominated phase of bed fining limits sediment accumulation in

alluvial sand-bed rivers as well. Tributary floods to the Little Snake River, Colorado

during the late-1950s and early 1960s caused a temporary increase and fining of the

sediment supply on the Yampa River (Figure 4-10; Topping et al., 2018). Measurements

of sediment transport suggest the supply of sediment caused short-term bed fining

followed by long-term bed coarsening on the Yampa River (Topping et al., 2018), but

there was no evidence of sand accumulation, such as channel narrowing (Merritt and

Cooper, 2000).

When the supply increase is large and sustained, accumulation after the initial

phase of fining can cause significant morphological change (Figure 4-10). On the Rio

Grande River in the Big Bend region of New Mexico, sediment from tributary flash

floods accumulates in the mainstem channel, forming inset floodplains that narrow the

channel and increase transport capacity (Dean and Schmidt, 2011; Dean et al., 2016).

Significant channel narrowing has also occurred on Coon Creek, Wisconsin as the result

of a widespread increase in supply caused by the clearing of forests for agricultural

purposes (Trimble, 1983).

The conceptual model presented here defines patterns of adjustment when the

flow rate is fixed and the supply increase is permanent. In real rivers, both the flow and

sediment supply often change together and may change again before the system reaches

steady-state. Numerical modeling indicates that bed texture does not change with the

flow rate when the supply is fixed and the response is completely topographic (Blom et

al., 2016). When the flow and supply rate change, the response will be a combination of

texture and topography. In the following sections, we use the conceptual model in Figure

4-10 to make inferences about the patterns of adjustment when both flow and supply rate

change.

In the case where the supply increases and fines and the flow rate changes, the

zone of degradation, aggradation, and no change in sediment storage in Figure 4-10 will

shift left or right depending on whether the flow rate increases or decreases. When the

flow decreases, the increase in transport capacity caused by bed fining will be offset by a

decrease in transport capacity from flow reduction. This means it is less likely that the bed will degrade and the zone of degradation in Figure 4-10 will shrink and shift left. Similarly, the condition of little to no change in sediment storage will shift left toward smaller supply rates. Bed fining will be less effective at reducing the amount of aggradation, and the slope will be steeper than if the flow rate was fixed. If both the flow and supply rate increase and the supply grain size fines, the increase in transport capacity by bed fining will be enhanced by a larger flow. The zone of bed degradation will expand and shift right towards larger supply rates. When sediment does accumulate, the amount of deposition may be comparatively small because the transport capacity is increased by bed fining and a larger flow rate.

In the case where the supply rate increases and coarsens and the flow rate changes, there is the potential for aggradation, degradation, or little to no change in storage depending on whether the flow increases or decreases. If the flow rate increases, the decrease in transport capacity by bed coarsening is offset by an increase in transport capacity from a larger flow. In this case, there is the potential for bed degradation when the flow increase is large and the supply increase is small. There is also the potential that little to no aggradation or degradation may occur if the flow increase is balanced by a decrease in transport capacity from bed coarsening. Flow reduction coupled with an increase in supply that is of a coarser grain size will always cause sediment to accumulate, but the amount of accumulation will be further enhanced by the combined decrease in transport capacity caused by flow reduction and bed coarsening.

6. Conclusion

This study uses mixed-sized transport models to evaluate the mutual adjustment between bed texture and bed topography in sand-bed rivers. The transport rate, transport grain size, and bed grain size are closely linked, such that an increase in sediment supply can result in bed fining or coarsening depending on how the supply grain size changes relative to the supply rate. The bed textural response can *dampen* or *enhance* the extent of sediment accumulation or evacuation leading to more or less morphological adjustment. The bed grain size fines when the supply rate increases and fines. Bed fining increases transport and *dampens* the slope increase needed to transport the new supply rate. In real rivers, this equates to a smaller morphologic change and the primary adjustment may be small changes in the grain size of sand on the channel bed which is of little management concern. When the supply grain size increases and coarsens, the bed grain size coarsens which reduces transport and *enhances* the slope increase needed to transport the new supply rate. In the field, this equates to a higher probability of significant morphologic change that can impact downstream flooding and damage infrastructure.

Bed textural changes also affect the path to steady-state, which is important because, in real rivers, the new steady-state condition may never be reached before watershed drivers change again. Early in the response, the bed grain size rapidly fines as a pulse of very fine sand moves through the system and transport quickly increases. When the supply grain size fines, the texture-dominated phase of bed fining brings the total mass balance close to equilibrium, which limits short-term aggradation. If the supply increase is temporary, such as in the case of dam removal or tributary flooding, aggradation may never occur because bed textural changes alone are sufficient to

transport the initial pulse of sediment through the system. From a management perspective, the increase in supply may have little to no effect on downstream flooding or infrastructure. When the supply grain size coarsens, the initial phase of bed fining is less effective at increasing transport, because fewer finer grains are in the supply, and aggradation happens more quickly. This means there might be a more immediate risk of flooding or damage to infrastructure that necessitates management interventions.

The bed textural response to changes in sediment supply is well-documented in gravel-bed rivers where bed sorting is easily observed. There has been less attention to the bed textural changes in sand-bed rivers where bed sorting is less apparent. The results of this study show the bed textural change can have a large effect on the sediment mass balance, which has important implications for forecasting and managing the channel response. Our results indicate that conditions of sediment deficit, surplus, or little to no change in the sediment storage are all possible outcomes when supply increases depending on how the supply grain size affects the bed texture. Therefore, it is inappropriate to assume that a disturbance will result in certain morphologic adjustments unless the interaction among the supply rate, supply grain size, and bed texture is considered.

References

Ahammad M, Czuba JA, Pfeiffer AM, Murphy BP, Belmont P. 2021. Simulated Dynamics of Mixed Versus Uniform Grain Size Sediment Pulses in a Gravel-Bedded River. Journal of Geophysical Research: Earth Surface **126** : e2021JF006194. DOI: 10.1029/2021JF006194

Allred TM, Schmidt JC. 1999. Channel narrowing by vertical accretion along the Green River near Green River, Utah. GSA Bulletin **111** : 1757–1772. DOI: 10.1130/0016-7606(1999)111<1757:CNBVAA>2.3.CO;2

An C, Gong Z, Naito K, Parker G, Hassan MA, Ma H, Fu X. 2021. Grain Size-Specific Engelund-Hansen Type Relation for Bed Material Load in Sand-Bed Rivers, With Application to the Mississippi River. Water Resources Research **57** : e2020WR027517. DOI: 10.1029/2020WR027517

Arbós CY, Blom A, Viparelli E, Reneerkens M, Frings RM, Schielen RMJ. 2021. River Response to Anthropogenic Modification: Channel Steepening and Gravel Front Fading in an Incising River. Geophysical Research Letters **48** : e2020GL091338. DOI: 10.1029/2020GL091338

Ashida K, Michiue M. 1972. Study on Hydraulic Resistance and Bedload Transport Rate in Alluvial Streams. Trans. Jpn. Soc. Civil Engng. **206** : 59–69.

Borland WM. 1960. Stream channel stability. United States Bureau of Reclamation. Denver

Brakenridge GR. 1984. Alluvial stratigraphy and radiocarbon dating along the Duck River, Tennessee: Implications regarding flood-plain origin. GSA Bulletin **95** : 9–25. DOI: 10.1130/0016-7606(1984)95<9:ASARDA>2.0.CO;2

Brandt SA. 2000a. Classification of geomorphological effects downstream of dams. CATENA **40** : 375–401. DOI: 10.1016/S0341-8162(00)00093-X

Brandt SA. 2000b. Prediction of downstream geomorphological changes after dam construction: A steam power approach. International Journal of Water Resources Development; Abingdon **16** : 343.

Buffington JM, Montgomery DR. 1999. Effects of sediment supply on surface textures of gravel-bed rivers. Water Resources Research **35** : 3523–3530. DOI: 10.1029/1999WR900232

Clark JJ, Wilcock PR. 2000. Effects of land-use change on channel morphology in northeastern Puerto Rico. GSA Bulletin **112** : 1763–1777. DOI: 10.1130/0016-7606(2000)112<1763:EOLUCO>2.0.CO;2

Colby BR, Hembree CC. 1955. Computations of total sediment discharge of the Niobrara River near Cody, Nebraska. USGS Water Supply Paper 1357 . USGS Washington

Cui Y, Paola C, Parker G. 1996. Numerical simulation of aggradation and downstream fining. Journal of Hydraulic Research **34** : 185–204. DOI: 10.1080/00221689609498496

Cui Y, Parker G, Lisle TE, Gott J, Hansler-Ball ME, Pizzuto JE, Allmendinger NE, Reed JM. 2003. Sediment pulses in mountain rivers: 1. Experiments. Water Resources Research **39** DOI: 10.1029/2002WR001803

Cui Y, Parker G, Lisle TE, Pizzuto JE, Dodd AM. 2005. More on the evolution of bed material waves in alluvial rivers. Earth Surface Processes and Landforms **30** : 107–114. DOI: 10.1002/esp.1156

Curran JC, Wilcock PR. 2005. Effect of sand supply on transport rates in a gravel-bed channel. Journal of Hydraulic Engineering **131** : 961–967.

Dean DJ, Schmidt JC. 2011. The role of feedback mechanisms in historic channel changes of the lower Rio Grande in the Big Bend region. Geomorphology **126** : 333–349. DOI: 10.1016/j.geomorph.2010.03.009

Dean DJ, Schmidt JC. 2013. The geomorphic effectiveness of a large flood on the Rio Grande in the Big Bend region: Insights on geomorphic controls and post-flood geomorphic response. Geomorphology **201** : 183–198. DOI: 10.1016/j.geomorph.2013.06.020

Dean DJ, Topping DJ, Grams PE, Walker AE, Schmidt JC. 2020. Does Channel Narrowing by Floodplain Growth Necessarily Indicate Sediment Surplus? Lessons From Sediment Transport Analyses in the Green and Colorado Rivers, Canyonlands, Utah. Journal of Geophysical Research: Earth Surface **125** : e2019JF005414. DOI: 10.1029/2019JF005414

Dean DJ, Topping DJ, Schmidt JC, Griffiths RE, Sabol TA. 2016. Sediment supply versus local hydraulic controls on sediment transport and storage in a river with large sediment loads. Journal of Geophysical Research: Earth Surface **121** : 2015JF003436. DOI: 10.1002/2015JF003436

Downs PW. 1995. Estimating the probability of river channel adjustment. Earth Surface Processes and Landforms **20** : 687–705. DOI: 10.1002/esp.3290200710

Doyle MW, Shields FD. 2000. Incorporation of bed texture into a channel evolution model. Geomorphology **34** : 291–309. DOI: 10.1016/S0169-555X(00)00014-3

Doyle MW, Stanley EH, Harbor JM. 2003. Channel adjustments following two dam removals in Wisconsin. Water Resources Research **39** DOI: 10.1029/2002WR001714

East AE et al. 2015. Large-scale dam removal on the Elwha River, Washington, USA: River channel and floodplain geomorphic change. Geomorphology **228** : 765–786. DOI: 10.1016/j.geomorph.2014.08.028

East AE, Logan JB, Dartnell P, Lieber-Kotz O, Cavagnaro DB, McCoy SW, Lindsay DN. 2021. Watershed Sediment Yield Following the 2018 Carr Fire, Whiskeytown National Recreation Area, Northern California. Earth and Space Science **8** : e2021EA001828. DOI: 10.1029/2021EA001828

East AE, Sankey JB. 2020. Geomorphic and Sedimentary Effects of Modern Climate Change: Current and Anticipated Future Conditions in the Western United States. Reviews of Geophysics **58** : e2019RG000692. DOI: 10.1029/2019RG000692

Eaton B, Millar R. 2017. Predicting gravel bed river response to environmental change: the strengths and limitations of a regime-based approach. Earth Surface Processes and Landforms **42** : 994–1008. DOI: 10.1002/esp.4058

Egiazaroff IV. 1965. Calculation of Nonuniform Sediment Concentrations. Journal of the Hydraulics Division **91** : 225–247. DOI: 10.1061/JYCEAJ.0001277

Elliott JG, Kircher JE, Von Guerard P. 1984. Sediment transport in the lower Yampa River, northwestern Colorado . US Geological Survey Water Resources Investigation Report. **84-414**.

Everitt B. 1993. Channel responses to declining flow on the Rio Grande between Ft. Quitman and Presidio, Texas. Geomorphology **6** : 225–242. DOI: 10.1016/0169-555X(93)90048-7

Ferguson RI, Church M, Rennie CD, Venditti JG. 2015. Reconstructing a sediment pulse: Modeling the effect of placer mining on Fraser River, Canada. Journal of Geophysical Research: Earth Surface **120** : 2015JF003491. DOI: 10.1002/2015JF003491

Gaeuman D, Stewart R, Schmandt B, Pryor C. 2017. Geomorphic response to gravel augmentation and high-flow dam release in the Trinity River, California. Earth Surface Processes and Landforms **42** : 2523–2540. DOI: 10.1002/esp.4191

Garcia M, Parker G. 1991. Entrainment of Bed Sediment into Suspension. Journal of Hydraulic Engineering **117** : 414–435. DOI: 10.1061/(ASCE)0733-9429(1991)117:4(414)

Gomez B, Coleman SE, Sy VWK, Peacock DH, Kent M. 2007. Channel change, bankfull and effective discharges on a vertically accreting, meandering, gravel-bed river. Earth Surface Processes and Landforms **32** : 770–785. DOI: 10.1002/esp.1424

Grams PE, Dean DJ, Walker AE, Kasprak A, Schmidt JC. 2020. The roles of flood magnitude and duration in controlling channel width and complexity on the Green River in Canyonlands, Utah, USA. Geomorphology **371** : 107438. DOI: 10.1016/j.geomorph.2020.107438

Grams PE, Schmidt JC. 2002. Streamflow regulation and multi-level flood plain formation: channel narrowing on the aggrading Green River in the eastern Uinta Mountains, Colorado and Utah. Geomorphology **44** : 337–360. DOI: 10.1016/S0169-555X(01)00182-9

Grams PE, Schmidt JC. 2005. Equilibrium or indeterminate? Where sediment budgets fail: Sediment mass balance and adjustment of channel form, Green River downstream from Flaming Gorge Dam, Utah and Colorado. Geomorphology **71** : 156–181. DOI: 10.1016/j.geomorph.2004.10.012

Gran KB. 2012. Strong seasonality in sand loading and resulting feedbacks on sediment transport, bed texture, and channel planform at Mount Pinatubo, Philippines. Earth Surface Processes and Landforms **37** : 1012–1022. DOI: 10.1002/esp.3241

Gran KB, Montgomery DR. 2005. Spatial and temporal patterns in fluvial recovery following volcanic eruptions: Channel response to basin-wide sediment loading at Mount Pinatubo, Philippines. Geological Society of America Bulletin **117** : 195–211.

Grant GE, Schmidt JC, Lewis SL. 2003. A Geological Framework for Interpreting Downstream Effects of Dams on Rivers. In A Peculiar River , O'Connor JE and Grant GE (eds). American Geophysical Union; 203–219.

Hazel JE, Grams PE, Schmidt JC, Kaplinski M. 2010. Sandbar response in Marble and Grand Canyons, Arizona, following the 2008 high-flow experiment on the Colorado River . U.S. Geological Survey Scientific Investigation Report. **2010-5015**

Henderson FM. 1966. Open channel flow . Macmillan: New York

Hirano M. 1971. On riverbed variation with armoring. Trans. Jpn. Soc. Civil Engng. **195** : 55–65.

Hoey TB, Ferguson R. 1994. Numerical simulation of downstream fining by selective transport in gravel bed rivers: Model development and illustration. Water Resources Research **30** : 2251–2260. DOI: 10.1029/94WR00556

Hoffman DF, Gabet EJ. 2007. Effects of sediment pulses on channel morphology in a gravel-bed river. GSA Bulletin **119** : 116–125. DOI: 10.1130/B25982.1

Iseya F, Ikeda H. 1987. Pulsations in Bedload Transport Rates Induced by a Longitudinal Sediment Sorting: A Flume Study using Sand and Gravel Mixtures. Geografiska Annaler: Series A, Physical Geography **69** : 15–27. DOI: 10.1080/04353676.1987.11880193

Julien PY, Klaassen GJ. 1995. Sand-Dune Geometry of Large Rivers during Floods. Journal of Hydraulic Engineering **121** : 657–663. DOI: 10.1061/(ASCE)0733-9429(1995)121:9(657)

Knighton AD. 1989. River adjustment to changes in sediment load: The effects of tin mining on the Ringarooma River, Tasmania, 1875–1984. Earth Surface Processes and Landforms **14** : 333–359. DOI: 10.1002/esp.3290140408

Kondolf GM. 1997. Hungry water: Effect of dams and gravel mining on river channels. Environmental Management **21**

Lane EW. 1955. Importance of fluvial morphology in hydraulic engineering. Proceedings (American Society of Civil Engineers); v. 81, paper no. 745

Leonard C, Legleiter C, Overstreet B. 2017. Effects of lateral confinement in natural and leveed reaches of a gravel-bed river: Snake River, Wyoming, USA. Earth Surface Processes and Landforms **42** : 2119–2138. DOI: 10.1002/esp.4157

Leopold LB. 1973. River Channel Change with Time: An Example: Address as Retiring President of The Geological Society of America, Minneapolis, Minnesota, November 1972. GSA Bulletin **84** : 1845–1860. DOI: 10.1130/0016-7606(1973)84<1845:RCCWTA>2.0.CO;2

Liébault F, Piégay H. 2001. Assessment of channel changes due to long-term bedload supply decrease, Roubion River, France. Geomorphology **36** : 167–186. DOI: 10.1016/S0169-555X(00)00044-1

Lisle TE, Nelson JM, Pitlick J, Madej MA, Barkett BL. 2000. Variability of bed mobility in natural, gravel-bed channels and adjustments to sediment load at local and reach scales. Water Resources Research **36** : 3743–3755. DOI: 10.1029/2000WR900238

Mackin JH. 1948. Concept of the graded river. Geological Society of America Bulletin **59** : 463–512.

Major JJ, Zheng S, Mosbrucker AR, Spicer KR, Christianson T, Thorne CR. 2019. Multidecadal Geomorphic Evolution of a Profoundly Disturbed Gravel Bed River System—A Complex, Nonlinear Response and Its Impact on Sediment Delivery. Journal of Geophysical Research: Earth Surface **124** : 1281–1309. DOI: 10.1029/2018JF004843

Miller SO, Ritter DF, Kochel RC, Miller JR. 1993. Fluvial responses to land-use changes and climatic variations within the Drury Creek watershed, southern Illinois. Geomorphology **6** : 309–329. DOI: 10.1016/0169-555X(93)90053-5

Montgomery DR, Panfil MS, Hayes SK. 1999. Channel-bed mobility response to extreme sediment loading at Mount Pinatubo. Geology **27** : 271–274. DOI: 10.1130/0091-7613(1999)027<0271:CBMRTE>2.3.CO;2

Moody JA, Pizzuto JE, Meade RH. 1999. Ontogeny of a flood plain. GSA Bulletin **111** : 291–303. DOI: 10.1130/0016-7606(1999)111<0291:OOAFP>2.3.CO;2

Moretto J, Rigon E, Mao L, Picco L, Delai F, Lenzi MA. 2014. Channel Adjustments and Island Dynamics in the Brenta River (Italy) Over the Last 30 Years. River Research and Applications **30** : 719–732. DOI: 10.1002/rra.2676

Nadler CT, Schumm SA. 1981. Metamorphosis of South Platte and Arkansas Rivers, Eastern Colorado. Physical Geography **2** : 95–115. DOI: 10.1080/02723646.1981.10642207

Nanson GC. 1980. Point bar and floodplain formation of the meandering Beatton River, northeastern British Columbia, Canada. Sedimentology **27** : 3–29. DOI: 10.1111/j.1365-3091.1980.tb01155.x

Nanson GC. 1986. Episodes of vertical accretion and catastrophic stripping: A model of disequilibrium flood-plain development. GSA Bulletin **97** : 1467–1475. DOI: 10.1130/0016-7606(1986)97<1467:EOVAAC>2.0.CO;2

van Niekerk A, Vogel KR, Slingerland RL, Bridge JS. 1992. Routing of Heterogeneous Sediments over Movable Bed: Model Development. Journal of Hydraulic Engineering **118** : 246–262. DOI: 10.1061/(ASCE)0733-9429(1992)118:2(246)

Nordin CF, Dempster GR. 1963. Vertical distribution of velocity and suspended sediment, Middle Rio Grande, New Mexico . Report [online] Available from: http://pubs.er.usgs.gov/publication/pp462B

Page KJ, Nanson GC, Frazier PS. 2003. Floodplain Formation and Sediment Stratigraphy Resulting from Oblique Accretion on the Murrumbidgee River, Australia. Journal of Sedimentary Research **73** : 5–14. DOI: 10.1306/070102730005

Parker G, Hassan M, Wilcock P. 2007. 10 Adjustment of the bed surface size distribution of gravel-bed rivers in response to cycled hydrographs. In Developments in Earth Surface Processes , Habersack H, Piégay H, and Rinaldi M (eds). Elsevier; 241–285.

Parker G, Wilcock PR. 1993. Sediment feed and recirculating flumes: Fundamental difference. Journal of Hydraulic Engineering **119** : 1192–1204.

Phillips CB. 2021. Alluvial River Bankfull Hydraulic Geometry. HydroShare DOI: doi.org/10.4211/hs.fa5503b04af343ffbaf33d5a15cb2579

Raudkivi AJ. 1976. Loose boundary hydraulics . Pergamom Press: Oxford

van Rijn LC. 1984. Sediment Transport, Part II: Suspended Load Transport. Journal of Hydraulic Engineering **110** : 1613–1641. DOI: 10.1061/(ASCE)0733-9429(1984)110:11(1613)

Rubin DM, Buscombe D, Wright SA, Topping DJ, Grams PE, Schmidt JC, Hazel JE, Kaplinski MA, Tusso R. 2020. Causes of Variability in Suspended-Sand Concentration Evaluated Using Measurements in the Colorado River in Grand Canyon. Journal of Geophysical Research: Earth Surface **125** : e2019JF005226. DOI: 10.1029/2019JF005226

Rubin DM, Topping DJ. 2001. Quantifying the relative importance of flow regulation and grain size regulation of suspended sediment transport α and tracking changes in grain size of bed sediment β. Water Resources Research **37** : 133–146.

Schmidt JC. 1999. Summary and synthesis of geomorphic studies conducted during the 1996 controlled flood in Grand Canyon. Geophysical Monograph - American Geophysical Union **110** : 329–342.

Schmidt JC, Wilcock PR. 2008. Metrics for assessing the downstream effects of dams. Water Resources Research **44** : W04404. DOI: 10.1029/2006WR005092

Schumm SA. 1969. River metamorphosis. Journal of the Hydraulics division **95** : 255–274.

Schumm SA, Harvey MD, Watson CC. 1984. Incised channels: morphology, dynamics, and control . Water Resources Publications

Schumm SA, Khan HR. 1972. Experimental Study of Channel Patterns. GSA Bulletin **83** : 1755–1770. DOI: 10.1130/0016-7606(1972)83[1755:ESOCP]2.0.CO;2

Shelley J, Hotchkiss RH, Boyd P, Gibson S. 2022. Discharging Sediment Downstream: Case Studies in Cost Effective, Environmentally Acceptable Reservoir Sediment Management in the United States. Journal of Water Resources Planning and Management **148** : 05021028. DOI: 10.1061/(ASCE)WR.1943-5452.0001494

Simon A. 1989. A model of channel response in disturbed alluvial channels. Earth Surface Processes and Landforms **14** : 11–26. DOI: 10.1002/esp.3290140103

Simon Andrew, Thomas Robert E., Curini Andrea, Shields F. Douglas. 2002. Case Study: Channel Stability of the Missouri River, Eastern Montana. Journal of Hydraulic Engineering **128** : 880–890. DOI: 10.1061/(ASCE)0733-9429(2002)128:10(880)

Sklar LS, Fadde J, Venditti JG, Nelson P, Wydzga MA, Cui Y, Dietrich WE. 2009. Translation and dispersion of sediment pulses in flume experiments simulating gravel augmentation below dams. Water resources research **45** DOI: https://doi.org/10.1029/2008WR007346

Sutherland DG, Ball MH, Hilton SJ, Lisle TE. 2002. Evolution of a landslide-induced sediment wave in the Navarro River, California. GSA Bulletin **114** : 1036–1048. DOI: 10.1130/0016-7606(2002)114<1036:EOALIS>2.0.CO;2

Thayer JB, Ashmore P. 2016. Floodplain morphology, sedimentology, and development processes of a partially alluvial channel. Geomorphology **269** : 160–174. DOI: 10.1016/j.geomorph.2016.06.040

Toffaleti FB. 1968. A procedure for computation of the total river sand discharge and detailed distribution, bed to surface . Technical Report. U.S. Army Corps of Engineers

Topping DJ, Grams PE, Griffiths RE, Dean DJ, Wright SA, Unema JA. 2021. Self-limitation of sand storage in a bedrock-canyon river arising from the interaction of flow and grain size. Journal of Geophysical Research: Earth Surface **n/a** : e2020JF005565. DOI: https://doi.org/10.1029/2020JF005565

Topping DJ, Mueller ER, Schmidt JC, Griffiths RE, Dean DJ, Grams PE. 2018. Long-Term Evolution of Sand Transport Through a River Network: Relative Influences of a Dam Versus Natural Changes in Grain Size From Sand Waves. Journal of Geophysical Research: Earth Surface **123** : 1879–1909. DOI: 10.1029/2017JF004534

Topping DJ, Rubin DM, Vierra LE. 2000. Colorado River sediment transport: 1. Natural sediment supply limitation and the influence of Glen Canyon Dam. Water Resources Research **36** : 515–542. DOI: 10.1029/1999WR900285

Toro-Escobar CM, Paola C, Parker G. 1996. Transfer function for the deposition of poorly sorted gravel in response to streambed aggradation. Journal of Hydraulic Research **34** : 35–53. DOI: 10.1080/00221689609498763

Trimble SW. 1981. Changes in Sediment Storage in the Coon Creek Basin, Driftless Area, Wisconsin, 1853 to 1975. Science **214** : 181–183. DOI: 10.1126/science.214.4517.181

Trimble SW. 1983. A sediment budget for Coon Creek basin in the Driftless Area, Wisconsin, 1853-1977. American Journal of Science **283** : 454–474. DOI: 10.2475/ajs.283.5.454

Venditti JG, Dietrich WE, Nelson PA, Wydzga MA, Fadde J, Sklar L. 2010. Effect of sediment pulse grain size on sediment transport rates and bed mobility in gravel bed rivers. Journal of Geophysical Research: Earth Surface **115**

Viparelli E, Haydel R, Salvaro M, Wilcock PR, Parker G. 2010a. River morphodynamics with creation/consumption of grain size stratigraphy 1: laboratory experiments. Journal of Hydraulic Research **48** : 715–726. DOI: 10.1080/00221686.2010.515383

Viparelli E, Nittrouer JA, Parker G. 2015. Modeling flow and sediment transport dynamics in the lowermost Mississippi River, Louisiana, USA, with an upstream alluvial-bedrock transition and a downstream bedrock-alluvial transition: Implications for land building using engineered diversions. Journal of Geophysical Research: Earth Surface **120** : 534–563. DOI: 10.1002/2014JF003257

Viparelli E, Sequeiros OE, Cantelli A, Wilcock PR, Parker G. 2010b. River morphodynamics with creation/consumption of grain size stratigraphy 2: numerical

model. Journal of Hydraulic Research **48** : 727–741. DOI: 10.1080/00221686.2010.526759

Walker AE, Moore JN, Grams PE, Dean DJ, Schmidt JC. 2020. Channel narrowing by inset floodplain formation of the lower Green River in the Canyonlands region, Utah. GSA Bulletin **132** : 2333–2352. DOI: 10.1130/B35233.1

Webb RH, Schmidt JC, Marzolf GR, Valdez RA. 1999. The controlled flood in Grand Canyon. Washington DC American Geophysical Union Geophysical Monograph Series **110**

Wilcock PR, DeTemple BT. 2005. Persistence of armor layers in gravel-bed streams. Geophysical Research Letters **32** DOI: 10.1029/2004GL021772

Wilcox AC, O'Connor JE, Major JJ. 2014. Rapid reservoir erosion, hyperconcentrated flow, and downstream deposition triggered by breaching of 38 m tall Condit Dam, White Salmon River, Washington. Journal of Geophysical Research: Earth Surface **119** : 1376–1394. DOI: 10.1002/2013JF003073

Williams G, Wolman G. 1984. Downstream effects of dams on alluvial rivers . USGS Professional Paper

Wright S, Parker G. 2004. Flow Resistance and Suspended Load in Sand-Bed Rivers: Simplified Stratification Model. Journal of Hydraulic Engineering **130** : 796–805. DOI: 10.1061/(ASCE)0733-9429(2004)130:8(796)

Wright S, Parker G. 2005a. Modeling downstream fining in sand-bed rivers. I: formulation. Journal of Hydraulic Research **43** : 613–620. DOI: 10.1080/00221680509500381

Wright S, Parker G. 2005b. Modeling downstream fining in sand-bed rivers. II: application. Journal of Hydraulic Research **43** : 621–631. DOI: 10.1080/00221680509500382

Ziliani L, Surian N. 2012. Evolutionary trajectory of channel morphology and controlling factors in a large gravel-bed river. Geomorphology **173–174** : 104–117. DOI: 10.1016/j.geomorph.2012.06.001

CHAPTER 5

CONCLUSION

Effective river management is partly dependent on the ability to predict channel

behavior and change in response to changes in water or sediment supply. The channel

response to a change in supply is complicated by the interaction between the supply grain

size and bed texture which affects the magnitude and direction of the sediment mass

balance. When the supply rate increases and fines, the bed grain size will fine, increasing

transport capacity without morphologic change. Conversely, the bed will coarsen if the

supply coarsens, reducing the transport capacity and potentially necessitating a larger

morphologic response. As managers plan for the impact of changing flow or sediment

supply rates associated with reservoir operations, dam decommissioning, wildfire, or land

use changes, it is important to identify circumstances when the perturbation is expected to

produce a large sediment mass imbalance that is likely to cause a meaningful adjustment

in the channel form or behavior, in contrast to circumstances when the sediment mass

balance may be completely modulated by bed textural change. The interaction between

bed surface grain size and bed topography to changing supply has largely focused on

easily observed sediment sorting in gravel-bed rivers (Buffington and Montgomery,

1999; Cui et al., 2003a, 2003b; Lisle et al., 2000; Sklar et al., 2009; Venditti et al., 2010;

Ferguson et al., 2015). On sand-bed rivers, bed sorting is harder to observe and measure,

yet there is increasing evidence small changes in the grain size of sand can have a large

effect on transport (Rubin and Topping, 2001; Topping et al., 2000; Rubin et al., 2020;

Topping et al., 2021). The need to understand how bed texture adjusts with supply grain

size and the resulting effect on the sediment mass balance and morphologic adjustment in sand-bed rivers motivates this dissertation research.

In Chapter 3, we present a sediment budget for an alluvial sand-bed section of the Yampa River, Colorado. We show it is necessary to partition sediment budget into narrow grain size classes to measure small-to-moderate morphological change and bed texture adjustment. Measurements of sediment transport at a network of acoustical sediment gages indicate sand was evacuated from the reach over the 6-year study period. However, there is no evidence of sand evacuation from repeat measurements of channel morphology, such as channel widening or an increase in channel activity.

A closer examination of the sediment budget partitioned into grain sizes of sand indicates the deficit is not uniform among all sand sizes. Some sand sizes accumulate while others erode. The only grain sizes to erode are fine and medium sand, and we infer that these sand sizes must erode from the channel bed, because this is the only residual term left in our sediment budget. We find that fine sand is winnowed at a faster rate than medium sand, causing the bed to coarsen. Bed coarsening appears to be in response to an increase in sediment supply from tributary floods during the late-1950s to early-1960s (Topping et al., 2018). We anticipate the bed will continue to coarsen until the transport capacity is decreased to match the supply rate. Very fine sand accumulates on the floodplains during moderate-to-large flows and vegetated islands increase in size; however, vegetated island expansion is not large enough to affect the characteristics or behavior of the channel, such as channel width, sinuosity, or lateral migration.

The findings of Chapter 3 demonstrate that processes of grain size sorting in the channel and floodplain complicate the prediction of channel change. Although the

sediment mass balance was in deficit, sediment evacuation was not large enough to produce a morphological response. Instead, the primary adjustment was a change in bed texture and the only morphological change resulted from small-to-unmeasurable storage of specific sand sizes in the floodplain. Such processes were not detected in the sediment budget calculated for all sand sizes, which highlights the importance of using a partitioned when trying to observe the complicated nature of the channel response.

Chapter 4 explores the mutual adjustment between bed texture and bed topography to an increase in sediment supply using a morphodynamic model. There are numerous examples of disturbances that cause the supply rate to increase and fine, such as wildfires, volcanic eruptions, and changes in grazing or forestry practices. It is often assumed that an increase in supply will cause sediment to accumulate and the expected channel response may include bed aggradation, channel narrowing, floodplain accretion, increase in avulsion frequency or migration, or change in planform. However, our modeling shows that the nature of bed textural change and its effect on sediment transport capacity can enhance, eliminate, or even reverse potential aggradation in response to this kind of disturbance. This has important implications for predicting the rate and magnitude of downstream channel adjustment and the potential threat to downstream infrastructure, flooding, and aquatic and riparian habitat.

Our modeling indicates that the bed surface will fine and the channel bed will aggrade, degrade, or have no change in storage depending on the supply increase relative to the supply fining. If the supply increase is small, the reach is likely to evacuate sediment rather than accumulate sediment, because the increase in transport capacity caused by bed fining is greater than the increase in supply rate. Thus, increased bank

erosion and channel shifting that threaten adjacent property may be more of a management concern than reduced flood conveyance. If the supply increase is large, the increase in transport capacity caused by bed fining may be insufficient to transport the supply, and sediment will accumulate. However, the amount of accumulation may be less than expected because bed fining makes the reach more efficient at transporting sediment independent of morphologic change. A condition of little to no sediment accumulation or evacuation may exist when supply increase is almost completely balanced by an increase in transport capacity by bed fining, and the disturbance may cause little to no downstream affect, alleviating most management concerns. How fast the bed texture changes relative to aggradation or degradation also matters because the disturbance may be short-lived and the new steady-state condition may never be reached. We find that bed textural changes happen rapidly and cause the total transport capacity to closely match the new supply rate, but the transport grain size is significantly finer than the steady-state condition. This quick increase in transport capacity initially limits sediment accumulation (or evacuation) which may delay most management problems. Sediment accumulates and evacuates in a second phase of adjustment over a longer period as the transport grain size slowly adjusts to match the supply grain size. If the disturbance is short-lived, the second phase of adjustment may never occur.

The results of Chapter 4 demonstrate that the magnitude and direction of the sediment mass balance and resulting morphologic response to an increase in sediment supply is largely driven by the interaction between the supply rate and grain size with the bed grain size. Most case studies of channel change focus on the supply or flow rate change with less attention to the supply grain size (e.g., Nadler and Schumm, 1981;

Trimble, 1981; Knighton, 1989; Miller et al., 1993; Church, 1995; Simon Andrew et al., 2002; Surian and Cisotto, 2007; Bollati et al., 2014). As a result, the morphological response among case studies is wildly different and difficult to predict. The findings here suggest that if both the supply rate and grain size are considered, the patterns of adjustment can be defined. Consider the example of the interaction between bed textural change and channel morphology on the Yampa River in Chapter 3. Tributary floods during the late-1950s to early-1960s delivered a pulse of sediment to the Yampa River that increased the annual supply by 57,000 MT, or 6% above the present-day annual supply, and the supply grain size fined (Topping et al., 2018). The steady-state results from Chapter 4 suggest there should be little to no sediment accumulation or evacuation, because the supply is finer and only increases slightly. The new steady-state condition is never reached, however, because the supply increase is only of a short duration. The first phase of adjustment associated with bed fining was inferred from measurements of sediment transport, but the channel morphology has been stable and the long-term response has been bed coarsening as the supply as the channel re-adjusts to a smaller supply rate (Topping et al., 2018; Chapter 4). A substantially larger increase in supply occurred on the Yampa River during the turn of the 20th century as a result of widespread arroyo cutting on tributaries (Kemper et al., 2022b). It is estimated that the annual supply increased by 500,000 MT, which is an order of magnitude larger than the increase caused by tributary floods in the late-1950s to early-1960s (Kemper et al., 2022b). The supply grain size was even finer than the tributary flood disturbance and lasted almost 6 decades (Kemper et al., 2022a). Steady-state results from Chapter 4 indicate sediment will accumulate following the arroyo cutting disturbance, because the supply increase was

large and sustained. Other work confirmed this hypothesis and showed there was an increase in channel migration and rapid floodplain aggradation on the Yampa River around this time (Kemper, 2021). However, the insights that emerged from this dissertation suggest the morphologic response was probably dampened by bed fining.

The two examples of supply disturbance on the Yampa River demonstrate the importance of considering the interaction between supply rate and grain size and bed grain size when anticipating the response to a disturbance in sand-bed rivers. Most of the world's rivers will undergo significant changes in the flow and sediment regimes in the coming decades as a result of climate change (Gudmundsson et al., 2021), and society will need to anticipate downstream impacts to guide decision-making and policy. Although small changes in the grain size of sand on the channel bed may seem insignificant at the onset, the findings which emerged from this dissertation research indicate they can have a strong control on the magnitude and direction of the sediment mass balance and resulting morphologic response.

References

Bollati IM, Pellegrini L, Rinaldi M, Duci G, Pelfini M. 2014. Reach-scale morphological adjustments and stages of channel evolution: The case of the Trebbia River (northern Italy). Geomorphology **221** : 176–186. DOI: 10.1016/j.geomorph.2014.06.007

Buffington JM, Montgomery DR. 1999. Effects of sediment supply on surface textures of gravel-bed rivers. Water Resources Research **35** : 3523–3530. DOI: 10.1029/1999WR900232

Church M. 1995. Geomorphic response to river flow regulation: Case studies and time-scales. Regulated Rivers: Research & Management **11** : 3–22. DOI: 10.1002/rrr.3450110103

Cui Y, Parker, G. G, Lisle TE, Gott J, Hansler-Ball ME, Pizzuto JE, Allmendinger NE, Reed JM. 2003a. Sediment pulses in mountain rivers: 1. Experiments. Water Resources Research **39** : 1239. DOI: 10.1029/2002WR001803

Cui Y, Parker G, Pizzuto J, Lisle TE. 2003b. Sediment pulses in mountain rivers: 2. Comparison between experiments and numerical predictions. Water Resources Research **39** : 1240. DOI: 10.1029/2002WR001805

Ferguson RI, Church M, Rennie CD, Venditti JG. 2015. Reconstructing a sediment pulse: Modeling the effect of placer mining on Fraser River, Canada. Journal of Geophysical Research: Earth Surface **120** : 1436–1454.

Gudmundsson L, Boulange J, Do HX, Gosling SN, Grillakis MG, Koutroulis AG, Leonard M, Liu J, Müller Schmied H, Papadimitriou L. 2021. Globally observed trends in mean and extreme river flow attributed to climate change. Science **371** : 1159–1162.

Kemper JT, Rathburn SL, Friedman JM, Nelson JM, Mueller ER, Vincent KR. 2022a. Fingerprinting historical tributary contributions to floodplain sediment using bulk geochemistry. CATENA **214** : 106231. DOI: 10.1016/j.catena.2022.106231

Kemper JT, Thaxton RD, Rathburn SL, Friedman JM, Mueller ER, Scott ML. 2022b. Sediment-Ecological Connectivity in a Large River Network. Earth Surface Processes and Landforms **47** DOI: 10.1002/esp.5277

Knighton AD. 1989. River adjustment to changes in sediment load: The effects of tin mining on the Ringarooma River, Tasmania, 1875–1984. Earth Surface Processes and Landforms **14** : 333–359. DOI: 10.1002/esp.3290140408

Lisle TE, Nelson JM, Pitlick J, Madej MA, Barkett BL. 2000. Variability of bed mobility in natural, gravel-bed channels and adjustments to sediment load at local and reach scales. Water Resources Research **36** : 3743–3755. DOI: 10.1029/2000WR900238

Miller SO, Ritter DF, Kochel RC, Miller JR. 1993. Fluvial responses to land-use changes and climatic variations within the Drury Creek watershed, southern Illinois. Geomorphology **6** : 309–329. DOI: 10.1016/0169-555X(93)90053-5

Nadler CT, Schumm SA. 1981. Metamorphosis of South Platte and Arkansas Rivers, Eastern Colorado. Physical Geography **2** : 95–115. DOI: 10.1080/02723646.1981.10642207

Rubin DM, Buscombe D, Wright SA, Topping DJ, Grams PE, Schmidt JC, Hazel JE, Kaplinski MA, Tusso R. 2020. Causes of Variability in Suspended-Sand Concentration Evaluated Using Measurements in the Colorado River in Grand Canyon. Journal of Geophysical Research: Earth Surface **125** : e2019JF005226. DOI: 10.1029/2019JF005226

Rubin DM, Topping DJ. 2001. Quantifying the relative importance of flow regulation and grain size regulation of suspended sediment transport α and tracking changes in grain size of bed sediment β. Water Resources Research **37** : 133–146.

Simon Andrew, Thomas Robert E., Curini Andrea, Shields F. Douglas. 2002. Case Study: Channel Stability of the Missouri River, Eastern Montana. Journal of Hydraulic Engineering **128** : 880–890. DOI: 10.1061/(ASCE)0733-9429(2002)128:10(880)

Sklar LS, Fadde J, Venditti JG, Nelson P, Wydzga MA, Cui Y, Dietrich WE. 2009. Translation and dispersion of sediment pulses in flume experiments simulating gravel augmentation below dams. Water resources research **45** DOI: https://doi.org/10.1029/2008WR007346

Surian N, Cisotto A. 2007. Channel adjustments, bedload transport and sediment sources in a gravel-bed river, Brenta River, Italy. Earth Surface Processes and Landforms **32** : 1641–1656. DOI: 10.1002/esp.1591

Topping DJ, Grams PE, Griffiths RE, Dean DJ, Wright SA, Unema JA. 2021. Self-Limitation of Sand Storage in a Bedrock-Canyon River Arising From the Interaction of Flow and Grain Size. Journal of Geophysical Research: Earth Surface **126** : e2020JF005565. DOI: 10.1029/2020JF005565

Topping DJ, Mueller ER, Schmidt JC, Griffiths RE, Dean DJ, Grams PE. 2018. Long-Term Evolution of Sand Transport Through a River Network: Relative Influences of a Dam Versus Natural Changes in Grain Size From Sand Waves. Journal of Geophysical Research: Earth Surface **123** : 1879–1909. DOI: 10.1029/2017JF004534

Topping DJ, Rubin DM, Vierra LE. 2000. Colorado River sediment transport: 1. Natural sediment supply limitation and the influence of Glen Canyon Dam. Water Resources Research **36** : 515–542. DOI: 10.1029/1999WR900285

Trimble SW. 1981. Changes in Sediment Storage in the Coon Creek Basin, Driftless Area, Wisconsin, 1853 to 1975. Science **214** : 181–183. DOI: 10.1126/science.214.4517.181

Venditti JG, Dietrich WE, Nelson PA, Wydzga MA, Fadde J, Sklar L. 2010. Effect of sediment pulse grain size on sediment transport rates and bed mobility in gravel bed rivers. Journal of Geophysical Research: Earth Surface **115**

APPENDICES

APPENDIX A

Supporting Information for Chapter 3

Text A-1.

Partitioning the suspended load:

To partition the daily suspended load flux, we first estimated the median grain size (D_{50}) of the suspended load on each day. The D_{50} at the Deerlodge Park gage was taken to be the daily average of the 15-minute multi-frequency measurements. There were several periods when the D_{50} of the suspended load was not measured, because one of the multi-frequency acoustical sensors was not working. During these periods, we interpolated the missing D_{50} using an iterative singular spectrum analysis (SSA) (Schoellhamer, 2001; Kondrashov and Ghil, 2006). At the Lily and Maybell gages, direct estimates of the D_{50} could not be made from the single-frequency side-looking acoustic Doppler profiler, but the D_{50} was occasionally measured using pump samples and EWI cross-section measurements. We linearly interpolated between these physical measurements to estimate the D_{50} of the suspended load on each day.

Using the daily D_{50} at each gage, we generated a grain size distribution for each day by identifying the EWI measurements with a D_{50} that bracketed our daily D_{50} and interpolating between the two EWI grain size distributions using a weighted linear method based on the distance between the daily D_{50} and the D_{50} for each EWI sample. If the daily D_{50} was finer or coarser than the D_{50} of the EWI samples, we adjusted the grain size distribution of the finest or coarsest EWI sample by the percent change between the daily D_{50} and the D_{50} of the EWI. Finally, we partitioned the daily suspended sand load flux based on the percent of each sand size in the daily grain size distribution.

Partitioning the bed load:

We estimated the daily D_{50} of the bed load at the Lily and Deerlodge Park gages based on a metric of relative bed coarseness (β) on each day. The metric β is a measure of the normalized bed material grain size and is calculated from measurements of suspended sand concentration and the D_{50} of the suspended sand load:

$$\beta = \frac{D_b}{D_{b-ref}} = \left(\frac{C_s}{C_{s-ref}}\right)^{-0.1}\left(\frac{D_s}{D_{s-ref}}\right); \qquad (A-1)$$

where D_b, C_s, and D_s are the D_{50} of the bed material grain size, the suspended sand concentration, and the D_{50} of the suspended load, respectively, and $D_{b\text{-}ref}$, $C_{s\text{-}ref}$, and $D_{s\text{-}ref}$ are corresponding reference values, taken to be the mean of each variable during the period of interest (Rubin and Topping, 2001, 2008). We calculated β on each day using the daily averaged sand concentrations and the D_{50} of the suspended load calculated in the section *Partitioning the suspended load*. The reference values were taken to be the average of the daily values during the entire study period. We used β to calculate the D_{50} of the bed load using:

$$D_b = \beta D_{b-ref}; \qquad (A-2)$$

where $D_{b\text{-}ref}$ is the average D_{50} of the bed material samples collected at each gage. The grain size distribution of the bed load was estimated on each day by identifying the cross-sectionally averaged bed material sample with a D_{50} that bracketed the β-estimated D_{50}, then interpolating between the bed material grain size distributions using the same weighted, linear method that was used to estimate the suspended load size distribution. At the Maybell gage, bed material samples were not collected, because the bed was predominately gravel, and we estimated the bed load grain size by shifting the grain size

distribution of the EWI sample with the coarsest D_{50} by the daily value of β. Finally, we partitioned the daily bed load flux by the percent of each sand size in the daily grain size distribution.

Text A-2.

We created a spatially distributed co-registration error surface for each image using a set of independent test-points by identifying the map coordinate of the same feature on the image being digitized and on the 2017 NAIP image. The test-points were automatically selected using the area-based algorithm of Leonard et al. (2020), and we removed test-points with correlation coefficients less than 0.8. The 2017 NAIP image was considered the base image and assumed to have zero co-registration error. The co-registration error associated with the other images was small (RMSE of 2.1 m), because the NAIP images were already georeferenced and orthorectified. We defined the digitizing error probabilistically, using a normal distribution with a mean of zero and a standard deviation of one-third of the maximum digitizing uncertainty, which we assumed to be 2 m (Donovan et al., 2019). The largest source of uncertainty was the interpretation of whether an alluvial surface was within the active channel or was part of the floodplain. We used a 10% vegetation density threshold to distinguish surfaces as channel (<10% vegetation density) or floodplain (>10% vegetation density). There was large uncertainty in deciphering the boundary based on this threshold, because fast-growing perennial vegetation can encroach on low-elevation bars that are regularly inundated during the annual flood but exposed for long periods during summer base flow when the aerial images were acquired. In such instances, we delineated a maximum and minimum extent of the active channel boundary (Leonard et al., 2020). Finally, we

created a distribution of probable active channel boundaries for each image given the digitizing error and the co-registration and interpretation uncertainty. The boundaries were overlaid to calculate the planimetric channel change for each image time-series: 2013 to 2015, 2015 to 2017, and 2017 to 2019.

Text A-3.

The elevation input into our Bayesian height model had to be detrended to remove the effect of the channel gradient. By detrending the elevation, the difference between any two detrended points represents the height rather than the channel gradient. We also used the detrended elevations to calculate the discharge needed to inundate floodplain surfaces and the corresponding depth of floodplain inundation. We detrended the topographic points using a longitudinal profile of the water surface elevation (WSE) collected in June 2020. The WSE was measured by logging a raw GNSS file on a Leica Viva GNSS GS15 receiver mounted on a raft while floating downstream. The raw GNSS positions were corrected by post-processing kinematics (PPK) in RTKLib (Takasu and Yasuda, 2009) using observation data from a local continuous operating reference station (CORS) network. The corrected WSE coordinates were converted to a channel-centered coordinate system (Legleiter and Kyriakidis, 2007), plotted against streamwise distance, and fitted with a smoothing spline. This allowed the WSE to be represented as a smoothly varying function that related streamwise distance to WSE. We converted the coordinates of the elevation data to the same channel-centered coordinate system, predicted the WSE at each coordinate using the smoothing spline, and subtracted the WSE from the elevation to remove the effect of the channel gradient.

Text A-4.

The input data for our Bayesian model were detrended elevations (Text A-3) from the pre- and post-1938 floodplain and the channel bed. We used the detrended elevations from the post-1938 floodplains formed during our study period as the input data for aggraded floodplains. We could not directly extract detrended elevations from the eroded pre- or post-1938 floodplains during our study period, because the original topography had been removed, so we extracted detrended elevations from the remaining floodplain surfaces that had undergone erosion. The detrended bed elevations were extracted from the 2015 LiDAR survey within the active channel boundary delineated from the 2015 aerial image. For the Little Snake River, the detrended bed elevations were the RTK coordinates designated as 'active channel' in the 2020 survey.

We created a distribution of the detrended elevation in the study area for the channel bed and eroded and deposited floodplain using Bayesian models. The purpose of the Bayesian model was to estimate the probability of the parameter values (i.e., mean and precision) of the channel bed and floodplain detrended elevations. These parameter values are then used to generate a posterior distribution of the eroded and aggraded floodplain heights throughout the study area. We assumed the detrended elevations were sampled from a population that was normally distributed and could be modeled by the following:

$$Z_{detrend} \sim normal(\mu, \tau); \qquad\qquad (A-3)$$

where μ is the mean and τ is the precision. We assigned uninformative prior distributions on μ and τ:

$$\mu \sim normal(0, 10^{-6}); \qquad\qquad (A-4)$$

$$\tau \sim gamma(0.01, 0.01); \qquad\qquad (A-5)$$

to obtain the posterior distribution of the detrended elevation using Gibbs sampling with

5000 Markov Chain Monte Carlo (MCMC) steps. At each MCMC step, we predict we μ

and τ and randomly sampled a detrended elevation $(Z_{detrend(pred)})$ from a normal

distribution defined by these parameters.

We calculated the height of eroded and deposited floodplain by subtracting the

$Z_{detrend(pred)}$ for the channel bed from the $Z_{detrend(pred)}$ for floodplains at each MCMC

step. This procedure was done separately for the channel margins and vegetated islands

by the following:

$$h_{i(chDep)} = Z_{i(chDep)} - Z_{i(bed)}; \qquad\qquad (A-6)$$

$$h_{i(chErs)} = Z_{i(chErs)} - Z_{i(bed)}; \qquad\qquad (A-7)$$

$$h_{i(vegDep)} = Z_{i(vegDep)} - Z_{i(bed)}; \qquad\qquad (A-8)$$

$$h_{i(vegErs)} = Z_{i(vegErs)} - Z_{i(bed)}; \qquad\qquad (A-9)$$

where $h_{i(chDep)}$, $h_{i(chErs)}$, $h_{i(vegDep)}$, $h_{i(vegErs)}$ are the height of the eroding and

depositing floodplains and the vegetated islands at the ith MCMC step, respectively,

$Z_{i(chDep)}$, $Z_{i(chErs)}$, $Z_{i(vegDep)}$, and $Z_{i(vegErs)}$ is the aggraded and eroded floodplain

$Z_{detrend(pred)}$ along the channel margins and vegetated islands at the ith MCMC step,

respectively, and $Z_{i(bed)}$ is the $Z_{detrend(pred)}$ for the active channel bed at the ith

MCMC step.

Text A-5.

Fused DEMs were created by combining two different types of remotely sensed

data that were collected before this study: (1) NIR LiDAR collected in fall 2011 and fall

2015 and (2) multispectral aerial images collected at the time of LiDAR acquisition in 2011 and acquired through the NAIP in August 2015. We generated the fused DEMs by subtracting optically-derived estimates of depth from LiDAR-derived water surface elevations (WSE) and combining the resulting bed elevations with terrestrial LiDAR elevations (Legleiter, 2012). The 2015 LiDAR survey had sufficient in-channel returns to produce an interpolated water surface elevation that was free of obvious artifacts, which allowed us to subtract depth estimates on a pixel-by-pixel basis. However, the 2015 LiDAR was collected at a discharge larger than the 2015 NAIP image (13.8 versus 4.6 m^3sec^{-1}, respectively), making the optically-derived depth smaller than the depth at the time of LiDAR acquisition. We corrected this difference by increasing the optically derived estimates of depth by the increase in stage height measured at the Deerlodge Park gage (i.e., 0.21 m). The 2011 LiDAR survey had a smaller number of in-channel returns that led to an interpolated water surface with clear artifacts. For this dataset, we estimated the WSE by the intersection of the DEM elevations with the perimeter of the wetted channel extent, transforming those coordinates to a channel-centered coordinate system and plotting against streamwise distance, allowing the WSE to be represented as a smoothly varying function that related streamwise distance to WSE. Each node of the wetted channel raster grid was converted to the same channel-centered coordinate system and the WSE was predicted based on the streamwise coordinate.

Text A-6.

Uncertainty in calculations of the net change in sediment storage results from elevation error in each DEM. In this study, we used the method described by Anderson (2019) to quantify uncertainty in our calculations of volumetric change from differences

in topography. For subaerial pixels, the error was the combination of spatially correlated random errors and systematic bias. The spatially correlated error was calculated from a semivariogram created from a subset of elevation differences on a stable alluvial fan. The magnitude of the spatially correlated error (σ_{sc}) was found to be 0.0045 based on the semivariogram sill and the random errors were correlated over a length of 2.04 m based on the semivariogram range. Systematic bias was quantified by calculating the elevation difference on stable alluvial fans and a road. The total systematic bias was taken to be the average of the alluvial fan (-0.05 m) and the road (0.0023) bias which was -0.024 m. We adjusted for this bias by shifting the 2015 DEM upward by 0.024 m and recalculating volumetric change. The residual systematic error (σ_{sys}) remaining was 0.026 m. The combined error for the DEMs was calculated from Equation 24 in Anderson (2019):

$$\sigma_{DEM} = nL^2 \sqrt{\frac{\sigma_{sc}^2}{n}\frac{\pi\omega^2}{5L^2} + \sigma_{sys}^2}; \qquad (A-10)$$

where σ_{DEM} is the total error associated with the volumetric change between the 2011 and 2015 LIDAR surveys, n is the total number of subaerial pixels over which the volume is calculated, L is the pixel length, σ_{sc} is the magnitude of random spatially correlated error, ω is the length over which random errors were correlated, and σ_{sys} is the residual systematic bias.

Volumetric calculations based on elevations derived from optical bathymetry must include this additional source of error. Bed elevation error was the combined error of the local WSE and the image-derived depth estimates added in quadrature (Table Text A-6-1). Local WSE error was considered equal to the RMSE of the LiDAR data based on a set of independent checkpoints for the 2015 DEM and the standard deviation of

residuals for the function that related streamwise distance to WSE in the 2011 DEM. We could not directly validate our depth retrieval method because measurements of channel depth were not collected at the time of image acquisition. In place of using a point-to-pixel method for validation, we estimated the image-derived mean depth at the Deerlodge gage as the mean of the pixel values that intersected the gaging cross-section and calculated the difference between the cross-sectionally average image-derived depth to the field-measured depth at the nearest discharge. The difference between the discharge at the time of the field-measured- and optically-derived-depth for this comparison was less than 0.5 m³sec⁻¹.

We used four separate equations to calculate the error in volumetric change depending on whether the elevation difference was based on cells that were wet for one year and subaerial for the other year and wet or subaerial for both years.

The total error for all raster cells that were wet in 2011 and subaerial in 2015 was taken to be the combination of the uncertainty between the two DEMs calculated by Equation A-10 and the error in bed elevation in Table Text A-6-1 added in quadrature:

$$\sigma_{wetted2011} = nL^2\sqrt{\frac{\sigma_{sc}^2}{n}\frac{\pi\omega^2}{5L^2} + \sigma_{sys}^2 + \sigma_{bed(2011)}^2}; \qquad (A-11)$$

where $\sigma_{bed(2011)}$ is the bed elevation error for 2011 and n is the number of raster cells that were wet in 2011 and dry in 2015. Similarly, the total error for all raster cells that were wet in 2015 and subaerial in 2011 was taken to be the combination of the uncertainty between the two DEMs calculated by Equation A-10 and the error in bed elevation in Table Text A-6-1:

$$\sigma_{wetted2015} = nL^2\sqrt{\frac{\sigma_{sc}^2}{n}\frac{\pi\omega^2}{5L^2} + \sigma_{sys}^2 + \sigma_{bed(2015)}^2}; \qquad (A-12)$$

where $\sigma_{bed(2015)}$ is the bed elevation error for 2015 (Table Text A-6-1) and n is the number

of raster cells that were wet in 2015 and subaerial in 2011.

The error for raster cells that were wet in 2011 and 2015 was taken to be the

combination of the uncertainty between the two DEMs calculated by Equation A-10 and

the error in bed elevation for both periods:

$$\sigma_{wetted2011\&2015} = nL^2 \sqrt{\frac{\sigma_{sc}^2}{n}\frac{\pi\omega^2}{5L^2} + \sigma_{sys}^2 + \sigma_{bed(2011)}^2 + \sigma_{bed(2015)}^2}; \qquad (A-13)$$

where n is the number of raster cells that were wet in 2011 and 2015.

Finally, the error for raster cells that were subaerial in 2011 and 2015

($\sigma_{subaerial}$) was calculated from Equation A-10 where n is the number of cells that were

dry in both surveys.

The total error was the sum of each error added in quadrature:

$$\sigma_{total} = \sqrt{\sigma_{subaerial}^2 + \sigma_{wetted2011}^2 + \sigma_{wetted2015}^2 + \sigma_{wetted2011\&2015}^2} \qquad (A-14)$$

where σ_{total} is the total volumetric error, $\sigma_{subaerial}$ is the volumetric error across all cells

that were subaerial in both years (Equation A-10), $\sigma_{wetted2011}$ is the total volumetric error

across all cells that were wet in 2011 and subaerial in 2015 (Equation A-11), $\sigma_{wetted2015}$ is

the total volumetric error across all cells that were wet in 2015 and subaerial in 2011

(Equation A-12), and $\sigma_{wetted2011\&2015}$ is the total volumetric error across all cells that were

wet in 2011 and 2015 (Equation A-13). We did not threshold cells on a specific level of

detection for volumetric calculations on the premise that all cells have an associated error

and discarding a subset of cells in a *post-hoc* manner would reduce the overall error in a

biased manner.

Table Text A-6-1: Optical depth retrieval error ($\sigma_{optical}$) in 2011 and 2015. The WSE error (σ_{WSE}) was taken to be that of the LiDAR in 2015 and the WSE-channel centered coordinate relation in 2011. The bed elevation error (σ_{bed}) was calculated as $\sqrt{(\sigma_{WSE}^2 + \sigma_{optical}^2)}$. All errors are in units of meters.

	$\sigma_{optical}$	σ_{WSE}	σ_{bed}
2011	0.19	0.19	0.19
2015	0.12	0.08	0.14
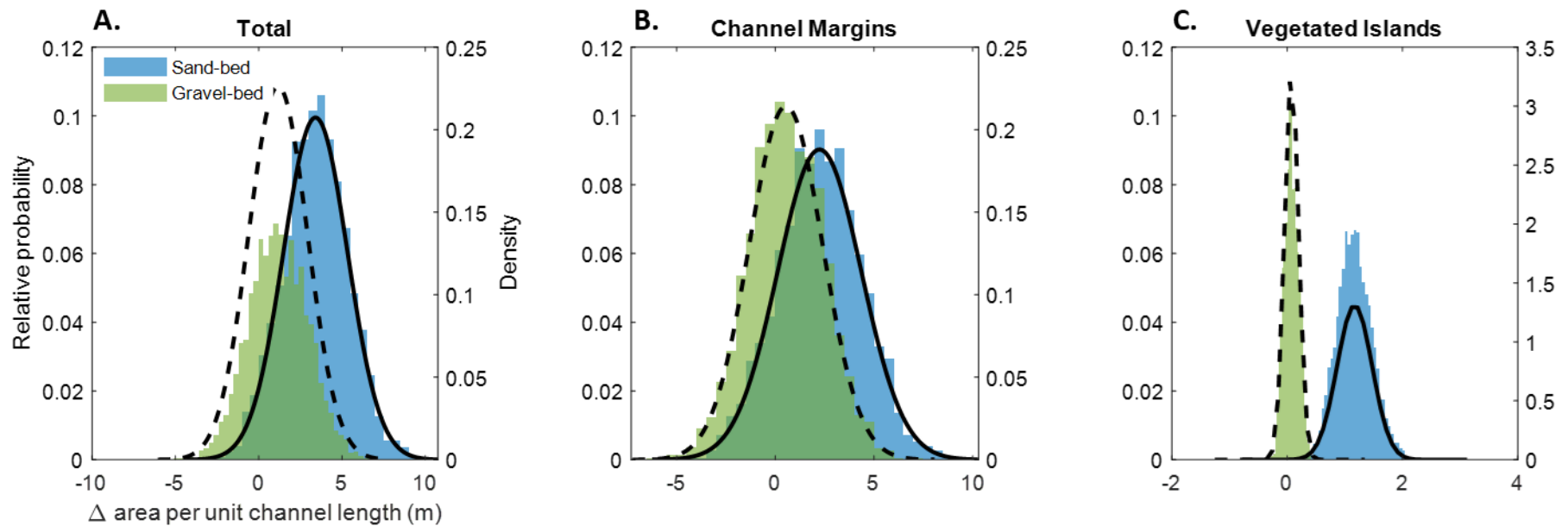
Figure A-1. Planimetric channel change measured in the sand-bed portion of the Yampa River and the Little Snake River (blue) compared to planform channel change in the gravel-bed portion of the Yampa River (green). Planimetric channel change was calculated from an aerial image time-series from 2013 to 2019. Positive values indicate accumulation and negative values erosion. Total planimetric channel change in (A) was subdivided into changes that occurred along the channel margins (B) and the vegetated islands (C). Probability density functions that fit the distribution of areal change are shown as dashed lines for the gravel-bed portion of the Yampa River and as solid lines for the sand-bed portion of the Yampa River and the Little Snake River. There was a tendency for the sand bed portion of the Yampa River and the Little Snake River to accumulate sediment along the channel margins and vegetated islands, but there was no significant planimetric change in the gravel-bed portion of the Yampa River.
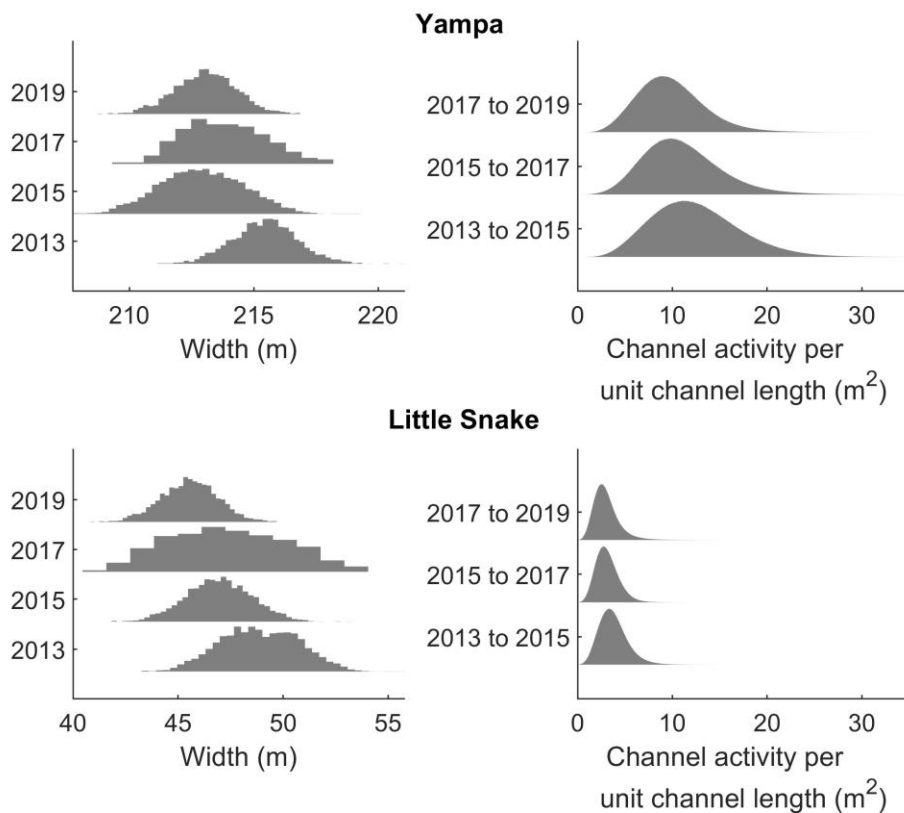
Figure A-2. Planimetric channel change measured from repeat aerial images on the sand bed segment of the Yampa River in Deerlodge Park and the Little Snake River downstream from the Lily gage (Figure 3-1). Channel width was calculated as the total active channel area divided by the centerline length and channel activity was calculated as the sum of erosional and depositional areas normalized by the channel centerline length.

Table A-1. Probability that the floodplain height in each row is greater than the floodplain height in each column (P[row>column]). Veg Ers = vegetated island erosion; Veg Dep = vegetated island deposition; Margins Ers = channel margin erosion; Margins Dep = channel margins deposition. Probabilities are calculated separately for the sand-bed portion of the Yampa River in Deerlodge Park and the Little Snake River (Figure 3-1). For example, row 2 column 1 is the probability that the height of floodplain accretion is greater than the height of the eroding floodplain along the vegetated islands in Deerlodge Park.

Deerlodge	Veg Ers	Veg Dep	Margins Ers	Margins Dep
Veg Ers	---------	0.8	0.26	0.68
Veg Dep	0.2	---------	0.06	0.47
Margins Ers	0.73	0.94	---------	0.84
Margins Dep	0.32	0.53	0.16	---------
Little Snake	Veg Ers	Veg Dep	Margins Ers	Margins Dep
Veg Ers	---------	0.71	0.23	0.41
Veg Dep	0.29	---------	0.11	0.21
Margins Ers	0.77	0.89	---------	0.71
Margins Dep	0.59	0.79	0.29	---------

Table A-2. Probability that the Yampa River floodplain height is greater than the Little Snake River floodplain height. Veg Ers = vegetated island erosion; Veg Dep = vegetated island deposition; Margins Ers = channel margin erosion; Margins Dep = channel margins deposition.

	P(Yampa>Little Snake)
Veg Ers	0.79
Veg Dep	0.76
Margins Ers	0.84
Margins Dep	0.57

Table A-3. The probability that the percent of the grain size in each row is greater than the percent of the grain size in each column (P[row>column]). Probabilities are calculated separately for the cap and the base facies. For example, row 2 column 1 is the probability that the percent of very fine sand in the cap facies is greater than the percent of silt/clay in the base facies.

Cap	silt/clay	v fine	fine	medium	coarse	v coarse
silt/clay	---------	0.78	0.79	0.88	0.97	0.99
v fine	0.22	---------	0.54	0.75	0.97	0.99
fine	0.2	0.45	---------	0.71	0.94	0.99
medium	0.11	0.25	0.29	---------	0.78	0.94
coarse	0.03	0.03	0.06	0.22	---------	0.84
v coarse	0.01	0	0.01	0.05	0.16	---------
Base	silt/clay	v fine	fine	medium	coarse	v coarse
silt/clay	---------	0.46	0.25	0.06	0.05	0.39
v fine	0.53	---------	0.28	0.08	0.06	0.41
fine	0.75	0.72	---------	0.23	0.15	0.66
medium	0.94	0.92	0.77	---------	0.34	0.9
coarse	0.95	0.94	0.85	0.66	---------	0.93
v coarse	0.61	0.57	0.34	0.1	0.08	---------

	2013 to 2019		2013 to 2015		2015 to 2017		2017 to 2019	
	95% CI	68% CI	95% CI	68% CI	95% CI	68% CI	95% CI	68% CI
Total Budget								
silt/clay	-0.4 to 1.2	-0.04 to 0.6	-1.2 to 3.6	-0.3 to 1.8	-3.3 to 1.8	-1.5 to 0.6	-1.8 to 2.7	-0.7 to 1.2
total sand	-3.2 to 4.3	-1.4 to 2.2	-7.2 to 14	-2.5 to 7.5	-15 to 7.0	-8.4 to 2.1	-9.5 to 10	-5.0 to 4.0
very fine sand	-0.3 to 0.8	-0.05 to 0.4	-0.86 to 2.4	-0.2 to 1.3	-2.3 to 1.3	-1.1 to 0.4	-1.4 to 1.8	-0.5 to 0.8
fine sand	-0.6 to 1.0	-0.2 to 0.5	-1.5 to 3.2	-0.3 to 1.5	-3.2 to 1.6	-1.5 to 0.5	-2.1 to 2.2	-0.7 to 1.0
medium sand	-0.98 to 1.3	-0.4 to 0.6	-2.3 to 4.1	-0.7 to 1.9	-4.5 to 1.9	-2.2 to 0.5	-3.0 to 2.8	-1.2 to 1.1
coarse sand	-1.3 to 1.4	-0.5 to 0.6	-2.5 to 4.9	-1.0 to 2.1	-5.4 to 2.2	-2.6 to 0.5	-3.9 to 3.0	-1.7 to 1.0
very coarse sand	-0.4 to 0.5	-0.1 to 0.2	-0.83to 1.5	-0.3 to 0.6	-1.8 to 0.6	-0.7 to 0.2	-1.3 to 0.9	-0.4 to 0.3
Channel Margins Budget								
silt/clay	-0.5 to 0.5	-0.1 to 0.2	-1 to 1.8	-0.3 to 0.6	-2.1 to 0.8	-0.8 to 0.2	1.5 to 1.2	-0.4 to 0.4
total sand	-2.9 to 3.0	-1.3 to 1.2	-5.9 to 11.2	-2.2 to 5.2	-12.3 to 5.3	-6.0 to 1.7	-8.7 to 7.5	-3.9 to 3
very fine sand	-0.1 to 0.1	-0.5 to 0.4	-2.4 to 3.8	-0.9 to 1.8	-4.4 to 2.0	-2.2 to 0.5	-3.1 to 2.9	-1.5 to 1.0
fine sand	-1.0 to 1.1	-0.4 to 0.4	-2.1 to 3.8	-0.7 to 1.7	-4.2 to 1.9	-2.0 to 0.5	-2.9 to 2.7	-1.3 to 1.0
medium sand	-0.8 to 0.8	-0.2 to 0.3	-1.5 to 3.0	-0.4 to 1.2	-3.2 to 1.4	-1.3 to 0.4	-2.4 to 2.0	-0.3 to 0.6
coarse sand	-0.4 to 0.4	-0.1 to 0.1	-0.7 to 1.4	-0.2 to 0.5	-1.6 to 0.6	-0.6 to 0.2	-1.2 to 0.8	-0.4 to 0.3
very coarse sand	-0.1 to 0.1	-0.04 to 0.04	-0.3 to 0.4	-0.08 to 0.1	-0.5 to 0.2	-0.2 to 0.05	-0.4 to 0.3	-0.1 to 0.08
Vegetated Islands Budget								
silt/clay	**0 to 0.2**	*0 to 0.02*	-0.04 to 0.3	*0 to 0.1*	-0.2 to 0.2	-0.07 to 0.06	-0.08 to 0.3	-0.01 to 0.1
total sand	**0 to 1.1**	*0.2 to 0.7*	-0.3 to 1.9	*0.1 to 1.0*	-1.3 to 1.1	-0.5 to 0.5	-0.5 to 2.0	-0.06 to 1.0
very fine sand	**0 to 0.4**	*0.05 to 0.2*	-0.09 to 0.7	*0 to 0.4*	-0.5 to 0.4	-0.2 to 0.2	-0.2 to 0.7	-0.02 to 0.4
fine sand	**0 to 0.4**	*0.05 to 0.2*	-0.9 to 0.7	*0 to 0.3*	-0.4 to 0.4	-0.2 to 0.1	-0.2 to 0.7	-0.02 to 0.3
medium sand	**0 to 0.3**	*0 to 0.1*	-0.08 to 0.5	-0.01 to 0.2	-0.3 to 0.3	-0.1 to 0.1	-0.1 to 0.5	-0.02 to 0.3
coarse sand	**0 to 0.1**	*0 to 0.06*	-0.03 to 0.3	*0 to 0.09*	-0.2 to 0.1	-0.05 to 0.05	-0.07 to 0.3	*0 to 0.1*
very coarse sand	**0 to 0.05**	*0 to 0.02*	-0.01 to 0.08	*0 to 0.03*	-0.05 to 0.04	-0.02 to 0.01	-0.02 to 0.09	*0 to 0.03*

[a]net change in sediment storage in 10^4xMT/yr

[b]net change in sediment storage is demonstrably significant for bolded values and likely significant for italic bolded values

Table A-4. Results of the partitioned morphological sediment budget during each temporal subset. The 95% and 68% credible intervals (CI) are reported. A bolded 95% CI indicates the budget is significant. A bolded and italic 68% CI indicates that the budget is likely significant.

References

Anderson SW. 2019. Uncertainty in quantitative analyses of topographic change: error propagation and the role of thresholding. Earth Surface Processes and Landforms **44** : 1015–1033. DOI: 10.1002/esp.4551

Donovan M, Belmont P, Notebaert B, Coombs T, Larson P, Souffront M. 2019. Accounting for uncertainty in remotely-sensed measurements of river planform change. Earth-Science Reviews **193** : 220–236. DOI: 10.1016/j.earscirev.2019.04.009

Kondrashov D, Ghil M. 2006. Spatio-temporal filling of missing points in geophysical data sets. Nonlinear Processes in Geophysics **13** : 151–159.

Legleiter CJ. 2012. Remote measurement of river morphology via fusion of LiDAR topography and spectrally based bathymetry. Earth Surface Processes and Landforms **37** : 499–518. DOI: 10.1002/esp.2262

Legleiter CJ, Kyriakidis PC. 2007. Forward and Inverse Transformations between Cartesian and Channel-fitted Coordinate Systems for Meandering Rivers. Mathematical Geology **38** : 927–958. DOI: 10.1007/s11004-006-9056-6

Leonard CM, Legleiter CJ, Lea DM, Schmidt JC. 2020. Measuring channel planform change from image time series: A generalizable, spatially distributed, probabilistic method for quantifying uncertainty. Earth Surface Processes and Landforms **45** : 2727–2744. DOI: https://doi.org/10.1002/esp.4926

Rubin DM, Topping DJ. 2001. Quantifying the relative importance of flow regulation and grain size regulation of suspended sediment transport α and tracking changes in grain size of bed sediment β. Water Resources Research **37** : 133–146.

Rubin DM, Topping DJ. 2008. Correction to "Quantifying the relative importance of flow regulation and grain size regulation of suspended sediment transport α and tracking changes in grain size of bed sediment β." Water Resources Research **44** : W09701. DOI: 10.1029/2008WR006819

Schoellhamer DH. 2001. Singular spectrum analysis for time series with missing data. Geophysical Research Letters **28** : 3187–3190.

Takasu T, Yasuda A. 2009. Development of the low-cost RTK-GPS receiver with an open source program package RTKLIB

APPENDIX B

Supporting Information for Chapter 4

Text B1.

Flow within the rectangular channel is described by the 1D shallow water

equation of mass and momentum conservation.

$$\frac{\partial h}{\partial t} + \frac{\partial uh}{\partial x} = 0 \qquad (B-1)$$

$$\frac{\partial uh}{\partial t} + \frac{\partial u^2 h}{\partial x} = -gh\frac{\partial h}{\partial x} + ghS - ghS_f \qquad (B-2)$$

where u is the mean flow velocity, h is the mean flow depth, x is the streamwise

coordinate, t is time, g is gradational acceleration, S is bed slope, and S_f is local fraction

slope. When flow is considered quasi-steady the time derivatives in Equations B-1 and B-

2 can be dropped, leading to the following backwater formulation:

$$q_w = uh \qquad (B-3)$$

$$S - \frac{\partial h}{\partial x} - \frac{u}{g}\frac{\partial u}{\partial x} = S_f \qquad (B-4)$$

where q_w is the volumetric flow rate per unit channel width, $q_w=Q/b$, with Q being the

flow discharge. The friction slope is specified using the Wright and Parker (2004b)

formulation that accounts for the effects of density stratification and flow resistance over

dunes:

$$S_f = \left[\left(\frac{D_{50}}{h}\right)^{\frac{5}{3}} \frac{\alpha q_*}{8.32}\left(\frac{k_c}{D_{50}}\right)^{\frac{1}{6}}\right]^2 \qquad (B-5)$$

where D_{50} is the median grain size of the bed material, q_* is the dimensionless discharge

$\left(\frac{q_w}{\sqrt{gD_{50}}\,D_{50}}\right)$, k_c is the composite roughness that accounts for skin friction and form drag,

and α is a parameter that accounts or density stratification caused by suspended sediment

transport.

Wright and Parker (2004b) originally defined α as a function of channel slope *(S)*

using the assumption of uniform flow for equilibrium conditions; however, flow in our

model is steady but nonuniform and therefore we substitute the friction slope *(S_f)* for the

channel slope *(S)* (Viparelli et al., 2015):

$$\alpha = \begin{cases} 1 - 0.06\left(\frac{C_5}{S_f}\right)^{0.77} & for \ \frac{C_5}{S_f} \leq 10 \\[3mm] 0.67 - 0.0025\left(\frac{C_5}{S_f}\right) & for \ \frac{C_5}{S_f} \leq 10 \end{cases} \qquad (B-6)$$

where C_5 total volumetric near-bed volumetric sediment concentration at 5% of the total

flow depth, calculated as the sum of the volumetric near-bed concentration over k^{th} grain

sizes (C_{5k}). In the case of equilibrium suspension, $C_{5k} = E_{sk}F_k$, where E_{sk} is the entrainment

rate for the kth grain size calculated by the Wright and Parker (2004b) relation and F_k is

the fraction of the kth grain size on the bed surface:

$$E_{sk} = \frac{B\,(\lambda X)^5}{\left[1 + \left(\frac{B}{0.3}\right)\right](\lambda X)^5} \qquad (B-7)$$

$$X = \left[\frac{u_{*s}}{W_{sk}}\,R_{pk}^{0.6}\right]S_f^{0.8}\left(\frac{D_k}{D_{50}}\right)^{0.2} \qquad (B-8)$$

where B is a constant equal to 7.8×10^{-7}, λ is a straining function that acts to suppress

entrainment bed sediment sorting increases $= 1-0.28\sigma_\phi$; $\sigma_\phi =$ standard deviation of the bed

material on the ϕ scale, $D_k = k^{th}$ grain size, $u_{*s} =$ shear velocity due to skin friction $=$

$\sqrt{gh_sS}$; h_s = depth due to skin friction calculated by Equation B-10, W_{sk} = fall velocity

for the kth grain size, and R_{pk} = particle Reynolds number for the kth grain size = $\frac{\sqrt{RgD_k}D_k}{v}$;

$R = (\rho_s/\rho)-1$ = submerged specific gravity and v = kinematic viscosity.

The roughness due to skin friction (k_c) is related to the composite roughness (k_c) by:

$$k_c = \left(\frac{\tau^*}{\tau_s^*}\right)^4 3D_{90} \qquad (B-9)$$

where τ^* = Shields number = hS/RD_{50}, D_{90} = grain size that is finer 90% of the bed

material, and τ^*_s = Shields number associated with skin friction defined as (Wright and

Parker, 2004b):

$$\tau_s^* = 0.05 + 0.7\left(\tau_* Fr^{0.7}\right)^{0.8} \qquad (B-10)$$

where Fr = Froude number = $qw/\sqrt{g}h^{1.5}$. The Wright and Parker (2004b) formulation

for frictional resistance requires an iterative solution of Equations B-5 through B-10.

Text B2.

The grain size specific formulation of the Exner equation is used to express the

conservation of sediment mass for grain size mixtures in the active layer (Parker et al.,

2007). The river bed is divided into an upper active layer that exchanges with the bed

material load, lower substrate layer that remains constant, and an interface layer that

exchanges sediment from the between the active layer and the substrate as the bed

aggrades and degrades (Hirano, 1971). The grain size of the bed material load, and in the

active, interface, and substrate layers are discretized by fraction of f_{tk}, f_{sk}, f_{ik}, and f_{bk},

respectively, in K=1:n bins segregated into ¼ φ sizes on the sedimentological scale. All

fractions sum to unity and the active layer is considered completely mixed at each timestep. The Exner equation for mass conservation of each grain size bin is given by:

$$(1 - \lambda_p)\left[f_{ik}\frac{\partial}{\partial t}(\eta - L_a) + \frac{\partial f_{sk}L_a}{\partial t}\right] = \frac{\partial q_s f_{tk}}{\partial x} \qquad (B-11)$$

where λ_p = bed porosity, η = bed elevation, q_s = total volumetric bed material transport rate per unit width, and L_a is the active layer thickness. For our sand bed model, the active layer thickness is specified as the height of the bedforms. The dune height is predicted as a function of flow depth using the relation of Julien and Klaassen (1995).

We arrive at the standard Exner equation that describes the morphodynamic evolution of the bed when Equation B-11 is summed over all grain size fractions:

$$(1 - \lambda_p)\frac{\partial \eta}{\partial t} = -\frac{\partial q_s}{\partial x}. \qquad (B-12)$$

Reducing Equation B-11 with Equation B-12 leads to the following relation describing the evolution of the bed grain size in the active layer:

$$(1 - \lambda_p)\left[L_a\frac{\partial f_{sk}}{\partial t} + (f_{sk} - f_{ik})\frac{\partial L_a}{\partial t}\right] = -\frac{\partial(q_s f_{sk})}{\partial x} + f_{ik}\frac{\partial q_s}{\partial x}. \qquad (B-13)$$

The interface layer (f_{ik}) evolves as the bed aggrades and erodes using the relation formulated by Hoey and Ferguson (1994) and Toro-Escobar et al (1996). During erosion, f_{ik} becomes that of the substrate layer. During aggradation, Hoey and Ferguson (1994) proposed a relations in which f_{ik} becomes a weighted fraction of the active layer and bed material transport:

$$f_{ik} = cf_{tk} + (1 - c)f_{sk} \qquad (B-14)$$

where c = constant that specifies the proportion of the active layer and bed material transport that gets passed to the interface layer. Bed material in transport can get passed

to the interface layer through kinetic sieving in gravel bed rivers. However, the gradation

of grain sizes in transport is smaller in sand bed rivers making it unlikely that finer grains

can pass through a complete dune height to the interface layer. Thus, following Wright

and Parker (2005), c was set to zero and the f_{ik} becomes the active layer during

aggradation.

Text B3.

Grain-size specific volumetric bed material transport rates are calculated using

two different models – one for suspended load and one for bed load – which are summed

over each size fraction to predict the total volumetric transport rate. For suspension, we

use the Wright and Parker (2004b) entrainment model (W-P) as described in Equations

B-7 and B-8, coupled with a Rouse profile and van Rijn (1984) initiation of suspension

criterion:

$$q_{ssk} = u_* h \left[\left(\frac{9.7}{\alpha} \right) C_{5k} \left(\frac{h}{k_c} \right)^{\frac{1}{6}} I \right] \qquad (B-15)$$

where q_{ssk} = volumetric suspended load transport rate for the kth grain size fraction, u_* =

shear velocity = $\sqrt{ghS}$, and I = integrated Rouse Profile. W-P is a modified version of the

Garcia and Parker (1991) entrainment model that accounts for reduced mixing due to

density stratification in the presence of large suspended loads. Both entrainment models

include a mixed-size hiding function tested against field data. Bed load is calculated from

the Ashida and Michiue (1972) relation (A-M) which includes the Egiazaroff (1965)

hiding function:

$$q_{bk} = 17 f_{sk} \sqrt{gRD_k}\, D_k\, (\tau_{*k} - \tau_{*ck})\left(\sqrt{\tau_{*k}} - \sqrt{\tau_{*cr(k)}}\right) \qquad (B-16)$$

where q_{bk} = volumetric bed load transport rate for the kth grain size fraction and τ_{*k} and

τ_{*ck} = the Shields number and critical Shields number for the kth grain size fraction,

respectively. A-M was developed from flume measurements of sand bed load, making

this relation ideal for our modeling purpose.

References

Ashida K, Michiue M. 1972. Study on Hydraulic Resistance and Bedload Transport Rate in Alluvial Streams. Trans. Jpn. Soc. Civil Engng. **206** : 59–69.

Egiazaroff IV. 1965. Calculation of Nonuniform Sediment Concentrations. Journal of the Hydraulics Division **91** : 225–247. DOI: 10.1061/JYCEAJ.0001277

Garcia M, Parker G. 1991. Entrainment of Bed Sediment into Suspension. Journal of Hydraulic Engineering **117** : 414–435. DOI: 10.1061/(ASCE)0733-9429(1991)117:4(414)

Hirano M. 1971. On riverbed variation with armoring. Trans. Jpn. Soc. Civil Engng. **195** : 55–65.

Hoey TB, Ferguson R. 1994. Numerical simulation of downstream fining by selective transport in gravel bed rivers: Model development and illustration. Water Resources Research **30** : 2251–2260. DOI: 10.1029/94WR00556

Julien PY, Klaassen GJ. 1995. Sand-Dune Geometry of Large Rivers during Floods. Journal of Hydraulic Engineering **121** : 657–663. DOI: 10.1061/(ASCE)0733-9429(1995)121:9(657)

Parker G, Hassan M, Wilcock P. 2007. 10 Adjustment of the bed surface size distribution of gravel-bed rivers in response to cycled hydrographs. In Developments in Earth Surface Processes , Habersack H, Piégay H, and Rinaldi M (eds). Elsevier; 241–285.

van Rijn LC. 1984. Sediment Transport, Part II: Suspended Load Transport. Journal of Hydraulic Engineering **110** : 1613–1641. DOI: 10.1061/(ASCE)0733-9429(1984)110:11(1613)

Toro-Escobar CM, Paola C, Parker G. 1996. Transfer function for the deposition of poorly sorted gravel in response to streambed aggradation. Journal of Hydraulic Research **34** : 35–53. DOI: 10.1080/00221689609498763

Viparelli E, Nittrouer JA, Parker G. 2015. Modeling flow and sediment transport dynamics in the lowermost Mississippi River, Louisiana, USA, with an upstream

alluvial-bedrock transition and a downstream bedrock-alluvial transition: Implications for land building using engineered diversions. Journal of Geophysical Research: Earth Surface **120** : 534–563. DOI: 10.1002/2014JF003257

Wright S, Parker G. 2004. Flow Resistance and Suspended Load in Sand-Bed Rivers: Simplified Stratification Model. Journal of Hydraulic Engineering **130** : 796–805. DOI: 10.1061/(ASCE)0733-9429(2004)130:8(796)

Wright S, Parker G. 2005. Modeling downstream fining in sand-bed rivers. I: formulation. Journal of Hydraulic Research **43** : 613–620. DOI: 10.1080/00221680509500381

APPENDIX C

License Agreement

JOHN WILEY AND SONS LICENSE
TERMS AND CONDITIONS

Oct 19, 2022

This Agreement between Dr. Christy Leonard ("You") and John Wiley and Sons ("John Wiley and Sons") consists of your license details and the terms and conditions provided by John Wiley and Sons and Copyright Clearance Center.

License Number	5412650327672
License date	Oct 19, 2022
Licensed Content Publisher	John Wiley and Sons
Licensed Content Publication	Earth Surface Processes and Landforms
Licensed Content Title	Measuring channel planform change from image time series: A generalizable, spatially distributed, probabilistic method for quantifying uncertainty
Licensed Content Author	Christina M. Leonard, Carl J. Legleiter, Devin M. Lea, et al
Licensed Content Date	Jul 7, 2020
Licensed Content Volume	45
Licensed Content Issue	11

Licensed Content Pages	18

Type of use	Dissertation/Thesis

Requestor type Author of this Wiley article

Format	Print and electronic

Portion	Full article

Will you be translating?	No

Title	River Response to Sediment Supply: The Sand Bed Case

Institution name	Utah State University

Expected presentation date	Oct 2022

Requestor Location	Dr. Christy Leonard 1591 East 1220 North LOGAN, UT 84341 United States Attn: Dr. Christy Leonard

Publisher Tax ID	EU826007151

Total	0.00 USD

Terms and Conditions

TERMS AND CONDITIONS

This copyrighted material is owned by or exclusively licensed to John Wiley & Sons, Inc. or one of its group companies (each a"Wiley Company") or handled on behalf of a society with which a Wiley Company has exclusive publishing rights in relation to a particular work (collectively "WILEY"). By clicking "accept" in connection with completing this licensing transaction, you agree that the following terms and conditions apply to this transaction (along with the billing and payment terms and conditions established by the Copyright Clearance Center Inc., ("CCC's Billing and Payment terms and conditions"), at the time that you opened your RightsLink account (these are available at any time at http://myaccount.copyright.com).

Terms and Conditions

- The materials you have requested permission to reproduce or reuse (the "Wiley Materials") are protected by copyright.

- You are hereby granted a personal, non-exclusive, non-sub licensable (on a stand-alone basis), non-transferable, worldwide, limited license to reproduce the Wiley Materials for the purpose specified in the licensing process. This license, **and any CONTENT (PDF or image file) purchased as part of your order,** is for a one-time use only and limited to any maximum distribution number specified in the license. The first instance of republication or reuse granted by this license must be completed within two years of the date of the grant of this license (although copies prepared before the end date may be distributed thereafter). The Wiley Materials shall not be used in any other manner or for any other purpose, beyond what is granted in the license. Permission is granted subject to an appropriate acknowledgement given to the author, title of the material/book/journal and the publisher. You shall also duplicate the copyright notice that appears in the Wiley publication in your use of the Wiley Material. Permission is also granted on the understanding that nowhere in the text is a previously published source acknowledged for all or part of this Wiley Material. Any third party content is expressly excluded from this permission.

- With respect to the Wiley Materials, all rights are reserved. Except as expressly granted by the terms of the license, no part of the Wiley Materials may be copied, modified, adapted (except for minor reformatting required by the new Publication), translated, reproduced, transferred or distributed, in any form or by any means, and no derivative works may be made based on the Wiley Materials without the prior permission of the respective copyright owner.**For STM Signatory Publishers clearing permission under the terms of the STM Permissions Guidelines only, the terms of the license are extended to include subsequent editions and for editions in other languages, provided such editions are for the work as a whole in situ and does not involve the separate exploitation of the permitted figures or extracts,** You may not alter, remove or suppress in any manner any copyright, trademark or other notices displayed by the Wiley Materials. You may not license, rent, sell, loan, lease, pledge, offer as security, transfer or assign the Wiley Materials on a stand-alone basis, or any of the rights granted to you hereunder to any other person.

- The Wiley Materials and all of the intellectual property rights therein shall at all times remain the exclusive property of John Wiley & Sons Inc, the Wiley Companies, or their respective licensors, and your interest therein is only that of having possession of and the right to reproduce the Wiley Materials pursuant to Section 2 herein during the continuance of this Agreement. You agree that you own no right, title or interest in or to the Wiley Materials or any of the intellectual property rights therein. You shall have no rights hereunder other than the license as provided for above in Section 2. No right,

license or interest to any trademark, trade name, service mark or other branding ("Marks") of WILEY or its licensors is granted hereunder, and you agree that you shall not assert any such right, license or interest with respect thereto

- NEITHER WILEY NOR ITS LICENSORS MAKES ANY WARRANTY OR REPRESENTATION OF ANY KIND TO YOU OR ANY THIRD PARTY, EXPRESS, IMPLIED OR STATUTORY, WITH RESPECT TO THE MATERIALS OR THE ACCURACY OF ANY INFORMATION CONTAINED IN THE MATERIALS, INCLUDING, WITHOUT LIMITATION, ANY IMPLIED WARRANTY OF MERCHANTABILITY, ACCURACY, SATISFACTORY QUALITY, FITNESS FOR A PARTICULAR PURPOSE, USABILITY, INTEGRATION OR NON-INFRINGEMENT AND ALL SUCH WARRANTIES ARE HEREBY EXCLUDED BY WILEY AND ITS LICENSORS AND WAIVED BY YOU.

- WILEY shall have the right to terminate this Agreement immediately upon breach of this Agreement by you.

- You shall indemnify, defend and hold harmless WILEY, its Licensors and their respective directors, officers, agents and employees, from and against any actual or threatened claims, demands, causes of action or proceedings arising from any breach of this Agreement by you.

- IN NO EVENT SHALL WILEY OR ITS LICENSORS BE LIABLE TO YOU OR ANY OTHER PARTY OR ANY OTHER PERSON OR ENTITY FOR ANY SPECIAL, CONSEQUENTIAL, INCIDENTAL, INDIRECT, EXEMPLARY OR PUNITIVE DAMAGES, HOWEVER CAUSED, ARISING OUT OF OR IN CONNECTION WITH THE DOWNLOADING, PROVISIONING, VIEWING OR USE OF THE MATERIALS REGARDLESS OF THE FORM OF ACTION, WHETHER FOR BREACH OF CONTRACT, BREACH OF WARRANTY, TORT, NEGLIGENCE, INFRINGEMENT OR OTHERWISE (INCLUDING, WITHOUT LIMITATION, DAMAGES BASED ON LOSS OF PROFITS, DATA, FILES, USE, BUSINESS OPPORTUNITY OR CLAIMS OF THIRD PARTIES), AND WHETHER OR NOT THE PARTY HAS BEEN ADVISED OF THE POSSIBILITY OF SUCH DAMAGES. THIS LIMITATION SHALL APPLY NOTWITHSTANDING ANY FAILURE OF ESSENTIAL PURPOSE OF ANY LIMITED REMEDY PROVIDED HEREIN.

- Should any provision of this Agreement be held by a court of competent jurisdiction to be illegal, invalid, or unenforceable, that provision shall be deemed amended to achieve as nearly as possible the same economic effect as the original provision, and the legality, validity and enforceability of the remaining provisions of this Agreement shall not be affected or impaired thereby.

- The failure of either party to enforce any term or condition of this Agreement shall not constitute a waiver of either party's right to enforce each and every term and condition of this Agreement. No breach under this agreement shall be deemed waived or excused by either party unless such waiver or consent is in writing signed by the party granting such waiver or consent. The waiver by or consent of a party to a breach of any provision of this Agreement shall not operate or be construed as a waiver of or consent to any other or subsequent breach by such other party.

- This Agreement may not be assigned (including by operation of law or otherwise) by you without WILEY's prior written consent.

- Any fee required for this permission shall be non-refundable after thirty (30) days from receipt by the CCC.

- These terms and conditions together with CCC's Billing and Payment terms and conditions (which are incorporated herein) form the entire agreement between you and WILEY concerning this licensing transaction and (in the absence of fraud) supersedes all prior agreements and representations of the parties, oral or written. This Agreement may not be amended except in writing signed by both parties. This Agreement shall be binding upon and inure to the benefit of the parties' successors, legal representatives, and authorized assigns.

- In the event of any conflict between your obligations established by these terms and conditions and those established by CCC's Billing and Payment terms and conditions, these terms and conditions shall prevail.

- WILEY expressly reserves all rights not specifically granted in the combination of (i) the license details provided by you and accepted in the course of this licensing transaction, (ii) these terms and conditions and (iii) CCC's Billing and Payment terms and conditions.

- This Agreement will be void if the Type of Use, Format, Circulation, or Requestor Type was misrepresented during the licensing process.

- This Agreement shall be governed by and construed in accordance with the laws of the State of New York, USA, without regards to such state's conflict of law rules. Any legal action, suit or proceeding arising out of or relating to these Terms and Conditions or the breach thereof shall be instituted in a court of competent jurisdiction in New York County in the State of New York in the United States of America and each party hereby consents and submits to the personal jurisdiction of such court, waives any objection to venue in such court and consents to service of process by registered or certified mail, return receipt requested, at the last known address of such party.

WILEY OPEN ACCESS TERMS AND CONDITIONS

Wiley Publishes Open Access Articles in fully Open Access Journals and in Subscription journals offering Online Open. Although most of the fully Open Access journals publish open access articles under the terms of the Creative Commons Attribution (CC BY) License only, the subscription journals and a few of the Open Access Journals offer a choice of Creative Commons Licenses. The license type is clearly identified on the article.

The Creative Commons Attribution License

The Creative Commons Attribution License (CC-BY) allows users to copy, distribute and transmit an article, adapt the article and make commercial use of the article. The CC-BY license permits commercial and non-

Creative Commons Attribution Non-Commercial License

The Creative Commons Attribution Non-Commercial (CC-BY-NC)License permits use, distribution and reproduction in any medium, provided the original work is properly cited and is not used for commercial purposes.(see below)

CURRICULUM VITAE

CHRISTINA LEONARD

Phone: (260) 402-2214   5210 Old Main Hill, BVR 361
christy.leonard@usu.edu   Logan, UT 84322-5210
https://qcnr.usu.edu/coloradoriver/leonard

EDUCATION

PhD   Utah State University, Watershed Sciences   Defense exam passed Sept., 2022
Dissertation: *Predicting a Sand Bed River Response to Supply Disturbance: Influence of Bed Texture on Channel Adjustment*
Advisor: John C. Schmidt

MA   University of Wyoming, Geography/Water Resources   2015
Thesis: *Evaluating the effects of floodplain constriction along a high energy gravel*
bed river: Snake River, WY
Advisor: Carl J. Legleiter

BS   University of Vermont, Geology   2009

EMPLOYMENT

Graduate Research Assistant, Utah State University   2017-present

Geologist, U.S. Army Corps of Engineers, Sacramento District   2009-2017
GS-11
Selected duties: Paleoflood hydrology for dam safety analysis, meander migration modeling, alluvial fan characterization for FEMA Flood Hazard Mapping, geotechnical and environmental drilling explorations, Section 404 of Clean Water Act compliance, groundwater monitoring well installation and sampling, well pumping tests.

Research Assistant, Geology, University of Vermont   2008

HONARS AND AWARDS

PEO Scholar Award *($20,000)*   2021

Geologic Society of America Graduate Student Research Grant *($1,200)*   2020

Babbitt Dissertation Fellowship *($10,000)*   2019

Colorado River Doctoral Scholar   2018

Outstanding Geography Student Award	2015
SMART* Scholarship *($60,000)* *Department of Defense Science Mathematics and Research for Transformation*	2013-2015
University of Wyoming Department of Geography Research Grant *($850)*	2014
Shelmon Center for Quaternary Studies Grant *($650)*	2014
University of Vermont Hawley Award *($2,000)*	2008
University of Vermont Pieratti Award *($1,000)*	2008
University of Vermont Presidential Scholarship *($15,000)*	2005-2009

RESEARCH EXPERIENCE

- Research code development for morphodynamic modeling.
- Software to characterize uncertainty in repeat aerial images.
- LiDAR point cloud processing.
- Image-derived bathymetry.
- Morphological sediment budgeting via topographic differencing and aerial images.
- 1D/2D hydraulic modeling.
- Real-time kinematic (RTK) and post-processing kinematic (PPK) surveying.
- Acoustic doppler current profiler (ADCP).
- Meander migration modeling.
- GIS and remote sensing.

TEACHING EXPERIENCE

Utah State University, Logan, UT   2018-present
Undergraduate Research Advisor, Department of Watershed Sciences
- Primary research advisor for 3 undergraduate research projects.

Utah State University, Logan, UT   2020
Teaching Assistant, Department of Watershed Sciences
- Lab development and teaching for graduate-level fluvial geomorphology course.

University of Wyoming, Laramie, WY   2015
Teaching Assistant, Geography Department
- Lab development for fluvial remote sensing course.

PUBLICIATIONS
Journal Publications

Leonard, C.M., Legleiter, C.J., Lea, D.M., and Schmidt J.C. 2020. Measuring channel planform change from image time series: A generalizable, spatially distributed, probabilistic method for quantifying uncertainty. *Earth Surface Processes and Landforms* 45: 2727-2744. DOI:10.1002/esp.4926.

Leonard, C.M., Legleiter, C.J., and Overstreet B.T. 2017. Effects of lateral confinement in natural and leveed reaches of a gravel-bed river: Snake River, Wyoming, USA. *Earth Surface Processes and Landforms* 42: 2119-2138. DOI:10.1002/esp.4157.

Leonard, C.M. and Schmidt J.C. *In Revision.* Fine-resolution grain size partitioning of a closed sediment budget. *Journal of Geophysical Research: Earth Surface*

Conference Papers
(Peer-Reviewed)

Leonard, C.M., Schmidt, J.C., Topping, D.J., and Griffiths, R.E. 2019. Interpreting flux-based sediment budgets in a habitat context: Linking precise temporal-resolution measurements of sediment flux to spatially robust characterization of channel change, *Proceedings of the 4th Joint Federal Interagency Conference on Sedimentation and Hydrologic Modeling*, June 24 – 28, 2019, Peppermill Hotel, Reno, Nevada, https://www.sedhyd.org/2019/openconf/modules/request.php?module=oc_proceedings&action=view.php&id=179&file=1/179.pdf&a=Accept.

MEETING ABSTRACTS

Leonard, C.M., Wilcock, P.R., and Schmidt, J.C., 2021. Texture or Tonnage? Sand River Response to Changes in Sediment Supply. *Fall Meeting of the American Geophysical Union*, New Orleans.

Leonard, C.M. and Schmidt, J.C, 2020. Incorporating continuous measurements of sediment transport into large river management: Case study on the Yampa and Little Snake Rivers. *Upper Colorado River Basin Water Forum*, Grand Junction.

Leonard, C.M., Schmidt, J.C, Topping, D.J., and Griffiths, R.E. 2020. Interpreting flux-based sediment budgets in a habitat context: How large must be the estimates of sediment deficit or surplus to be of concern to river and land managers? *40th Annual Researchers Meeting of the Upper Colorado River Endangered Fish Recovery Program*, Durango.

Leonard, C.M., Schmidt, J.C, Topping, D.J., and Griffiths, R.E. 2019. Partitioning a mass-balance sediment budget by sand-size classes to understand where, when, and why channel change occurs. *Fall Meeting of the American Geophysical Union*, San Francisco.

Pearce, J., Hall, B., Parola, A., Comport, B., and **Leonard, C**. 2019. Reducing uncertainty in estimating rare flood events using paleoflood analyses: Insights from an

investigation near Stillhouse Hollow Dam, Texas. *Fall Meeting of the American Geophysical Union*, San Francisco.

Leonard, C.M., Schmidt, J.C, Topping, D.J., and Griffiths, R.E. 2019. Interpreting flux-based sediment budgets in a habitat context: Linking precise temporal-resolution measurements of sediment flux to spatially robust characterization of channel change Federal *Interagency Sedimentation and Hydrologic Modeling Conference*, Reno.

Leonard, C.M., Topping, D.J., Griffiths, R.E., and Schmidt, J.C. 2018. Linking hi temporal resolution flux-based sediment budgets with channel change: *Establishing morphological meaning to measurements of sediment flux*. Fall Meeting of the American Geophysical Union, Washington, D.C.

Leonard, C.M., Hunter, L.E., Blodgett, P.J., Wiest, J.C., and Stonestreet, S.E. 2016. Using an Integrated Approach to Characterizing Alluvial Fan Flooding Hazards: A case study on a highly managed and developed alluvial fan. *Annual Meeting of the Floodplain Management Association*, Sacramento.

Kelson, K.I., England, J.F., Smith, C.H., **Leonard, C.M.**, Hall, B.M., Koutsunis, N.A., Duren, A.M., Humphrey, C., Nygaard, C.J., Potts, S.S., Mahan S. 2016. Initial USACE Paleoflood Analyses in a Risk-Informed Decision Making Framework: Improving Hydrologic Loading Input for USACE Dam Safety Evaluations. *Fifth International Paleoflood Conference*, Rapid City.

Leonard, C.M. and Legleiter, C.J. 2015. Linking River Management-Induced Perturbations of Hydrologic and Sediment Regimes to Geomorphic Processes Along a Highly-Dynamic Gravel-Bed River: Snake River, WY. *Fall Meeting of the American Geophysical Union*, San Francisco.

Leonard, C.M. and Legleiter, C.J. 2015. Evaluating the Effects of River Management by Levees on Sediment Transport and Channel Change along a Dynamic Gravel-Bed River. *Annual Meeting of the American Association of Geographers*, Chicago.

Leonard, C.M. and Legleiter, C.J. 2014. Evaluating the Effects of Constriction by Levees on a Dynamic Gravel-Bed River through Morphological Sediment Budgeting and Bed Mobility Studies, Snake River, WY. *Fall Meeting of the American Geophysical Union*, San Francisco.

PROFESSIONAL AFFILIATIONS

Geologist-in-Training Certification: ID 422 State of California Board of Professional Engineers, Land Surveyors, and Geologists *(2012-present)*

PROFESSIONAL SERVICE

Peer-Reviewed Articles for: Water Resources Research *(2020)* and Earth Surface Dynamics *(2019)*

Software review for USGS Optical River Bathymetry Toolkit (ORByT) *(2019)*